Global Gyrokinetic Study of Profile Formation and Turbulent Transport in Tokamak Plasmas

Mikiya Muto

Abstract

Turbulent transport is a key challenge in realizing nuclear fusion energy, and research based on gyrokinetic simulations is being conducted. In particular, the simulations employing the local flux-tube model have been extensively performed since their computational costs are relatively small. While these simulations are capable of evaluating turbulent transport for given background profiles, they cannot compute the changes in the profiles caused by the transport.

In this study, we first focus on entropy and perform full-f simulations to investigate the interaction between profile formation and turbulent transport. This study analyzes the fluctuation entropy related to turbulent fluctuation, which has been investigated in previous studies, and the thermodynamic entropy associated with profile formation, which cannot be computed in local simulations. The equations of these entropies are derived and the temporal evolution of each term is calculated. In addition to the result consistent with previous research, which shows that the fluctuation entropy is primarily changed by the entropy generation due to collisional dissipation D and the entropy destruction due to turbulent transport $-\Gamma$, it is shown that the thermodynamic entropy is mainly changed by Γ and the entropy destruction due to energy input/output. This indicates that the fluctuation and thermodynamic entropies interact through the entropy changes caused by the turbulent transport, signifying that the temperature profile and turbulence interact via the heat flux. Γ reduces the fluctuation entropy and increases the thermodynamic entropy, thereby not generating net entropy. The entropy equations show that the net entropy is generated due to dissipation in velocity space. Intuitively, it would seem that a larger flow would result in less randomness and, consequently, smaller entropy generation. However, it is foud that a larger flow increases D, leading to greater entropy production.

In applied research on the interaction between profiles and turbulence, we examine the interaction between profile formation and a vortex mode in the presence of a magnetic island. The vortex mode is a mesoscale mode with the same mode numbers as the magnetic island and previous studies have shown that it significantly impacts on the turbulent transport. However, the influence of the vortex mode on the profiles and the resulting changes in the dynamics of the vortex mode are not yet understood. To

self-consistently calculate the temporal evolution of the turbulence, vortex mode, and background profiles, it is necessary to conduct full-f gyrokinetic simulations. However, a standard computational method for flux-surface averaging in the presence of a magnetic island, necessary for solving the gyrokinetic Poisson equation, does not currently exist. Therefore, this study develops a new algorithm called the labeling method, which groups real-space grids based on the nearest magnetic field line. By implementing the labeling method, the previous study result that the electrostatic potential with the same mode numbers as the magnetic island and the $(m, n) = (0, 0)$ electrostatic potential oscillate together at the geodesic acoustic mode frequency is reproduced. The ion temperature gradient (ITG) turbulence simulation in the presence of the magnetic island reveal quasi-periodic transport reduction due to the interaction between the temperature profile and vortex mode. During the transport reduction phase, both the heat flux and thermal diffusivity decrease inside the island. If the heating power is increased, the transport reduction could lead to the formation of a transport barrier due to the magnetic island.

Many previous studies using global simulations have focused only on the dynamics of bulk ions and electrons, therefore discussion on profile formation and turbulent transport in the presence of impurities is insufficient. We analyze the profile formation and turbulent transport for both positive and negative impurity density gradients. When the impurity density gradient is positive, an impurity mode (IM) is theoretically predicted to become unstable and experimentally observed. However, an evaluation of the turbulent transport through global simulations is not conducted. Therefore, the IM turbulence simulations are performed. The simulation results reveal that the impurity particle flux due to the IM turbulence is an order of magnitude larger than that caused by the ITG turbulence. Additionally, the IM turbulence generates the inward ion heat flux, leading to an increase in the core bulk ion temperature. The study also examines methods of controlling particle fluxes through heating in the case of the negative impurity density gradient, not only to expel impurities but also to simultaneously facilitate fuel supply. When only electrons are heated, the particle fluxes are small, and the density profiles hardly change. When only ions are heated, the ITG turbulence drives the inward bulk ion particle flux Γ_i and the outward impurity particle flux $Z\Gamma_z$. These fluxes satisfy $\Gamma_i + Z\Gamma_z \simeq 0$ and the electron particle flux is small. When both ions and electrons are heated, the bulk ion and electron pinches are an order of magnitude greater than when only ions are heated. Simultaneously, the large outward impurity transport relaxes the impurity density profile. This result suggests that both fuel supply and impurity exhaust can be achieved by the ion and electron heating.

Acknowledgements

I would like to express gratitude to Prof. Yasuaki Kishimoto, Prof. Akihiro Ishizawa, and Dr. Kenji Imadera for their continuous support and encouragement. Prof. Kishimoto always gave me direction for my research, which helped me to always have a sense of purpose. I also learned the fascination of plasma physics and fun of research from him. Through daily discussions with Prof. Ishizawa, I was able to deepen my understanding of plasma turbulence and advance my research. Thanks to Dr. Imadera's guidance, I became able to develop codes, analyze data, and discuss results, even though I had had no knowledge or experience at all. Without their help, I would not have conducted my research. It was a great honor to have discussions and work with the great theoretical plasma physicists.

I would like to thank Ms. Tomoko Takahashi, our secretary, for all her help in purchasing goods, travel expenses, and other paperworks. I would also like to thank my mates in Fundamental Plasma and Fusion Lab. In particular, I would like to thank Mr. Daichi Nakajima, Mr. Hiroaki Ohta, Mr. Jianfu Liu, Mr. Rui Zhao, Mr. Shuhei Okuda, Mr. Shuhei Genko, Mr. Rintaro Matsumura, and Mr. Shota Yamada who were involved in the development of GKNET with me. Everyone's help was essential to my research. I am grateful to Dr. Wei Wang of Southwestern Institute of Physics in China for his assistance. I would also like to thank Dr. Naoaki Miyato of the Quantum Science and Technology Agency. He taught me the basic concepts of microscopic turbulence and fluid and gyrokinetic theory.

The simulations were performed on the JFRS-1 at the Japan International Fusion Energy Research Centre, the Plasma Simulator at the Japan National Institute for Fusion Science, and the Camphor 2 at Kyoto University through the HPCI System Research Project. This work was supported by JST SPRING, Grant Number JPMJSP2110.

Contents

Chapter 1

Introduction

1.1 Nuclear fusion energy

Energy demand is increasing with the advancement of society and the growth of population. On the other hand, thermal power generation, one of the main power generation methods today, has problems. Power generation using fossil fuels releases carbon dioxide, sulfur oxides, and nitrogen oxides, which contribute to global warming and environmental pollution. The main fossil fuels are coal, petroleum, and natural gas, each with specific advantages and disadvantages. Coal is a fossil of plant dating from the Paleozoic to around the Cenozoic Era. It is inexpensive and the reserves are less uneven, however, due to its solid state, coal mining and transportation present challenges. Petroleum is formed by the decomposition of dead animals and plants deposited during the Mesozoic Era by earth pressure and geothermal heat, and while it is easy to handle because it is liquid, the distribution of the reserves is uneven. Natural gas emits less carbon dioxide than coal or oil. However, storage and transportation of it pose challenges. Fossil fuels could be depleted because the timescale for consuming fossil fuels is very short compared to the timescale for making them. Power generation by fission energy, a method of power generation that does not cause global warming or air pollution, has also been put to practical use. Fission energy is the energy produced by the nuclear fission. The binding energy per nucleon reaches a maximum at a mass number of about 60, as shown in Fig. 1.1.

Figure 1.1 shows the binding energy per nucleon $B(Z,N)/(Z+N)$ as a function of the number of protons Z and neutrons N based on the semi-empirical mass formula

$$B(Z,N) = 15.753(Z+N) - 17.804(Z+N)^{2/3} - 0.710\frac{Z^2}{(Z+N)^{1/3}} - 23.69\frac{(N-Z)^2}{(Z+N)} + \delta(Z,N), \tag{1.1}$$

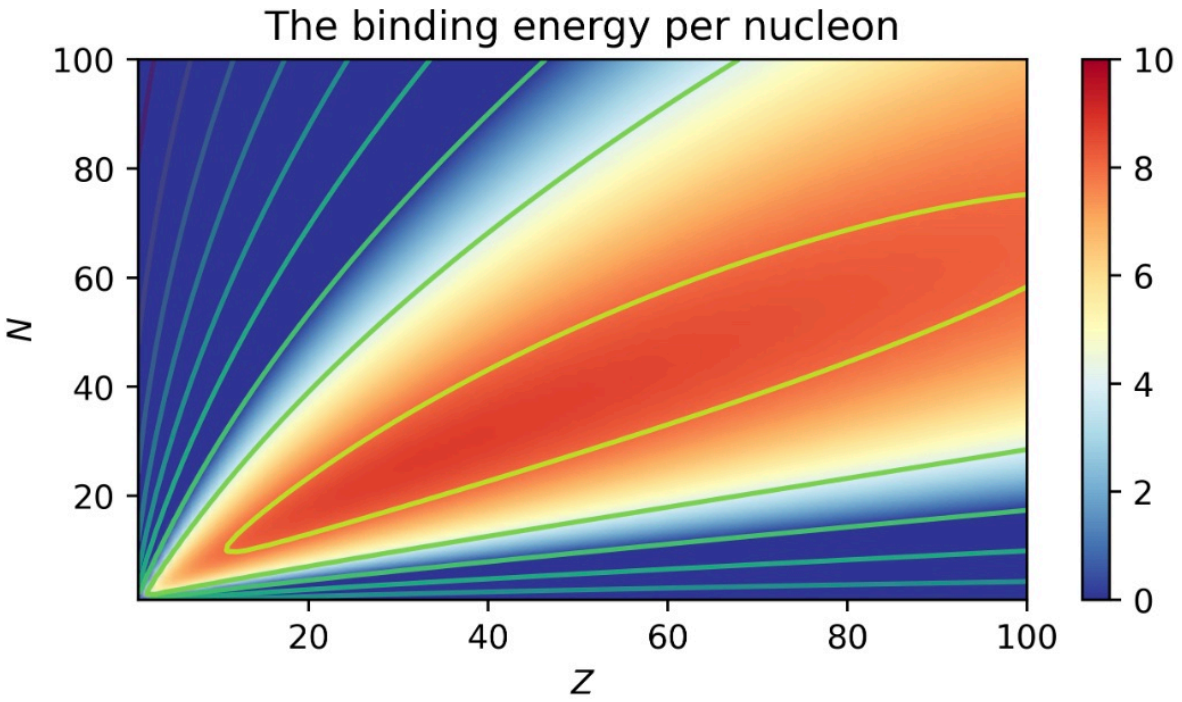

Fig. 1.1: The binding energy per nucleon based on the semi-empirical mass formula (MeV) .

where $\delta(Z, N)$ is given by

$$\delta(Z,N) = \begin{cases} \dfrac{12}{(Z+N)^{1/2}} & \text{(for even } Z, N) \\ -\dfrac{12}{(Z+N)^{1/2}} & \text{(for odd } Z, N) \\ 0 & \text{(for odd } Z+N) \end{cases} .$$

Since nuclei with mass numbers greater than about 60 become more stable by splitting, in a fission reaction, a nucleus with a large atomic number reacts with a neutron and splits into two or more nuclei, and then releases neutrons. The released neutrons react with other fissile materials, causing a chain reaction. In nuclear power plants, electricity is generated by controlling the chain reaction. In addition to not emitting carbon dioxide, nuclear power has the advantage of relatively low fuel costs. This is because 1 gram of uranium can extract more energy than can be extracted from 3 tons of coal. However, nuclear power generation also has the problem of radioactive waste disposal and risks such as nuclear meltdown. Power generations by renewable energy sources such as solar energy and wind energy, which emit as little greenhouse gases as nuclear power generation, cannot play the role of baseload or middle power sources that the thermal and nuclear power generation currently play. This is because they cannot generate long-term and stable power.

Is there a way to generate electricity that would solve all the environmental, resource depletion, safety, and long-term supply problems? Fortunately, there is. It is fusion power generation. Figure 1.1 suggests that nuclei with smaller mass numbers become more stable by combining to become larger nuclei. This reaction is the nuclear fusion reaction. The following fusion reactions could be used in fusion reactors,

$$ {}^{2}_{1}\mathrm{D} + {}^{2}_{1}\mathrm{D} \longrightarrow {}^{3}_{1}\mathrm{T}\,(1.01\,\mathrm{MeV}) + \mathrm{p}\,(3.03\,\mathrm{MeV}), \tag{1.2} $$

$$ {}^{2}_{1}\mathrm{D} + {}^{2}_{1}\mathrm{D} \longrightarrow {}^{3}_{2}\mathrm{He}\,(0.82\,\mathrm{MeV}) + \mathrm{n}\,(2.45\,\mathrm{MeV}), \tag{1.3} $$

$$ {}^{2}_{1}\mathrm{D} + {}^{3}_{1}\mathrm{T} \longrightarrow {}^{4}_{2}\mathrm{He}\,(3.52\,\mathrm{MeV}) + \mathrm{n}\,(14.06\,\mathrm{MeV}). \tag{1.4} $$

Here, D is a deuterium nucleus, T is a tritium nucleus, p is a proton, and n is a neutron. These reaction equations indicate that no carbon dioxide is produced in the fusion reaction. Since about 0.015% of the hydrogen in seawater is deuterium, deuterium is an almost inexhaustible fuel. Tritium, on the other hand, is virtually nonexistent in nature, so it is produced from lithium. If the technology to extract lithium from seawater is established, all the fuel for fusion power generation can be taken from seawater, and the amount of the fuel is unlimited. Tritium is produced by the reactions,

$$ {}^{6}_{3}\mathrm{Li} + \mathrm{n} \longrightarrow {}^{4}_{2}\mathrm{He} + {}^{3}_{1}\mathrm{T}, \tag{1.5} $$

$$ {}^{7}_{3}\mathrm{Li} + \mathrm{n} \longrightarrow {}^{4}_{2}\mathrm{He} + \mathrm{n}. \tag{1.6} $$

All reactants in a fusion reaction are positively charged nuclei. This means that in order for a fusion reaction to occur, the nuclei must be brought closer against the Coulomb repulsion. In other words, the fuels must be hot enough to cross the Coulomb barrier. The reaction cross section as a function of the center-of-mass kinetic energy shows that the DT reaction Eq. (1.4) is the most suitable for use as a fusion reaction [1, 2]. When the fusion reaction power of the DT reaction is P_f, the $\alpha-$particle heating power P_α is $(1/5)P_f$. P_f is approximated as $P_f \propto n^2T^2$, where n is the density and T is the temperature. Therefore, the energy multiplication factor Q is

$$ Q = \frac{P_f}{P_h} \propto \frac{n^2T^2}{nT/\tau_E} = nT\tau_E, \tag{1.7} $$

where P_h is the external heating power and τ_E is the energy confinement time. At $Q = 1$ (break even condition), the external heating power equals the fusion output power. Q is an important indicator of the performance of a fusion device.

1.2 Tokamaks

1.2.1 Confinement

For the fusion reaction, the fuels must be heated above 10 keV. Since no material exists that can withstand such a high temperature, the fuels must be confined so that it does not come in contact with the wall. We note here that at high temperatures, deuterium and tritium atoms are ionized and split into positively charged nuclei and negatively charged electrons. Charged particles are subject to the Lorentz force $q_s/c\boldsymbol{v}\times\boldsymbol{B}$ in the presence of a magnetic field $\boldsymbol{B}$, where q_s is the charge of the particle species s and $\boldsymbol{v}$ is the velocity. From the equation of motion

$$m_s\frac{d\boldsymbol{v}}{dt}=\frac{q_s}{c}\boldsymbol{v}\times\boldsymbol{B}, \tag{1.8}$$

it is found that the charged particle rotates around the magnetic field at the frequency $\Omega_s = q_sB/m_sc$ and radius $\rho = v_\perp/|\Omega_s| = m_sv_\perp c/|q_s|B$, where m_s is the mass of the particle species s, c is the speed of light, $B = |\boldsymbol{B}|$, $v_\perp$ is the velocity perpendicular to the magnetic field. Therefore, for example, when a torus vacuum vessel is prepared and a magnetic field is generated by applying a current in the poloidal direction, it is considered that the plasma may be confined without contacting the wall. In reality, however, a toroidal magnetic field alone cannot confine the plasma for the following reasons. Since the magnetic field is stronger inside the torus and weaker outside, the plasma moves due to the magnetic drift

$$\boldsymbol{v}_{ds}=\frac{v_\parallel^2+v_\perp^2/2}{\Omega_s}\frac{\boldsymbol{B}\times\nabla B}{B^2}, \tag{1.9}$$

where $v_\parallel$ is the velocity parallel to the magnetic field. The magnetic drift is in the opposite direction for ions and electrons, resulting in charge separation and the associated electric field $\boldsymbol{E}$. The $E\times B$ drift

$$\boldsymbol{v}_E=\frac{c\boldsymbol{E}\times\boldsymbol{B}}{B^2} \tag{1.10}$$

caused by the electric field causes the plasma to move outward and cannot be confined. It is worth noting that the $E\times B$ drift is independent of charge and therefore has the same direction both for ions and for electrons. Here, a coil is placed in the center of the torus container and a current is applied to generate a longitudinal magnetic field. Then, an electric field in the toroidal direction is generated from the Faraday's law of induction. This electric field creates a plasma current. The plasma current creates a poloidal magnetic field, which causes the magnetic field to twist. The helical magnetic field does not cause charge separation due to the magnetic drift, so the plasma can be confined. Such a magnetic confinement fusion device is called a tokamak. Figure 1.2 shows the coils and magnetic field of a tokamak magnetic confinement fusion device.

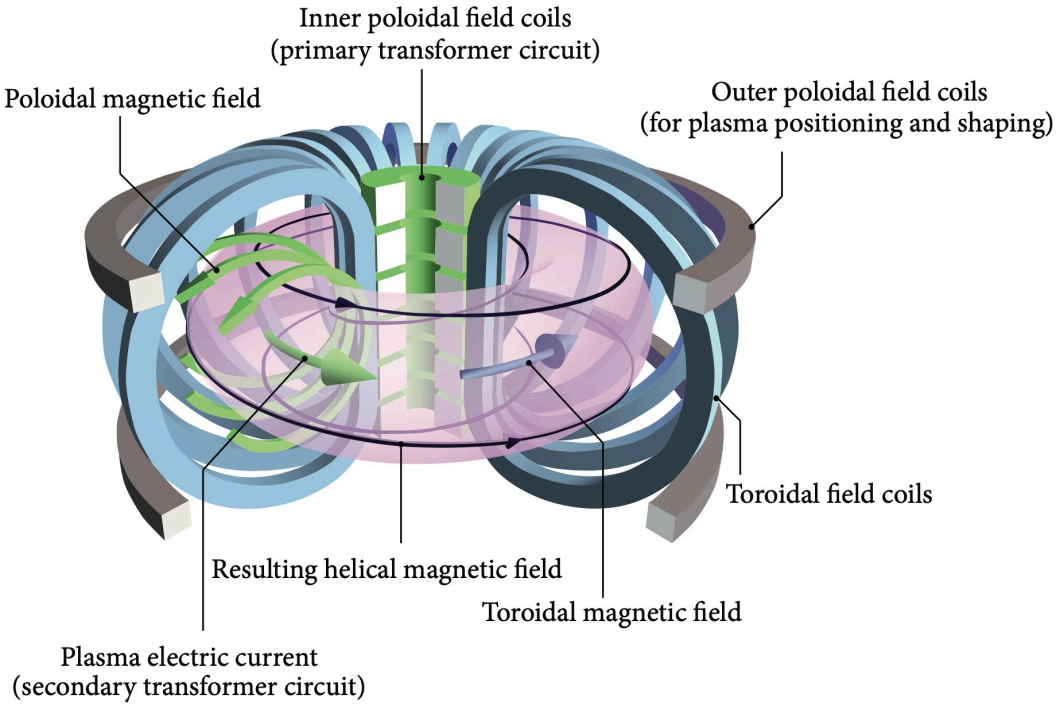

Fig. 1.2: Tokamak [3]. (CC BY 4.0)

The safety factor $q = rB_\varphi/(RB_\theta)$ is a value that expresses how much the magnetic field is twisted by the poloidal field. Here, R is the torus major radius, r is the torus minor radius, B_φ is the toroidal magnetic field, and B_θ is the poloidal magnetic field. The magnetic shear $\hat{s} = (r/q)\partial q/\partial r$ is the spatial variation of the safety factor and is an important physical quantity in the discussion of instabilities and waves. When the safety factor is an irrational number, a flux surface is formed. Under static equilibrium, the equation of motion for magnetohydrodynamics (MHD) is expressed as $\nabla p = \boldsymbol{J} \times \boldsymbol{B}/c$, where p is the pressure and $\boldsymbol{J}$ is current density. From $\boldsymbol{B} \cdot \nabla p = \boldsymbol{J} \cdot \nabla p = 0$, we see that the pressure is constant on the flux surface and that the current flows on the flux surface. Flute perturbations ($k_\perp/k_\parallel \ll 1$) tend to grow on rational surfaces where the safety factor is a rational number where $k_\perp$ and $k_\parallel$ are the wavenumbers perpendicular and parallel to the magnetic field, respectively. High wavenumber fluctuations in the direction parallel to the magnetic field are easily dissipated because the plasma is free to move along the magnetic field lines. On the other hand, in the direction perpendicular to the magnetic field, when high wavenumber fluctuations occur, they cannot be canceled because the plasma is wrapped around the magnetic field.

Tokamak plasmas are analyzed using the toroidal coordinate system (r, θ, φ), shown

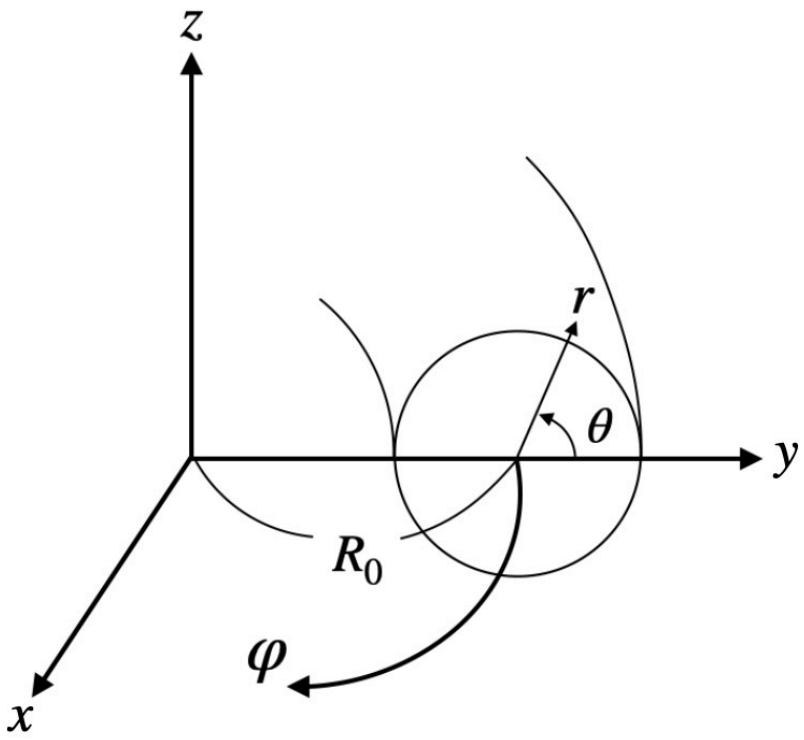

Fig. 1.3: Toroidal coordinate system.

in Fig. 1.3. θ and φ represent poloidal and toroidal angles, respectively. The toroidal and Cartesian (x, y, z) coordinate systems satisfy the relations,

$$\begin{cases} x = (R_0 + r\cos\theta)\sin\varphi = R\sin\varphi \\ y = (R_0 + r\cos\theta)\cos\varphi = R\cos\varphi \\ z = r\sin\theta \end{cases} . \tag{1.11}$$

The Jacobian $\mathcal{J}$ is rR. We put $\boldsymbol{r} = x\boldsymbol{e}_x + y\boldsymbol{e}_y + z\boldsymbol{e}_z$, from the definition of covariant bases, the covariant bases of (r, θ, φ) are

$$\begin{cases} \boldsymbol{e}_r = \dfrac{1}{h_r}\dfrac{\partial \boldsymbol{r}}{\partial r} = \cos\theta\sin\varphi\ \boldsymbol{e}_x + \cos\theta\cos\varphi\ \boldsymbol{e}_y + \sin\theta\ \boldsymbol{e}_z \\ \boldsymbol{e}_\theta = \dfrac{1}{h_\theta}\dfrac{\partial \boldsymbol{r}}{\partial \theta} = -\sin\theta\sin\varphi\ \boldsymbol{e}_x - \sin\theta\cos\varphi\ \boldsymbol{e}_y + \cos\theta\ \boldsymbol{e}_z \\ \boldsymbol{e}_\varphi = \dfrac{1}{h_\varphi}\dfrac{\partial \boldsymbol{r}}{\partial \varphi} = \cos\varphi\ \boldsymbol{e}_x - \sin\varphi\ \boldsymbol{e}_y \end{cases} , \tag{1.12}$$

where h_r, h_θ, and h_φ are the scale factors in each direction of the toroidal coordinate system. The outer product of the basis vectors is

$$\begin{cases} \boldsymbol{e}_r \times \boldsymbol{e}_\theta = \boldsymbol{e}_\varphi \\ \boldsymbol{e}_\theta \times \boldsymbol{e}_\varphi = \boldsymbol{e}_r \\ \boldsymbol{e}_\varphi \times \boldsymbol{e}_r = \boldsymbol{e}_\theta \end{cases} , \tag{1.13}$$

which means that the toroidal coordinate system is a right-handed system. From Eq. (1.12), the first fundamental form I is

$$\mathrm{I} = r^2 d\theta^2 + R^2 d\varphi^2. \tag{1.14}$$

Since the differentials of Eq. (1.12) are

$$\begin{cases} \boldsymbol{e}_{\theta\theta} = \dfrac{\partial^2 \boldsymbol{r}}{\partial\theta\partial\theta} = -r\cos\theta\sin\varphi\ \boldsymbol{e}_x - \cos\theta\cos\varphi\ \boldsymbol{e}_y - r\sin\theta\ \boldsymbol{e}_z \\ \boldsymbol{e}_{\varphi\varphi} = \dfrac{\partial^2 \boldsymbol{r}}{\partial\varphi\partial\varphi} = -R\sin\varphi\ \boldsymbol{e}_x - R\cos\varphi\ \boldsymbol{e}_y \\ \boldsymbol{e}_{\theta\varphi} = \dfrac{\partial^2 \boldsymbol{r}}{\partial\theta\partial\varphi} = -r\sin\theta\cos\varphi\ \boldsymbol{e}_x + r\sin\theta\sin\varphi\ \boldsymbol{e}_y \end{cases}, \tag{1.15}$$

the second fundamental form II is

$$\mathrm{II} = -r^2 d\theta^2 - R\cos\theta d\varphi^2. \tag{1.16}$$

From Eq. (1.12) and Eq.(1.15), the Gaussian curvature K and mean curvature H are

$$K = \frac{\cos\theta}{rR}, \quad H = -\frac{\cos\theta}{2R} - \frac{1}{2r}. \tag{1.17}$$

From Eq. (1.17), the principal curvatures κ_1 and κ_2 are $\kappa_1 = -\cos\theta/R$ and $\kappa_2 = -1/r$, respectively. Let B_0 be the magnitude of the magnetic field at the magnetic axis, the magnetic field $\boldsymbol{B}$ is

$$\boldsymbol{B} = \left(0, \quad \frac{rB_0}{qR}, \quad \frac{R_0 B_0}{R}\right). \tag{1.18}$$

We assume that the inverse aspect ratio $\varepsilon_t = r/R$ is small ($\varepsilon_t \ll 1$), then

$$\frac{B_\theta}{B_\varphi} \ll 1 \tag{1.19}$$

is satisfied.

In the absence of a magnetic field gradient, the poloidal cross-section of the plasma orbit coincides with the flux surface. However, because the tokamak magnetic field always has a gradient, the particle orbit does not coincides with the flux surface. The trajectory of the poloidal section of the particle satisfying $v_{s\parallel} \gg v_{s\perp}$ can be calculated from the equation of motion,

$$\begin{cases} \dfrac{dr}{dt} &= -v_{ds}\sin\theta & (1.20) \\ r\dfrac{d\theta}{dt} &= -v_{ds}\cos\theta + v_\parallel \dfrac{B_\theta}{B} & (1.21) \end{cases}$$

where $v_{ds} = (v_\perp^2/2 + v_\parallel^2)/(\Omega_s R)$. Assuming $v_\parallel^2$ is constant, we obtain [2]

$$\frac{d}{dt}\left\{\left(R - R_0 - \frac{v_{ds}}{\omega_l}\right)^2 + z^2\right\} = 0, \tag{1.22}$$

where $\omega_l \equiv v_\parallel B_\theta/(rB) = v_\parallel/(qR)$ is the reciprocal of the time to pass through the connection length. From Eq. (1.22), the difference between the flux surface and the particle orbit is $\Delta_c \equiv v_{ds}/\omega_l$. Using the approximation $v_{ds} \simeq v_{Ts}^2/(\Omega_s R)$, it can be evaluated [4, 5] as

$$|\Delta_c| = \left|\frac{v_{ds}}{\omega_l}\right| \simeq q\rho_s = \varepsilon_t \rho_{ps}, \tag{1.23}$$

where v_{Ts} is the thermal velocity, ρ_s is the Larmor radius evaluated by the thermal velocity, and $\rho_{ps} = m_s v_{Ts} c/(|q_s|B_\theta)$ is the poloidal Larmor radius. Equation (1.23) indicates that the plasma cannot be confined in the limit of zero poloidal magnetic field because of $\Delta_c \to \infty$. It is also suggested that a larger poloidal magnetic field will result in a smaller Δ_c and thus better confinement.

1.2.2 Trapped particles

For magnetically confined plasmas, the scales of temporal and spatial variation of the magnetic field are much smaller than the temporal and spatial scales of the gyromotion. The magnetic drift Eq. (1.9) and $E \times B$ drift Eq. (1.10) of the guiding center are also slower than the gyromotion. Thus, points with the same guiding center can be considered to have the same guiding center at a later time. The adiabatic invariant J can be obtained by taking integrals along the gyro-orbit [190].

$$J = \oint \boldsymbol{p}\frac{\partial \boldsymbol{q}}{\partial \alpha} d\alpha \simeq 2\pi \frac{m_s}{q_s}\mu, \tag{1.24}$$

where α is the gyro phase, $\boldsymbol{p} = m_s\boldsymbol{v} + q_s\boldsymbol{A}$ is the canonical momentum, and $\boldsymbol{A}$ is the vector potential. μ is the magnetic moment and satisfies

$$\frac{d\mu}{dt} = \frac{d}{dt}\left(\frac{m_s v_\perp^2}{2B}\right) = 0. \tag{1.25}$$

Equation (1.25) can be proved by perturbation expansion for the equations of motion [190]. Using the magnetic moment, the kinetic energy can be written as

$$W = \frac{1}{2}m_s v^2 = \frac{1}{2}m_s v_\parallel^2 + \mu B. \tag{1.26}$$

It can be seen that the particles are subjected to the mirror force $\boldsymbol{F}_\parallel = -\mu\nabla_\parallel B$ in the direction parallel to the magnetic field lines. Since the kinetic energy and magnetic moment are conserved, $v_\perp$ increases and $v_\parallel$ decreases when a particle moves from a small magnetic field to a large magnetic field. Where $v_\parallel$ becomes zero, the particle is reflected. Because the maximum value of the magnetic field $B_{\max}$ divided by the minimum value of the magnetic field $B_{\min}$ is $B_{\max}/B_{\min} = (1+\varepsilon_t)/(1-\varepsilon_t) \simeq 1 + 2\varepsilon_t$, the condition for a particle to be trapped by the magnetic field is

$$\left(\frac{v_\parallel}{v}\right)^2 < 2\varepsilon_t. \tag{1.27}$$

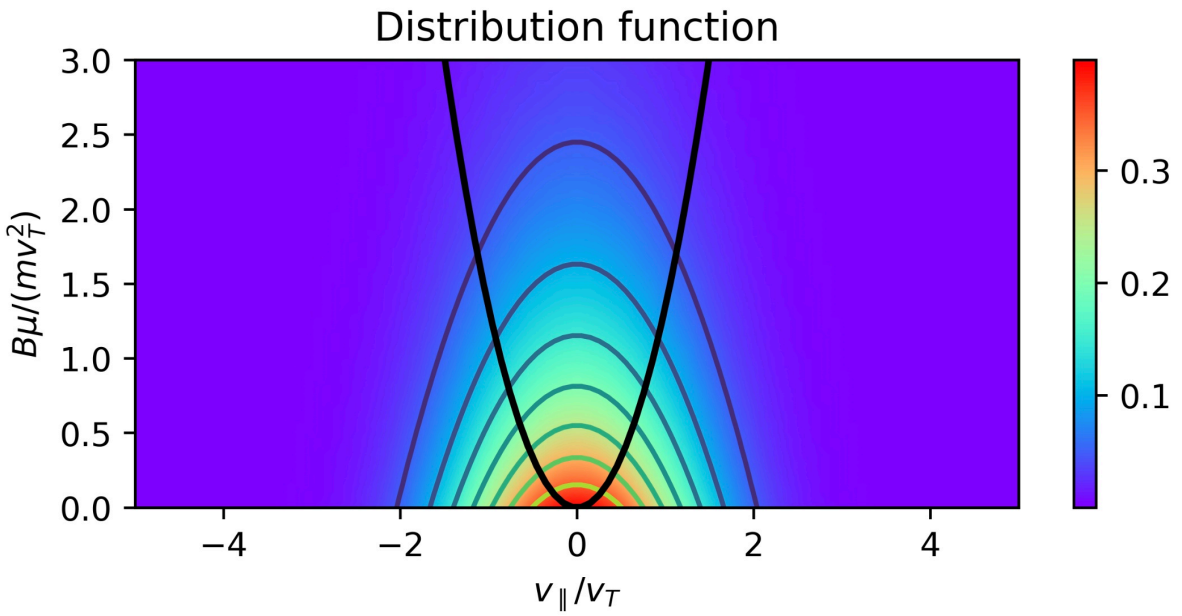

Fig. 1.4: Contour plot of the Mawellian. The black curve represents the boundary between trapped and passing particles.

Figure 1.4 is the contour plot of the Maxwellian. The black curve represents the boundary between trapped and passing particles. The particles inside the curve are trapped. The passing particles in tokamak plasmas satisfy

$$0 < \frac{B\mu}{m_s v_{Ts}^2} < \frac{1}{2}\left(\frac{v_\parallel}{v_{Ts}}\right)^2 \frac{(R_0 - r)(R + r\cos\theta)}{R_0 r(1 + \cos\theta)}. \tag{1.28}$$

Assuming the distribution function is the Maxwellian and calculating the fraction of the passing particle α_{pass}, we get

$$\alpha_{\text{pass}} = \int_\infty^\infty \int_0^{Cv_{s\parallel}^2} \frac{1}{\sqrt{2\pi T_s^3}} \exp\left(-\frac{v_{s\parallel}^2 + 2\mu_s B}{2T_s}\right) B d\mu_s dv_{s\parallel} = 1 - \sqrt{\frac{r(1+\cos\theta)}{R_0 + r\cos\theta}}, \tag{1.29}$$

where $C \equiv (R_0 - r)(R_0 + r\cos\theta)/\{2R_0 r(1 + \cos\theta)\}$. Equation (1.29) shows that the proportion of the trapped particles is about $\varepsilon_t^{1/2}$ of the total.

Figure 1.5 shows the projection of the trajectories of trapped and passing particles onto the poloidal cross section. The red circle represents the flux surface and the green circle represents the drift surface described by Eq. (1.22). The difference between the magnetic and drift planes Δ_c is given by Eq. (1.23). The trapped particles have banana orbits as represented by the blue curve. The banana width Δ_b is obtained from the

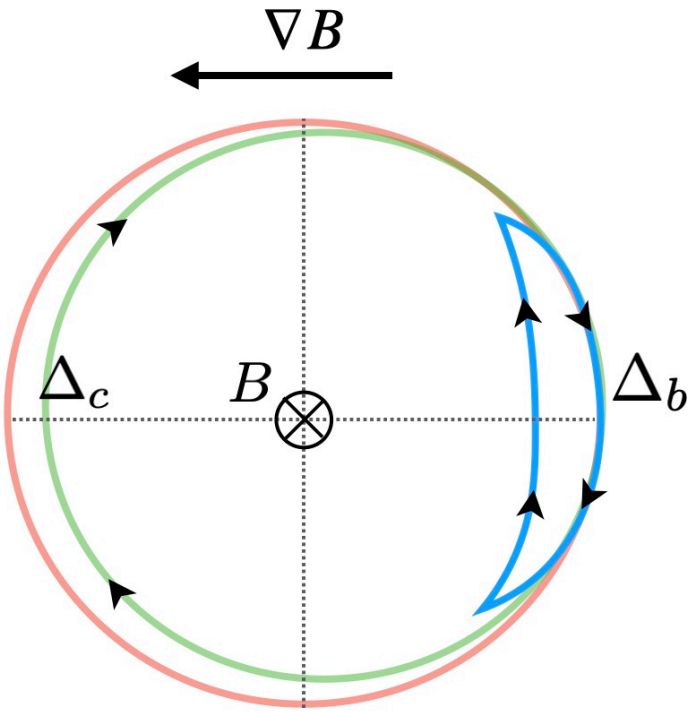

Fig. 1.5: Projection of trajectories of trapped and passing particles on poloidal cross sections.

equation of motion and the trapped condition Eq. (1.27). For $\boldsymbol{v}_{\parallel} \cdot \boldsymbol{B}_{\theta} > 0$, Eq. (1.20), Eq. (1.21), and Eq. (1.27) lead to

$$\begin{cases} \dfrac{dr}{dt} = -v_{ds} \sin\theta \\ r\dfrac{d\theta}{dt} = \dfrac{rv}{qR_0}\sqrt{2\varepsilon_t}\sqrt{\kappa^2 - \sin^2(\theta/2)} \end{cases}, \tag{1.30}$$

where $\kappa^2 \equiv \cos^2\beta/(2\varepsilon_t) < 1$, β is the pitch angle at $\theta = 0$ where the magnetic field is minimum. In Eq. (1.21), we used $\mu \simeq m_s v_{\perp}^2/(2B_0)(1+\varepsilon_t)$ and ignored the term due to the magnetic drift. From Eq. (1.30), we get

$$r = \int \frac{dr}{d\theta} d\theta \simeq -\int \frac{q\rho_s}{2\sqrt{\varepsilon_t}} \frac{\sin\theta}{\sqrt{2\kappa^2 - 1 + \cos\theta}} d\theta = \frac{q\rho_s}{\sqrt{\varepsilon_t}}\sqrt{2\kappa^2 - 1 + \cos\theta} + r_0. \tag{1.31}$$

The trapped particle is reflected at $(r, \theta) = (r_0, \theta_0)$. The banana width $\Delta_b = r - r_0$ at $\theta = 0$ is obtained [4] as

$$\Delta_b = \frac{q\rho_s}{\sqrt{\varepsilon_t}}\sqrt{2}\kappa \simeq \frac{q\rho_s}{\sqrt{\varepsilon_t}}. \tag{1.32}$$

Equations (1.23) and (1.32) show that the banana width is $\varepsilon_t^{-1/2}$ times larger than Δ_c. Since the trapped particles have a slower velocity parallel to the magnetic field ($v_{\parallel} \sim \sqrt{\varepsilon_t} v$) than the passing particles, they are more strongly affected by the magnetic drift and deviate significantly from the flux surface. $\Delta_b > \Delta_c > \rho_s$ is generally satisfied

in tokamak plasmas. The period around the banana orbit τ_b is calculated from

$$\tau_b = \oint \frac{dl}{v_\parallel} = m_s \frac{\partial}{\partial W} \oint v_\parallel dl = \frac{\partial J_\parallel}{\partial W}. \tag{1.33}$$

$J_\parallel$ represents the longitudinal invariant and is calculated [4, 7] as

$$J_\parallel = m_s \oint v_\parallel dl = 8\sqrt{2\varepsilon_t} m_s R_0 q v \left\{ E(\kappa) - \left(1 - \kappa^2\right) K(\kappa) \right\}, \tag{1.34}$$

from Eq. (1.30). The complete elliptic integral of the first kind $K(\kappa)$ is defined as

$$K(\kappa) \equiv \int_0^{\pi/2} \frac{d\theta}{\sqrt{1 - \kappa^2 \sin^2 \theta}}, \quad (0 \leq \kappa < 1) \tag{1.35}$$

and the complete elliptic integral of the second kind $E(\kappa)$ is defined as

$$E(\kappa) \equiv \int_0^{\pi/2} \sqrt{1 - \kappa^2 \sin^2 \theta} d\theta, \quad (0 \leq \kappa < 1). \tag{1.36}$$

When the particle is deeply trapped ($\kappa \to 0$), $K(\kappa)$ can be approximated as $(\pi/2)(1 + \kappa^2/2)$ [5]. From Eqs. (1.33) and (1.34), we obtain [4, 7]

$$\tau_b = 4\sqrt{2} \frac{R_0 q}{v\sqrt{\varepsilon_t}} K(\kappa) \simeq \frac{R_0 q}{v_{Ts}\sqrt{\varepsilon_t}}. \tag{1.37}$$

The trapped particles move across magnetic field lines due to the magnetic drift. In other words, the filed line label $\xi = \varphi - q\theta$ changes over time. The time variation of ξ is

$$\frac{d\xi}{dt} = \boldsymbol{v}_{s,d} \cdot \nabla(\varphi - q\theta) \simeq \frac{v_s^2}{2\Omega_s R r} \left(q \cos\theta + \frac{dq}{dr} r\theta \sin\theta \right). \tag{1.38}$$

Taking the bounce average of Eq. (1.38), we obtain [5, 7]

$$v_\xi \equiv \left\langle \frac{d\xi}{dt} \right\rangle_b = \varepsilon_t \frac{v^2 q}{2\Omega_s r^2} G(\hat{s}, \kappa), \tag{1.39}$$

where $G(\hat{s}, \kappa)$ is defined as

$$G(\hat{s}, \kappa) \equiv \left[2\frac{E(\kappa)}{K(\kappa)} - 1 + 4\hat{s} \left(\frac{E(\kappa)}{K(\kappa)} + \kappa^2 - 1 \right) \right] \tag{1.40}$$

and $\langle \cdot \rangle_b$ represents the bounce average. Equation (1.39) shows that the direction of the precession drift is opposite for trapped electrons and trapped ions. Sometimes $G(\hat{s}, \kappa)$ is approximated as

$$G'(\hat{s}) = 0.64\hat{s} + 0.57 \tag{1.41}$$

that does not depend on κ [8]. Note that the bounce average of the longitudinal invariant Eq. (1.34) is $\left\langle dJ_{s\parallel}/dt \right\rangle_b = 0$. The time derivative of the flux label $\chi \equiv (1/4\pi^2) \int \boldsymbol{B} \cdot \nabla\theta dV$ is

$$\left\langle \frac{d\chi}{dt} \right\rangle_b = -\frac{1}{q_s} \frac{\partial J_\parallel / \partial \xi}{\partial J_\parallel / \partial W} = 0, \tag{1.42}$$

which indicates that the center of the banana orbit is always on the same flux surface [9].

1.2.3 Neoclassical transport

In tokamak plasmas, the collision frequency ν, which is the frequency at which the pitch angle changes by 90°, is much smaller than the gyrofrequency. Therefore, the particles can complete their gyro motion. In the absence of a magnetic field gradient, the particle can be considered as performing a random walk with a step size ρ. The diffusion coefficient in this case is estimated to be $D_{cl} \sim \nu\rho^2$. In reality, however, the magnetic field gradient cannot be ignored, so the diffusion coefficient is always larger than D_{cl}. Since trapped particles become passing particles when they are scattered by an angle of about $\sqrt{\varepsilon_t}$ by collision, their effective collision frequency is $\nu_{\text{eff}} \sim \nu/\varepsilon_t$. This relationship is derived from the equation for the time variation of the distribution function f due to pitch angle scattering [4],

$$\frac{\partial f}{\partial \lambda} = \frac{\nu}{2}\frac{\partial}{\partial \lambda}\left(1-\lambda^2\right)\frac{\partial f}{\partial \lambda}, \tag{1.43}$$

where $\lambda \equiv v_\parallel/v$. When ν_{eff} is smaller than τ_b^{-1} given by Eq. (1.37), then both the trapped and passing particles can complete the orbits represented in Fig. 1.5. The frequency region satisfying $\nu < \varepsilon_t^{3/2} v_T/qR_0$ is called the banana regime. The diffusion coefficient in the banana regime is evaluated as $D_b \sim \varepsilon_t^{1/2}\Delta_b^2\nu_{\text{eff}} \sim \varepsilon_t^{-3/2}\rho^2 q^2\nu$ from Eq. (1.32). Since q is greater than 1 and ε_t is smaller than 1, D_b is significantly larger than D_{cl}. On the other hand, when the collision frequency satisfies $\nu > v_T/qR_0$, even passing particles cannot complete their orbits. This frequency region is referred to as the Pfirsch-Schlüte regime, and the diffusion coefficient is estimated as $D_{PS} \sim \Delta_c^2\nu \sim \rho^2 q^2\nu$ from Eq. (1.23). D_b is $\varepsilon_t^{-3/2}$ times larger than D_{PS}. This is due to the difference in magnitude of Δ_b and Δ_c, in other words, the difference in the velocity, in the direction along the magnetic field, of the trapped and passing particles. The frequency region between the banana regime and Pfirsch-Schlüte regime is referred to as the plateau regime. In this regime, particles that satisfy the resonance condition $v_\parallel/v_T \sim (\nu R_0 q/v_T)^{1/3}$ contribute to the diffusion process [2]. These particles move over distances of around the connection length while experiencing the magnetic drift before being scattered due to collisions. The step time is $\tau_p \sim R_0 q/v_\parallel$ and the step size is $\Delta_p \sim v_d\tau_p \sim \rho q v_T/v_\parallel$. Therefore, the diffusion coefficient in the plateau regime is estimated as

$$D_p \sim \left(\frac{v_\parallel}{v_T}\right)\Delta_p^2\nu\left(\frac{v_T}{v_\parallel}\right)^2 \sim \frac{\rho^2 q v_T}{R_0}. \tag{1.44}$$

The diffusion coefficient in the plateau regime is independent of collision frequency. Figure 1.6 illustrates the collision frequency dependence of the neoclassical diffusion coefficient, summarizing the discussion above.

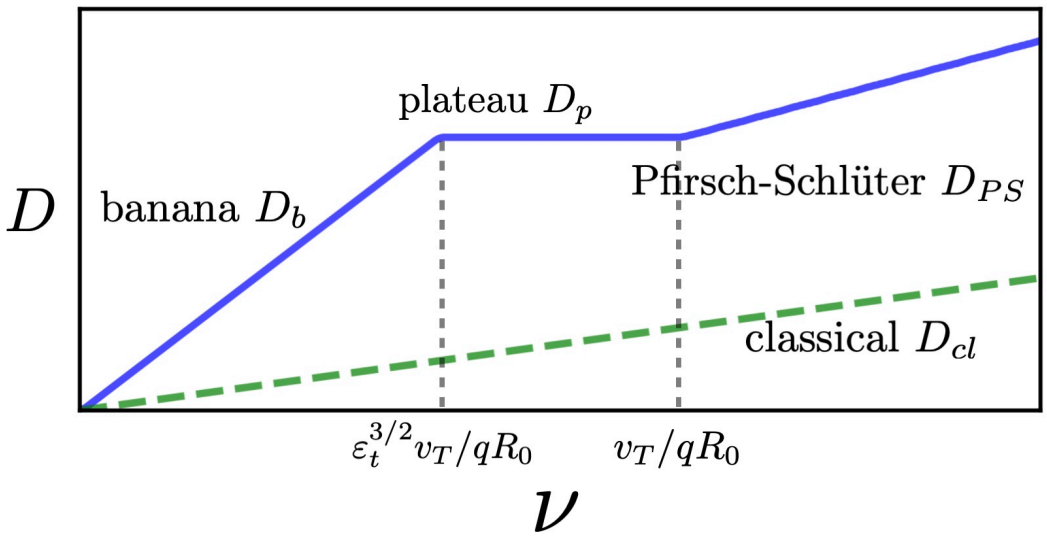

Fig. 1.6: Collision frequency dependence of the neoclassical diffusion coefficient.

It is noteworthy that these neoclassical diffusion coefficients do not exhibit a dependence on temperature gradients or density gradients. This characteristic establishes a precise linear relationship between a flow and thermodynamic force, enabling the application of the non-equilibrium thermodynamics [10]. In fact, it has been proved that the Onsager reciprocal relations holds in the neoclassical transport [11]. Although the neoclassical diffusion coefficients are larger than the classical diffusion coefficient D_{cl} due to the non-uniformity of the magnetic field, the diffusion coefficient is expected to be smaller in high temperature plasmas because the collision frequency is proportional to the $-1/2$ power of temperature. However, the experimentally observed transport is more than one order of magnitude larger than the neoclassical transport. This anomalous transport is believed to be caused by plasma turbulence [2, 12].

1.3 Plasma turbulence

1.3.1 Microinstabilities

In fusion plasmas, particle and heat transport across flux surfaces are caused by turbulent eddies with spatial scales significantly smaller than device size. A typical example of a small characteristic length is the Larmor radius of ions or electrons. Microinstabilities that create small-scale eddies and the associated turbulent transport have been investigated using the kinetic models based on the gyrokinetic theory [13, 96, 15, 16, 17, 18, 19, 20] and fluid models [21, 22, 23, 243, 86, 87]. Both kinetic and fluid models have their own strengths and weaknesses. The gyrokinetic theory removes phenomena on time scales below the gyroperiod and spatial scales below the

gyro radius from the Vlasov equation

$$\frac{df_s}{dt} = \frac{\partial f_s}{\partial t} + \frac{d\boldsymbol{x}}{dt} \cdot \nabla f_s + \frac{d\boldsymbol{v}}{dt} \cdot \frac{\partial f_s}{\partial \boldsymbol{v}} = 0 \tag{1.45}$$

and Maxwell equations

$$\nabla \cdot \boldsymbol{E} = 4\pi \sum_s q_s \int f_s d^3\boldsymbol{v}, \tag{1.46}$$

$$\nabla \cdot \boldsymbol{B} = 0, \tag{1.47}$$

$$\nabla \times \boldsymbol{E} = -\frac{1}{c}\frac{\partial \boldsymbol{B}}{\partial t}, \tag{1.48}$$

$$\nabla \times \boldsymbol{B} = -\frac{4\pi}{c} \sum_s q_s \int \boldsymbol{v} f_s d^3\boldsymbol{v} + \frac{1}{c}\frac{\partial \boldsymbol{E}}{\partial t}, \tag{1.49}$$

using the perturbation theory, as will be explained in the next chapter. The process reduces the dimension of velocity space by one. The gyrokinetic models are suitable for the studies of micro-turbulences which are much slower than the gyromotion of charged particles. However, it is still difficult to conduct analytical studies and numerical simulations using them because the distribution function is expressed in five dimensions of phase space: the position of the guiding center $\boldsymbol{X} = \boldsymbol{x} - \boldsymbol{b} \times \boldsymbol{v}/\Omega_s$, kinetic energy w, and magnetic moment μ. Fluid models described in three dimensions in real space are easier to handle than kinetic models. However, due to the presence of the advection term in the Vlasov and Boltzmann equations, fluid models have the problem that the equation for nth-order moment include $n+1$st-order moment and the system of equations is not closed. This is referred to as the closure problem. By employing the Hammett-Perkins model [21, 22] as a closure model, kinetic effects such as the Landau damping can be incorporated, and the dispersion relation of the fluid model matches that derived from a kinetic model. However, the thermal diffusion coefficient in the fluid simulation using the Hammett-Perkins model are reported to be much larger than that in the gyrokinetic simulation [27].

The ion temperature gradient (ITG) instability has received the most attention as a microinstability on the ion gyroradius scale [28, 29]. This is because it is believed to be the cause of anomalous ion heat transport in the core region. We derive dispersion relations for slab ITG mode (sITG mode) and toroidal ITG mode (tITG mode) and discuss the physical mechanisms. The electrostatic linear gyrokinetic equation for particle species s is given by

$$\left\{ \frac{\partial}{\partial t} + i(\omega_E + \omega_{ds}) + \frac{v_\parallel}{qR}\frac{\partial}{\partial \theta} \right\} h_{s\boldsymbol{k}_\perp} = \left\{ \frac{\partial}{\partial t} + i(\omega_E + \omega_{*Ts}) \right\} \frac{q_s \phi_{\boldsymbol{k}_\perp}}{T_s} J_0\left(k_\perp \rho_s\right) f_{0s}, \tag{1.50}$$

where $h_{s\boldsymbol{k}_\perp}(\boldsymbol{X}, w, \mu, t) = \delta f_{s\boldsymbol{k}_\perp}(\boldsymbol{X}, w, \mu, t) + q_s \langle \phi \rangle_{\alpha s} / T_s f_{0s}(w)$ is the nonadiabatic part of the perturbed distribution function $\delta f_{s\boldsymbol{k}_\perp}$, $\langle \phi \rangle_{\alpha s} = (1/2\pi) \oint \phi d\alpha$ is the gyro-averaged

electrostatic potential, $\omega_E \equiv \boldsymbol{k}_\perp \cdot \boldsymbol{v}_E$, $\omega_{ds} \equiv \boldsymbol{k}_\perp \cdot \boldsymbol{v}_{ds}$, $\omega_{*Ti} \equiv \omega_{*s}\{1 + \eta_s(m_s v^2/(2T_s) - 3/2)\}$, $\eta_s \equiv d\ln T_s/d\ln n_s$, $\omega_{*s} \equiv \{cT_s/(e_s B)\}\boldsymbol{k}\cdot\boldsymbol{b}\times\nabla \ln n_s$, J_0 is the Bessel function of the first kind of order zero representing the finite Larmor radius effects, and $f_{0s}(w) \equiv n_0\{m_s/(2\pi T_s)\}^{3/2}\exp(-w/T_s)$ is the equilibrium part (Maxwellian) of the distribution function. As we use the field-aligned coordinate system [30], the θ derivative of Eq. (1.50) represents the derivative along the magnetic field lines. Considering only the vicinity of a certain poloidal angle, and assuming a parallel wave number $k_\parallel$, the Fourier transformation of Eq. (1.50) for ions with respect to time yields

$$h_{i\boldsymbol{k}_\perp} = \frac{\omega - \omega_E - \omega_{*Ti}}{\omega - \omega_E - \omega_{di} - k_\parallel v_\parallel}\frac{e\phi_{\boldsymbol{k}_\perp}}{T_s}J_0\left(k_\perp\rho_i\right)f_{0i}. \tag{1.51}$$

Here we assume the adiabatic electron approximation $\tilde{n}_{e\boldsymbol{k}_\perp}/n_0 = e\phi_{\boldsymbol{k}_\perp}/T_e$ where $\tilde{n}_{e\boldsymbol{k}_\perp}$ is the perturb part of the density. It corresponds to keeping the electron energy constant and the mass close to zero, and the electrons move along the magnetic field lines at an infinite velocity [31]. From the adiabatic electron approximation and the quasi-neutrality condition $\tilde{n}_{e\boldsymbol{k}_\perp} = \tilde{n}_{i\boldsymbol{k}_\perp} = \int d^3\boldsymbol{v}\{-(e\phi_{\boldsymbol{k}_\perp}/T_i)f_{0i} + h_{i\boldsymbol{k}_\perp}\exp(-i\boldsymbol{k}_\perp\cdot\boldsymbol{\rho}_i)\}$, we obtain the dispersion relation for the ITG modes:

$$1 + \frac{T_i}{T_e} - \frac{1}{n_0}\int d^3\boldsymbol{v}\frac{\omega - \omega_E - \omega_{*Ti}}{\omega - \omega_E - \omega_{di} - k_\parallel v_\parallel}\frac{q_s\phi_{\boldsymbol{k}_\perp}}{T_s}J_0\left(k_\perp\rho_i\right)f_{0i} = 0. \tag{1.52}$$

The condition where the denominator of the integrand in Eq. (1.52) becomes zero corresponds to the resonance condition between particles and waves. From Eq. (1.52), it is evident that ω_E only contributes to the Doppler shift and does not affect the growth rate. Therefore, for simplicity, $\omega - \omega_E$ is replaced by ω. Under the assumptions of the long wavelength approximation $k_\perp\rho_i \ll 1$ and fluid approximation $v_{Ti}/|\omega/k_\parallel| \ll 1$, by approximating $1/(\omega - \omega_{di} - k_\parallel v_\parallel) \simeq (1/\omega)(1 + k_\parallel v_\parallel/\omega + \omega_{di}/\omega + k_\parallel^2 v_\parallel^2/\omega)$, we obtain the dispersion relation for the fluid approximation of the ITG modes [32, 33],

$$1 + \tau\frac{\omega_{*i}}{\omega} + \left(k_\perp^2\rho_c^2 - \frac{k_\parallel^2 c_s^2}{\omega^2} - \tau\frac{\hat{\omega}_{di}}{\omega}\right)\left(1 - \frac{\omega_{*pi}}{\omega}\right) = 0, \tag{1.53}$$

where $\rho_c \equiv c_s/\Omega_i$, $c_s \equiv \sqrt{T_e/m_i}$, $\hat{\omega}_{di} \equiv 2cT_i/(eB)\boldsymbol{k}_\perp\cdot\boldsymbol{b}\times(\boldsymbol{b}\cdot\nabla\boldsymbol{b})$, $\omega_{*pi} = \omega_{*i}(1+\eta_i)$、$\tau \equiv T_e/T_i$. Assuming a uniform magnetic field, flat density profile, and steep temperature gradient, from Eq. (1.53), we get the dispersion relation for the sITG mode:

$$\omega = \left(k_\parallel^2 c_s^2|\omega_{*pi}|\right)^{1/3}\frac{-1 + i\sqrt{3}}{2}. \tag{1.54}$$

Equation (1.54) shows that the sITG mode is caused by parallel ion motion. The dispersion relation for the slab ITG modes can also be derived directly from a fluid model of the slab configuration. From the ion continuity equation, the equation of parallel

motion of ions, the ion energy equation, and the adiabatic electron approximation, we obtain

$$\frac{1}{\tau}\frac{\partial \Phi}{\partial t} = i\omega_{*i}\Phi - iv_{Ti}k_z U_{i\parallel}, \tag{1.55}$$

$$\frac{\partial U_{i\parallel}}{\partial t} = -iv_{Ti}k_z(\Phi + P), \tag{1.56}$$

$$\frac{\partial P}{\partial t} = i(1+\eta_i)\omega_{*i}\Phi - i\frac{5}{3}v_{Ti}k_z U_{i\parallel}, \tag{1.57}$$

where $\Phi \equiv e\phi_{\boldsymbol{k}_\perp}/T_i$, $U_{i\parallel} = \tilde{V}_{i\parallel\boldsymbol{k}_\perp}/v_{Ti}$, $P \equiv \tilde{p}_{i\boldsymbol{k}_\perp}/p_i$. From Eqs. (1.55), (1.56), and (1.57), the dispersion relation for the sITG mode

$$\left\{\frac{\omega^2}{k_\parallel^2 v_{Ti}^2}\left(\frac{\omega}{\tau}+\omega_{*i}\right) - 1\omega\right\} - \frac{5}{3}\frac{\omega}{\tau} + \left(\eta_i - \frac{2}{3}\right)\omega_{*i} = 0 \tag{1.58}$$

is derived [34]. In the limit $v_{Ti}/|\omega/k_\parallel| \ll 1$, Eq. (1.58) can be approximated to be equal to

$$\omega = \left\{k_\parallel^2 v_{Ti}^2 \tau\left(\eta_i - \frac{2}{3}\right)\omega_{*i}\right\}^{1/3}\frac{-1+i\sqrt{3}}{2}. \tag{1.59}$$

Equation (1.59) is similar to Eq. (1.54), but the mode does not become unstable when $\eta_i = 2/3$ in this fluid model. The physical mechanism for the sITG mode is as follows. Temperature fluctuations $\tilde{T}_i$ cause differences in the speed at which ions move along the direction of the magnetic field lines. This leads to the generation of density fluctuations $\tilde{n}_i$ between the regions where $\tilde{T}_i > 0$ and where $\tilde{T}_i < 0$, resulting in the creation of electric fields to cancel the charge separation. The $E \times B$ drift due to the electric fields further increase the temperature in the region $\tilde{T}_i > 0$ and further decrease the temperature in the region $\tilde{T}_i < 0$. In this way, the initial fluctuations exponentially amplify.

By neglecting the dynamics in the parallel direction and employing the long wavelength approximation in Eq. (1.53), the dispersion relation for the tITG mode

$$\omega = i\sqrt{\tau\frac{\hat{\omega}_{di}\omega_{*pi}}{1+k_\perp^2\rho_c^2}} \tag{1.60}$$

is derived. On the other hand, in the fluid model (Eqs. (1.55), (1.56) , and (1.57)), by substituting the parallel fluid velocity with the diamagnetic drift and introducing the Braginskii closure [35] $\boldsymbol{q} = 5cp_i/(2eB)\boldsymbol{b}\times\nabla T_i$ to equation Eq. (1.57), we obtain

$$\frac{1}{\tau}\frac{\partial \Phi}{\partial t} = i\omega_{*i}\Phi - i\omega_{di}(\Phi + P), \tag{1.61}$$

$$\frac{\partial P}{\partial t} = i(1+\eta_i)\omega_{*i}\Phi - i\frac{5}{3}\omega_{di}\left[\Phi\left(-\frac{1}{\tau}\right) + 2P\right]. \tag{1.62}$$

From Eqs. (1.61) and (1.62), the dispersion relation for the tITG mode

$$\omega = \frac{5}{3}\omega_{di} + \frac{\tau}{2}\left(\omega_{di} - \omega_{*i}\right) + \sqrt{\tau\omega_{*i}\omega_{di}(\eta_c - \eta_i)} \tag{1.63}$$

is derived. η_c is the threshold for the tITG mode, defined as

$$\eta_c \equiv \frac{2}{3} + \frac{\tau}{4}\left(\frac{\omega_{di}}{\omega_{*i}} + \frac{\omega_{*i}}{\omega_{di}} - 2\right) + \frac{10}{9\tau}\tau\frac{\omega_{di}}{\omega_{*i}}. \tag{1.64}$$

In this model, it becomes unstable when $\eta_i > \eta_c$. From Eqs. (1.60) and (1.63), it is understood that in order for the tITG mode to become unstable, $\omega_{*p}\omega_{di}$ needs to be greater than 0. This condition implies that the product of the pressure gradient and magnetic field gradient is positive, indicating that the tITG mode is unstable in the bad curvature region.

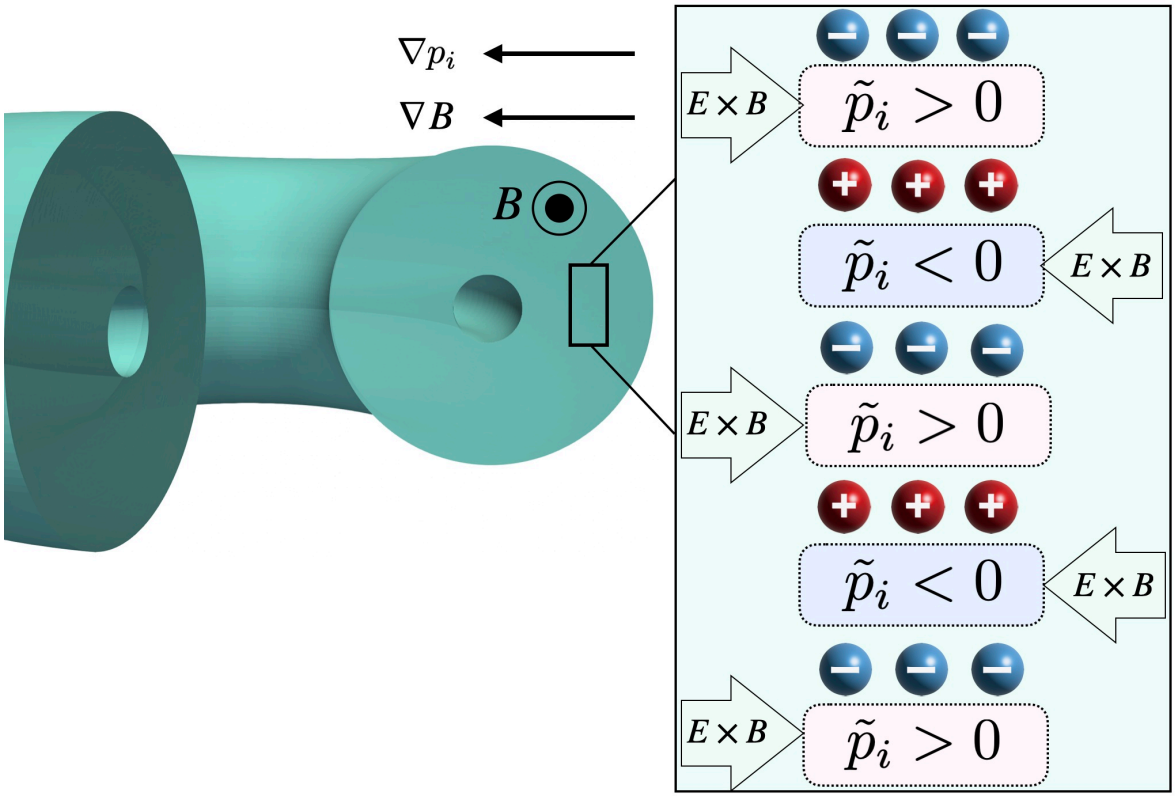

Fig. 1.7: Physical mechanism of the tITG mode.

Figure 1.7 shows the physical mechanism of the tITG mode. The physical mechanism of the tITG mode is similar to that of the sITG mode. With the presence of pressure fluctuations $\tilde{p}_i$, the magnitude of the magnetic drift, which depends on particle velocity, varies. This results in regions between the peaks and troughs of the fluctuations where $\tilde{n}_i > 0$ and $\tilde{n}_i < 0$. This leads to the generation of electric fields due to

the charge separation, and the $E \times B$ drift. As depicted in Fig. 1.7, in regions where $\tilde{p}_i < 0$, the pressure becomes higher, whereas in regions where $\tilde{p}_i < 0$, the pressure becomes lower. Thus, the initial pressure fluctuations amplify exponentially with time.

Another ion-scale microinstability that is of interest, similar to the ITG modes, is the trapped electron mode (TEM) [36, 37]. The ITG mode becomes unstable when the density gradient is small, while the TEM becomes unstable when the density gradient is large. When both the temperature and density gradients are large, both the ITG mode and TEM become unstable[38, 39]. It has been observed that when the critical gradient $\zeta_c = R/L_T + 4(R/L_n) = 22$ is exceeded, both the ITG and TEM become unstable, thereby increasing the particle fluxes and changing the direction of convection [40]. Since the TEM is unstable due to the motion of the trapped electrons, we employ the bounce-averaged gyrokinetic equations for electrons [41]

$$\left(\frac{\partial}{\partial t} + i\langle\omega_{de}\rangle_b\right) h_{s\boldsymbol{k}_\perp} = -\left(\frac{\partial}{\partial t} + i\omega_{*Te}\right)\frac{e\phi_{\boldsymbol{k}_\perp}}{T_s} f_{0e}. \tag{1.65}$$

Equation (1.65) is obtained by taking the bounce average of Eq. (1.50), neglecting the finite Larmor radius effects of electrons, and using $\langle v_\parallel/(qR)\partial h_{e\boldsymbol{k}_\perp}/\partial\theta\rangle_b = 0$, $\langle\phi_{\boldsymbol{k}_\perp}\rangle_b \simeq \phi_{\boldsymbol{k}_\perp}$, and the fact that the lowest order of $h_{s\boldsymbol{k}_\perp}$ is independent of θ. From equations Eq. (1.39) and Eq. (1.41), the precession drift frequency of trapped electrons is

$$\langle\omega_{de}\rangle_b \simeq \omega_{*e}\frac{L_n w}{RT_e}G'(\hat{s}) = \omega_{\rm pre}\frac{w}{T_e}, \tag{1.66}$$

where $\omega_{\rm pre} \equiv \omega_{*e}L_n G'(\hat{s})/T_e$. From Eq. (1.65), the adiabatic part of the distribution function of trapped electrons is determined as

$$h_{e\boldsymbol{k}_\perp,\rm trap} = -\frac{\omega - \omega_{*Te}}{\omega - \langle\omega_{de}\rangle_b}\frac{e\phi_{\boldsymbol{k}_\perp}}{T_s} f_{0e}. \tag{1.67}$$

Thus, the electron density fluctuation is [9]

$$\tilde{n}_e \simeq n_0\frac{e\phi_{\boldsymbol{k}_\perp}}{T_e} + 4\pi\sqrt{2\varepsilon_t}\frac{e\phi_{\boldsymbol{k}_\perp}}{T_e}\int_0^\infty dv\frac{\omega - \omega_{*Te}}{\omega - \langle\omega_{de}\rangle_b}v^2 f_{0e}. \tag{1.68}$$

On the other hand, in the limit $\omega \gg v_{Ti}/qR$, from Eq. (1.51), the density fluctuation of ions is obtained as

$$\tilde{n}_i = -n_0\frac{e\phi_{\boldsymbol{k}_\perp}}{T_i} + n_0 e\phi_{\boldsymbol{k}_\perp}\left\{\frac{1}{T_i}\left(1 - \frac{\omega_{*i}}{\omega}\right)\Gamma_{0i} - \eta_i\frac{\omega_{*i}}{\omega}k_\perp^2\rho_{Ti}^2\left(\Gamma_{1i} - \Gamma_{0i}\right)\right\}, \tag{1.69}$$

where $\Gamma_{0i} \equiv I_0(k_\perp^2\rho_{Ti}^2)\exp(-k_\perp^2\rho_{Ti}^2)$, $\Gamma_{1i} \equiv I_1(k_\perp^2\rho_{Ti}^2)\exp(-k_\perp^2\rho_{Ti}^2)$, I_0 and I_1 are the modified Bessel function of the first kind of order zero and of fist order, respectively. From Eqs. (1.68) and (1.69), we obtain the dispersion relation of the TEM:

$$1+\tau-\left(\tau + \frac{\omega_{*e}}{\omega}\right)\Gamma_{0i} - \eta_i\frac{\omega_{*e}}{\omega}k_\perp^2\rho_{Ti}^2(\Gamma_{1i} - \Gamma_{0i}) = \frac{4\pi\sqrt{2\varepsilon_t}}{n_0}\int_0^\infty dv\frac{\omega - \omega_{*Te}}{\omega - \langle\omega_{de}\rangle_b}v^2 f_{0e}. \tag{1.70}$$

Assuming $\gamma \ll \omega_r$ and $\sqrt{\varepsilon_t} \ll 1$, and using $1/\omega \simeq 1/\omega_r - i\gamma/\omega_r^2$, Eq. (1.70) can be approximated as [9]

$$\{1+\tau(1-\Gamma_{0i})\}\frac{\gamma}{\omega_r} = 2\sqrt{2\pi\varepsilon_t}\left(\frac{\omega_r}{\omega_{\rm pre}}\right)^{3/2} e^{-\frac{\omega_r}{\omega_{\rm pre}}}\left[\frac{\omega_{*e}}{\omega_r}\left\{1+\eta_e\left(\frac{\omega_r}{\omega_{\rm pre}}-\frac{3}{2}\right)\right\}-1\right]. \tag{1.71}$$

We employed the Sokhotski-Plemelj theorem $\lim_{\gamma\to+0} 1/(\omega - \langle\omega_{de}\rangle_b) = \mathcal{P}1/(\omega_r - \langle\omega_{de}\rangle_b) - i\pi\delta(\omega_r - \langle\omega_{de}\rangle_b)$ on the right-hand side of Eq. (1.70). The physical mechanism of the TEM is similar to that of the ITG modes. The role played by the magnetic drift in the case of the tITG mode is played by the precession drift in the case of the TEM. When temperature and density fluctuations occur, the precession drift causes charge separation and associated $E \times B$ drift, which amplifies the fluctuations.

1.3.2 Turbulent transport

When linearly unstable modes grow, nonlinear coupling between modes leads to the coexistence of countless waves with different wavenumbers and frequencies. The turbulent diffusion coefficient $D_{\rm turb}$ for the slab configuration can be estimated from the continuity equation

$$\frac{\partial n}{\partial t} + \nabla\cdot(n\boldsymbol{V}) = \frac{\partial n_0}{\partial t} + \frac{\partial \tilde{n}}{\partial t} + \nabla\cdot\left(n_0\tilde{\boldsymbol{V}} + \tilde{n}\tilde{\boldsymbol{V}}\right) = 0, \tag{1.72}$$

where $\tilde{\boldsymbol{V}}(\boldsymbol{r},t) = \boldsymbol{B}\times\nabla\phi/B^2$ is the fluctuation part of the flow velocity. The average of the fluctuating part of a physical quantity Ψ becomes zero $\langle\tilde{\Psi}\rangle = 0$. From the first order of Eq. (1.72), we derive the relationship between the fluctuating density and electrostatic potential fluctuation. By extracting the first order terms of Eq. (1.72), we get the relationship between the fluctuating density and electrostatic potential fluctuation:

$$\tilde{n}_{\boldsymbol{k}} = \frac{1}{\omega_{\boldsymbol{k}}}(\nabla n_0)\cdot\left(\frac{\boldsymbol{b}\times\boldsymbol{k}}{B}\phi_{\boldsymbol{k}}\right) = n_0\frac{\omega_{*\boldsymbol{k}}}{\omega_{\boldsymbol{k}}}\frac{e\phi_{\boldsymbol{k}}}{T_e}. \tag{1.73}$$

Equation (1.73) indicates that plasma motion generated by the electric field fluctuations couples with the density gradient, leading to the generation of density fluctuations. Taking the average of Eq. (1.72) results in

$$\frac{\partial n_0}{\partial t} + \nabla\cdot\left\langle\tilde{n}\tilde{\boldsymbol{V}}\right\rangle = 0. \tag{1.74}$$

The second term on the left-hand side of Eq. (1.74) is the term ignored in linear theory. Modes grow and this nonlinear term becomes larger, causing transport. Since both the density and velocity fluctuation are superpositions of countless waves, substituting

$$\tilde{n}(\boldsymbol{r},t) = \frac{1}{2\pi}\int_{-\infty}^{\infty}\tilde{n}_{\boldsymbol{k}}\, e^{i(\boldsymbol{k}\cdot\boldsymbol{r}-\omega_{\boldsymbol{k}}t)}d\boldsymbol{k} \quad\text{and}\quad \tilde{\boldsymbol{V}}(\boldsymbol{r},t) = \frac{1}{2\pi}\int_{-\infty}^{\infty}\tilde{\boldsymbol{V}}_{\boldsymbol{k}}\, e^{i(\boldsymbol{k}\cdot\boldsymbol{r}-\omega_{\boldsymbol{k}}t)}d\boldsymbol{k} \tag{1.75}$$

into Eq. (1.74) yields

$$\frac{\partial n_0}{\partial t} + \nabla \cdot \left(\int_{-\infty}^{\infty} d\boldsymbol{k}\ \tilde{n}_{\boldsymbol{k}} \tilde{\boldsymbol{V}}_{-\boldsymbol{k}}\ e^{2\gamma_{\boldsymbol{k}} t} \right) = 0 \tag{1.76}$$

We employed the relationships $2\pi\delta(\boldsymbol{k}+\boldsymbol{k}') = \int_{-\infty}^{\infty} \exp\{i(\boldsymbol{k}+\boldsymbol{k}')\cdot\boldsymbol{r}\}\, d\boldsymbol{r}$, $\omega_{\boldsymbol{k}} = \omega_{\boldsymbol{k}r} + i\gamma_{\boldsymbol{k}}$ ($\omega_{\boldsymbol{k}r}, \gamma_{\boldsymbol{k}} \in \mathbb{R}$), $\omega_{\boldsymbol{k}r} = -\omega_{-\boldsymbol{k}r}$, and $\gamma_{\boldsymbol{k}} = \gamma_{-\boldsymbol{k}}$. The second term on the left-hand side of the equation Eq. (1.74) represents the divergence of the particle flux $\boldsymbol{\Gamma}$, and since $\Gamma = D_{\mathrm{turb}} n_0 / L_n$, the diffusion coefficient can be written as

$$D_{\mathrm{turb}} = \frac{L_n}{n_0} \int_{-\infty}^{\infty} d\boldsymbol{k}\ \tilde{n}_{\boldsymbol{k}} \tilde{V}_{-\boldsymbol{k}x}\ e^{2\gamma_{\boldsymbol{k}} t} = i \frac{L_n}{n_0 B} \int_{-\infty}^{\infty} d\boldsymbol{k}\ k_y \tilde{n}_{\boldsymbol{k}} \phi_{-\boldsymbol{k}x}\ e^{2\gamma_{\boldsymbol{k}} t}. \tag{1.77}$$

Substituting Eq. (1.73) into Eq. (1.77) yields

$$D_{\mathrm{turb}} = \left(\int_{-\infty}^{\infty} L_n \frac{k_y \gamma_{\boldsymbol{k}}}{\omega_{*\boldsymbol{k}}} \frac{|\tilde{n}_{\boldsymbol{k}}|^2}{n_0^2}\ e^{2\gamma_{\boldsymbol{k}} t}\ d\boldsymbol{k} \right) \frac{T_e}{eB}. \tag{1.78}$$

Equation (1.78) indicates important things. The first important point is that when the density fluctuations $\tilde{n}_{\boldsymbol{k}}$ and electrostatic potential fluctuations $\phi_{\boldsymbol{k}}$ are in phase, no particle transport occurs because of $D_{\mathrm{turb}} = 0$. Although the $E \times B$ drift creates positive and negative radial flows, the density fluctuations are equal at both regions, therefore the particle transport cancels out and the net particle transport is zero. The second important point is that lower frequency waves contribute more to the diffusion when the fluctuation amplitudes are comparable. Accurate evaluation of Eq. (1.78) is difficult because of the need to consider nonlinear processes. However, it is possible to evaluate phenomenologically by using the mixing length theory. Since D_{turb} is proportional to $\exp(2\gamma_{\boldsymbol{k}} t)$, it becomes a reasonable approximation to consider the only fluctuation with the highest linear growth rate. In the mixing length theory, a density fluctuation is assumed to grow until the gradient of them becomes comparable to the gradient of a equilibrium density ($k_x \tilde{n} \sim n_0 / L_n$). The validity of this assumption has been confirmed through experiments such as Alcator A and Princeton Large Torus (PLT) [42]. Substituting this relationship into Eq. (1.78) leads to

$$D_{\mathrm{turb}} \sim \frac{\gamma_{\boldsymbol{k}}}{k_x^2}. \tag{1.79}$$

Equation (1.79) can be interpreted as a balance between the linear growth of a mode and the stabilizing effect of turbulent diffusion $k_x^2 D_{\mathrm{turb}}$ [2]. Equation Eq. (1.79) is consistent with the diffusion coefficient of a random walk where the correlation length is the radial wavelength and the correlation time is the inverse of the linear growth rate. The mode width of drift waves, such as the ITG modes localized on the flux surface ($x = x_m$) where $q(x_m) = m/n$, have been studied by eigenvalue analysis [43, 44, 45], and D_{turb} can be estimated by applying the results to Eq. (1.79). In the sheared

slab configuration $\boldsymbol{B} = (0, B_0(x - x_m)/L_s, B_0)$, the lowest order eigenmode function satisfies [44]

$$\frac{d\phi_0}{d\xi^2} + \left(E_0 - \xi^2\right)\phi_0 = 0. \tag{1.80}$$

The temperatures of ions and electrons are assumed to be equal, and L_s represents the characteristic spatial scale at which the pitch of the magnetic field lines varies radially near the rational surface. ξ and E_0 are defined as

$$\xi = \sqrt{\frac{iL_n}{L_s\Omega_0}}\frac{x - x_m}{\rho_{sT}} \quad \text{and} \quad E_0 = -\frac{iL_s\Omega_0}{L_n}\left(-k_y^2 + \frac{1 - \Omega_0}{1 + L_n/L_T + \Omega_0}\right), \tag{1.81}$$

respectively, and ϕ_0 and Ω_0 are the lowest order normalized eigenfunction and eigenvalue, respectively. Equation Eq. (1.80) is the Weber equation and is isomorphic to the Schrödinger equation for a particle moving under a harmonic oscillator potential. Upon assuming $|\mathrm{Re}(\Omega_0)| \gg |\mathrm{Im}(\Omega_0)|$, the eigenfunction is a oscillatory function in the x direction. A physically meaningful solution is one that satisfies $\lim_{|x|\to\infty} |\phi_0| \to 0$ and $\mathrm{Im}(\Omega_0) > 0$ [171]. The asymptotic solution of Eq. (1.80) is given by [45]

$$\lim_{|x|\to 0} \phi_0 = C \exp\left\{-i\frac{L_n}{2L_s\Omega_0}\frac{(x - x_m)^2}{\rho_s^2}\right\}, \tag{1.82}$$

where C is a constant. Thus, the mode width of the drift wave Δx is found to be

$$\Delta x \simeq \rho_s\sqrt{\frac{L_s}{L_n}}. \tag{1.83}$$

Equation (1.83) can also be obtained from the balance between the acoustic wave term and the finite inertial dispersion term in the mode equation ($\rho_s^2/\Delta x^2 \simeq v_{Ts}^2 k_y^2 \Delta x^2/(\omega^2 L_s^2)$) [47].

Figures 1.8(a), 1.8(b), and 1.8(c) show the the $(m, n) = (m, 20)$ electrostatic potentials of the tITG mode for the magnetic shears $\hat{s}_1$, $\hat{s}_2$, and $\hat{s}_3$, shown in Fig. 1.9, respectively. The parameters other than magnetic shear are the same as for the Cyclone base case parameters. The magnetic shears are $\hat{s}_1(r_s) \simeq 0.26, \hat{s}_2(r_s) \simeq 0.48$, and $\hat{s}_3(r_s) \simeq 0.78$ at $r_s = 0.5a_0$ and $\hat{s}_3(r_s)$ is the same as in the Cyclone base case. Figure 1.8 shows that the mode width of the tITG mode decreases as the magnetic shear increases, as indicated in Eq. (1.83). Upon assuming that the characteristic timescale of drift waves is approximately the diamagnetic drift ω_{*i}, the turbulent diffusion coefficient can be estimated as

$$D_{\mathrm{turb}} \sim (\Delta x)^2 \omega_{*i} \propto \rho_* \frac{T}{eB} \equiv \chi_{GB}, \tag{1.84}$$

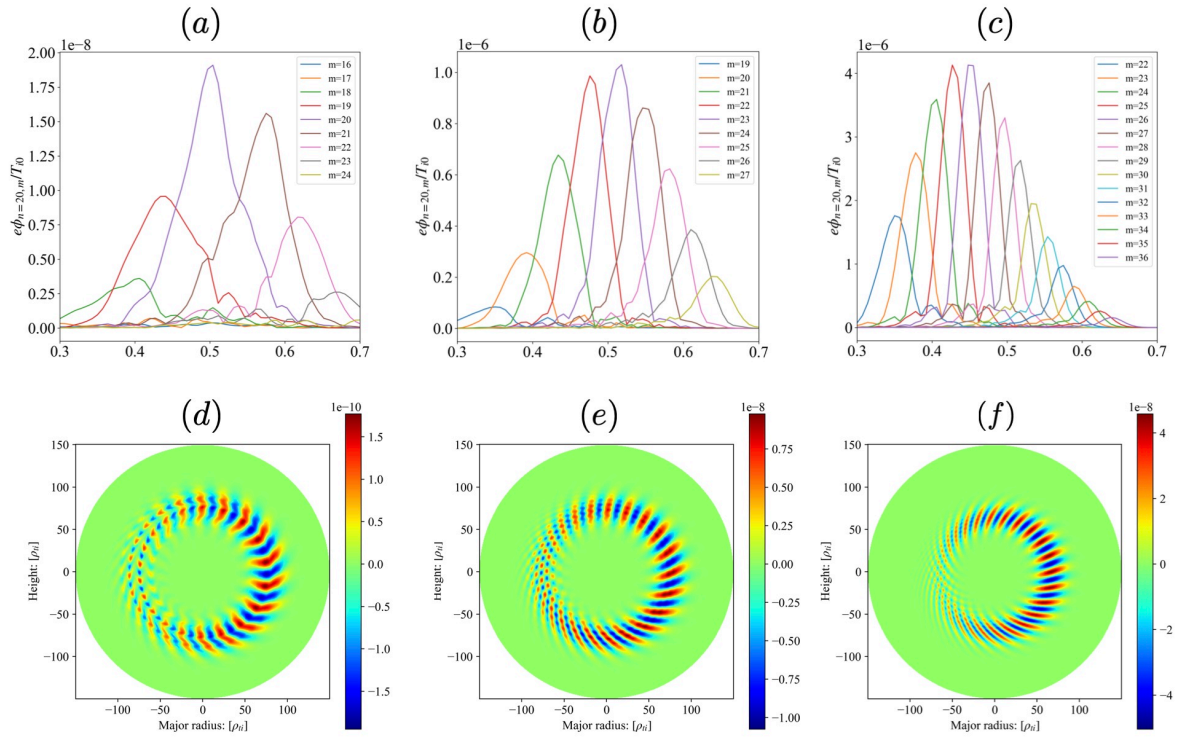

Fig. 1.8: (a), (b) and (c) represent the radial profiles of the $(m, n) = (m, 20)$ electrostatic potential. (d), (e) and (f) are contour maps of the $n = 20$ electrostatic potential. (a) and (d) are the simulation result for the case where $\hat{s}_1(r_s) \simeq 0.26$, (b) and (e) are for the case where $\hat{s}_2(r_s) \simeq 0.48$, and (c) and (f) are for the case where $\hat{s}_3(r_s) \simeq 0.78$. [By courtesy of Mr. Okuda of Kyoto University]

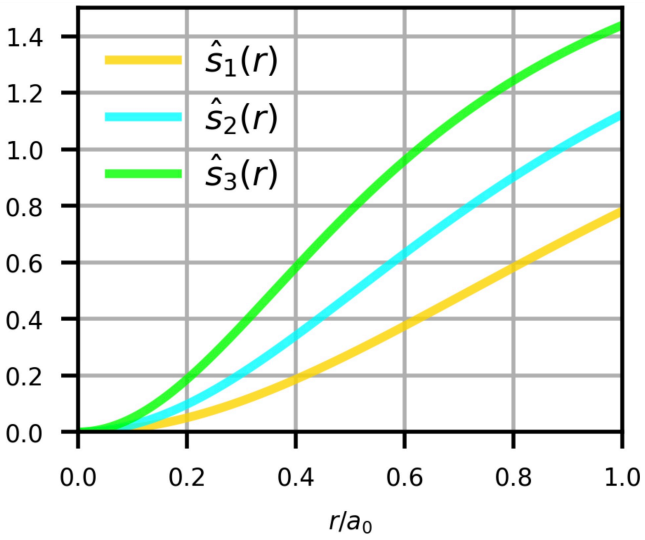

Fig. 1.9: Radial profiles of the magnetic shear for each case in Fig. 1.8.

where we used $\rho_* \equiv \rho_s/a_0$ and $L_n \sim a_0$. The gyroBohm diffusion coefficient χ_{GB} is proportional to the 3/2 power of temperature, indicating that transport increases with increasing temperature. Since χ_{GB} is proportional to a_0^{-1}, the larger the device

size is, the smaller the transport is. χ_{GB} is the diffusion coefficient corresponding to the transport brought about by local and microscale fluctuations. On the other hand, since Δx given by Eq. (1.83) is proportional to $\hat{s}^{-1/2}$ and the distance between adjacent rational surfaces $\Delta x_m \simeq x_m/(m\hat{s})$ is proportional to $\hat{s}^{-1}$, $\Delta x > \Delta x_m$ is satisfied as the magnetic shear increases. Indeed, from Fig. 1.8, it is evident that as the magnetic shear increases, the spacing between the rational surfaces decreases, leading to the overlap of the modes. In such cases, the interaction between modes must be considered [49, 50]. This interaction is due to the $\cos\theta$ dependence of the magnetic field. Due to the coupling between the magnetic field and $E \times B$ drift, the poloidal mode number of the potential contained in the $E \times B$ drift changes by ± 1. Hence, the equation of ϕ_m includes ϕ_{m+1} and ϕ_{m-1}. The mode structure due to toroidal coupling has been investigated using the two-dimensional eigenequation [51, 52]

$$L\left[\omega, \nabla_\parallel, \frac{\partial}{\partial r}, \frac{\partial}{\partial \theta}, r, \theta\right]\phi(r,\theta) = 0 \tag{1.85}$$

in the (r,θ) coordinate. Upon assuming that the eigenmode are centered on the rational surface $r = r_m$, the potential is expressed as $\phi = \exp(im\theta)\sum_l \phi_l(r)\exp(il\theta)$ where $\phi_l(r) = A(x)\hat{\phi}\exp(-il\theta_0)$ and $x \equiv n(\partial q/\partial r)_{r_m}(r - r_m) = k_\theta \hat{s}(r_m)(r - r_m)$. $A(x)$ represents a slowly varying envelope and is written as

$$A(x) = \exp\left(-i\int_0^x \theta_1(x')dx'\right). \tag{1.86}$$

$\hat{\phi}$ is the shape function and is the same for all poloidal harmonics. $\exp(-il\theta_0)$ corresponds to the phase difference between adjacent modes, and θ_0 is the ballooning angle. θ_1 in Eq. (1.86) is obtained as $\theta_1(x) \simeq -(\partial\omega/\partial x)/(\partial\omega/\partial\theta_0)x$ by expanding $\omega\left[\theta_0 + \theta_1(x), x\right] = \omega(\theta_0, x)$ which is the first order equation of Eq. (1.85) . Therefore, from Eq. (1.86), we get

$$A(x) \simeq \exp\left(-i\frac{\partial\omega/\partial x}{\partial\omega/\partial\theta_0}\frac{x^2}{2}\right). \tag{1.87}$$

For $A(x)$ to converge as x increases, $\mathrm{Im}((\partial\omega/\partial x)/(\partial\omega/\partial\theta_0)) > 0$ must be satisfied. The eigenfrequency is approximated as $\omega(\theta_0, x) = \omega_r(\theta_0, x) + i\gamma(\theta_0, x) \simeq \omega_r(0) + (\partial\omega_r/\partial x)_0 x + i\hat{\gamma}_0\cos\theta_0$. The real frequency is dominated by x and the growth rate is dominated by θ_0. From Eq. (1.87), we obtain

$$A(x) \simeq \exp\left(-\frac{(\partial\omega_r/\partial x)_0}{2\hat{\gamma}_0\sin\theta_0}x^2\right) = \exp\left(-\frac{x^2}{(n(\partial q/\partial r)_{r_m}\Delta r)^2}\right). \tag{1.88}$$

Approximating with $(\partial\omega_r/\partial r)_0 \sim \omega_d/L_T \sim \hat{\gamma}_0/L_T$, we find

$$\Delta r = \frac{\sqrt{2}}{\hat{s}k_\theta}\left|\frac{\hat{\gamma}_0\sin\theta_0}{(\partial\omega_r/\partial x)_0}\right|^{1/2} \simeq \sqrt{2}\left|\frac{\sin\theta_0(L_T\rho_s)}{\hat{s}(k_\theta\rho_s)}\right|^{1/2} \sim \sqrt{\frac{L_T\rho_s}{\hat{s}}}. \tag{1.89}$$

Δr is one order of magnitude larger than the microscale mode width Δx given by Eq. (1.83). In other words, the drift waves have a mesoscale structure due to toroidal coupling. Figs. 1.8(d), 1.8(c) and 1.8(f) show contour maps of the $n = 20$ electrostatic potential of the tITG mode for the magnetic shears $\hat{s}_1$, $\hat{s}_2$ and $\hat{s}_3$ shown in Fig. 1.9, respectively. It is found that large mesoscale vortex structures are formed when the magnetic shear is large. On the other hand, when the magnetic shear is small, the different modes are difficult to couple, and smooth global structures are not formed. Using Eq. (1.89) to evaluate the turbulent diffusion coefficient results in

$$D_{\rm turb} \sim (\Delta r)^2 \, \omega_{*i} \propto \frac{T}{eB} \equiv \chi_B. \tag{1.90}$$

χ_B is referred to as the Bohm diffusion coefficient, and it is greater than χ_{GB}. It is proportional to temperature, indicating that transport is greater in high temperature plasmas. χ_B, unlike χ_{GB}, does not depend on the size of devices. The flux tube model ($\rho_* \to 0$) is known to give results consistent with the gyroBohm scale [19]. By performing the global gyrokinetic simulations with different device sizes, Lin *et al.* showed that the turbulent transport is consistent with the Bohm scaling where ρ_* is large and gyroBohm scaling where ρ_* is small [53]. Transport coefficients are closely linked to confinement performance. the L-mode ITER89P scaling $\tau_E^{\rm ITER89P} = 0.048 A^{0.5} I_p^{0.85} B_0^{0.2} R_0^{1.2} a_0^{0.3} \kappa^{0.5} n^{0.1} P_h^{-0.5}$ corresponds to the Bohm scaling and the H-mode IPB98(y, 2) scaling $\tau_E^{\rm IPB98(y,2)} = 0.145 A^{0.19} I_p^{0.93} B_0^{0.15} R_0^{1.39} a_0^{0.58} \kappa^{0.78} n^{0.41} P_h^{-0.69}$ corresponds to the gyroBohm scaling [2], where A is the ion mass number, I_p is the plasma current (MA), B_0 is the toroidal magnetic field at the plasma center (T), κ is the ellipticity, n is the line-averaged density (10^{20} m^{-3}), and P_h is the heating power (MW).

In the nonlocal ballooning theory discussed above, the lowest order linear growth rate is $\gamma_0(\theta_0, x) = \hat{\gamma}_0 \cos\theta_0$. The linear growth rate is maximized for $\theta_0 \to 0$, and the mode width is $\Delta r \to 0$ from Eq. (1.89). That is, at the lowest order, the mode width of the mode with the largest linear growth rate is zero. Higher order correction terms for the growth rate need to be taken into account. By taking the correction term as $-\hat{\gamma}_0/(k_\theta \hat{s} \Delta r)^2$ and expanding the growth rate in terms of θ_0, we obtain

$$\gamma \simeq \hat{\gamma}_0 \left(\cos\theta_0 - \frac{(\partial\omega_r/\partial x)_0}{2\hat{\gamma}_0 |\sin\theta_0|} \right) \simeq \hat{\gamma}_0 \left(1 - \frac{\theta_0^2}{2} - \frac{(\partial\omega_r/\partial x)_0}{2\hat{\gamma}_0 |\theta_0|} \right). \tag{1.91}$$

The radial variation in the background profiles has a stabilizing effect. Because flux-tube simulations cannot account for variations in the equilibrium profiles, they overestimate turbulent transport compared to global simulations [48]. From Eq. (1.91), the ballooning angle at which the linear growth rate is maximized is expressed as

$$(\theta_0)_{\rm max} \simeq \mp \left| \frac{(\partial\omega_r/\partial r)_{r_m}}{k_\theta \hat{\gamma}_0 \hat{s}} \right|^{1/3}. \tag{1.92}$$

Therefore, from Eq. (1.89), the mode width with the largest linear growth rate is

$$\Delta r = \sqrt{2} \left| \frac{\sin(\theta_0)_{\max}}{k_\theta^2 \hat{s}^2 (\theta_0)^3_{\max}} \right|^{1/2}. \tag{1.93}$$

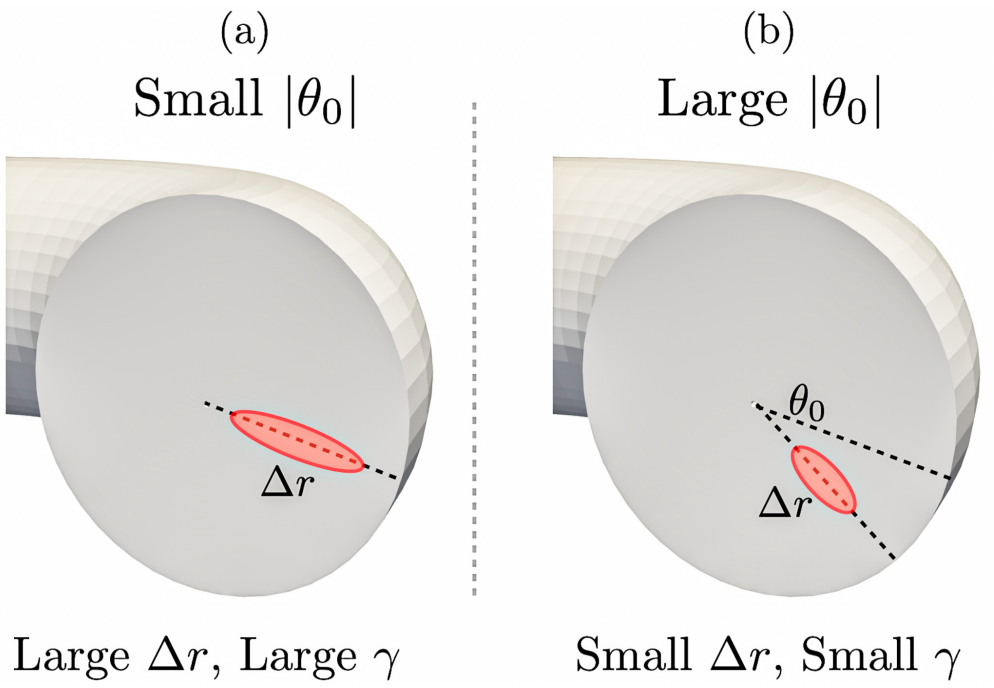

Fig. 1.10: Mode structure for small ballooning angle (a) and mode structure for large ballooning angle (b).

Figure 1.10 shows the mode width and linear growth rate for small (a) and large (b) ballooning angles. When the ballooning angle is small, the mode width and linear growth rate are large. On the other hand, when the ballooning angle is large, the mode width and linear growth rate are small. When poloidal flow V_θ or toroidal flow V_φ is present in the background, $\partial\omega_r/\partial r$ replaces $\partial\omega_r/\partial r + \partial\omega_f/\partial r$ in the equations for ballooning angle and mode width (Eq. (1.92) and Eq. (1.93)). $\omega_f \equiv k_\theta V_\theta + k_\varphi V_\varphi$ is the Doppler shift frequency. Thus, it can be seen that the background flow has a significant effect on the linear growth rate of the mode.

1.3.3 Profile stiffness

We consider how turbulence transport affects the density and temperature profiles. The time evolution of the wave energy $\varepsilon \equiv |e\phi_{\boldsymbol{k}}/T|^2$ is modeled as [54]

$$\frac{\partial \varepsilon}{\partial t} = 2\left(\gamma_L - \gamma_{NL}\right)\varepsilon, \tag{1.94}$$

where $\gamma_L \equiv \gamma_0(R/L_T - R/L_{Tc})$ is the linear growth rate of the mode, R/L_{Tc} is the critical temperature gradient, and γ_{NL} is the nonlinear decay rate. In this model, the wave energy does not increase unless the critical temperature gradient R/L_{Tc} is exceeded. This feature is based on experiments on Joint European Torus (JET) [55, 56] and turbulence simulation results [48]. They show that turbulent transport increases rapidly above the critical temperature gradient, as shown in Fig. 1.11.

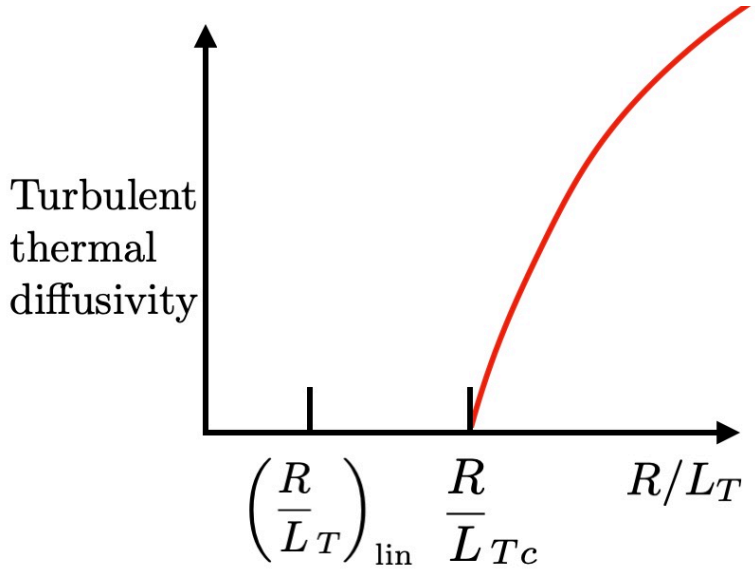

Fig. 1.11: Schematic graph of turbulent thermal diffusivity against R/L_T

The critical temperature gradient inferred from experiments on JET and obtained from gyrofluid simulations is smaller and closer to a linear critical gradient than that obtained from gyrokinetic simulations [55, 48]. The difference in the results between gyrofluid simulations and gyrokinetic simulations is explained by the difference in Rosenbluth-Hinton residual zonal flows [64]. The critical temperature gradient obtained from gyrokinetic simulations is $R/L_{Tc} \simeq 6$ and the thermal diffusion coefficient is $\chi L_n/(\rho_i^2 v_T) \simeq 15.4[1.0 - 6.0(R/L_T)^{-1}]$ [48]. Calculations incorporating the effects of plasma shape have also been performed, yielding $\chi \propto [1.0 - \alpha_E(\gamma_E/\gamma_L)]$ [57, 58], where $\alpha_E \equiv 0.71(3\varepsilon_t)^{0.6}(\kappa/1.5)$ and γ_E is $E \times B$ shear rate. In Eq. (1.94), when $\gamma_0 \gg \gamma_{NL}$ and R/L_{Tc} is exceeded, ε becomes significantly large, leading to $R/L_T = R/L_{Tc}$. Therefore, the temperature profile is

$$T(r) = T(a_0) \exp\left(\frac{a_0 - r}{L_{Tc}}\right). \tag{1.95}$$

Equation (1.95) shows that the temperature profile is proportional to the temperature at the edge $T(a_0)$. In ASDEX Upgrade experiments, it has been observed that

there exists a linear relationship between the edge and core temperatures [59]. In the following, we consider the case where $\gamma_L \sim \gamma_{NL} \sim \omega_{*p}$ and the fluctuation scale is sufficiently fast compared to the transport scale. In this case, the diffusion coefficient D due to the $E \times B$ drift is $D \sim D_0\varepsilon \equiv v_T L_T \varepsilon$ [54]. Thus, the nonlinear decay rate is estimated to be $\gamma_{NL} \sim \gamma_{N0}\varepsilon \equiv k_r^2 D_0 \varepsilon$ from Eq. (1.79). The ratio of the nonlinear decay rate $\gamma_{N0}^{(GB)}$ evaluated by the gyroBohm diffusion coefficient Eq. (1.84) to the nonlinear decay rate $\gamma_{N0}^{(B)}$ evaluated by the Bohm diffusion coefficient Eq. (1.90) is $\gamma_{N0}^{(B)}/\gamma_{N0}^{(GB)} \simeq \rho/L_T \ll 1$. This means that the nonlinear effect of suppressing mode growth is much greater for micro-scale vortex structures than for mesoscale vortex structures. At the transport scale, phenomena at the fluctuation scale can be considered steady-state, thus $\varepsilon = (\gamma_0/\gamma_{N0})\,(R/L_T - R/L_{Tc})$ holds. Therefore, the diffusion coefficient is $D = D_0\,(\gamma_0/\gamma_{N0})\,(R/L_T - R/L_{Tc})$. Substituting D into the energy equation assuming adiabatic response yields [54]

$$\frac{3}{2}n\frac{\partial T}{\partial t} = \frac{\partial}{\partial r}\left\{nD_0\frac{\gamma_0}{\gamma_{N0}}\left(\frac{R}{L_T} - \frac{R}{L_{Tc}}\right)\right\}\frac{\partial T}{\partial r} + P_{\rm in}, \tag{1.96}$$

where $P_{\rm in}$ is the input power. The temperature gradient at steady state is found to be

$$\frac{R}{L_T} = \frac{1}{2}\frac{R}{L_{Tc}} + \frac{1}{2}\sqrt{\left(\frac{R}{L_{Tc}}\right)^2 + 4\overline{Q}\frac{\gamma_{N0}}{\gamma_0}}, \quad \overline{Q} \equiv \frac{R}{nD_0T}\int_0^r P_{\rm in}(r')dr'. \tag{1.97}$$

Therefore, the difference between the temperature gradient and the critical temperature gradient $\Delta(R/L_T)$ is obtained as

$$\Delta\left(\frac{R}{L_T}\right) \equiv \frac{R}{L_T} - \frac{R}{L_{Tc}} = \frac{1}{2}\frac{R}{L_T}\left[\sqrt{1 + 4\left(\frac{R}{L_{Tc}}\right)^{-2}\overline{Q}\frac{\gamma_{N0}}{\gamma_0}} - 1\right]. \tag{1.98}$$

In the high temperature limit, let us substitute $\gamma_{N0}^{(GB)}$ and $\gamma_{N0}^{(B)}$ into Eq. (1.98), denoting the resulting expressions as $\Delta\,(R/L_T)^{(GB)}$ and $\Delta\,(R/L_T)^{(B)}$, respectively. Their ratio is $\Delta\,(R/L_T)^{(B)}\,/\Delta\,(R/L_T)^{(GB)} \simeq \rho/L_T \ll 1$. This means that when turbulent transport scales to the Bohm scaling, the temperature profile is closer to Eq. (1.95) than when it scales to the gyroBohm scaling. The small variation in temperature profile is often described as "stiff," and it is suggested that reducing the profile stiffness plays a crucial role in internal transport barrier (ITB) formation [56]. In experiments on JET, it has been observed that toroidal flow relaxes profile stiffness [55] and that this effect works particularly strongly in low magnetic shear [56]. The experimental results are explained by the electromagnetic stabilization of the ITG mode. [60]. The $\hat{s}$ dependence of the electromagnetic stabilization is qualitatively consistent with the $\hat{s}$ dependence of stiffness obtained in the experiments on JET. δf gyrokinetic simulations have shown that when the flow shear rate $\gamma_{\rm tor}$ is small, R/L_{Tc} is large but stiffness increases, and when $\gamma_{\rm tor}$ is moderate (large but not too large), both R/L_{Tc} and stiffness decrease [61].

This is due to the unstable mode changing to the parallel velocity gradient (PVG) mode [62, 63]. Similarly or even more than toroidal flows, poloidal flows are drawing significant attention, as we will explain in the next section.

1.3.4 Poloidal Flows

There are three major poloidal flows in toroidal plasmas. They are the geodesic acoustic mode (GAM) [65], zonal flow [73], and flow due to mean electric field [88], respectively. GAM is a mode in which the $(m, n) = (0, 0)$ electrostatic potential is coupled to the $(m, n) = (1, 0)$ pressure fluctuation due to the toroidal effect. The zonal flow is the $(m, n) = (0, 0)$ flow driven by nonlinear coupling of waves (Reynolds stress), and the mean electric field is the electric field generated to satisfy the radial force balance. The characteristics of each are described below.

From Eq. (1.72), the time evolution equation for the normalized density fluctuation $\tilde{N} = \tilde{n}/n_0$:

$$\frac{\partial \tilde{N}}{\partial t} - \frac{2}{R}\sin\theta \tilde{V}_{E\times B} + \nabla_{\parallel}\tilde{V}_{\parallel} = 0 \tag{1.99}$$

is derived. Due to the toroidal effect, the divergence of the $E \times B$ flow is not zero. $\kappa = \sin\theta/R$ in the second term of Eq. (1.99) is the geodesic curvature. From the momentum equation

$$n_0 m \frac{\partial \tilde{\boldsymbol{V}}}{\partial t} = -\nabla\tilde{p} + \tilde{\boldsymbol{J}} \times \boldsymbol{B} \tag{1.100}$$

and the charge neutrality condition

$$\nabla \cdot \tilde{\boldsymbol{J}} = 0, \tag{1.101}$$

the time evolution equations for $\tilde{V}_{E\times B}$ and $\tilde{V}_{\parallel}$ are derived as

$$\frac{\partial \tilde{V}_{E\times B}}{\partial t} + \frac{c_s^2}{\pi R}\oint \tilde{N}\sin\theta d\theta = 0 \tag{1.102}$$

and

$$\frac{\partial \tilde{V}_{\parallel}}{\partial t} + c_s^2 \nabla_{\parallel}^2 \tilde{N} = 0, \tag{1.103}$$

respectively [66]. Assuming that the $E \times B$ flow causes up-down asymmetric density perturbations and that $\tilde{N} \propto \exp i\left\{(k_r, 0, k_{\parallel})^T \cdot \boldsymbol{r} - \omega t\right\}\sin\theta$, the GAM dispersion relation equation

$$-\omega_{\mathrm{GAM}}^2 + \frac{2c_s^2}{R^2} + k_{\parallel}^2 c_s^2 = 0 \tag{1.104}$$

is derived from Eqs. (1.99), (1.102), and (1.103). Thus, the frequency of the GAM is obtained as

$$\omega_{\mathrm{GAM}}^2 = \frac{c_s^2}{R^2}\left(2 + k_{\parallel}^2 R^2\right) \simeq \frac{c_s^2}{R^2}\left(2 + \frac{1}{q^2}\right). \tag{1.105}$$

From Eqs. (1.105), (1.102), and (1.103), the toroidal velocity of the GAM is [67]

$$\tilde{V}_{\parallel} = \frac{1}{q}\cos\theta\,\tilde{V}_{E\times B}. \tag{1.106}$$

From Eqs. (1.105) and (1.102), the density fluctuation of the GAM is

$$\frac{\tilde{n}}{n_0} = k_r\rho\sqrt{2+\frac{1}{q^2}}\frac{e\phi}{T}\sin\theta. \tag{1.107}$$

Historically, the GAM was first theoretically predicted in 1968 by Winsor *et al.* They derived the equation [65]

$$\omega^2\int|\tilde{\rho_m}|^2\mathcal{J}dS = c_s^2\left[\left|\int\tilde{\rho}_m\frac{\boldsymbol{B}\times\nabla\psi\cdot\nabla B^2}{B^4}\mathcal{J}dS\right|^2\Big/\int\frac{|\nabla\psi|^2}{B^2}\mathcal{J}dS+\int\frac{|\boldsymbol{B}\cdot\nabla\tilde{\rho}_m|^2}{B^2}\mathcal{J}dS\right]. \tag{1.108}$$

from Eqs. (1.72), (1.100), (1.101) and

$$\rho_{m0}^{-\Gamma}\frac{\partial\tilde{p}}{\partial t}-\Gamma p_0\rho_{m0}^{\Gamma}\frac{\partial\tilde{\rho}_m}{\partial t}+\tilde{\boldsymbol{V}}\cdot\nabla\left(p_0\rho_{m0}^{-\Gamma}\right)=0. \tag{1.109}$$

Here, Γ is the ratio of specific heats, ρ_m is the mass density, ψ is the flux label, and the integral represents the flux-surface average. The first term on the right-hand side, which depends on the magnetic field gradient in the $\boldsymbol{B}\times\nabla\psi$ direction, represents the GAM. On the other hand, the second term on the right-hand side represents the normal acoustic mode along the magnetic field. Substituting the magnetic field $\boldsymbol{B} = B_0/(1+\varepsilon_t\cos\theta)\left\{\boldsymbol{e}_z + r/\left(q\sqrt{R_0^2-r^2}\right)\boldsymbol{e}_\theta\right\}$ into Eq. (1.108) yields the GAM frequency Eq. (1.105). Equation (1.105) are the result from the fluid models, and the derivation using the gyrokinetic model was done by Sugama and Watanabe [68]. According to the Sugama and Watabae theory (SW Theory), the time evolution of an initially given $(m,n) = (0,0)$ electrostatic potential $\phi_{k_r}(0)$ is given by $\phi_{k_r}(0) = \phi_{k_r}(\infty) + [\phi_{k_r}(0) - \phi_{k_r}(\infty)]\cos(\omega_{\rm GAM}t)\exp(\gamma t)$. The GAM frequency $\omega_{\rm GAM}$ and decay rate γ are given by [68]

$$\omega_{\rm GAM} = \frac{\sqrt{11}}{2}q\left(\frac{v_{Ti}}{qR_0}\right)\sqrt{1+\frac{86}{121q^2}} \tag{1.110}$$

and

$$\gamma = -\frac{\sqrt{\pi}}{2}\left(q\hat{\omega}_{\rm GAM}\right)^2\left(\frac{v_{Ti}}{qR_0}\right)\frac{121q^2}{121q^2+86}\Big[e^{-\hat{\omega}_{\rm GAM}^2}\left(\hat{\omega}_{\rm GAM}^2+3\right) + \frac{q^2}{256}(k_r\rho_i)^2\,e^{-\hat{\omega}_{\rm GAM}^3/4}\left(\hat{\omega}_{\rm GAM}^4+11\hat{\omega}_{\rm GAM}^2+66\right)\Big], \tag{1.111}$$

respectively, assuming $\hat{\omega}_{\rm GAM}^2 \equiv \left(qR_0\omega_{\rm GAM}/v_{Ti}\right)^2 \gg 1$ and $T_e/T_i = 1$.

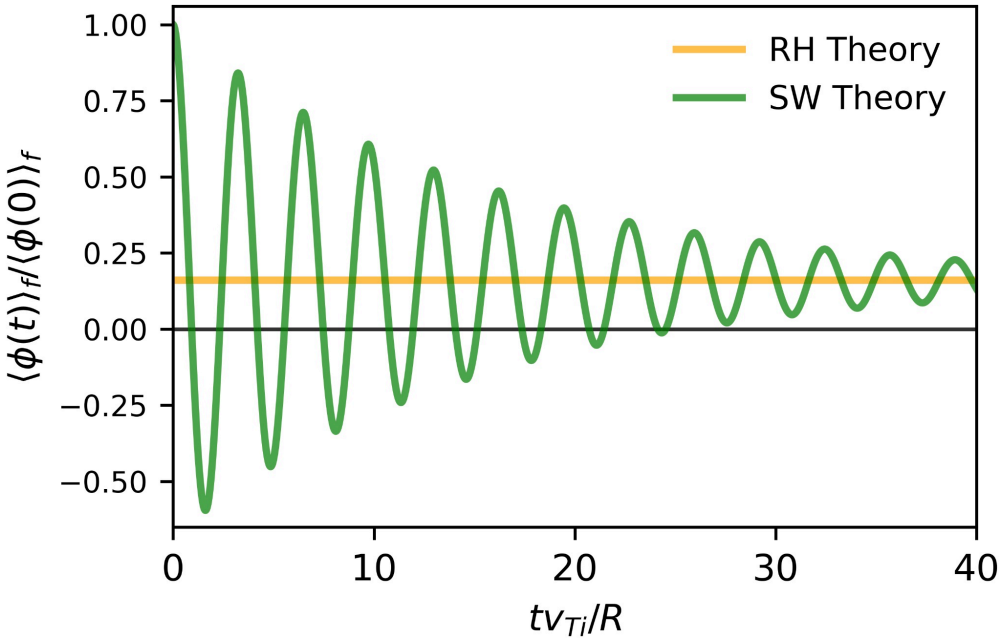

Fig. 1.12: Time evolution of the $(m, n) = (0, 0)$ electrostatic potential based on the SW theory. The yellow horizontal line is the residual zonal flow based on the RH theory.

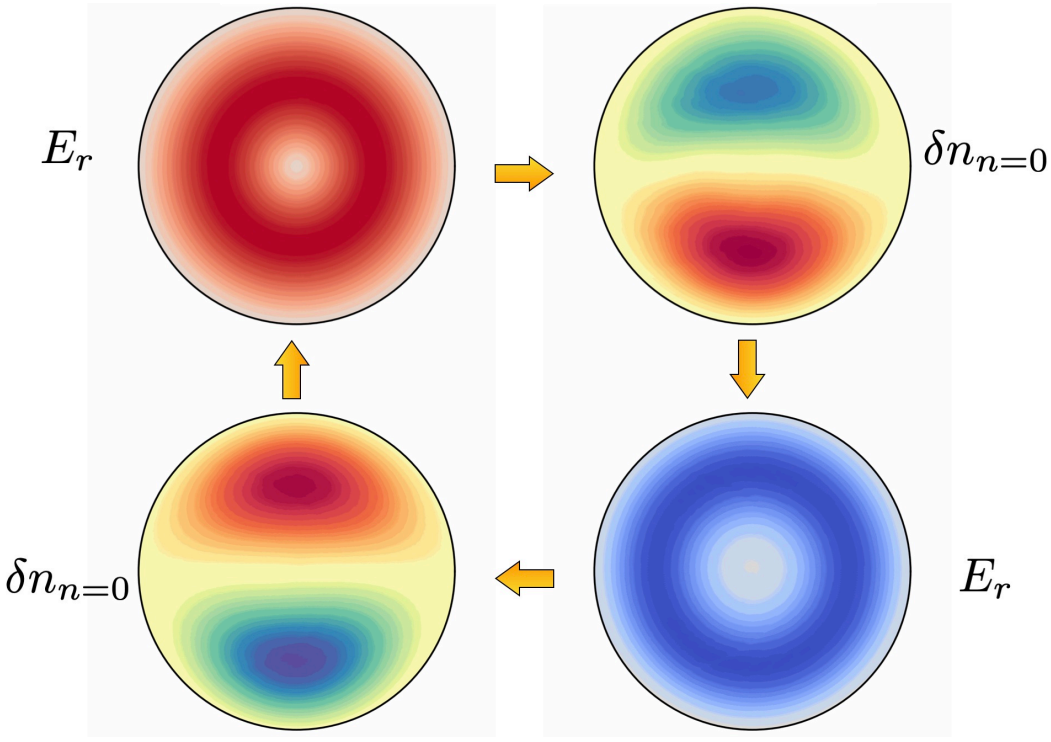

Fig. 1.13: Physical mechanism of the GAM.

Figure 1.12 shows the time evolution of the $(m, n) = (0, 0)$ electrostatic potential based on Eqs. (1.110) and (1.111). The yellow horizontal line is the residual zonal flow $\phi_{k_r}(\infty) = \phi_{k_r}(0)/(1+1.6q^2/\varepsilon_t^{1/2})$ derived by Rosenbluth and Hinton (RH Theory) [64].

The GAM repeats the cycle: positive radial electric field $E_r > 0 \rightarrow$ up-down asymmetric density perturbation $\delta n_{n=0} \propto -\sin\theta \rightarrow$ negative radial electric field $E_r < 0 \rightarrow$ density perturbation in opposite phase $\delta n_{n=0} \propto \sin\theta \rightarrow$ positive radial electric field E_r, as shown in Fig. 1.13. The radial electric field and density fluctuations in the figure were obtained from the GAM simulations using the global gyrokinetic code GyroKinetic Numerical Experiment of Tokamak (GKNET) [92]. The background density and temperature distributions are $n(r) = T(r) = 1$, the magnetic shear is $\hat{s}_3$, shown in Fig. 1.9, and the initial distribution function is given as

$$\delta f_i(\boldsymbol{X}, v_\parallel, \mu, t=0) = 10^{-5}\left[\left(\frac{\pi}{a_0}\right)^2 \cos\left(\frac{\pi r}{a_0}\right) + \frac{\pi}{a_0 r}\sin\left(\frac{\pi r}{a_0}\right)\right] f_{0i}. \tag{1.112}$$

The physical mechanism of GAM is described as follows [69, 70]. The $E \times B$ flow is created when a positive radial electric field $E_r > 0$ is generated. The toroidal effect leads to larger $E \times B$ flow outside the torus, resulting in the creation of up-down asymmetric pressure perturbations $\delta p_{n=0} \propto -\sin\theta$. Due to the pressure gradient, a diamagnetic current is generated. To maintain the quasi-neutrality Eq. (1.101), a polarization current flows to balance the diamagnetic current. This leads to changes in the radial electric field, causing its direction to reverse. GAM has been observed in many devices such as the DIII-D and ASDEX-U [71]. GAM damping tests are widely used as benchmarks for gyrokinetic simulations [72].

In Eq. (1.100), when $\tilde{n}$ does not depend on θ, then ω equals zero. In this case, $\tilde{n} = 0$ from Eq. (1.103). Thus, unlike the GAM, zonal flow has no density fluctuations and does not oscillate in time. From Eq. (1.99), the velocity in the toroidal direction is obtained as [67]

$$\tilde{V}_\parallel = -2q\cos\theta \tilde{V}_{E\times B}. \tag{1.113}$$

To investigate the mechanism of zonal flow generation, we introduce the partial ensemble average $\langle\cdot\rangle$. Using the average, the electrostatic potential $\phi = \bar{\phi} + \tilde{\phi}$ is expressed as the sum of $\bar{\phi} \equiv \langle\phi\rangle$, which varies slowly on the large scale, and $\tilde{\phi}$, which varies quickly on the small scale. When $\bar{\phi}$ and $\tilde{\phi}$ are Fourier expanded, the former has a large contribution from low wavenumber components, while the latter has a large contribution from high wavenumber components. The $E \times B$ flow can likewise be separated into large- and small-scale flow as $\boldsymbol{V}_{E\times B} = \bar{\boldsymbol{V}}_{ZF} + \tilde{\boldsymbol{V}}_{E\times B}$. The dynamics are described in the Modified Hasegawa-Mima euqation (MHM equation) [74, 75]

$$\left(\frac{\partial}{\partial t} + \bar{\boldsymbol{V}}_{ZF}\cdot\nabla_\perp\right)\frac{e\tilde{\phi}}{T_e} + \boldsymbol{V}_*\cdot\nabla_\perp\frac{e\tilde{\phi}}{T_e} - \rho_s^2\left(\frac{\partial}{\partial t} + \boldsymbol{V}_{E\times B}\cdot\nabla_\perp\right)\nabla_\perp^2\frac{e\phi}{T_e} = 0. \tag{1.114}$$

The equation represents the dynamics of a two-dimensional slab configuration, with $\boldsymbol{r} = x\boldsymbol{e}_x + y\boldsymbol{e}_y$ and $\boldsymbol{k} = k_x\hat{\boldsymbol{k}}_x + k_y\hat{\boldsymbol{k}}_y$. Linearizing Eq. (1.114), we find that the frequency

of the wave is

$$\omega_k = \frac{k_y V_*}{1+\rho_s^2 k^2} + \boldsymbol{k}\cdot\bar{\boldsymbol{V}}_{ZF}. \tag{1.115}$$

The Doppler shift is caused by the zonal flow. From Eq. (1.115), we obtain

$$\frac{\partial\omega_k}{\partial\boldsymbol{k}} = \frac{V_*}{1+\rho_s^2k^2}\hat{\boldsymbol{k}}_y - \frac{2V_*k_y\rho_s^2}{(1+\rho_s^2k^2)^2}\boldsymbol{k} + \bar{\boldsymbol{V}}_{ZF} \tag{1.116}$$

and

$$\frac{\partial^2\omega_k}{\partial\boldsymbol{k}\partial\boldsymbol{k}} = \frac{8V_*k_y\rho_s^4}{(1+\rho_s^2k^2)^3}\boldsymbol{k}\boldsymbol{k} - \frac{2V_*\rho_s^2}{(1+\rho_s^2k^2)^2}\left(\boldsymbol{k}\hat{\boldsymbol{k}}_y + \hat{\boldsymbol{k}}_y\boldsymbol{k} + k_y\boldsymbol{I}\right) + \frac{\partial\bar{\boldsymbol{V}}_{ZF}}{\partial\boldsymbol{k}}, \tag{1.117}$$

where $\boldsymbol{I}$ is the unit matrix. Taking the average of Eq. (1.114) and extracting the large-scale dynamics,

$$\frac{\partial}{\partial t}\bar{V}_{ZF} = -\frac{\partial}{\partial x}R_{xy} \tag{1.118}$$

is derived [76, 77] from the incompressibility condition $\nabla\cdot\boldsymbol{V}_{E\times B} = 0$. $R_{xy} \equiv -c^2/B^2\left\langle(\partial\tilde{\phi}/\partial x)(\partial\tilde{\phi}/\partial y)\right\rangle$ is the Reynolds stress. Equation (1.118) shows that the zonal flow is generated by the nonlinear coupling of the drift waves. In the limit $q/k \ll 1$ where the wavenumber of the drift wave $\boldsymbol{k}$ is sufficiently larger than that of the zonal flow $\boldsymbol{q}$, the Reynolds stress is

$$R_{xy} = -\frac{c^2}{B^2}\int d\boldsymbol{k}\frac{k_xk_y}{(1+\rho_s^2k^2)^2}N_{\boldsymbol{k}}. \tag{1.119}$$

$N_{\boldsymbol{k}}$ is the wave action, defined [76] as

$$N_{\boldsymbol{k}} \equiv (1+\rho_s^2k^2)^2\int d\boldsymbol{q}\; e^{i\boldsymbol{q}\cdot\boldsymbol{r}}\left\langle\tilde{\phi}_{\boldsymbol{k}}\tilde{\phi}_{\boldsymbol{q}-\boldsymbol{k}}\right\rangle. \tag{1.120}$$

From Eqs. (1.118) and (1.119), we obtain the equations describing the zonal flow dynamics [67]:

$$\frac{\partial}{\partial t}\bar{V}_{ZF} = \frac{c^2}{B^2}\frac{\partial}{\partial x}\int d\boldsymbol{k}\frac{k_xk_y}{(1+\rho_s^2k^2)^2}N_{\boldsymbol{k}}. \tag{1.121}$$

Since Eq. (1.121) contains $N_{\boldsymbol{k}}$, we close the system of the equations by finding the governing equation for $N_{\boldsymbol{k}}$. Differentiating Eq. (1.120) by time and using $q/k \ll 1$, we obtain

$$\frac{\partial N_{\boldsymbol{k}}}{\partial t} - \frac{\partial\omega_k}{\partial\boldsymbol{r}}\cdot\frac{\partial N_{\boldsymbol{k}}}{\partial\boldsymbol{k}} + \frac{\partial\omega_k}{\partial\boldsymbol{k}}\cdot\frac{\partial N_{\boldsymbol{k}}}{\partial\boldsymbol{r}} = 0. \tag{1.122}$$

Equation (1.122) has a Hamiltonian structure, indicating that the action spectrum of the drift wave is constant along any trajectory derived from the Hamiltonian [67]. From Eqs. (1.121) and (1.122), the linear equation for $\bar{V}_{ZF}$

$$\frac{\partial}{\partial t}\bar{V}_{ZF} = -D_{ZF}\frac{\partial^2}{\partial x^2}\bar{V}_{ZF} \tag{1.123}$$

is derived, where Ω is the complex frequency of the zonal flow and D_{ZF} is defined as

$$D_{ZF} \equiv -\frac{c^2}{B^2}\int d\boldsymbol{k}\frac{i}{\Omega - q_x\partial\omega_k/\partial k_x}\frac{k_xk_y^2}{(1+\rho_s^2k^2)^2}\frac{\partial N_{\boldsymbol{k}}}{\partial k_x}. \tag{1.124}$$

Equation (1.123) shows that the zonal flow grows with time when $\partial N_{\boldsymbol{k}}/\partial k_x < 0$.

Zonal flows are believed to be generated through the modulational instability [78, 79, 80]. The complex amplitude a of a quasi-monochromatic drift wave $\psi(\boldsymbol{r},t) = a(\boldsymbol{r},t)\exp i(\boldsymbol{k}\cdot\boldsymbol{r}-\omega_k t)$ of wavenumber $\boldsymbol{k}$ and frequency ω_k satisfies the Nonlinear Schrödinger equation [78]

$$i\frac{\partial a}{\partial t} + i\frac{V_*}{1+\rho_s^2k^2}\left\{\hat{\boldsymbol{k}}_y - \frac{2k_y\rho_s^2}{1+\rho_s^2k^2}\boldsymbol{k}\right\}\cdot\nabla a \\ - \frac{V_*\rho_s^2}{(1+\rho_s^2k^2)^2}\left\{\boldsymbol{k}\hat{\boldsymbol{k}}_y + \hat{\boldsymbol{k}}_y\boldsymbol{k} + k_y\boldsymbol{I} - \frac{4k_y\rho_s^2}{1+\rho_s^2k^2}\boldsymbol{k}\boldsymbol{k}\right\} : \nabla\nabla a = \frac{(1+\rho_s^2k^2)^2k_y}{\rho_s^2V_*}|a|^2a \tag{1.125}$$

from Eqs. (1.116) and (1.117) when the spectral width $\Delta k/k$ and the complex amplitude $|a|/k$ are of the same order. The coefficient in the second term on the left-hand side of Eq. (1.125) represents the group velocity v_g and does not contribute to the deformation of a. The third term on the left-hand side is a term proportional to $\partial^2\omega/\partial\boldsymbol{k}\partial\boldsymbol{k}$, known as the group velocity dispersion term. This term describes the deformation of a caused by the change in the group velocity with wavenumber. The right-hand side of Eq. (1.125) represents the nonlinear frequency shift, and using $\varsigma \equiv (1+\rho_s^2k^2)^2k_y/\rho_s^2V_*|a|^2$, the solution which is independent of positions is $a = a'\ \exp(-i\varsigma t)$. Adding perturbations to the uniform solution and performing a stability analysis, the instability condition for the modulation instability is derived as

$$\left\{-\frac{V_*k_y\rho_s^2}{(1+\rho_s^2k^2)^2} + \frac{4V_*k_yk_x^2\rho_s^4}{(1+\rho_s^2k^2)^3}\right\}\left\{\frac{(1+\rho_s^2k^2)^2k_y}{\rho_s^2V_*}\right\} < 0 \Longleftrightarrow 1 - 3\rho_s^2k_x^2 + \rho_s^2k_y^2 > 0. \tag{1.126}$$

The linear growth rate has the maximum value

$$\gamma_{\max} = \frac{(1+\rho_s^2k^2)^2k_y}{V_*\rho_s^2}|a'|^2 \tag{1.127}$$

when

$$q_x = \sqrt{\frac{(1+\rho_s^2k^2)^5}{1-3\rho_s^2k^2+\rho_s^2k_y^2}}\frac{a'}{V_*\rho_s^2}. \tag{1.128}$$

Fig. 1.14 shows the physical mechanism of the modulational instability when the group velocity is a decreasing function of wavenumber and $\varsigma > 0$. When the amplitude increases due to fluctuations, since $\varsigma > 0$, i.e., the phase velocity of the drift wave v_p increases, the wavenumber increases in the front and decreases in the back. As the group velocity is a decreasing function of wavenumber, the group velocity is smaller in the front and larger in the back. Since the group velocity is the propagation speed of energy, the amplitude increases further where the amplitude increases. Through such

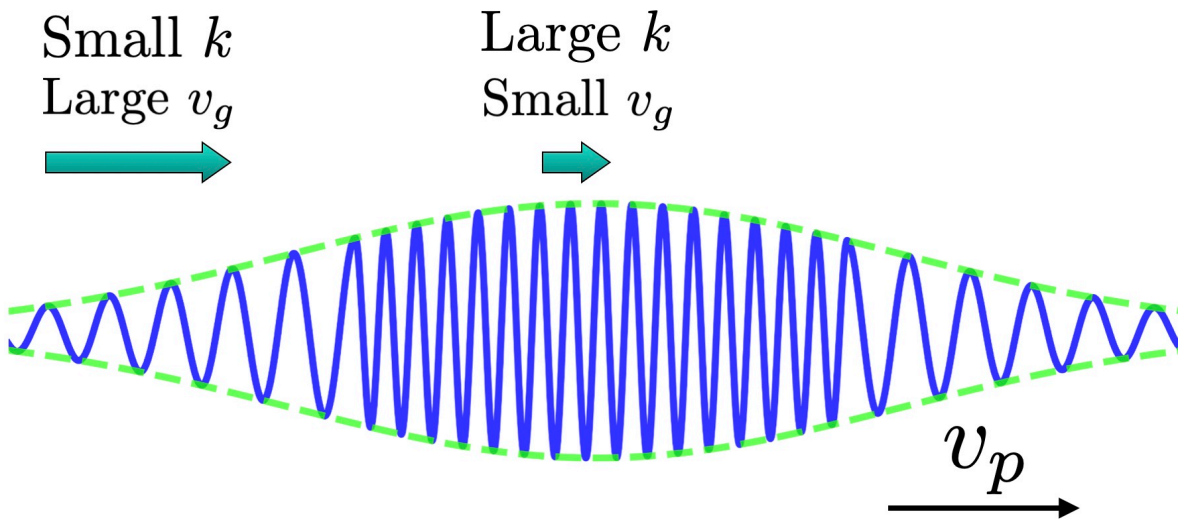

Fig. 1.14: Physical mechanism of the modulational instability.

a mechanism, fluctuations exponentially grow. The modulation analysis is also useful for studying structures called streamers ($q_x \ll 1$) [81], which are radially elongated vortices generated through nonlinear three-wave coupling. Li and Kishimoto showed by the modulation analysis that zonal flows and streamers are selectively generated by the anisotropy of a carrier wave [82]. When the drift wave satisfies ($k_x \ll k_y$), zonal flows are generated, and when it satisfies ($k_x \gg k_y$), streamers are generated. This result indicates that zonal flow and streamer generation can be controlled by controlling the magnetic shear, since k_x is proportional to $\hat{s}^{-1/2}$ from Eq. (1.83). They showed by 3D electron temperature gradient (ETG) mode turbulence simulations that zonal flows dominate when the magnetic shear is small and streamers dominate when the magnetic shear is large [82]. It is worth noting here that ETG turbulence has a slower zonal flow growth rate than ITG turbulence [83]. This is because in the case of ITG turbulence, the zonal flow with $k_\parallel = 0$ is not shielded by the Boltzmann electrons, however in the case of ETG turbulence, the zonal flow is also shielded by the Boltzmann ions.

In order to investigate the impact of zonal flows on turbulent transport, ITG turbulence simulations with the adiabatic electron model were performed using GKNET. The temperature gradients are $(R/L_{Ti}, R/L_{Te}) = (10, 6.92)$. The other parameters are the same as for the Cyclone base case parameters. We compared the case of the normal simulation with the case where the $(m, n) = (0, 0)$ electrostatic potential is numerically removed. Figure 1.15 shows the $n = 16$ electrostatic potentials for each case. In the linear phase $tv_{Ti}/R_0 = 40$, the electrostatic potential structures are exactly the same,

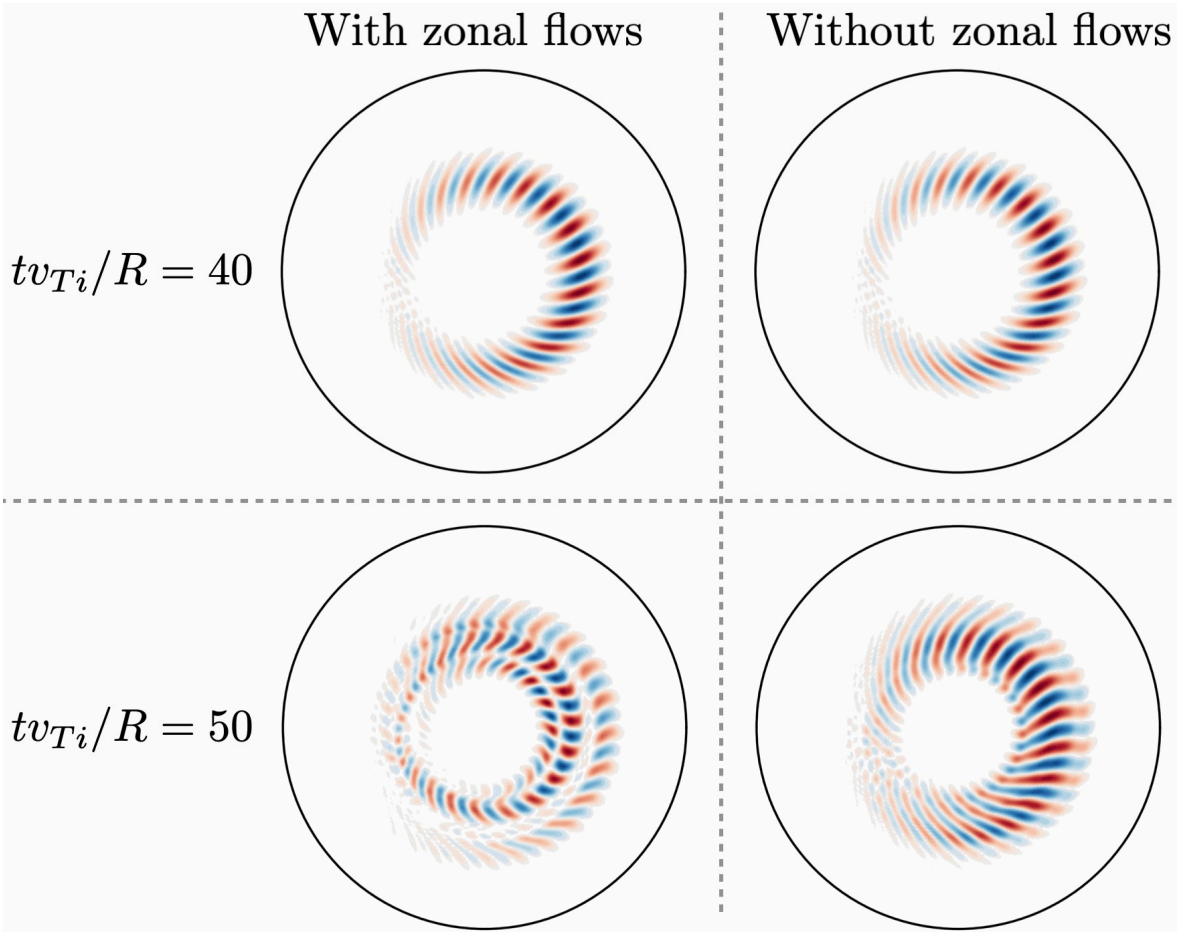

Fig. 1.15: $n = 16$ electrostatic potential structure with and without zonal flow.

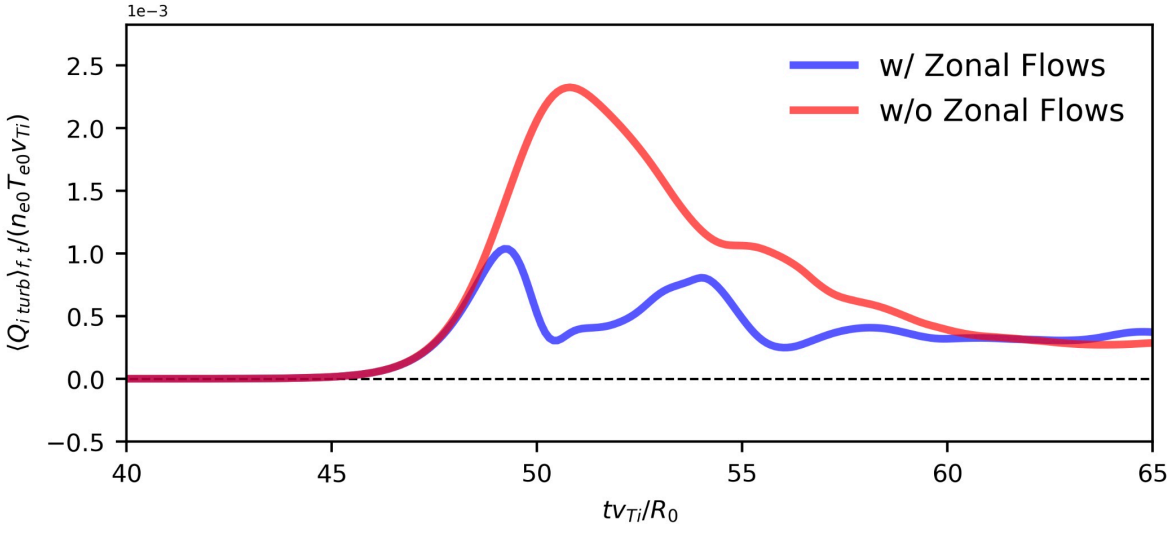

Fig. 1.16: Time evolution of turbulent heat flux with and without zonal flow.

however after nonlinear saturation $tv_{Ti}/R_0 = 50$, the wavenumber of the electrostatic potentials are different and k_x is larger in the presence of zonal flows. This is due to the deformation and tearing of the turbulent eddies by the zonal flow shear [84, 85].

As k_x increases, the transport is expected to be small because the turbulent diffusion coefficient becomes small from Eq. (1.79). Furthermore, an increase in k_x leads to a decrease in the drift frequency as indicated by Eq. (1.115). Therefore, the energy of the drift wave is expected to decrease from conservation of the action density [83]. Figure 1.16 illustrates that the turbulent heat flux is more than two times smaller in the presence of zonal flows compared to the case without zonal flows. Thus, zonal flows are the key to achieving fusion power generation because they suppress turbulent transport. Static zonal flows are more important for turbulent transport suppression, because energy transport from oscillating zonal flows to turbulence has been observed [86]. Since static zonal flows are dominant in low q region and oscillatory zonal flows are dominant in high q region [87], it is better to extend the low q region to improve confinement.

The other poloidal flow in toroidal plasmas is the flow due to the mean radial electric field. The mean electric field is determined to satisfy the radial force balance [84]

$$E_r + \frac{k}{B}\frac{\partial T}{\partial r} - \frac{rB}{qR}V_{\parallel} - \frac{1}{nB}\frac{\partial p}{\partial r} = 0. \tag{1.129}$$

k is the coefficient of neoclassical poloidal flow, given by [72, 89]

$$k = \frac{\dfrac{1.17 - 0.35\sqrt{\nu_\star}}{1 + 0.7\sqrt{\nu_\star}} - 2.1\nu_\star^2\varepsilon_t^3}{1 + \nu_\star^2\varepsilon_t^3}. \tag{1.130}$$

The neoclassical poloidal flow rotates in the ion diamagnetic direction in the low frequency range, however as the collision frequency increases, the direction reverses and the poloidal flow rotates in the electron diamagnetic direction [90, 91]. In the collisionless case, k equals 1.17 and becomes a constant. In the absence of momentum injection, the pressure gradient term becomes dominant, leading to the generation of the negative radial electric field. The Doppler shift frequency due to the mean radial electric field cancels with the drift frequency of the ITG mode, resulting in a smaller ballooning angle [92]. From Eq. (1.91), it is evident that the presence of the mean electric field leads to an increase in the linear growth rate of the ITG mode. Zonal flow evolves on a turbulent timescale, whereas the mean radial electric field evolves on a transport timescale. The mean radial electric field is driven by equilibrium profiles whereas zonal flow is only generated by nonlinear wave coupling [83]. Hence, the mean radial electric field can be controlled by heating or momentum injection. Imadera and Kishimoto have shown using GKNET that the ITB is formed by co-injection of momentum [92]. Due to the momentum injection, the toroidal rotation term $-rB/(qR)V_{\parallel} < 0$ in Eq. (1.129) becomes dominant, causing the radial electric field to become positive $E_r > 0$. In the inner region where the radial electric field shear is positive, the ballooning angle is negative and the momentum flux is positive [93]. On the other hand, in the outer region where the radial electric field shear is negative, the ballooning angle is positive

and the momentum flux is negative. Hence, momentum diffusion is reduced, large radial field shear is maintained, and the ITB is formed. In the case with counter-injection of momentum, the sign of the generated radial electric field is reversed, so the direction of the momentum fluxes is also reversed from that in the case with the co-injection of momentum, and the momentum diffusion is larger. Hence, ITB is less likely to form in the case of counter-injection of momentum.

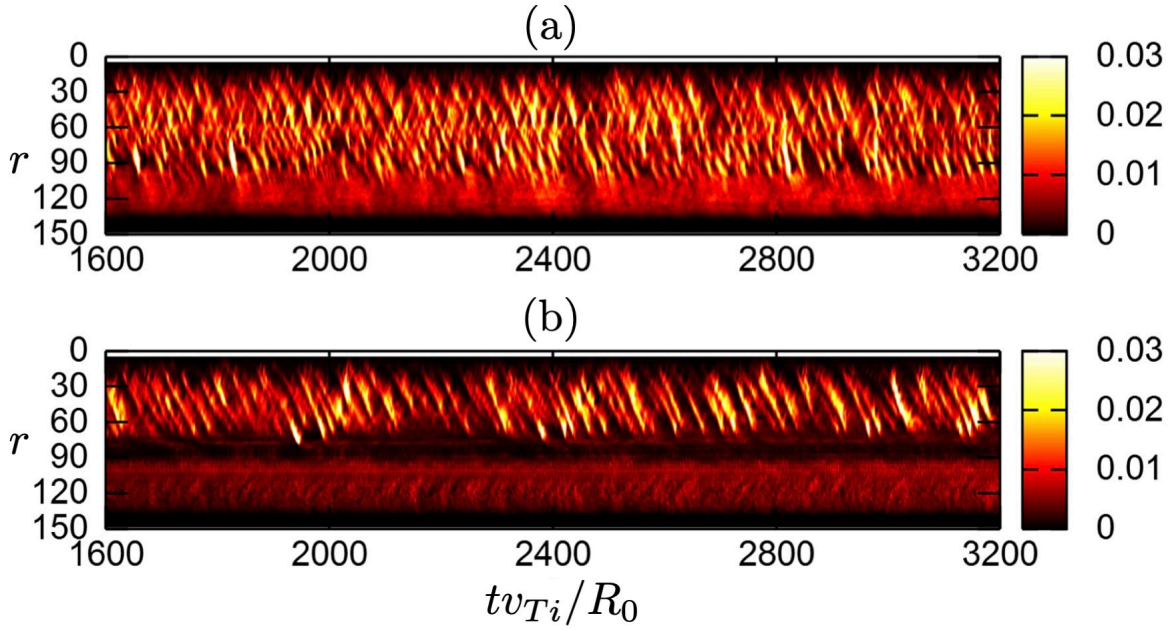

Fig. 1.17: Spatiotemporal evolution of the heat flux with (a) and without (b) momentum injection. [By courtesy of Dr. Imadera of Kyoto University]

In the case of reversed magnetic shear, the ITB is also formed by the co-injection of momentum, as shown in Fig .1.17. Interestingly, in the case of the reversed magnetic shear, the radial position where the ITB is formed is near the flux surface with the lowest safety factor $q_{\min}$, regardless of the location of momentum sources [92]. This is due to the fact that the toroidal rotation has the maximum value near the $q_{\min}$ surface by the momentum fluxes and that the toroidal rotation term in Eq. (1.129) is inversely proportional to the safety factor. Thus, it can be seen that the mean radial electric field also contributes significantly to confinement improvement.

1.4 Overview of this thesis

Plasma turbulence driven by microinstabilities has been studied through gyrokinetic simulations. Especially, the simulations employing the flux-tube model have been extensively conducted since their computational costs are relatively small. While they

can evaluate the turbulent transport for given background profiles, they do not evaluate the changes in the profiles due to the transport and the associated variation in the turbulence. Research on the interaction between turbulence and profiles remains insufficient. Since many previous studies using δf global simulations have focused on the dynamics of ions and electrons, research on turbulent impurity transport and the associated profile formations is insufficient as well. Impurity accumulation can lead to increased radiative losses and fuel dilution. Conversely, it was reported that the stabilization of instabilities by accumulated impurities can improve confinement performance. Therefore, it is necessary to analyze the turbulent transport and profile formations when the impurity density gradient is positive and negative. In this study, we first focus on entropy and perform full-f simulations to investigate the interaction between the profile formation and turbulent transport, and their relationship with dissipation. In addition, the role of equilibrium electric field in profile formation and the interaction between profile variation and turbulence in the presence of magnetic islands are elucidated. Subsequently, by conducting δf global simulations that introduce impurities, we examine the impact of the impurity mode driven by a hollow (outwardly peaked) impurity density profile on impurity transport. Furthermore, we investigate methods to control turbulent transport through heating, to relax a peaked (inwardly peaked) impurity density profile and simultaneously increase the gradients of bulk ion and electron density profiles .

In Chapter 2, the gyrokinetic theory is described and the gyrokinetic equations are derived. The equation of motion in noncanonical Hamiltonian mechanics corresponds to the equation of the vortex lines of the fundamental 1-form in the seven-dimensional extended phase space $(\boldsymbol{z}, t)$. Since the equation of motion is derived from the exterior derivative of the fundamental 1-form, closed forms contained within the fundamental 1-form can be neglected. In the Lie transform perturbation theory, the fundamental 1-form is transformed by the pullback of a map given by vector fields, thereby removing the gyrophase dependence. This method is simpler than directly averaging the Vlasov equation over the spacetime scale of the gyro-motion and has the advantage of rigorously treating symmetries and conservation laws. The drift-kinetic Vlasov equation is obtained by the guiding center transformation in terms of the small parameter $\varepsilon_B \sim \rho/L_B \ll 1$. The phase space and energy conservations are strictly satisfied. When electrostatic potential fluctuations are introduced, the guiding center fundamental 1-form again has the gyrophase dependence. The gyrokinetic Vlasov equation is obtained by the gyrocenter transformation in terms of the small parameter $\varepsilon_\delta \sim e\phi/T \ll 1$. In this study, since the electrostatic approximation is employed, the form of the symplectic part remains unchanged by the gyrocenter transformation, and the Jacobian and the Poisson brackets are the same as those in the guiding center coordinates. The

density is represented by the distribution function in the particle phase space coordinates, but what is obtained from the gyrokinetic Vlasov equation is the distribution function in the gyrocenter coordinates. From the push-forward representation of the densities, the gyrokinetic Poisson equation is derived. The expression of the gyrokinetic Poisson equation differs between the adiabatic electron model, where all electrons are treated adiabatically, and the hybrid electron model, where trapped electrons are treated kinetically.

In Chapter 3, the numerical schemes and algorithms used in the global gyrokinetic code GKNET are explained. The algorithm implemented to cancel numerical fluxes near a singularity result in the magnetic field and vector potential becoming discontinuous functions. To resolve the discontinuity by using the gauge transformation, the gyrokinetic Vlasov equation is reformulated using the curl. GKNET adopts the Euler method, discretizing the phase space. The gyrokinetic Vlasov equation is discretized using the Morinishi scheme, which numerically conserves the $L1$ norm and the $L2$ norm, and the time integration is computed using the fourth-order Runge-Kutta method. The finite Larmor radius effect is evaluated by the Padé approximation or calculating along gyro-orbits using interpolation functions. The latter method can more accurately evaluate the gyrophase averaging, but it requires longer computation times when the Larmor radius is large. The gyrokinetic Poisson equation is solved by lower-upper decomposition after Fourier transformation along the θ and φ directions and making band diagonal matrices of r, k_θ, and k_φ.

In Chapter 4, the gyrokinetic entropy balance and dynamics are discussed. By decomposing the distribution function f into the equilibrium part f_0 and the fluctuating part δf and expanding the entropy density $s^{(\mathrm{all})} = -f \log f$, the first-order entropy density $s^{(1)} = -\delta f \left(1 + \log f_0\right)$ and the second-order entropy density $s^{(2)} = -\delta f^2 / \left(2 f_0\right)$ can be defined. Integration of the first-order entropy density over the velocity space is proportional to the change in the pressure profile and represents entropy change associated with profile relaxation. On the other hand, integrating the second-order entropy density over the phase space coincides with the opposite sign of the fluctuation entropy, often used in gyrokinetic studies. The fluctuation entropy represents entropy change related to structure formation in velocity space. While the first-order entropy is the thermodynamic entropy associated with profile formation, the second-order entropy pertains to entropy related to turbulent fluctuations. From the gyrokinetic Vlasov equation, the equations for the first- and second-order entropy densities are newly derived, and each term of these equations is evaluated using full-f gyrokinetic simulations. It is found that the first-order entropy $\mathcal{S}^{(1)} = \int s^{(1)} \mathcal{J} d^5\boldsymbol{z}$ primarily changes due to the entropy generation by heat flux Γ and the entropy destruction by energy input/output $-E$. Meanwhile, the second-order entropy $\mathcal{S}^{(2)} = \int s^{(2)} \mathcal{J} d^5\boldsymbol{z}$ mainly

changes by the entropy generation due to collisional dissipation D and the entropy destruction due to phase mixing $-\Gamma$. This is consistent with the fluctuation entropy balance equation obtained in previous studies. The fact that both the first- and second-order entropies change due to Γ implies that the temperature profile and turbulence interact through the heat flux. Γ does not generate net entropy, and the net entropy is produced through dissipation in velocity space. Intuitively, it would seem that the larger flow, the smaller entropy generation because ordered structure is large. However, large flow leads to large D, resulting in increased entropy generation. Therefore, higher confinement performance corresponds to greater entropy generation. D is determined byΓ and is independent of collision frequency. In the entire plasma, since the first-order entropy increases due to the entropy generation by heat flux, $\partial \mathcal{S}^{(1)}/\partial t$ and Γ are in phase. Locally, the dynamics of the first-order entropy is dominated by the advection term, leading to an increase in the first-order entropy generation rate followed by a rise in Γ. This suggests a time lag in the heat flux response to change in the temperature profile, with the delay time being on the order of the inverse of the linear growth rate. Similarly, the dynamics of the second-order entropy is dominated by the advection term and it propagates with the heat avalanches. This implies that locally generated turbulence propagates without dissipation.

In Chapter 5, the effects of magnetic islands on turbulence and profile formation are discussed. To investigate the interaction between turbulence and profile in the presence of magnetic islands, it is necessary to perform full-f gyrokinetic simulations. In order to solve the gyrokinetic Poisson equation, the flux-surface averaging must be performed, but no standard computational method exists in the presence of magnetic islands. In this study, a new algorithm called the labeling method is developed, which groups real-space grid points by the nearest magnetic field line. By implementing the labeling method, the previous study result that the electrostatic potential with the same mode numbers as the magnetic island and the $(m, n) = (0, 0)$ electrostatic potential oscillate together at the GAM frequency is reproduced. In neoclassical simulations, solving only the gyrokinetic Vlasov equation results in the flattening of the both temperature and density profiles at the O-point. On the other hand, self-consistently solving the gyrokinetic Vlasov and Poisson equations reveals that while the temperature profile is flattened, the density profile is not relaxed. This result is explained by the balance between the forces due to the mean radial electric field and due to the parallel streaming. The profile formation inside magnetic islands is a critical issue, as it pertains to the stability of the neoclassical tearing mode. The finding in this study, that the mean radial electric field maintains the density gradient inside the magnetic island, suggests the need to consider the electric field that satisfies the radial force balance for properly evaluating the destabilizing effects. In flux-driven ITG turbulence simulations with a

magnetic island, a quasi-periodic transport reduction due to the interaction between the temperature profile and turbulence is discovered. Since the temperature profile is relaxed in side the magnetic island, the large temperature gradient is formed at the inner boundary of the island and drives the ITG mode. Since the mode satisfying $k_{\parallel} = 0$ inside the magnetic island has the same mode numbers as the magnetic island, a mesoscale vortex mode with the mode numbers grows. Analysis based on the Hasegawa-Mima equation confirm that the vortex mode is excited by two drift waves. The vortex mode transports heat from the O-point to the X-point, reducing the temperature gradient inside the magnetic island. Since the temperature gradient is small, turbulence is not excited, and the shear effect of the vortex mode prevents the heat flux from penetrating into the island, resulting in reduced heat flux inside the magnetic island. However, as the turbulence intensity is small, the amplitude of the vortex mode also diminishes. When it becomes smaller than the amplitude of the turbulence, the turbulent structure becomes similar to that without the magnetic island. Turbulence driven by the temperature gradient re-excites the vortex mode, leading to the quasi-periodic transport reduction. If the heating power is increased, a positive feedback loop where the temperature gradient at the boundary of the magnetic island is increased, and the accompanying large radial electric field further increases the temperature gradient may occur. This could lead to the formation of a transport barrier due to the magnetic island.

In Chapter 6, results on turbulent transport and profile formation in cases of positive and negative impurity density gradients are presented. While it is theoretically predicted and observed experimentally that the toroidal impurity mode (tIM) become unstable when the impurity density gradient is positive, there is no analysis of the physical mechanisms or evaluation of the turbulent transport by global gyrokinetic simulations. In this study, a fluid model is first used to analytically derive the condition under which the tIM becomes unstable. It is demonstrated that the tIM can be explained as an interchange instability. The tIM simulation results reveal that the impurity particle flux caused by the tIM turbulence is an order of magnitude greater than that caused by the ITG turbulence. Additionally, it is found that the tIM turbulence induces an inward ion heat flux, leading to an increase in the core bulk ion temperature. This is attributed to the significant contribution of the non-diagonal terms of the heat flux. In the presence of the positive impurity density gradient and the large ion temperature gradient, the ITG mode becomes dominant, but it is shown that the large impurity transport is driven by the subdominant IM. The study also examines methods of controlling particle fluxes through heating in the case of a negative impurity density gradient, not only to expel impurities but also to simultaneously facilitate fuel supply. When only electrons are heated, the particle fluxes are small, and the density profiles

hardly change. When only ions are heated, the ITG turbulence drives the inward bulk ion particle flux Γ_i and the outward impurity particle flux $Z\Gamma_z$. These fluxes satisfy $\Gamma_i + Z\Gamma_z \simeq 0$ and the electron particle flux is small. When both ions and electrons are heated, the bulk ion and electron pinches are an order of magnitude greater than when only ions are heated, leading to an increase in their density gradients. Additionally, the large outward impurity transport relaxes the impurity density profile. These particle transports are thought to be driven by the dominant ITG mode and subdominant TEM. This result suggests that heating can achieve both fuel supply and impurity exhaust, significantly contributing to the realization of fusion energy. In Chapter 7, a summary of the results obtained in this study is presented.

Chapter 2

Gyrokinetic theory

2.1 Lie transform perturbation theory

In this chapter, we derive the gyrokinetic Vlasov equation and the gyrokinetic Poisson equation used in this study. To this end, this section describes the basic concepts of the gyrokinetic theory and the Lie transform perturbation theory used to derive the equations. It is noted that since the electrostatic model is used in this study, magnetic field fluctuations are not considered, however a general discussion is presented.

As mentioned in the introduction, fluid models cannot precisely evaluate turbulent transport in fusion plasmas. Hence, when we perform the simulations of plasma turbulences, solving kinetic equations is necessary, however directly utilizing the 6D Vlasov equation Eq. (1.45) is not practical due to computational resource limitations. Therefore, a theory has been developed to approximate the gyromotion of charged particles, which is much faster than the dynamics of turbulence, and to reduce the number of dimensions to be treated. That is the gyrokinetic theory. In numerical simulations, the reduction of the dimension reduces the number of required phase-space grids dramatically, and the computation time can be reduced to a realistic level. The gyrokinetic theory that can deal with phenomena such as drift wave turbulence of which characteristic time scale is slower than the cyclotron frequency is an approximation theory and its validity is limited to dynamics satisfying the gyrokinetic orderings. In the gyrokinetic ordering, our focus is on the parameters ε_ω, ε_B, $\varepsilon_\perp$, and ε_δ [18]. ε_ω is the ratio of the cyclotron frequency Ω to the characteristic frequency ω of fluctuations, satisfying

$$\frac{\omega}{\Omega} \sim \varepsilon_\omega \ll 1. \tag{2.1}$$

This shows that phenomena such as cyclotron waves are outside the scope of the theory. The parameter ε_B characterizes the ratio of the magnetic field scale length L_B to the

gyro radius ρ and satisfies

$$\frac{\rho}{L_B} \sim \varepsilon_B \ll 1. \tag{2.2}$$

The two small parameters $\varepsilon_\omega, \varepsilon_B$ are common to both the drift and gyrokinetic ordering. The parameter $\varepsilon_\perp$ is of different order for standard gyrokinetic and drift kinetic theory,

$$k_\perp \rho \sim \varepsilon_\perp \begin{cases} \sim 1 & \text{(standard gyrokinetic orderings)} \\ \ll 1 & \text{(drift orderings)} \end{cases}. \tag{2.3}$$

It is noted that the ordering $\varepsilon_\perp \ll 1$ in the drift kinetic theory may also be used in the gyrokinetic theory. This is because this condition can be used to approximate the finite Larmor radius (FLR) effects in a simple form that is easy to solve numerically. In the case of core region ITG turbulence, $\varepsilon_\perp \ll 1$ is considered to be satisfied, and for instance, the assumption is adopted in the full-f Eulerian code GT5D [117]. In this study, $\varepsilon_\perp \ll 1$ is applied only to the calculation of the double gyro-averaging which is explained later. The order of the ratio of the perpendicular to the parallel electric field fluctuations is estimated to be

$$\frac{\delta E_\parallel}{\delta E_\perp} \sim \frac{k_\parallel}{k_\perp} \sim \frac{\varepsilon_\omega}{\varepsilon_\perp}. \tag{2.4}$$

In the case of the standard gyrokinetic theory, the perpendicular electric field fluctuations are found to be large, however this is not so in the case of drift kinetic theory. ε_δ is a parameter related to the magnitude of the fluctuation and satisfies

$$\frac{\delta f}{f} \sim \frac{e\phi}{T} \sim \varepsilon_\delta \ll 1. \tag{2.5}$$

In the presence of magnetic fluctuations, it can be deduced from Eq.(2.5) that the ratio of the magnitude of the magnetic fluctuations to the equilibrium magnetic field is of the order of ε_δ. In the case of the standard gyrokinetic orderings, it is easy to see that

$$\frac{e\rho\nabla_\perp\phi}{T} \sim \frac{v_E}{v_T} \ll 1. \tag{2.6}$$

This is referred to as the slow flow condition. In the case of the MHD, $v_E \sim v_T$ is used. The slow flow condition is satisfied even when $\varepsilon_\perp \ll 1$ and $e\phi/T \sim 1$. However, in this case, it is pointed out that the rigorous discussion requires the incorporation of higher-order terms derived from the guiding-center transformation in the quasi neutrality condition and Hamiltonian [95]. In this study, the four parameters are assumed to satisfy $\varepsilon \sim \varepsilon_\omega \sim \varepsilon_B \sim \varepsilon_\perp \sim \varepsilon_\delta$. These are the perturbation parameters when discussing the perturbation theory. In the standard gyrokinetic theory, parameter ε_B is used for the guiding-center transformation, and parameter ε_δ is used for the gyro-center transformation.

Since the Lie transform perturbation theory also bears the name of perturbation theory, the idea is basically no different from other perturbation theories such as the multiple-scale method. It only pushes unnecessary things into the extra degrees of freedom. In the Lie transform perturbation theory, the gyrophase is eliminated by operating the fundamental 1-form, rather than by directly transforming or averaging the equations of motion such as Eq. (1.45). First, we show that the equation of motion in the noncanonical Hamiltonian theory [96] can be derived from the fundamental 1-form. The fundamental 1-form Γ on the seven dimensional extended phase space is written as

$$\Gamma = \gamma_i(\boldsymbol{z}, t)dz^i - H(\boldsymbol{z}, t)dt \tag{2.7}$$

with the seven-dimensional noncanonical coordinates $(\boldsymbol{z}, t)$ and Hamiltonian H. γ_i is expressed by the Lagrangian L and the six-dimensional canonical coordinate $(\boldsymbol{q}, \boldsymbol{p})$ and is given by

$$\gamma_i = \frac{\partial L(\boldsymbol{z}, \dot{\boldsymbol{z}}, t)}{\partial \dot{z}^i} = \boldsymbol{p}(\boldsymbol{z}, t) \cdot \frac{\partial \boldsymbol{q}(\boldsymbol{z}, t)}{\partial z^i}. \tag{2.8}$$

Since the equation of motion is the equation of vortex lines of the fundamental 1-form [13], the exterior derivative of Eq. (2.7) is taken to obtain the equation of motion. When the components of the Lagrange brackets is defined as

$$\omega_{ij} \equiv \left[z^i, z^j\right] = \frac{\partial \gamma_j}{\partial z^i} - \frac{\partial \gamma_i}{\partial z^j}, \tag{2.9}$$

the exterior derivative of Eq.(2.7) is written by

$$\Upsilon \equiv d\Gamma = \sum_{i<j} \omega_{ij} dz^i \wedge dz^j - \left(\frac{\partial \gamma_i}{\partial t} + \frac{\partial H}{\partial z^i}\right) dz^i \wedge dt. \tag{2.10}$$

The first term on the right-hand side is the Lagrange tensor. The interior product of the vector field

$$V = \frac{dz^i}{dt}\frac{\partial}{\partial z^i} + \frac{\partial}{\partial t} \tag{2.11}$$

and the 2-form given by Eq.(2.10) is

$$i_V \Upsilon = \frac{dz^i}{dt}\omega_{ij} dz^j + \left(\frac{\partial \gamma_i}{\partial t} + \frac{\partial H}{\partial z^i}\right) dz^i - \left(\frac{\partial \gamma_i}{\partial t} + \frac{\partial H}{\partial z^i}\right) dt. \tag{2.12}$$

When $i_V \Upsilon = 0$ and the components of the Poisson bracket, which is the inverse matrix of the Lagrange bracket, is written by

$$J^{ij} \equiv \left\{z^i, z^j\right\} = \frac{\partial z^i}{\partial q^k}\frac{\partial z^j}{\partial p_k} - \frac{\partial z^j}{\partial q^k}\frac{\partial z^i}{\partial p_k}, \tag{2.13}$$

we obtain

$$\frac{dz^i}{dt} = J^{ij}\left(\frac{\partial H}{\partial z^j} + \frac{\partial \gamma_j}{\partial t}\right). \tag{2.14}$$

Equation (2.14) can also be derived by directly calculating the Euler-Lagrange equation from the Lagrangian expressed in the noncanonical coordinates [97]. From Eq. (2.14), we can see that transforming the fundamental 1-form is equivalent to transforming the equation of motion. It is important to note that since the equation of motion is the equation of vortex lines of the fundamental 1-form, it is determined by the exterior derivative of the fundamental 1-form. This means that the equation of motion does not change when closed forms are added to the fundamental 1-form Eq.(2.7). In the Lie transform perturbation theory, the original fundamental 1-form Γ is transformed into

$$\overline{\Gamma} \equiv \left(T^{-1}\right)^* \Gamma + dS, \tag{2.15}$$

through the pull-back by a map T^{-1}. T is a map that is given by a vector field G and is defined as

$$T = \exp\left(\varepsilon G\right). \tag{2.16}$$

S is a scalar field and dS in Eq. (2.15) vanishes when we take the exterior derivative. It means that dS does not affect the equations of motion. Expanding $\bar{\Gamma}, \Gamma, \gamma, H$, and S as

$$a = a_0 + \varepsilon a_1 + \varepsilon^2 a_2 + \cdots, \quad \left(a = \bar{\Gamma}, \Gamma, \gamma, H, S\right), \tag{2.17}$$

we obtain the equations:

$$\overline{\Gamma}_0 = \Gamma_0 + dS_0, \tag{2.18}$$

$$\overline{\Gamma}_1 = \Gamma_1 - \mathcal{L}_G \Gamma_0 + dS_1, \tag{2.19}$$

$$\overline{\Gamma}_2 = \Gamma_2 - \mathcal{L}_G \Gamma_1 + \frac{1}{2}\mathcal{L}_G^2 \Gamma_0 + dS_2. \tag{2.20}$$

$\mathcal{L}_G$ is the Lie derivative given by the vector field G. When it acts on a fundamental 1-form, we get

$$\mathcal{L}_G \Gamma = \left(d\, i_G + i_G\, d\right)\Gamma \tag{2.21}$$

by the Cartan's homotopy formula [98]. The Lie derivative is a differential operator that does not change tensor properties, and from Eq. (2.21), it is evident that the Lie derivative of a 1-form remains a 1-form. For the reason that the exterior derivative of the fundamental 1-form is the equation of motion, the first term on the right-hand side of Eq. (2.21) is not necessary to calculate since it disappears anyway. Henceforth, when performing calculations involving the Lie derivative of 1-forms, we implicitly assume that terms arising from the first term on the right-hand side of Eq. (2.21) are included in the exterior derivative of scalar fields, and we will not explicitly write. Here, we define the maps

$$T_n = \exp\left(\varepsilon^n G_n\right), \quad (n = 1, 2, 3, \cdots) \tag{2.22}$$

by vector fields G_n $(n = 1, 2, 3, \cdots)$ and introduce the composite map $T = \cdots T_3 T_2 T_1$. The fundamental 1-form is pulled back by the inverse map of the composite map [13]. In this case, the relations

$$\overline{\Gamma}_0 = \Gamma_0 + dS_0, \tag{2.23}$$

$$\overline{\Gamma}_1 = \Gamma_1 - \mathcal{L}_{G_1}\Gamma_0 + dS_1, \tag{2.24}$$

$$\overline{\Gamma}_2 = \Gamma_2 - \mathcal{L}_{G_1}\Gamma_1 + \left(\frac{1}{2}\mathcal{L}_{G_1}^2 - \mathcal{L}_{G_2}\right)\Gamma_0 + dS_2, \tag{2.25}$$

are established between the transformed fundamental 1-form $\overline{\Gamma}$ and the original fundamental 1-form Γ. The G_n and S_n appearing here correspond to the degrees of freedom in perturbation theory, and the gyrophase dependence can be removed by choosing them well so that the gyrophase dependence is eliminated. In this study, we are not interested in orders higher than the third order, so it is enough to know G_1, G_2, and S_1. We do not consider higher orders as in Eq. (2.17), but only up to the first-order $a = a_0 + \varepsilon a_1,\ (a = \Gamma, \gamma, H, S)$.

Next, we will obtain the expressions of G_1, G_2, and S_1, and the symplectic components and Hamiltonian after transformations. We assume that the zeroth-order Hamiltonian H_0 before transformations is independent of the gyrophase. First, we calculate the symplectic components. From Eq. (2.24), the transformed first-order 1-form $\overline{\gamma}_1$ can be expressed as

$$\overline{\gamma}_1 = \gamma_1 - i_{G_1}\omega_0 + dS_1, \tag{2.26}$$

where we denote the exterior derivative of γ_n $(n = 0, 1, 2)$ as $\omega_n = d\gamma_n$ $(n = 0, 1, 2)$. By solving Eq. (2.26) for the components of the vector field G_1, we obtain

$$G_1^j = \left\{S_1, z^j\right\}_0 + \Delta\gamma_{1i} J_0^{ij}, \tag{2.27}$$

where J_0^{ij} is the component of the Poisson bracket obtained from the zeroth order 1-form γ_0 and it is used to define the Poisson bracket of arbitrary scalar functions F and G,

$$\{F, G\}_0 \equiv J_0^{ij} \frac{\partial F}{\partial z^i} \frac{\partial G}{\partial z^j}. \tag{2.28}$$

$\Delta\gamma_{1i}$ is defined as $\Delta\gamma_{1i} \equiv \gamma_{1i} - \overline{\gamma}_{1i}$ and represents the difference between the symplectic components changed by the pull back transformation. The second-order 1-form is obtained as

$$\overline{\gamma}_2 = -i_{G_2}\omega_0 - \frac{1}{2} i_{G_1}(\omega_1 + \overline{\omega}_1) \tag{2.29}$$

from $\overline{\omega_1} = d\overline{\gamma}_1$ and Eq. (2.25). It is noted that the closed form arising from the Lie derivative disappear because the second-order scalar field is zero. G_2 is obtained as

$$G_2^j = -\frac{1}{2} G_1^k \left(\omega_{1ki} + \overline{\omega}_{1ki}\right) J_0^{ij} \tag{2.30}$$

from $\overline{\gamma}_2 = 0$. The transformed first-order Hamiltonian $\overline{H}_1$ can similarly be calculated, and from Eq. (2.24),

$$\overline{H}_1 = K_1 + \overline{\gamma}_{1i} \left\{ z^i, H_0 \right\}_0 - \{S_1, H_0\}_0 \tag{2.31}$$

can be obtained. K_1 is the effective first-order Hamiltonian before transformations, and is defined as $K_1 \equiv H_1 - \gamma_{1i} \{z^i, H_0\}_0$. We chose the first-order gauge function S_1 such that $\langle S_1 \rangle = 0$, where $\langle \cdot \rangle$ represents the gyro averaging operation. S_1 is determined from the equation

$$\{S_1, H_0\}_0 \equiv K_1 - \langle K_1 \rangle . \tag{2.32}$$

This equation can also be derived by the variational principle [99] and we obtain

$$\overline{H}_1 = \langle K_1 \rangle + \overline{\gamma}_{1i} \left\{ z^i, H_0 \right\}_0 . \tag{2.33}$$

The transformed second-order Hamiltonian can be calculated in the same way by Eq. (2.25). The gyro averaged second-order Hamiltonian is obtained as

$$\begin{aligned} \overline{H}_2 = &- \frac{1}{2} \left\langle \{S_1, \{S_1, H_0\}_0\}_0 \right\rangle - \left\langle \Delta\gamma_{1j} \left\{ z^j, K_1 \right\}_0 \right\rangle \\ &- \frac{1}{2} \left\langle \Delta\gamma_{1j} J_0^{jk} \{\lambda_{1k}, H_0\}_0 \right\rangle - \frac{1}{2} \left\langle \lambda_{1i} \Delta\gamma_{1j} \left\{ z^j, \left\{ z^i, H_0 \right\}_0 \right\}_0 \right\rangle , \end{aligned} \tag{2.34}$$

where $\lambda_{1i} = \gamma_{1i} + \overline{\gamma}_{1i}$ is the sum of the first-order symplectic components before and after transformations. The Lie transformed symplectic components and Hamiltonian, as well as the vector and scalar fields were obtained.

2.2 Gyrokinetic Vlasov equation

In order to derive the gyrokinetic Vlasov equation, the particle coordinates $\boldsymbol{z} = (\boldsymbol{x}, \boldsymbol{v})$ are transformed into the guiding-center coordinates $\boldsymbol{Z} = (\boldsymbol{X}, U, \zeta, \mu)$ by the guiding-center transformation and further into the gyrocenter coordinates $\overline{\boldsymbol{Z}} = (\overline{\boldsymbol{X}}, \overline{U}, \overline{\zeta}, \overline{\mu})$ by the gyrocenter transformation. First, let us derive the equations describing the motion of particles in the guiding-center coordinates. In the following, we consider the electrostatic model and assume that the magnetic field is constant with time. The fundamental 1-form γ is written

$$\gamma = \left(\varepsilon m \boldsymbol{v} + \frac{e}{c} \boldsymbol{A} \right) \cdot d\boldsymbol{x} - \varepsilon \frac{1}{2} m |\boldsymbol{v}|^2 dt \tag{2.35}$$

in the particle coordinates. It is noted that ε should strictly be written as ε_B because

$$\frac{mv}{\frac{e}{c}A} \sim \frac{\rho}{L_B} \sim \varepsilon_B . \tag{2.36}$$

We aim to remove the gyrophase dependence through the guiding-center transformation from Eq. (2.35), however, the gyrophase does not explicitly appear in Eq. (2.35). To address this, we perform a coordinate transformation in velocity space. The velocity $\boldsymbol{v}$ is divided into the component parallel to the magnetic field $u \equiv \boldsymbol{v}\cdot\boldsymbol{b}$ and the component perpendicular to the magnetic field $\boldsymbol{w} \equiv \boldsymbol{v} - u\boldsymbol{b}$. The unit vector perpendicular to the magnetic field is defined as $\boldsymbol{c} \equiv \boldsymbol{w}/|\boldsymbol{w}|$. From $\boldsymbol{a} = \boldsymbol{b}\times\boldsymbol{c}$, we construct a right-handed set of unit vectors $(\boldsymbol{a}, \boldsymbol{b}, \boldsymbol{c})$. Using the unit vectors $\boldsymbol{a}$ and $\boldsymbol{c}$ perpendicular to the magnetic field, we define the unit vectors e_1 and e_2 as

$$\boldsymbol{e}_1 \equiv \cos\alpha\boldsymbol{a} - \sin\alpha\boldsymbol{c} \tag{2.37}$$

and

$$\boldsymbol{e}_2 \equiv -\sin\alpha\boldsymbol{a} - \cos\alpha\boldsymbol{c}, \tag{2.38}$$

respectively. α is the gyrophase and the angle between $\boldsymbol{a}$ and $\boldsymbol{e}_1$. The unit vectors $\boldsymbol{e}_1$ and $\boldsymbol{e}_2$ constitute a right-handed set of unit vectors $(\boldsymbol{e}_1, \boldsymbol{e}_2, \boldsymbol{b})$. After performing the transformation of the velocity coordinates and expressing the velocity in terms of $u, w \equiv |\boldsymbol{w}|$, and α, Eq. (2.35) becomes

$$\gamma = \left(\varepsilon m u\boldsymbol{b} + \varepsilon m w\boldsymbol{c} + \frac{e}{c}\boldsymbol{A}\right)\cdot d\boldsymbol{x} - \varepsilon\left(\frac{1}{2}mu^2 + \frac{1}{2}mw^2\right)dt. \tag{2.39}$$

The fundamental 1-form Eq. (2.39) is transformed by the pull back of the inverse map of the map $T_{\mathrm{GC}} \equiv \exp(\varepsilon V)$ which is given by the vector field

$$V \equiv -\boldsymbol{\rho}\cdot\nabla - \boldsymbol{\rho}\cdot\boldsymbol{R}\frac{\partial}{\partial\alpha}, \tag{2.40}$$

where $\boldsymbol{\rho}$ and $\boldsymbol{R}$ are defined as

$$\boldsymbol{\rho} \equiv \frac{cmw}{eB}\boldsymbol{a} \quad \text{and} \quad \boldsymbol{R} \equiv \nabla\boldsymbol{e}_1\cdot\boldsymbol{e}_2, \tag{2.41}$$

respectively. The vector field V is a part of the vector field in the standard guiding-center transformation [100]. If it is necessary to systematically remove the gyrophase dependence to higher orders to derive the drift kinetic equations, the standard vector field should be used. Since we focus mainly on turbulent rather than neoclassical transport, we do not consider higher orders in the guiding-center transformation. The vector field V does not change its form depending on how the gyrophase is chosen [97]. When the gyrophase is shifted by ψ, denoted as $\alpha' \equiv \alpha + \psi$, $\boldsymbol{R}$ transforms into $\boldsymbol{R}' \equiv \boldsymbol{R}+\nabla\psi$, and the α component of the vector field V changes from $-\boldsymbol{\rho}\cdot\boldsymbol{R}$ to $-\boldsymbol{\rho}\cdot\boldsymbol{R}'$, which means that the form of V remains unchanged. Using the map T_{GC}, the fundamental 1-form is transformed from Eq. (2.15) to $\Gamma = \left(T_{\mathrm{GC}}^{-1}\right)^*\gamma + dS$. From the perspective of considering the transformation as a coordinate transformation, it corresponds to the transformation from the coordinates $(\boldsymbol{x}, u, \alpha, w)$ to coordinates $(\boldsymbol{X}, U, \zeta, W)$. By

obtaining γ in the passive point of view [15] from Eqs. (2.18), (2.19), and (2.20), and disregarding the second-order terms with the gyrophase dependence in the $\boldsymbol{X}$ component, we get

$$\gamma = \left(\frac{e}{c}\boldsymbol{A} + \varepsilon m U \boldsymbol{b}\right) \cdot d\boldsymbol{X} + \varepsilon^2 \frac{cm}{e}\mu d\zeta - \varepsilon\left(\frac{1}{2}mU^2 + \mu B\right) dt, \tag{2.42}$$

where μ is the magnetic moment and is defined as

$$\mu \equiv \frac{mW^2}{2B} = \frac{mw^2}{2B}. \tag{2.43}$$

We introduce the modified vector potential

$$\boldsymbol{A}^* \equiv \boldsymbol{A} + \varepsilon \frac{cm}{e} U \boldsymbol{b} \tag{2.44}$$

and the zeroth order Hamiltonian

$$H_0 \equiv \frac{1}{2}mU^2 + \mu B, \tag{2.45}$$

and Eq. (2.42) can be written as

$$\gamma = \frac{e}{c}\boldsymbol{A}^* \cdot d\boldsymbol{X} + \varepsilon^2 \frac{cm}{e}\mu d\zeta - \varepsilon H_0 dt. \tag{2.46}$$

Calculating the components of the Lagrange bracket from Eqs. (2.46) and (2.9) reveals that the non-zero components are only

$$\left[X^i, X^j\right] = \frac{e}{c}\varepsilon_{ijk} B^*_k, \tag{2.47}$$

$$\left[X^i, U\right] = -\varepsilon m b_i, \tag{2.48}$$

$$[\zeta, \mu] = -\varepsilon^2 \frac{cm}{e}, \tag{2.49}$$

where $\boldsymbol{B}^* = \nabla \times \boldsymbol{A}^*$ is the modified magnetic field. ε_{ijk} is the completely antisymmetric tensor of rank 3, being +1 for (i, j, k) being an even permutation of $(1, 2, 3)$, -1 for (i, j, k) being an odd permutation of $(1, 2, 3)$, and 0 otherwise. The determinant of the Lagrange bracket is $\varepsilon^6 m^4 {B^*_\parallel}^2$ where $B^*_\parallel \equiv \boldsymbol{B}^* \cdot \boldsymbol{b}$. We can see that the Jacobian $\mathcal{J}$ of the transformation from the particle coordinates $\boldsymbol{z}$ to guiding-center coordinates $\boldsymbol{Z}$ becomes $B^*_\parallel / m$ [101]. From Eq. (2.46), the Poisson bracket is

$$\begin{aligned}\{F, G\} =& \varepsilon^{-2}\frac{e}{cm}\left(\frac{\partial F}{\partial \zeta}\frac{\partial G}{\partial \mu} - \frac{\partial F}{\partial \mu}\frac{\partial G}{\partial \zeta}\right) + \varepsilon^{-1}\frac{\boldsymbol{B}^*}{mB^*_\parallel} \cdot \left(\nabla F \frac{\partial G}{\partial U} - \frac{\partial F}{\partial U}\nabla G\right) \\ & - \varepsilon^0 \frac{c}{eB^*_\parallel}\left(\boldsymbol{b} \cdot \nabla F \times \nabla G\right),\end{aligned} \tag{2.50}$$

where F and G are arbitrary scalar functions. The terms of Eq. (2.50) are arranged in the order of $\varepsilon^{-2}, \varepsilon^{-1}$, and ε^0. Each term corresponds to the gyromotion, motion parallel

to the magnetic field, and motion perpendicular to the magnetic field, respectively [18]. It is noteworthy that replacing the differential operator ∇ in Eq. (2.50) with

$$\nabla' \equiv \nabla + \left\{ \boldsymbol{R} + \frac{1}{2} \left(\boldsymbol{b} \cdot \nabla \times \boldsymbol{b} \right) \boldsymbol{b} \right\} \frac{\partial}{\partial \zeta} \tag{2.51}$$

yields the same equation obtained by performing the standard guiding-center transformation. From Eqs. (2.50) and (2.14), we obtain the equations of motion:

$$\frac{d\boldsymbol{X}}{dt} = \frac{\boldsymbol{B}^*}{mB_\parallel^*} \frac{\partial H_0}{\partial U} + \frac{c}{eB_\parallel^*} \boldsymbol{b} \times \nabla H_0 \tag{2.52}$$

$$\frac{dU}{dt} = -\frac{\boldsymbol{B}^*}{mB_\parallel^*} \cdot \nabla H_0 \tag{2.53}$$

$$\frac{d\zeta}{dt} = \frac{e}{cm} \frac{\partial H_0}{\partial \mu} \tag{2.54}$$

$$\frac{d\mu}{dt} = 0 \tag{2.55}$$

Since the equations do not depend on gyrophase, when the initial distribution function in the guiding-center coordinates is independent of gyrophase, the distribution function $F(\boldsymbol{Z}) \equiv \left(T_{\mathrm{GC}}^{-1}\right)^* f(\boldsymbol{Z})$ does not depend on gyrophase even after the time evolution. Hence, we obtain the drift kinetic equation:

$$\frac{\partial F}{\partial t} + \frac{d\boldsymbol{X}}{dt} \cdot \nabla F + \frac{dU}{dt} \frac{\partial F}{\partial U} = 0. \tag{2.56}$$

Next, an electrostatic potential fluctuation ϕ_1 is introduced. The Hamiltonian becomes

$$H = H_0 + \varepsilon H_1, \tag{2.57}$$

where $H_1 \equiv e\phi_1$. It is noted that ε on the right-hand side of Eq. (2.57) should strictly be written as ε_δ. Since the electrostatic potential fluctuation has gyrophase dependence, $\phi_1 \left(T_{\mathrm{GC}}^{-1} \boldsymbol{x}, t\right) = \phi_1 \left(\boldsymbol{X} + \boldsymbol{\rho} + \mathcal{O}\left(\varepsilon_B^2\right), t\right)$, the Hamiltonian also has gyrophase dependence. $T_{\mathrm{GC}}^{-1} \boldsymbol{x}$ denotes the particle position in the guiding-center phase space. The transformation to remove this gyrophase dependence is the gyrocenter transformation, which is a transformation from the guide center coordinates $\boldsymbol{Z} = (\boldsymbol{X}, U, \zeta, \mu)$ to gyrocenter coordinates $\overline{\boldsymbol{Z}} = \left(\overline{\boldsymbol{X}}, \overline{U}, \overline{\zeta}, \overline{\mu}\right)$ from the viewpoint of considering the transformation as a coordinate transformation. We will denote all quantities transformed by the gyrocenter transformation with an overbar. In the case of the electrostatic model, the symplectic structure does not change because there is no vector potential fluctuation. Therefore, the gyrocenter transformation does not change the equations of motion or the Jacobian. It is worth mentioning that even in the case of the electromagnetic model, by introducing the electromagnetic fluctuation $\boldsymbol{A}_1$ initially and performing the standard guiding-center transformation with the particle velocity as $\boldsymbol{v}' \equiv \boldsymbol{v} + (e/cm)\boldsymbol{A}_1$,

the electromagnetic fluctuation can be pushed into the Hamiltonian [32]. The composite map $T_{\mathrm{GY}} \equiv \cdots T_3 T_2 T_1$ is defined by the map $T_n = \exp\left(\varepsilon^n G_n\right)$ $(n = 1, 2, 3, \cdots)$ determined by the vector field G_n $(n = 1, 2, 3, \cdots)$ as in Eq. (2.22). The G_1, G_2, and S_1 involved in this transformation and the transformed Hamiltonians $\overline{H} = \left(T_{\mathrm{GY}}^{-1}\right)^* H$ have already been computed in the previous section. From Eqs. (2.27), the vector field G_1 is obtained as

$$G_1^j = \left\{S_1, Z^j\right\}. \tag{2.58}$$

Because $K_1 - \langle K_1 \rangle = H_1 - \langle H_1 \rangle$, the first-order scalar field satisfies

$$\{S_1, H_0\} = e\phi_1 - e\langle \phi_1 \rangle \tag{2.59}$$

from Eq. (2.32). Thus, the first-order scalar field is represented by an indefinite integral, as

$$S_1 = \frac{e}{\Omega} \int \tilde{\phi}_1 d\overline{\zeta}, \tag{2.60}$$

where $\tilde{\phi}_1 \equiv \phi_1 - \langle \phi_1 \rangle$. The transformed Hamiltonian is obtained from Eqs. (2.33) and (2.34) as

$$\overline{H}_1 = e\langle \phi_1 \rangle \quad \text{and} \quad \overline{H}_2 = -\frac{e}{2}\left\langle \left\{S_1, \tilde{\phi}_1\right\} \right\rangle, \tag{2.61}$$

respectively. Approximating the second-order Hamiltonian, we obtain

$$\overline{H}_2 \simeq -\frac{e^2}{2B}\frac{\partial}{\partial \overline{\mu}}\left\langle \tilde{\phi}_1^2 \right\rangle = -\frac{e^2}{2B}\frac{\partial}{\partial \overline{\mu}}\left(\left\langle \phi_1^2 \right\rangle - \langle \phi_1 \rangle^2\right). \tag{2.62}$$

Equation (2.62) is often used as the second-order Hamiltonian of the electrostatic model [18, 95]. In summary, the transformed Hamiltonian is

$$\overline{H} = \frac{1}{2} m \overline{U}^2 + \overline{\mu} B + e\langle \Phi \rangle, \tag{2.63}$$

where

$$\Phi \equiv \varepsilon \phi_1 - \varepsilon^2 \frac{e}{2B}\frac{\partial \tilde{\phi}_1^2}{\partial \overline{\mu}}. \tag{2.64}$$

Therefore, the fundamental 1-form becomes

$$\gamma = \frac{e}{c}\boldsymbol{A}^* \cdot d\overline{\boldsymbol{X}} + \frac{cm}{e}\overline{\mu} d\overline{\zeta} - \overline{H} dt, \tag{2.65}$$

where the modified vector potential is defined as

$$\boldsymbol{A}^* \equiv \boldsymbol{A} + \frac{cm}{e}\overline{U}\boldsymbol{b}. \tag{2.66}$$

The equations of motion are obtained as

$$\frac{d\overline{\boldsymbol{X}}}{dt} = \frac{\boldsymbol{B}^*}{mB_\parallel^*}\frac{\partial \overline{H}}{\partial \overline{U}} + \frac{c}{eB_\parallel^*}\boldsymbol{b} \times \overline{\nabla}\, \overline{H}, \tag{2.67}$$

$$\frac{d\overline{U}}{dt} = -\frac{\boldsymbol{B}^*}{mB_\parallel^*} \cdot \overline{\nabla}\, \overline{H}, \tag{2.68}$$

$$\frac{d\overline{\zeta}}{dt} = \frac{e}{cm}\frac{\partial \overline{H}}{\partial \overline{\mu}}, \tag{2.69}$$

$$\frac{d\overline{\mu}}{dt} = 0. \tag{2.70}$$

Substituting Eq. (2.63) into these equations of motion yields the widely used equations [117, 118, 103]

$$\frac{d\overline{\boldsymbol{X}}}{dt} = \overline{U}\boldsymbol{b} + \frac{c}{eB_\parallel^*}\boldsymbol{b} \times \left(e\overline{\nabla} \left\langle \Phi \right\rangle + m\overline{U}^2 \boldsymbol{b} \cdot \overline{\nabla}\boldsymbol{b} + \overline{\mu}\overline{\nabla} B \right), \tag{2.71}$$

$$\frac{d\overline{U}}{dt} = -\frac{\boldsymbol{B}^*}{mB_\parallel^*} \cdot \left(e\overline{\nabla} \left\langle \Phi \right\rangle + \overline{\mu}\overline{\nabla} B \right), \tag{2.72}$$

$$\frac{d\overline{\zeta}}{dt} = \Omega, \tag{2.73}$$

$$\frac{d\overline{\mu}}{dt} = 0. \tag{2.74}$$

The second, third, and fourth terms on the right-hand side of Eq. (2.71) represent the $E \times B$ drift, curvature drift, and ∇B drift, respectively. The first and second terms on the right-hand side of Eq. (2.72) represent the force due to the electric field and the mirror force, respectively. Since the equations do not depend on gyrophase, when the initial distribution function in the gyrocenter coordinates is independent of gyrophase, the distribution function $\overline{F}(\overline{\boldsymbol{Z}}) \equiv \left(T_{\mathrm{GY}}^{-1}\right)^* F(\overline{\boldsymbol{Z}})$ does not depend on gyrophase even after the time evolution. Hence, we obtain the gyrokinetic Vlasov equation:

$$\frac{\partial \overline{F}}{\partial t} + \frac{d\overline{\boldsymbol{X}}}{dt} \cdot \overline{\nabla}\, \overline{F} + \frac{d\overline{U}}{dt}\frac{\partial \overline{F}}{\partial \overline{U}} = 0. \tag{2.75}$$

2.3 Gyrokinetic Poisson equation

Since the electrostatic potential also varies with the motion of charged particles, an equation describing the field is necessary. This is the gyrokinetic Poisson equation, also referred to as the quasi-neutrality condition. In this section, we consider only protons and electrons. Assuming the quasi-neutrality condition $n_{0i} = n_{0e}$ holds initially, we obtain

$$\tilde{n}_i(\boldsymbol{r}) = \tilde{n}_e(\boldsymbol{r}) \tag{2.76}$$

from Eq. (1.46). It is note that since the Debye length is sufficiently small, the left-hand side of Eq. (1.46) can be neglected. The gyrokinetic Poisson equation is obtained by expressing the fluctuation densities by the perturbed part of the distribution functions

$\delta\overline{F}_s(\overline{\boldsymbol{Z}})$ in the gyrocenter coordinates. Using the Dirac delta function δ, the ion density at position $\boldsymbol{r}$ is described as

$$\begin{aligned} n_i(\boldsymbol{r}) &= \int d^6\boldsymbol{z} f_i(\boldsymbol{z})\delta^3(\boldsymbol{x}-\boldsymbol{r}) \\ &= \int d^6\overline{\boldsymbol{Z}}\,\overline{\mathcal{J}}\left[(T_{\mathrm{GY}})^*\,\overline{F}_i\right]\left(\overline{\boldsymbol{Z}}\right)\delta^3\left(\left[T_{\mathrm{GC}}^{-1}\boldsymbol{x}\right]\left(\overline{\boldsymbol{Z}}\right)-\boldsymbol{r}\right), \end{aligned} \tag{2.77}$$

where the distribution function in the guiding-center coordinates is represented as the pull back transformation of the distribution function in the gyrocenter coordinates [95, 104]. $\overline{\mathcal{J}}$ is defined as $\overline{\mathcal{J}} \equiv \mathcal{J}\left(\overline{\boldsymbol{Z}}\right)$. $(T_{\mathrm{GY}})^*\,\overline{F}_i$ can be approximated as [19]

$$(T_{\mathrm{GY}})^*\,\overline{F}_i \simeq \overline{F}_i + \left\{S_1, \overline{F}_{0i}\right\} \simeq \overline{F}_i + \frac{e\tilde{\phi}_1}{B}\frac{\partial\overline{F}_{0i}}{\partial\overline{\mu}}, \tag{2.78}$$

where the distribution function in the gyrocenter coordinates $\overline{F}_i$ is divided into the equilibrium part $\overline{F}_{0i}$ and the fluctuation part $\delta\overline{F}_i$. We assume the local Maxwellian for the equilibrium distribution function and Eq. (2.78) becomes

$$(T_{\mathrm{GY}})^*\,\overline{F}_i = \overline{F}_{0i} + \delta\overline{F}_i - \frac{e\tilde{\phi}_1}{T_i}\overline{F}_{0i}. \tag{2.79}$$

By approximating the guide center coordinates with $\left[T_{\mathrm{GC}}^{-1}\boldsymbol{x}\right]\left(\overline{\boldsymbol{Z}}\right) \simeq \overline{\boldsymbol{X}} + \overline{\boldsymbol{\rho}}$ using $\overline{\boldsymbol{\rho}} \equiv \boldsymbol{\rho}\left(\overline{\boldsymbol{Z}}\right)$,

$$\begin{aligned} n_i(\boldsymbol{r}) = &\int d^6\overline{\boldsymbol{Z}}\,\overline{\mathcal{J}}\,\overline{F}_{0i}\,\delta^3\left(\overline{\boldsymbol{X}}+\overline{\boldsymbol{\rho}}-\boldsymbol{r}\right) + \int d^6\overline{\boldsymbol{Z}}\,\overline{\mathcal{J}}\,\delta\overline{F}_i\,\delta^3\left(\overline{\boldsymbol{X}}+\overline{\boldsymbol{\rho}}-\boldsymbol{r}\right) \\ &- \int d^6\overline{\boldsymbol{Z}}\,\overline{\mathcal{J}}\,\frac{e\tilde{\phi}_1}{T_i}\overline{F}_{0i}\,\delta^3\left(\overline{\boldsymbol{X}}+\overline{\boldsymbol{\rho}}-\boldsymbol{r}\right) \end{aligned} \tag{2.80}$$

is obtained from Eq. (2.77). Since the first term on the right-hand side of Eq. (2.80) is n_{0i}, the ion density fluctuation is expressed as

$$\tilde{n}_i = \int d^6\overline{\boldsymbol{Z}}\,\overline{\mathcal{J}}\,\delta\overline{F}_i\,\delta^3\left(\overline{\boldsymbol{X}}+\overline{\boldsymbol{\rho}}-\boldsymbol{r}\right) - \int d^6\overline{\boldsymbol{Z}}\,\overline{\mathcal{J}}\,\frac{e\tilde{\phi}_1}{T_i}\overline{F}_{0i}\,\delta^3\left(\overline{\boldsymbol{X}}+\overline{\boldsymbol{\rho}}-\boldsymbol{r}\right). \tag{2.81}$$

The second term on the right-hand side of Eq. (2.81) represents the gyrokinetic polarization density. We denote this term as

$$\tilde{n}_p \equiv -\int d^6\overline{\boldsymbol{Z}}\,\overline{\mathcal{J}}\,\frac{e\tilde{\phi}_1}{T_i}\overline{F}_{0i}\,\delta^3\left(\overline{\boldsymbol{X}}+\overline{\boldsymbol{\rho}}-\boldsymbol{r}\right). \tag{2.82}$$

There are two commonly used representations of $\tilde{n}_p$. One representation uses the double gyro-averaging. By using $\delta^3\left(\overline{\boldsymbol{X}}+\overline{\boldsymbol{\rho}}-\boldsymbol{r}\right) = \exp\left(\overline{\boldsymbol{\rho}}\cdot\overline{\nabla}\right)\delta^3\left(\overline{\boldsymbol{X}}-\boldsymbol{r}\right)$ and neglecting the gradients of the background profiles since they are of higher order, we obtain [105]

$$\tilde{n}_p = -\int d^6\overline{\boldsymbol{Z}}\,\overline{\mathcal{J}}\delta^3\left(\overline{\boldsymbol{X}}-\boldsymbol{r}\right)\frac{e}{T_i}\overline{F}_{0i}\,e^{-\overline{\boldsymbol{\rho}}\cdot\overline{\nabla}_\perp}\tilde{\phi}_1\left(\overline{\boldsymbol{X}}+\overline{\boldsymbol{\rho}}\right). \tag{2.83}$$

Substituting $\tilde{\phi}_1\left(\overline{\boldsymbol{X}}+\overline{\boldsymbol{\rho}}\right)=\phi_1\left(\overline{\boldsymbol{X}}+\overline{\boldsymbol{\rho}}\right)-\left\langle\phi_1\left(\overline{\boldsymbol{X}}+\overline{\boldsymbol{\rho}}\right)\right\rangle$ into Eq. (2.83) yields

$$\tilde{n}_p=-\int d^3\overline{\boldsymbol{X}}\delta^3\left(\overline{\boldsymbol{X}}-\boldsymbol{r}\right)\frac{en_{0i}}{T_i}\phi_1+\int d^6\overline{\boldsymbol{Z}}\,\overline{\mathcal{J}}\delta^3\left(\overline{\boldsymbol{X}}-\boldsymbol{r}\right)\frac{e}{T_i}\overline{F}_{0i}\,e^{-\overline{\boldsymbol{\rho}}\cdot\overline{\nabla}_\perp}\left\langle\phi_1\left(\overline{\boldsymbol{X}}+\overline{\boldsymbol{\rho}}\right)\right\rangle. \tag{2.84}$$

The second term on the right-hand side of the equation represents the double gyro-averaged electrostatic potential. By using

$$\langle\langle\phi_1\rangle\rangle\left(\overline{\boldsymbol{X}}\right)\equiv\frac{1}{n_{0i}}\int d\overline{U}d\overline{\mu}d\overline{\zeta}\,\overline{\mathcal{J}}\,\overline{F}_{0i}\,\left\langle e^{\overline{\boldsymbol{\rho}}\cdot\overline{\nabla}_\perp}\right\rangle^2\phi_1\left(\overline{\boldsymbol{X}}\right), \tag{2.85}$$

$\tilde{n}_p$ is expressed as [19, 106]

$$\tilde{n}_p=-\int d^3\overline{\boldsymbol{X}}\delta^3\left(\overline{\boldsymbol{X}}-\boldsymbol{r}\right)\frac{en_{0i}}{T_i}\phi_1(\overline{\boldsymbol{X}})+\int d^3\overline{\boldsymbol{X}}\delta^3\left(\overline{\boldsymbol{X}}-\boldsymbol{r}\right)\frac{en_{0i}}{T_i}\langle\langle\phi_1\rangle\rangle\left(\overline{\boldsymbol{X}}\right). \tag{2.86}$$

This is the representation using the double gyro-averaging. The other is the approximate representation by taking the long wavelength limit $\varepsilon_\perp\ll1$. By using the zeroth-order Bessel function of the first kind,

$$J_0(z)=\frac{1}{2\pi}\int_0^{2\pi}e^{iz\cos\overline{\zeta}}\,d\overline{\zeta}, \tag{2.87}$$

because

$$\left\langle\phi_1\left(\overline{\boldsymbol{X}}+\overline{\boldsymbol{\rho}}\right)\right\rangle=\int d\boldsymbol{k}\hat{\phi}_{1\boldsymbol{k}}\,e^{i\boldsymbol{k}\cdot\overline{\boldsymbol{X}}}J_0\left(k_\perp\rho\right), \tag{2.88}$$

$\tilde{n}_p$ can be represented as

$$\tilde{n}_p=-\int d^3\overline{\boldsymbol{X}}\delta^3\left(\overline{\boldsymbol{X}}-\boldsymbol{r}\right)\frac{en_{0i}}{T_i}\phi_1+\int d^6\overline{\boldsymbol{Z}}\overline{\mathcal{J}}\delta^3\left(\overline{\boldsymbol{X}}-\boldsymbol{r}\right)\frac{e}{T_i}\overline{F}_{0i}\int d\boldsymbol{k}\hat{\phi}_{1\boldsymbol{k}}e^{i\boldsymbol{k}\cdot\overline{\boldsymbol{X}}}J_0\left(k_\perp\rho\right)^2. \tag{2.89}$$

From the theory of Bessel functions we have the expression,

$$\int_0^\infty d\overline{W}\,\overline{W}\exp\left(-\frac{\overline{W}^2}{2v_{Ti}^2}\right)J_0\left(\frac{k_\perp\overline{W}}{\Omega_i}\right)^2=v_{Ti}^2\Gamma_0\left(k_\perp^2\rho_i^2\right), \tag{2.90}$$

where Γ_0 is defined as $\Gamma_0(b)=I_0(b)e^{-b}$ and I_0 is the zeroth-order modified Bessel function of the first kind. In the long wavelength limit, Γ_0 is approximated as [31]

$$\Gamma_0\left(k_\perp^2\rho_i^2\right)\simeq1-k_\perp^2\rho_i^2. \tag{2.91}$$

From Eq. (2.89), Eq. (2.90) and Eq. (2.91), we get [117, 118]

$$\tilde{n}_p=\int d^3\overline{\boldsymbol{X}}\delta^3\left(\overline{\boldsymbol{X}}-\boldsymbol{r}\right)\frac{en_{0i}}{T_i}\overline{\nabla}_\perp\cdot\rho_i^2\overline{\nabla}_\perp\phi_1(\overline{\boldsymbol{X}}). \tag{2.92}$$

From Eqs. (2.76), (2.81), and (2.86), we obtain the gyrokinetic Poisson equation

$$\frac{1}{\lambda_{Di}^2}\int d^3\overline{\boldsymbol{X}}\delta^3\left(\overline{\boldsymbol{X}}-\boldsymbol{r}\right)\left(\phi_1-\langle\langle\phi_1\rangle\rangle\right)+4\pi e\tilde{n}_e=4\pi e\int d^6\overline{\boldsymbol{Z}}\,\overline{\mathcal{J}}\,\delta\overline{F}_i\,\delta^3\left(\overline{\boldsymbol{X}}+\overline{\boldsymbol{\rho}}-\boldsymbol{r}\right), \tag{2.93}$$

where

$$\lambda_{Ds} \equiv \sqrt{\frac{T_s}{4\pi n_{0s} e^2}} \tag{2.94}$$

is the Debye length of particle species s. From Eqs. (2.76), (2.81), and (2.92), the long wavelength approximated gyrokinetic Poisson equation

$$-\int d^3\overline{\boldsymbol{X}} \delta^3\left(\overline{\boldsymbol{X}} - \boldsymbol{r}\right) \overline{\nabla}_\perp \cdot \frac{\rho_i^2}{\lambda_{Di}^2} \overline{\nabla}_\perp \phi_1 + 4\pi e \tilde{n}_e = 4\pi e \int d^6\overline{\boldsymbol{Z}}\, \overline{\mathcal{J}}\, \delta\overline{F}_i\, \delta^3\left(\overline{\boldsymbol{X}} + \overline{\boldsymbol{\rho}} - \boldsymbol{r}\right) \tag{2.95}$$

is derived.

In this study, we employ the adiabatic electron model and the hybrid electron model [107, 108]. The adiabatic electron model assumes that electrons can move very fast in the direction parallel to the magnetic field and, as a result, always satisfy Boltzmann equilibrium. The flux-surface averaged electron density fluctuation can be assumed to be zero. Therefore, the electron density fluctuation in the adiabatic electron approximation can be expressed as [109]

$$\tilde{n}_e = \frac{e n_{0e}}{T_e}\left(\phi_1 - \langle\phi_1\rangle_f\right). \tag{2.96}$$

The second term on the right-hand side of Eq. (2.96) represents the flux-surface averaged electrostatic potential fluctuation. Substituting Eq. (2.96) into Eq. (2.95), we obtain the gyrokinetic Poisson equation in the adiabatic electron model:

$$-\overline{\nabla}_\perp \cdot \frac{\rho_i^2}{\lambda_{Di}^2} \overline{\nabla}_\perp \phi_1(\overline{\boldsymbol{X}}) + \frac{1}{\lambda_{De}^2}\left(\phi_1(\overline{\boldsymbol{X}}) - \left\langle\phi_1(\overline{\boldsymbol{X}})\right\rangle_f\right) = 8\pi^2 e \int \left\langle \delta\overline{F}_i(\overline{\boldsymbol{X}} + \overline{\boldsymbol{\rho}}, \overline{U}, \overline{\mu})\right\rangle \overline{\mathcal{J}} d\overline{U} d\overline{\mu}. \tag{2.97}$$

In the adiabatic electron model, as discussed in the Introduction, turbulent particle flux becomes zero, preventing the study of particle transport. The dynamics of electrons are largely disregarded, making it impossible to conduct research on TEM turbulence. However, it is not possible to perform electrostatic gyrokinetic simulations using the full kinetic electron model. This is because the ω_H mode [110, 111], the electrostatic limit of the kinetic Alfvén wave, appears. The frequency of the ω_H mode, $\omega_H = (k_\parallel/k_\perp)\sqrt{m_i/m_e}\Omega_i$, is of the same order as the cyclotron frequency. Consequently, from the perspective of the gyrokinetic ordering, the ω_H mode is considered unphysical. To simulate electron dynamics while avoiding the ω_H mode, we employ the hybrid electron model. In the hybrid electron model, the electron density fluctuation is defined as

$$\begin{cases} \tilde{n}_{e,(m,n)=(0,0)} = \displaystyle\int d^6\overline{\boldsymbol{Z}}\, \overline{\mathcal{J}}\, \delta\overline{F}_{e,(m,n)=(0,0)}\, \delta^3\left(\overline{\boldsymbol{X}} + \overline{\boldsymbol{\rho}} - \boldsymbol{r}\right), & (2.98) \\ \tilde{n}_{e,(m,n)\neq(0,0)} = \displaystyle\int d^6\overline{\boldsymbol{Z}}\, \overline{\mathcal{J}}\, \delta\overline{F}_{e,\mathrm{trap},(m,n)\neq(0,0)}\, \delta^3\left(\overline{\boldsymbol{X}} + \overline{\boldsymbol{\rho}} - \boldsymbol{r}\right) - \frac{\alpha_{\mathrm{pass}} n_{0e} e \phi_{1,(m,n)\neq(0,0)}}{T_e}. & (2.99) \end{cases}$$

α_{pass} which is the flux-surface averaged fraction of passing electrons, is given by Eq. (1.29). Equation (2.98) means that the $(m,n) = (0,0)$ electron density fluctuation

is calculated with the full kinetic electron model. On the other hand, Eq. (2.99) implies treating $(m,n) \neq (0,0)$ passing electrons as adiabatic electrons and considering only the dynamics of $(m,n) \neq (0,0)$ trapped electrons. This allows us to avoid the emergence of the ω_H mode associated with $(m,n) \neq (0,0)$ passing electrons and simultaneously enables simulations for the TEM arising from the motion of trapped electrons. Substituting Eqs. (2.98) and (2.99) into equation Eq. (2.95), we obtain the gyrokinetic Poisson equation in the hybrid electron model.

Chapter 3

Global gyrokinetic code GKNET

3.1 Normalized equations

In this chapter, we provide an overview of the global gyrokinetic code, GKNET (GyroKinetic Numerical Experiment of Tokamak) [112], employed in this study. For clarity, the gyro-center coordinates $(\overline{\boldsymbol{X}}, \overline{U}, \overline{\mu})$ and the guiding-center distribution function $\overline{F}_s = \overline{F}_{0s} + \delta\overline{F}_s$ are denoted as $(\boldsymbol{R}, v_\parallel, \mu)$ and $f_s = f_{0s} + \delta f_s$, respectively. In GKNET, the equations are described in the toroidal coordinates as shown in Fig. 1.3, where $\boldsymbol{R} = (r, \theta, \varphi)$. The motion of the particle species s is computed by numerically solving the gyrokinetic Vlasov equation:

$$\frac{\partial f_s}{\partial t} + \frac{d\boldsymbol{R}}{dt} \cdot \nabla f_s + \frac{dv_\parallel}{dt}\frac{\partial f_s}{\partial v_\parallel} = S_{\rm src} + S_{\rm snk} + C_{\rm coll}, \tag{3.1}$$

where $S_{\rm src}$, $S_{\rm snk}$, and $C_{\rm coll}$ are the source, sink, and collision terms, respectively. The advection velocities on the left-hand side of Eq. (3.1) are given by Eqs. (2.67) and (2.68). The electric field that varies due to the motion of plasma is calculated by the gyrokinetic Poisson equation Eq. (2.95).

The toroidal coordinates are periodic in the θ and φ directions and possess a singularity at $r = 0$. In numerical calculations of advection equations like Eq. (3.1), the presence of a singularity can lead to a breakdown in the conservation properties near the singularity. As an example, we consider a physical quantity $g(r, \theta, t)$ that satisfies the advection equation

$$\frac{\partial g(r,\theta,t)}{\partial t} = -\frac{\partial}{\partial r}\left\{v(r,\theta,t)g(r,\theta,t)\right\}. \tag{3.2}$$

When discretized using a second-order central difference, it is represented as

$$\left.\frac{\partial g}{\partial t}\right|_{j,k} = -\frac{v_{j+1,k}g_{j+1,k} - v_{j-1,k}g_{j-1,k}}{2\Delta r} = -\Gamma_{j+1,k} + \Gamma_{j-1,k}. \tag{3.3}$$

We let Δr and $\Delta\theta$ respectively represent the grid spacing of the minor radius and poloidal angle. The value of an arbitrary function a on the polar coordinates at the

point $(j\Delta r, k\Delta\theta)$ is denoted as $a_{j,k}$, and the flux is defined as $\Gamma \equiv vg/(2\Delta r)$. We consider that the radial direction is discretized by N_r grid points. It is straightforward to see that summing over j from 2 to N_r+1 in Eq. (3.3) yields $\Gamma_{1,k}+\Gamma_{2,k}-\Gamma_{N_r+1,k}-\Gamma_{N_r+2,k}$. Due to $\Gamma_{1,k}+\Gamma_{2,k}$, the numerical conservation properties are compromised. In nonlinear simulations, ensuring the conservation of conserved quantities is of importance from the perspective of the reliability of the computational results. In GKNET, an algorithm ensuring the conservation properties near the singularity has been implemented [113].

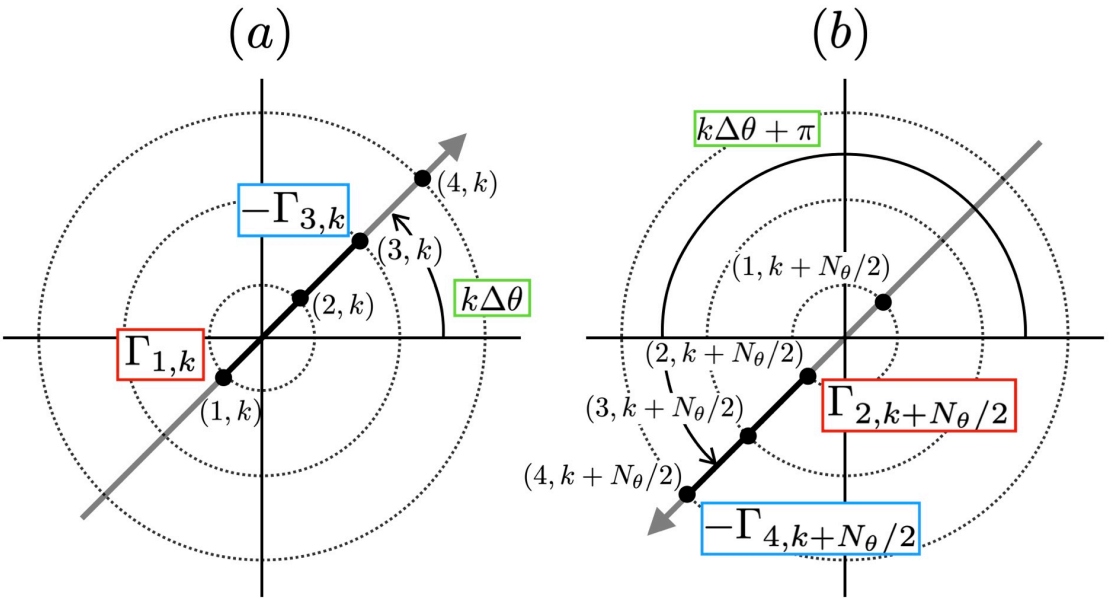

Fig. 3.1: (a) Fluxes at $k\Delta\theta$ and (b) fluxes at $k\Delta\theta+\pi$.

Figure 3.1 (a) and (b) show the fluxes at poloidal angle $k\Delta\theta$ and at poloidal angle $k\Delta\theta+\pi$, respectively. N_θ represents the number of grid points in the poloidal direction, and for clarity, the point $(j\Delta r, k\Delta\theta)$ is denoted as (j,k). Figure 3.1 shows that one point could have two notations when the radial discretization is performed across the singularity in the polar coordinate system. For instance, $(1,k)$ and $(2,k+N_\theta/2)$ both point to the exact same location. Since the fluxes $\Gamma_{1,k}$ and $\Gamma_{2,k+N_\theta/2}$ are equal, by inverting the sign of $\Gamma_{1,k}$ and summing in the poloidal direction, it cancels out with $\Gamma_{2,k+N_\theta/2}$. In GKNET, this is achieved by reversing the sign of the magnetic field and vector potential for $r<0$. However, by merely inverting the signs of the magnetic field and vector potential, they become discontinuous functions, and their derivatives diverge. To alleviate the discontinuity, the magnetic field and vector potential are parallel transported using a gauge transformation. To accomplish this, Eqs. (2.67) and (2.68) are reformulated as [92]

$$\frac{d\boldsymbol{R}}{dt} = \frac{1}{B^*_{\parallel s}}\left[v_\parallel(\nabla\times\boldsymbol{A}) + \frac{B}{\Omega_s}v_\parallel^2(\nabla\times\boldsymbol{b}) + \frac{c}{q_s}H_s\nabla\times\boldsymbol{b} - \frac{c}{q_s}\nabla\times(H_s\boldsymbol{b})\right], \tag{3.4}$$

$$\frac{dv_\parallel}{dt} = -\frac{1}{m_s B^*_{\parallel s}} \left[(\nabla \times \boldsymbol{A}) \cdot \nabla H_s + \frac{B}{\Omega_s} v_\parallel \nabla \cdot (H_s \nabla \times \boldsymbol{b}) \right]. \tag{3.5}$$

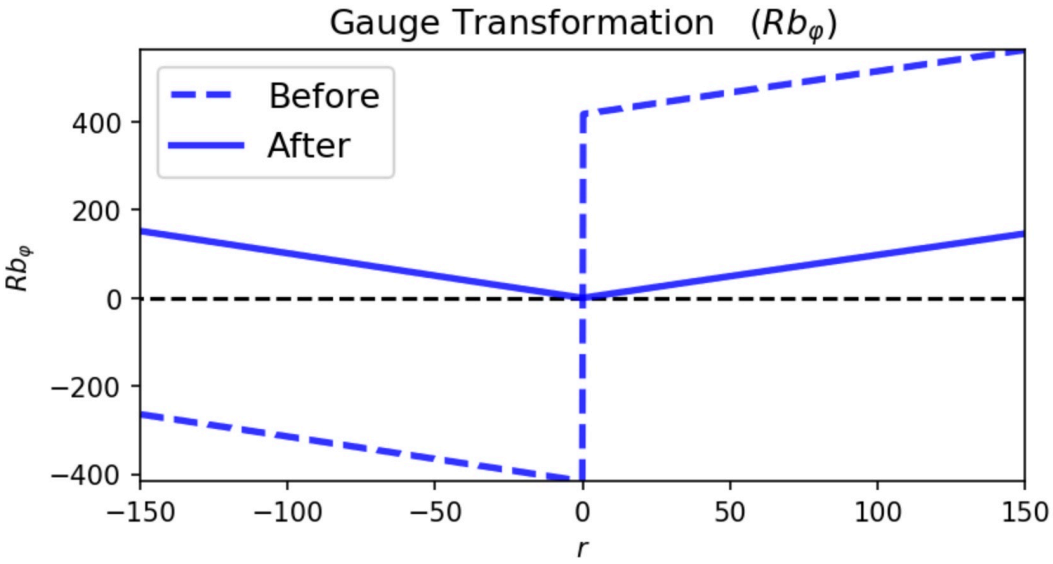

Fig. 3.2: Radial profile of the function Rb_φ before and after the gauge transformation.

Figure 3.2 depicts the radial profile of Rb_φ both before and after the gauge transformation ($Rb_\varphi - R_0$). b_φ is the unit vector in the toroidal direction of the magnetic field. From Fig. 3.2, it is evident that using the gauge transformation ensures continuity at $r = 0$. In other words, one chooses the gauge degrees of freedom to ensure continuity at $r = 0$. By employing this method, it has been confirmed that there is an approximate 35% improvement in energy conservation when we conduct a simulation up to $t = 1000 R_0/v_{Ti}$.

Normalization is performed as follows.

$$\left(\Omega_{0i} t, \frac{r}{\rho_{Ti}}, \frac{v_\parallel}{v_{Ts}}, \frac{B_0 \mu}{m_s v_{Ts}^2}, \frac{H_s}{T_{0e}} \right) \longrightarrow \left(t, r, v_\parallel, \mu, H_s \right) \tag{3.6}$$

$$\left(\frac{B^*_{\parallel s}}{B_0}, \frac{A}{B_0 \rho_{Ti}}, \frac{e\phi_1}{T_{0e}}, \frac{2\pi f_s v_{Ts}^3}{n_{0s}}, \frac{T_s}{T_{0e}} \right) \longrightarrow \left(B^*_{\parallel s}, A, \phi, f_s, n, T_s \right) \tag{3.7}$$

$T_{0s} \equiv T_s(r_s)$ and $n_{0s} \equiv n_s(r_s)$ are the temperature and density at $r_s \equiv 0.5 a_0$, respectively. B_0, $v_{Ts} = \sqrt{T_{0s}/m_s}$, $\Omega_{0i} = eB_0/m_i c$, and $\rho_{Ti} = v_{Ti}/\Omega_{0i}$ are the magnitude of the magnetic field at the magnetic axis, thermal velocity, ion cyclotron frequency, and ion gyro radius, respectively. At r_s, the temperatures of ions, impurities, and electrons are always assumed to be the same $T_{0s} = T_{0e}$. It is noted that while time normalization is used as $\Omega_{0i} t$ during calculations, the simulation results are output with time normalization $t v_{\mathrm{ti}0}/R_0$. The normalization time $t v_{\mathrm{ti}0}/R_0 = 100$ corresponds to about 0.22 [ms] in real time. This was estimated with the ion density as $n_{0i} = 5 \times 10^{19}$ [m^{-3}],

the ion temperature as $T_{0i} = 2$ [keV], the equilibrium magnetic field as $B_0 = 2$ [T], the toroidal minor radius as $a_0 = 0.34$ [m], and the major radius as $R_0 = 0.95$ [m]. Normalizing Eqs. (3.4) and (3.5), we obtain

$$\begin{aligned}\frac{dr}{dt} =& \frac{1}{rRB^*_{\parallel s}}\left\{\sqrt{\frac{m_i}{m_s}}v_\parallel\left[\frac{\partial(RA_\varphi)}{\partial\theta} - \frac{\partial(rA_\theta)}{\partial\varphi}\right] + \frac{q_i}{q_s}v_\parallel^2\left[\frac{\partial(Rb_\varphi)}{\partial\theta} - \frac{\partial(rb_\theta)}{\partial\varphi}\right]\right.\\ &\left. + \frac{q_i}{q_s}H_s\left[\frac{\partial(Rb_\varphi)}{\partial\theta} - \frac{\partial(rb_\theta)}{\partial\varphi}\right] - \frac{q_i}{q_s}\left[\frac{\partial(H_sRb_\varphi)}{\partial\theta} - \frac{\partial(H_srb_\theta)}{\partial\varphi}\right]\right\},\end{aligned} \tag{3.8}$$

$$\begin{aligned}\frac{1}{r}\frac{d\theta}{dt} =& \frac{1}{rRB^*_{\parallel s}}\left\{\sqrt{\frac{m_i}{m_s}}v_\parallel\left[\frac{\partial A_r}{\partial\varphi} - \frac{\partial(RA_\varphi)}{\partial r}\right] + \frac{q_i}{q_s}v_\parallel^2\left[\frac{\partial b_r}{\partial\varphi} - \frac{\partial(Rb_\varphi)}{\partial r}\right]\right.\\ &\left. + \frac{q_i}{q_s}H_s\left[\frac{\partial b_r}{\partial\varphi} - \frac{\partial(Rb_\varphi)}{\partial r}\right] - \frac{q_i}{q_s}\left[\frac{\partial(H_sb_r)}{\partial\varphi} - \frac{\partial(H_sRb_\varphi)}{\partial r}\right]\right\},\end{aligned} \tag{3.9}$$

$$\begin{aligned}\frac{1}{R}\frac{d\varphi}{dt} =& \frac{1}{rRB^*_{\parallel s}}\left\{\sqrt{\frac{m_i}{m_s}}v_\parallel\left[\frac{\partial(rA_\theta)}{\partial r} - \frac{\partial A_r}{\partial\theta}\right] + \frac{q_i}{q_s}v_\parallel^2\left[\frac{\partial(rb_\theta)}{\partial r} - \frac{\partial b_r}{\partial\theta}\right]\right.\\ &\left. + \frac{q_i}{q_s}H_s\left[\frac{\partial(rb_\theta)}{\partial r} - \frac{\partial b_r}{\partial\theta}\right] - \frac{q_i}{q_s}\left[\frac{\partial(H_srb_\theta)}{\partial r} - \frac{\partial(H_sb_r)}{\partial\theta}\right]\right\},\end{aligned} \tag{3.10}$$

$$\begin{aligned}\frac{dv_\parallel}{dt} =& -\frac{1}{rRB^*_{\parallel s}}\left\{\sqrt{\frac{m_i}{m_s}}\left[\frac{\partial(RA_\varphi)}{\partial\theta} - \frac{\partial(rA_\theta)}{\partial\varphi}\right]\frac{\partial H_s}{\partial r} + \sqrt{\frac{m_i}{m_s}}\left[\frac{\partial A_r}{\partial\varphi} - \frac{\partial(RA_\varphi)}{\partial r}\right]\frac{\partial H_s}{\partial\theta}\right.\\ &+ \sqrt{\frac{m_i}{m_s}}\left[\frac{\partial(rA_\theta)}{\partial r} - \frac{\partial A_r}{\partial\theta}\right]\frac{\partial H_s}{\partial\varphi} + \frac{q_i}{q_s}v_\parallel\left[\frac{\partial}{\partial r}\left\{H_s\left[\frac{\partial(Rb_\varphi)}{\partial\theta} - \frac{\partial(rb_\theta)}{\partial\varphi}\right]\right\}\right.\\ &\left.\left. + \frac{\partial}{\partial\theta}\left\{H_s\left[\frac{\partial b_r}{\partial\varphi} - \frac{\partial(Rb_\varphi)}{\partial r}\right]\right\} + \frac{\partial}{\partial\varphi}\left\{H_s\left[\frac{\partial(rb_\theta)}{\partial r} - \frac{\partial b_r}{\partial\theta}\right]\right\}\right]\right\}.\end{aligned} \tag{3.11}$$

Substituting the magnetic field $\boldsymbol{B}$ Eq. (1.18) and Hamiltonian Eq. (2.63) into these equations leads to

$$\mathcal{J}\frac{dr}{dt} = v_{0x} + v_{1x}, \tag{3.12}$$

$$\mathcal{J}\frac{1}{r}\frac{d\theta}{dt} = v_{0y} + v_{1y}, \tag{3.13}$$

$$\mathcal{J}\frac{1}{R}\frac{d\varphi}{dt} = v_{0z} + v_{1z}, \tag{3.14}$$

$$\mathcal{J}\frac{dv_\parallel}{dt} = v_{0v_\parallel} + v_{1v_\parallel}, \tag{3.15}$$

where

$$v_{0x} = \frac{q_i}{q_s}\left(v_\parallel^2 + \mu B\right)\frac{\partial}{\partial\theta}\left(Rb_\varphi - R_0\right), \tag{3.16}$$

$$v_{1x} = \langle\phi\rangle_{\alpha s}\frac{\partial}{\partial\theta}\left(Rb_\varphi - R_0\right) - \frac{\partial}{\partial\theta}\left(\langle\phi\rangle_{\alpha s}Rb_\varphi\right) + \frac{\partial}{\partial\varphi}\left(\langle\phi\rangle_{\alpha s}rb_\theta\right), \tag{3.17}$$

$$v_{0y} = -\sqrt{\frac{m_i}{m_s}} v_\parallel \frac{\partial}{\partial r}\left(RA_\varphi\right) - \frac{q_i}{q_s}\left(v_\parallel^2 + \mu B\right)\frac{\partial}{\partial r}\left(Rb_\varphi - R_0\right) + \frac{q_i}{q_s}\mu\frac{\partial}{\partial r}\left(BRb_\varphi - R_0\right), \tag{3.18}$$

$$v_{1y} = \frac{\partial}{\partial r}\left(\langle\phi\rangle_{\alpha s} Rb_\varphi - \langle\phi\rangle_{\alpha s, r=0} R_0\right) - \langle\phi\rangle_{\alpha s}\frac{\partial}{\partial r}\left(Rb_\varphi - R_0\right), \tag{3.19}$$

$$v_{0z} = \sqrt{\frac{m_i}{m_s}} v_\parallel \frac{\partial}{\partial r}\left(rA_\theta\right) + \frac{q_i}{q_s}\left(v_\parallel^2 + \mu B\right)\frac{\partial}{\partial r}\left(rb_\theta\right) - \frac{q_i}{q_s}\mu\frac{\partial}{\partial r}\left(Brb_\theta\right), \tag{3.20}$$

$$v_{1z} = -\frac{\partial}{\partial r}\left(\langle\phi\rangle_{\alpha s} rb_\theta\right) + \langle\phi\rangle_{\alpha s}\frac{\partial}{\partial r}\left(rb_\varphi\right), \tag{3.21}$$

$$\begin{aligned} v_{0v_\parallel} = &-\mu\left[-\sqrt{\frac{m_i}{m_s}}\frac{\partial}{\partial r}\left(RA_\varphi\right)\frac{\partial B}{\partial\theta} + \frac{q_i}{q_s}v_\parallel\left[\frac{\partial}{\partial r}\left\{B\frac{\partial}{\partial\theta}\left(Rb_\varphi - R_0\right)\right\}\right.\right. \\ &\left.\left. - \frac{\partial}{\partial\theta}\left\{B\frac{\partial}{\partial r}\left(Rb_\varphi - R_0\right)\right\}\right]\right], \end{aligned} \tag{3.22}$$

$$\begin{aligned} v_{1v_\parallel} = &\sqrt{\frac{m_i}{m_s}} q_s \frac{\partial}{\partial r}\left(RA_\varphi\right)\frac{\partial\langle\phi\rangle_{\alpha s}}{\partial\theta} - \sqrt{\frac{m_i}{m_s}} q_s \frac{\partial}{\partial r}\left(rA_\theta\right)\frac{\partial\langle\phi\rangle_{\alpha s}}{\partial\varphi} \\ &- v_\parallel\left[\frac{\partial}{\partial r}\left\{\langle\phi\rangle_{\alpha s}\frac{\partial}{\partial\theta}\left(Rb_\varphi - R_0\right)\right\} - \frac{\partial}{\partial\theta}\left\{\langle\phi\rangle_{\alpha s}\frac{\partial}{\partial r}\left(Rb_\varphi - R_0\right)\right\}\right. \\ &\left. + \frac{\partial}{\partial\varphi}\left\{\langle\phi\rangle_{\alpha s}\frac{\partial}{\partial r}\left(rb_\varphi\right)\right\}\right]. \end{aligned} \tag{3.23}$$

The zeroth order velocities represent the motion along the magnetic field and magnetic drift, while the first order velocities signifies the $E \times B$ drift. While $E \times B$ drift inherently does not depend on the particle species, in the gyrokinetic theory, it varies by species due to the FLR effect. $\langle\phi\rangle_{\alpha s, r=0}$ is evaluated using a fifth-order polynomial interpolation. Normalizing the gyrokinetic Poisson equation, we obtain

$$-\sum_s \frac{n_{0s}}{n_{0e}}\frac{m_s}{m_i}\nabla_\perp \cdot n_s \nabla_\perp \phi = -\tilde{n}_e + \sum_s \frac{n_{0s}}{n_{0e}}\frac{q_s}{q_i}\left\langle \iint \delta f_s B_{\parallel s}^* dv_\parallel d\mu \right\rangle_{\alpha s}. \tag{3.24}$$

In the case of the adiabatic electron model, $\tilde{n}_e$ is given by

$$\tilde{n}_e = \frac{n_e}{T_e}\left(\phi - \langle\phi\rangle_f\right). \tag{3.25}$$

In the case of the hybrid electron model, $\tilde{n}_e$ is given by

$$\tilde{n}_{e,(m,n)=(0,0)} = \iint \delta f_{e,(m,n)=(0,0)} B_{\parallel e}^* dv_\parallel d\mu \tag{3.26}$$

and

$$\tilde{n}_{e,(m,n)\neq(0,0)} = \frac{n_e}{T_e}\alpha_{\text{pass}}\phi_{(m,n)\neq(0,0)} + \iint \delta f_{e,\text{trap},(m,n)\neq(0,0)} B_{\parallel e}^* dv_\parallel d\mu. \tag{3.27}$$

Among the five-dimensional coordinate $(r, \theta, \varphi, v_\parallel, \mu)$, the radial r, poloidal angle θ, and magnetic moment μ directions are decomposed by MPI. For the μ direction, it

is set to hold data for one grid per core. The coordinates in the r and θ directions are each divided based on the square root of the quotient obtained by dividing the total number of cores by the number of the grid number in the μ direction. For instance, when we perform a simulation using 2048 cores, the coordinates in the μ direction are divided into 8 regions, and the coordinates in the r and θ directions are divided into 16 regions each.

3.2 Vlasov solver

3.2.1 Morinishi scheme

The gyrokinetic Vlasov equation Eq. (3.1), when the terms of the right-hand side are ignored, is a hyperbolic partial differential equation, which can generally be written as

$$\frac{\partial f}{\partial t} + u^i \frac{\partial f}{\partial x^i} = 0, \tag{3.28}$$

where $\boldsymbol{x} \equiv (\boldsymbol{R}, v_\parallel)$. Since the density, energy and entropy also follow the advection equation, their time evolution can also be calculated by the algorithm for solving Eq. (3.28). The primary numerical schemes for solving the gyrokinetic Vlasov equation are the Particle-in-cell (PIC), Euler, and semi-Lagrangian methods [19]. In PIC methods, by placing markers randomly in phase space and following the motion of the markers along their characteristics, the distribution function is computed. This method has issues such as sampling noise and challenges associated with the implementation of collision terms. A renowned code that employs the PIC methods is ORB5 [114, 115, 116]. In Euler methods, phase space is discretized and the distribution function is computed using a finite difference scheme. This approach is subject to challenges such as restriction on the time step due to the Courant-Friedrichs-Lewy (CFL) stability condition and issues with numerical dissipation. A renowned code that employs the Euler methods is GT5D [117, 118, 119]. The semi-Lagrangian methods can be viewed as a hybrid approach, incorporating the advantages of both PIC methods and Euler methods. In semi-Lagrangian methods, the distribution function is calculated using the fact that the distribution function at a node x_{node} at time $t + \Delta t$ is equal to the distribution function at the point x^* at time t on the characteristics [120]. Because x^* is not necessarily on a node, an appropriate interpolation scheme should be used. A renowned code that employs the semi-Lagrangian methods is GYSELA [120, 121, 122]. GKNET is a code that utilizes the Euler methods, discretizing the phase space and computing the distribution function using the fourth-order Morinishi scheme [123, 124], a type of finite difference method. The term "fourth-order" implies that the truncation error of the differential operator is $\mathcal{O}\left((\Delta x^i)^4\right)$ where Δx^i is the grid spacing in the direction

x^i. This can be verified by substituting the exact solution into the difference equation. The reason for employing the Morinishi scheme is that it numerically conserves both the $L1$ and $L2$ norms. The proof is provided as follows. From the phase space conservation

$$\frac{\partial v^i}{\partial x^i} = 0, \tag{3.29}$$

Eq. (3.28) can be expressed as

$$\mathcal{J}\frac{\partial f}{\partial t} + \frac{\partial}{\partial x^i}\left(v^i f\right) = 0, \tag{3.30}$$

where $\mathcal{J}$ is the Jacobian and $\boldsymbol{v} = (v^r, v^\theta, v^\varphi, v^{v_\parallel}) \equiv \mathcal{J}\boldsymbol{u}$. The Morinishi scheme was originally proposed for incompressible fluids, and Eq. (3.29) corresponds to that incompressibility condition. The fourth-order Morinishi scheme rewrites the second term on the left-hand side of Eq. (3.30) as

$$\frac{\partial}{\partial x^i}\left(v^i f\right) = \frac{1}{2}\frac{\partial}{\partial x^i}\left(v^i f\right) + \frac{1}{2}v^i\frac{\partial f}{\partial x^i}, \tag{3.31}$$

and then discretizes the differential operators in Eq. (3.31) using the fourth-order central difference scheme. The fourth-order central difference of the differential operator in the r direction is given by

$$\left.\frac{\partial a}{\partial r}\right|_{\mathrm{P}} = \frac{-a_{j+2,k,l,m} + 8a_{j+1,k,l,m} - 8a_{j-1,k,l,m} + a_{j-2,k,l,m}}{12\Delta r} + \mathcal{O}\left(\Delta r^4\right), \tag{3.32}$$

where $a_{j,k,l,m}$ represents the value of a function $a(\boldsymbol{x})$ on the node $\mathrm{P} = (0.5\Delta r + j\Delta r, 0.5\Delta\theta + k\Delta\theta, l\Delta\varphi, 0.5\Delta v_\parallel - 0.5L_{v_\parallel} + m\Delta v)$ in the phase space. Discretizing Eq. (3.31) using Eq. (3.32), we obtain

$$\begin{aligned}
\left.\frac{\partial}{\partial x^i}\left(v^i f\right)\right|_{\mathrm{P}} = \; & \frac{1}{3\Delta r}\Big\{\left(v^r_{j,k,l,m}\, f_{j+1,k,l,m} - v^r_{j,k,l,m}\, f_{j-1,k,l,m}\right) \\
& - \frac{1}{8}\left(v^r_{j,k,l,m}\, f_{j+2,k,l,m} - v^r_{j,k,l,m}\, f_{j-2,k,l,m}\right) \\
& + \left(v^r_{j+1,k,l,m}\, f_{j+1,k,l,m} - v^r_{j-1,k,l,m}\, f_{j-1,k,l,m}\right) \\
& - \frac{1}{8}\left(v^r_{j+2,k,l,m}\, f_{j+2,k,l,m} - v^r_{j-2,k,l,m}\, f_{j-2,k,l,m}\right)\Big\} \\
& + \frac{1}{3\Delta\theta}\Big\{\left(v^\theta_{j,k,l,m}\, f_{j,k+1,l,m} - v^\theta_{j,k,l,m}\, f_{j,k-1,l,m}\right) \\
& - \frac{1}{8}\left(v^\theta_{j,k,l,m}\, f_{j,k+2,l,m} - v^\theta_{j,k,l,m}\, f_{j,k-2,l,m}\right) \\
& + \left(v^\theta_{j,k+1,l,m}\, f_{j,k+1,l,m} - v^\theta_{j,k-1,l,m}\, f_{j,k-1,l,m}\right) \\
& - \frac{1}{8}\left(v^\theta_{j,k+2,l,m}\, f_{j,k+2,l,m} - v^\theta_{j,k-2,l,m}\, f_{j,k-2,l,m}\right)\Big\}
\end{aligned}$$

$$
\begin{aligned}
&+\frac{1}{3\Delta\varphi}\Big\{\left(v^{\varphi}_{j,k,l,m}\,f_{j,k,l+1,m}-v^{\varphi}_{j,k,l,m}\,f_{j,k,l-1,m}\right)\\
&\quad-\frac{1}{8}\left(v^{\varphi}_{j,k,l,m}\,f_{j,k,l+2,m}-v^{\varphi}_{j,k,l,m}\,f_{j,k,l-2,m}\right)\\
&\quad+\left(v^{\varphi}_{j,k,l+1,m}\,f_{j,k,l+1,m}-v^{\varphi}_{j,k,l-1,m}\,f_{j,k,l-1,m}\right)\\
&\quad-\frac{1}{8}\left(v^{\varphi}_{j,k,l+2,m}\,f_{j,k,l+2,m}-v^{\varphi}_{j,k,l-2,m}\,f_{j,k,l-2,m}\right)\Big\}\\
&+\frac{1}{3\Delta v_{\parallel}}\Big\{\left(v^{v_{\parallel}}_{j,k,l,m}\,f_{j,k,l,m+1}-v^{v_{\parallel}}_{j,k,l,m}\,f_{j,k,l,m-1}\right)\\
&\quad-\frac{1}{8}\left(v^{v_{\parallel}}_{j,k,l,m}\,f_{j,k,l,m+2}-v^{v_{\parallel}}_{j,k,l,m}\,f_{j,k,l,m-2}\right)\\
&\quad+\left(v^{v_{\parallel}}_{j,k,l,m+1}\,f_{j,k,l,m+1}-v^{v_{\parallel}}_{j,k,l,m-1}\,f_{j,k,l,m-1}\right)\\
&\quad-\frac{1}{8}\left(v^{v_{\parallel}}_{j,k,l,m+2}\,f_{j,k,l,m+2}-v^{v_{\parallel}}_{j,k,l,m-2}\,f_{j,k,l,m-2}\right)\Big\}\\
&+\mathcal{O}\left(\Delta r^4,\Delta\theta^4,\Delta\varphi^4,\Delta v_{\parallel}^4\right). \qquad (3.33)
\end{aligned}
$$

When we sum (or integrate) Eq. (3.33) over all directions, most terms cancel out, leaving only the fluxes at the boundaries. Thus, the conservation of the $L1$ norm has been demonstrated. Similarly, the conservation of the $L2$ norm can also be demonstrated. Upon multiplying Eq. (3.30) by f and then discretizing it, one obtains

$$
\begin{aligned}
f\frac{\partial}{\partial x^i}\left(v^i f\right)\Big|_{\mathrm{P}} = \;&\frac{1}{3\Delta r}\Big\{\left(f_{j+1,k,l,m}\,v^{r}_{j,k,l,m}\,f_{j,k,l,m}-f_{j,k,l,m}\,v^{r}_{j-1,k,l,m}\,f_{j-1,k,l,m}\right)\\
&\quad-\frac{1}{8}\left(f_{j+2,k,l,m}\,v^{r}_{j,k,l,m}\,f_{j,k,l,m}-f_{j,k,l,m}\,v^{r}_{j-2,k,l,m}\,f_{j-2,k,l,m}\right)\\
&\quad+\left(f_{j,k,l,m}\,v^{r}_{j+1,k,l,m}\,f_{j+1,k,l,m}-f_{j-1,k,l,m}\,v^{r}_{j,k,l,m}\,f_{j,k,l,m}\right)\\
&\quad-\frac{1}{8}\left(f_{j,k,l,m}\,v^{r}_{j+2,k,l,m}\,f_{j+2,k,l,m}-f_{j-2,k,l,m}\,v^{r}_{j,k,l,m}\,f_{j,k,l,m}\right)\Big\}\\
&+\frac{1}{3\Delta\theta}\Big\{\left(f_{j,k+1,l,m}\,v^{\theta}_{j,k,l,m}\,f_{j,k,l,m}-f_{j,k,l,m}\,v^{\theta}_{j,k-1,l,m}\,f_{j,k-1,l,m}\right)\\
&\quad-\frac{1}{8}\left(f_{j,k+2,l,m}\,v^{\theta}_{j,k,l,m}\,f_{j,k,l,m}-f_{j,k,l,m}\,v^{\theta}_{j,k-2,l,m}\,f_{j,k-2,l,m}\right)\\
&\quad+\left(f_{j,k,l,m}\,v^{\theta}_{j,k+1,l,m}\,f_{j,k+1,l,m}-f_{j,k-1,l,m}\,v^{\theta}_{j,k,l,m}\,f_{j,k,l,m}\right)\\
&\quad-\frac{1}{8}\left(f_{j,k,l,m}\,v^{\theta}_{j,k+2,l,m}\,f_{j,k+2,l,m}-f_{j,k-2,l,m}\,v^{\theta}_{j,k,l,m}\,f_{j,k,l,m}\right)\Big\}\\
&+\frac{1}{3\Delta\varphi}\Big\{\left(f_{j,k,l+1,m}\,v^{\varphi}_{j,k,l,m}\,f_{j,k,l,m}-f_{j,k,l,m}\,v^{\varphi}_{j,k,l-1,m}\,f_{j,k,l-1,m}\right)\\
&\quad-\frac{1}{8}\left(f_{j,k,l+2,m}\,v^{\varphi}_{j,k,l,m}\,f_{j,k,l,m}-f_{j,k,l,m}\,v^{\varphi}_{j,k,l-2,m}\,f_{j,k,l-2,m}\right)
\end{aligned}
$$

$$
\begin{aligned}
&+ \left(f_{j,k,l,m}\, v^{\varphi}_{j,k,l+1,m}\, f_{j,k,l+1,m} - f_{j,k,l-1,m}\, v^{\varphi}_{j,k,l,m}\, f_{j,k,l,m}\right) \\
&- \frac{1}{8}\left(f_{j,k,l,m}\, v^{\varphi}_{j,k,l+2,m}\, f_{j,k,l+2,m} - f_{j,k,l-2,m}\, v^{\varphi}_{j,k,l,m}\, f_{j,k,l,m}\right)\Big\} \\
&+ \frac{1}{3\Delta v_{\parallel}}\Big\{\left(f_{j,k,l,m+1}\, v^{v_{\parallel}}_{j,k,l,m}\, f_{j,k,l,m} - f_{j,k,l,m}\, v^{v_{\parallel}}_{j,k,l,m-1}\, f_{j,k,l,m-1}\right) \\
&- \frac{1}{8}\left(f_{j,k,l,m+2}\, v^{v_{\parallel}}_{j,k,l,m}\, f_{j,k,l,m} - f_{j,k,l,m}\, v^{v_{\parallel}}_{j,k,l,m-2}\, f_{j,k,l,m-2}\right) \\
&+ \left(f_{j,k,l,m}\, v^{v_{\parallel}}_{j,k,l,m+1}\, f_{j,k,l,m+1} - f_{j,k,l,m-1}\, v^{v_{\parallel}}_{j,k,l,m}\, f_{j,k,l,m}\right) \\
&- \frac{1}{8}\left(f_{j,k,l,m}\, v^{v_{\parallel}}_{j,k,l,m+2}\, f_{j,k,l,m+2} - f_{j,k,l,m-2}\, v^{v_{\parallel}}_{j,k,l,m}\, f_{j,k,l,m}\right)\Big\} \\
&+ \mathcal{O}\left(\Delta r^4, \Delta\theta^4, \Delta\varphi^4, \Delta v_{\parallel}^4\right). \qquad (3.34)
\end{aligned}
$$

When we sum Eq. (3.34) over each direction, just as in Eq. (3.33), only the boundary values remain. Thus, the conservation of the $L2$ norm is also demonstrated. The numerical conservation of the $L2$ norm is of importance for the suppression of numerical oscillations. It is worth noting that the proof of these conservation laws is analogous to that in the Arakawa Jacobian [125, 126].

3.2.2 Source/sink model and collision operator

The source term S_{src} and the sink term S_{snk} in the normalized gyrokinetic Vlasov equation are given by

$$
S_{\mathrm{src}} = A_{\mathrm{src}}(r)\tau_{\mathrm{src}}^{-1}\frac{1}{\mathcal{J}\sqrt{2\pi}}\left(\frac{1}{\sqrt{1.1}}e^{-\frac{v_{\parallel}^2}{2.2}} - e^{-\frac{v_{\parallel}^2}{2}}\right)e^{-\mu B} \qquad (3.35)
$$

and

$$
S_{\mathrm{snk}} = A_{\mathrm{snk}}(r)\tau_{\mathrm{snk}}^{-1}\left\{f_s(t=0) - f_s(t)\right\}, \qquad (3.36)
$$

respectively. A_{src} and A_{snk} are the radial profiles of the source and sink terms, respectively; τ_{src}^{-1} and τ_{snk}^{-1} are their corresponding time scales. The source term causes the temperatures to rise over time, which corresponds to the increase in the particle velocities due to heating. In this model the source term is constant in time. Increasing τ_{src}^{-1} increases the heating power. If there are no collision terms, there is a possibility that the distribution function may become negative in low velocity region because of this term. Hence, a collision term is essential when a source term is included. Equation (3.36) is a Krook-type operator, which acts to bring the distribution function closer to the initial one. This enables the suppression of numerical oscillations at the boundaries. The collision term C_{coll} is a self-collision operator abd given as

$$
C_{\mathrm{coll}} = C_T(f_s) + \mathcal{P}f_{0s}. \qquad (3.37)
$$

The first and second terms on the right-hand side represent the test particle operator and field particle operator, respectively. In this study, we used the linear Fokker-Planck operator [91]

$$C_T(f_s) = \frac{\partial}{\partial v_\parallel}\left\{\mathcal{D}\frac{\partial}{\partial v_\parallel}f_s - \mathcal{V}f_s\right\}. \tag{3.38}$$

as the test particle operator. The diffusive operator $\mathcal{D}$ and the convective operator $\mathcal{V}$ are defined as

$$\mathcal{D} = \frac{3\sqrt{\pi}}{2(q(r=0.5a_0)R_0)}\left(\frac{a_0}{R_0}\right)^{3/2}\nu_\star\frac{n_s}{\sqrt{T_s}}\frac{\Phi(\upsilon)-G(\upsilon)}{2\upsilon} \tag{3.39}$$

and

$$\mathcal{V} = -\frac{v_\parallel}{T_s}\mathcal{D}, \tag{3.40}$$

respectively, where υ is defined as $\upsilon \equiv \sqrt{\left(v_\parallel^2/2+\mu B\right)/T}$, and $\nu_\star = qR_0\nu_{ss}/(v_{Ts}\varepsilon_t^{3/2})$ is the dimensionless collision frequency. The collision frequency ν_{ss} is given by

$$\nu_{ss} = \frac{4\sqrt{\pi}}{3}\frac{n_s q_s^4 \log\Lambda}{m_s^2 v_{Ts}^2}, \tag{3.41}$$

where $\log\Lambda$ is referred to as the Coulomb logarithm. Λ is defined as $\Lambda \equiv \lambda_D/r_c$ and is proportional to $(r_d/r_c)^{3/2}$ where $r_c \equiv e^2/T_s$ and $r_d \equiv n_s^{-1/3}$ are the distance of closest approach and the average distance between particles, respectively. Because we consider a weakly coupled plasma where the kinetic energy is larger than the potential energy of the interaction, Λ is large [190]. It is noteworthy that Λ corresponds to the number of particles in a Debye sphere. The error function $\Phi(\upsilon)$ and the Chandrasekhar function $G(\upsilon)$ are respectively defined as

$$\Phi(\upsilon) \equiv \frac{2}{\sqrt{\pi}}\int_0^\upsilon e^{-t^2}dt \tag{3.42}$$

and

$$G(\upsilon) \equiv \frac{\Phi(\upsilon) - \upsilon\frac{\partial\Phi(\upsilon)}{\partial\upsilon}}{2\upsilon^2}. \tag{3.43}$$

The collision term acts to restore the distribution function to a Maxwellian

$$f_{0s} = \frac{1}{\sqrt{2\pi T_s^3}}\exp\left(-\frac{v_\parallel^2+2\mu B}{2T_s}\right). \tag{3.44}$$

If the distribution function is a Maxwellian, the collision term becomes zero. This can be easily verified by substituting a Maxwellian into Eq. (3.38). The field particle operator is defined such that the velocity space integration of the product of the collision term C_{coll} and a vector $\mathcal{M} = (1, v_\parallel, v_\parallel^2+2\mu B)^T$ is zero. This ensures the numerical conservation of the density, momentum, and energy. The operator $\mathcal{P}$ is given by [127, 128]

$$\mathcal{P} = -\left[aF(x) + bG(x,\xi) + cH(x)\right], \tag{3.45}$$

where

$$x \equiv \frac{1}{2T_s}\left(v_\parallel^2 + 2\mu B\right), \quad \xi \equiv \frac{v_\parallel}{\sqrt{v_\parallel^2 + 2\mu B}} \tag{3.46}$$

and

$$\phi(x) \equiv -\frac{2}{\sqrt{\pi}} e^{-x}\sqrt{x} + \Phi(\sqrt{x}). \tag{3.47}$$

a, b, and c are defined as

$$a = \int C_T(f_s) B dv_\parallel d\mu, \tag{3.48}$$

$$b = \int v_\parallel C_T(f_s) B dv_\parallel d\mu, \tag{3.49}$$

and

$$c = \int \left(v_\parallel^2 + 2\mu B\right) C_T(f_s) B dv_\parallel d\mu, \tag{3.50}$$

respectively. $F(x), G(x,\xi)$, and $H(x)$ are defined as

$$F(x) = 1 - 3\sqrt{\frac{\pi}{2}} x^{-1/2}\left(\phi(x) - \frac{d\phi(x)}{dx}\right), \tag{3.51}$$

$$G(x,\xi) = \frac{6}{\sqrt{2T_s}}\sqrt{\frac{\pi}{2}}\frac{\xi}{x}\phi(x), \tag{3.52}$$

and

$$H(x) = \frac{1}{T_s}\sqrt{\frac{\pi}{2}} x^{-1/2}\left(\phi(x) - \frac{d\phi(x)}{dx}\right), \tag{3.53}$$

respectively. Eqs. (3.51), (3.52), and (3.53) satisfy

$$\int \mathcal{M} F(x) f_{0s} B dv_\parallel d\mu = \begin{pmatrix} 1 \\ 0 \\ 0 \end{pmatrix}, \tag{3.54}$$

$$\int \mathcal{M} G(x) f_{0s} B dv_\parallel d\mu = \begin{pmatrix} 0 \\ 1 \\ 0 \end{pmatrix}, \tag{3.55}$$

and

$$\int \mathcal{M} H(x) f_{0s} B dv_\parallel d\mu = \begin{pmatrix} 0 \\ 0 \\ 1 \end{pmatrix}, \tag{3.56}$$

respectively, hence it is evident that

$$\int \mathcal{M} C_{\text{coll}} B dv_\parallel d\mu = \int \mathcal{M}\left[C_T(f_s) + \mathcal{P} f_{0s}\right] \mathcal{J} dv_\parallel d\mu = \begin{pmatrix} 0 \\ 0 \\ 0 \end{pmatrix}. \tag{3.57}$$

3.2.3 Time integration

When we calculate the integration of a function vector $\boldsymbol{y}(t_{n+1}) = \boldsymbol{y}^{(n+1)}$ at time t_{n+1} using a single stage explicit method, it can generally be expressed as

$$\boldsymbol{y}^{(n+1)} = \boldsymbol{y}^{(n)} + \Delta t\ \boldsymbol{F}(t_n, \boldsymbol{y}^{(n)}) \tag{3.58}$$

using an appropriate approximation function $\boldsymbol{F}(t_n, \boldsymbol{y}^{(n+1)})$, where Δt represents the time step size, and $t_{n+1} = t_n + \Delta t$. The computation time and accuracy depend on the choice of the function $\boldsymbol{F}$.

A function $\boldsymbol{y}(t)$ is assumed to be sufficiently smooth, and its derivative is assumed to be expressed using the function $\boldsymbol{f}(t, \boldsymbol{y})$ as

$$\frac{d\boldsymbol{y}}{dt} = \boldsymbol{f}(t, \boldsymbol{y}). \tag{3.59}$$

Expanding $\boldsymbol{y}(t + \Delta)$ up to the order of Δt yields

$$\boldsymbol{y}(t + \Delta t) = \boldsymbol{y}(t) + \Delta t \boldsymbol{f}(t, \boldsymbol{y}). \tag{3.60}$$

Thus, from Eqs. (3.75) and (3.77), we obtain

$$\boldsymbol{F}(t, \boldsymbol{y}) = \boldsymbol{f}(t, \boldsymbol{y}). \tag{3.61}$$

This scheme is referred to as the first-order explicit Euler method, and can be represented as

$$\boldsymbol{y}^{(n+1)} = \boldsymbol{y}^{(n)} + \Delta t \boldsymbol{f}(t_n, \boldsymbol{y}^{(n)}). \tag{3.62}$$

The implicit scheme with the same approximation function $\boldsymbol{F}$ is represented as

$$\boldsymbol{y}^{(n+1)} = \boldsymbol{y}^{(n)} + \Delta t \boldsymbol{f}(t_{n+1}, \boldsymbol{y}^{(n+1)}), \tag{3.63}$$

which is known as the first-order implicit Euler method. In the case of implicit methods, unlike explicit methods, since there is data at time t_{n+1} on the right-hand side, it is necessary to solve a system of equations, which takes longer than explicit methods. On the other hand, explicit methods are often vulnerable to numerical instabilities and typically require a larger number of grid points. In the first-order explicit Euler method, to reduce the truncation error to one-tenth, one must decrease Δt to one-tenth, resulting in a tenfold increase in computational effort.

By retaining higher-order terms in the Taylor expansion, it is possible to improve the first-order Euler scheme and construct a more accurate scheme. However, in the case, higher-order derivatives of $\boldsymbol{f}(t, \boldsymbol{y})$ appear, making it less desirable for numerical computations. In Runge-Kutta methods, in order to enhance accuracy without including derivatives of $\boldsymbol{f}(t, \boldsymbol{y})$, a linear combination of $\boldsymbol{f}(t, \boldsymbol{y})$ is used as $\boldsymbol{F}$. The function $\boldsymbol{F}$

of the 2-stage 2nd-order Runge-Kutta method (RK4) is denoted as

$$\begin{cases} \boldsymbol{k}_1 = \boldsymbol{f}(t, \boldsymbol{y}) & (3.64) \\ \boldsymbol{k}_2 = \boldsymbol{f}(t + \alpha_1 \Delta t, \boldsymbol{y} + \beta_{21} \boldsymbol{k}_1 \Delta t) & (3.65) \\ \boldsymbol{F}(t, \boldsymbol{y}) = \Delta t (w_1 \boldsymbol{k}_1 + w_2 \boldsymbol{k}_2) & (3.66) \end{cases}$$

where $\alpha_1, \beta_{21}, w_1$, and w_2 are unknowns. Among the unknowns, two can be arbitrarily chosen, while the remaining two are determined from the expression where $\boldsymbol{y}(t + \Delta)$ is expanded up to the order of Δt^2 and from Eq. (3.66). The commonly used expression for the method is

$$\begin{cases} \boldsymbol{k}_1 = \boldsymbol{f}(t_n, \boldsymbol{y}^{(n)}) \\ \boldsymbol{k}_2 = \boldsymbol{f}(t_n + \Delta t, \boldsymbol{y}^{(n)} + \boldsymbol{k}_1 \Delta t) \\ \boldsymbol{y}^{(n+1)} = \boldsymbol{y}^{(n)} + \dfrac{\Delta t}{2} (\boldsymbol{k}_1 + \boldsymbol{k}_2) \end{cases} \quad (3.67)$$

which is referred to as the Heun's method. The function $\boldsymbol{F}$ of the 4-stage 4th-order Runge-Kutta method (RK4) is denoted as

$$\begin{cases} \boldsymbol{k}_1 = \boldsymbol{f}(t, \boldsymbol{y}) & (3.68) \\ \boldsymbol{k}_2 = \boldsymbol{f}(t + \alpha_1 \Delta t, \boldsymbol{y} + \beta_{21} \boldsymbol{k}_1 \Delta t) & (3.69) \\ \boldsymbol{k}_3 = \boldsymbol{f}(t + \alpha_2 \Delta t, \boldsymbol{y} + \beta_{31} \boldsymbol{k}_1 \Delta t + \beta_{32} \boldsymbol{k}_2 \Delta t) & (3.70) \\ \boldsymbol{k}_4 = \boldsymbol{f}(t + \alpha_3 \Delta t, \boldsymbol{y} + \beta_{41} \boldsymbol{k}_1 \Delta t + \beta_{42} \boldsymbol{k}_2 \Delta t + \beta_{43} \boldsymbol{k}_3 \Delta t) & (3.71) \\ \boldsymbol{F}(t, \boldsymbol{y}) = \Delta t (w_1 \boldsymbol{k}_1 + w_2 \boldsymbol{k}_2 + w_3 \boldsymbol{k}_3 + w_4 \boldsymbol{k}_4) & (3.72) \end{cases}$$

where $\alpha_1, \alpha_2, \alpha_3, \beta_{21}, \beta_{31}, \beta_{32}, \beta_{41}, \beta_{42}, \beta_{43}, w_1, w_2, w_3$, and w_4 are unknowns. Among the unknowns, two can be arbitrarily chosen, while the remaining eleven are determined from the expression where $\boldsymbol{y}(t + \Delta)$ is expanded up to the order of Δt^4 and from Eq. (3.72). The commonly used expression for the method is

$$\begin{cases} \boldsymbol{k}_1 = \boldsymbol{f}(t_n, \boldsymbol{y}^{(n)}) \\ \boldsymbol{k}_2 = \boldsymbol{f}\left(t_n + \dfrac{1}{2}\Delta t, \boldsymbol{y}^{(n)} + \dfrac{1}{2}\boldsymbol{k}_1 \Delta t\right) \\ \boldsymbol{k}_3 = \boldsymbol{f}\left(t_n + \dfrac{1}{2}\Delta t, \boldsymbol{y}^{(n)} + \dfrac{1}{2}\boldsymbol{k}_2 \Delta t\right) \\ \boldsymbol{k}_4 = \boldsymbol{f}\left(t_n + \Delta t, \boldsymbol{y}^{(n)} + \boldsymbol{k}_3 \Delta t\right) \\ \boldsymbol{y}^{(n+1)} = \boldsymbol{y}^{(n)} + \dfrac{\Delta t}{6} (\boldsymbol{k}_1 + 2\boldsymbol{k}_2 + 2\boldsymbol{k}_3 + \boldsymbol{k}_4) \end{cases} . \quad (3.73)$$

The stability of these numerical time integration methods is analyzed using a linear ordinary differential equation,

$$\frac{dy}{dt} = \lambda y, \tag{3.74}$$

where λ is an arbitrary complex constant. The exact solution of Eq. (3.74) is $y = y_0 e^{\lambda t}$ where $y(0) = y_0$ is the initial value. For $\mathrm{Re}(\lambda) < 0$, it converges to 0 as t approaches infinity. The conditions under which the numerical solutions obtained by the first-order explicit Euler method, first-order implicit Euler method, RK2, and RK4 do not diverge as the number of time steps approaches infinity can be expressed as

$$|1 + z| \leq 1 \qquad \text{(Explicit Euler)},$$

$$\left|\frac{1}{1 - z}\right| \leq 1 \qquad \text{(Implicit Euler)},$$

$$\left|1 + z + \frac{1}{2}z^2\right| \leq 1 \qquad \text{(RK2)},$$

$$\left|1 + z + \frac{1}{2}z^2 + \frac{1}{6}z^3 + \frac{1}{2}z^4\right| \leq 1 \qquad \text{(RK4)},$$

respectively, where $z \equiv \lambda \Delta t$.

Figure 3.3 shows the stability regions for the 1st-order explicit Euler method, 1st-order implicit Euler method, 2nd-order Runge-Kutta method (RK2), and 4th-order Runge-Kutta method (RK4). From Fig. 3.3, it can be observed that for a large value of $|\mathrm{Re}(\lambda)|$, one must select a smaller value for Δt when employing explicit methods. On the other hand, the implicit Euler method is always stable in the region where $\mathrm{Re}(\lambda) < 1$. Additionally, from the figure, it can be observed that as the order of the Runge-Kutta method increases, its stability region expands. It is noted that the first-order explicit Euler method is equivalent to the first-order Runge-Kutta method. However, it should be cautioned that even if the exact solution converges for $\mathrm{Re}(\lambda) < 0$, it doesn't guarantee that the numerical solution from the fourth-order Runge-Kutta method converges.

In GKNET, numerical integration is computed using the 4-stage 4th-order Runge-Kutta method. It is known that in Runge-Kutta methods of five stages or more, increasing the number of stages does not necessarily increase the order of accuracy. For instance, the maximum order of accuracy for a five-stage Runge-Kutta method is fourth-order, which is the same as that of the RK4. When the advection terms in Eq. (3.30) is discretized using the Morinishi scheme as in Eq. (3.33), Eq. (3.30) becomes an ordinary differential equation with respect to time

$$\frac{df_{j,k,l,m}}{dt} = -\frac{1}{\mathcal{J}} \frac{\partial}{\partial x^i} \left(v^i f\right)\Big|_{\mathrm{P}}. \tag{3.75}$$

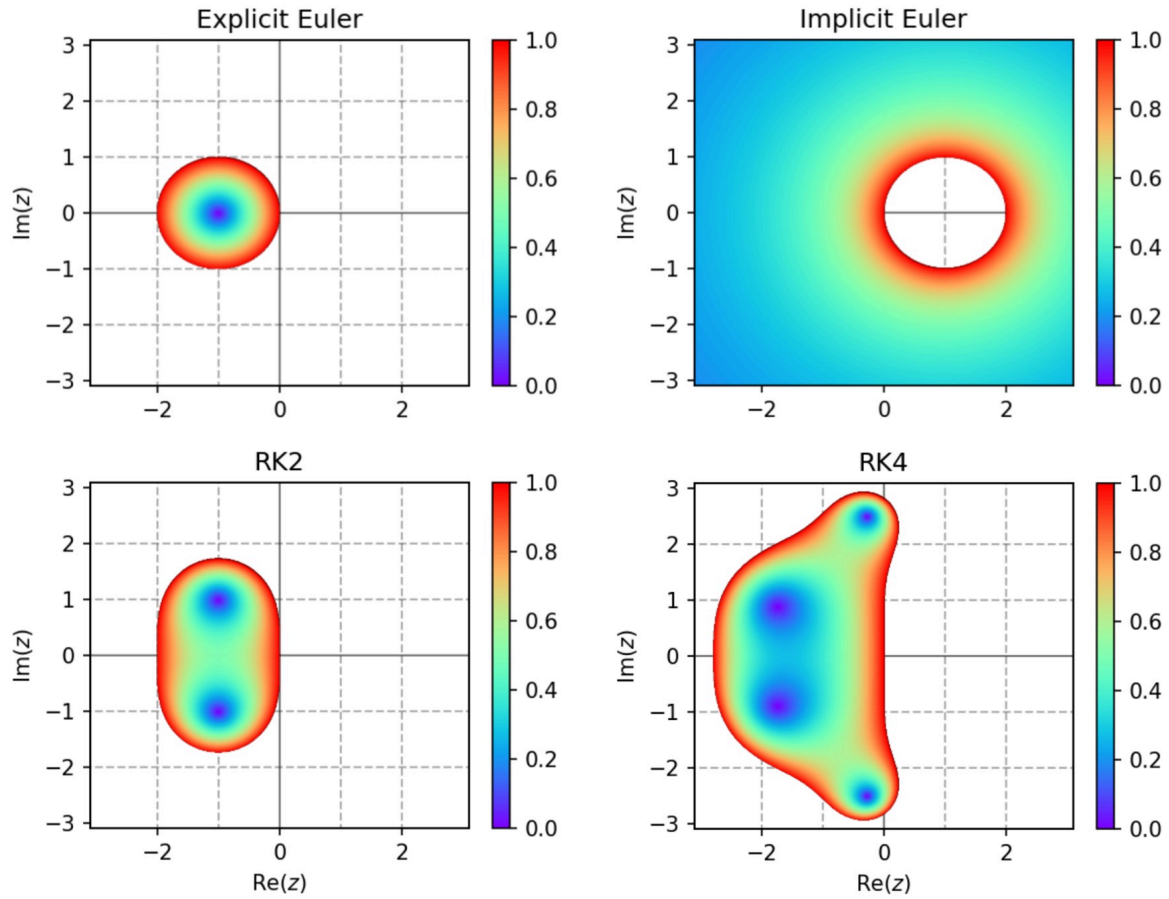

Fig. 3.3: Stability regions for the first-order explicit Euler method, first-order implicit Euler method, second-order Runge-Kutta method (RK2), and fourth-order Runge-Kutta method (RK4).

Omitting the subscripts representing the position, and denoting the right-hand side of the equation as $F_{ts}(f)$, we obtain

$$\frac{df}{dt} = F_{ts}(f). \tag{3.76}$$

Thus, the algorithm employed in GKNET for computing the distribution function $f^{(n+1)}$ at the subsequent time from the distribution function $f^{(n)}$ at the time step n can be expressed as

$$\begin{cases} k_1 = F_{ts}\left(f^{(n)}\right) \\ k_2 = F_{ts}\left(f^{(n)} + \frac{1}{2}k_1\Delta t\right) \\ k_3 = F_{ts}\left(f^{(n)} + \frac{1}{2}k_2\Delta t\right) \\ k_4 = F_{ts}\left(f^{(n)} + k_3\Delta t\right) \\ f^{(n+1)} = f^{(n)} + \frac{\Delta t}{6}\left(k_1 + 2k_2 + 2k_3 + k_4\right) \end{cases} . \tag{3.77}$$

3.3 Field solver

3.3.1 Finite Larmor radius effect

The gyrophase averaging represents a kinetic effect and appears in the gyrokinetic Hamiltonian Eq. (2.63) and the gyrokinetic Poisson equation Eq. (3.24). The gyrophase average of a physical quantity Ψ is represented by

$$\langle \Psi \rangle_\alpha = \sum_{\boldsymbol{k}} \Psi_{\boldsymbol{k}} J_0 \left(k_\perp \rho \right) e^{i \boldsymbol{k} \cdot \boldsymbol{R}}. \tag{3.78}$$

There are two methods to compute the finite Larmor radius effect. One approach is to calculate the effect using the Padé approximation of J_0 [129]. When we use the Padé approximation, J_0 can be approximated as

$$J_0 \left(k_\perp \rho \right) \simeq \frac{1}{1 + \left(k_\perp \rho \right)^2 / 4}. \tag{3.79}$$

Figure 3.4 represents a plot of the Bessel function J_0 and its Padé approximation as a function of $k_\perp \rho$. From Fig. 3.4, it is evident that the Padé approximation provides a good approximation of the Bessel function in the long wavelength region. However, in the high wavenumber region, the Padé approximation overestimates the gyro averaged value. In GKNET, because the real space is discretized, when the FLR effect is evaluated by the Padé approximation,

$$\left(1 - \frac{\rho^2}{4} \nabla_\perp^2 \right) \langle \Psi \rangle_\alpha = \Psi \tag{3.80}$$

is solved. This equation is derived from Eqs. (3.78) and (3.79). For electrons, since ρ_e is extremely small, $\langle \Psi \rangle_{\alpha e}$ equals Ψ. By normalizing and discretizing Eq. (3.80), the system of equations

$$\begin{aligned} \langle \Psi \rangle_{\alpha,j} - \frac{\mu}{2B} \left(\frac{q_i}{q_s} \right)^2 \left(\frac{m_s}{m_i} \right) \Bigg[& \frac{\langle \Psi \rangle_{\alpha,j-2} - 16 \langle \Psi \rangle_{\alpha,j-1} + 30 \langle \Psi \rangle_{\alpha,j} - 16 \langle \Psi \rangle_{\alpha,j+1} + \langle \Psi \rangle_{\alpha,j-2}}{12 \Delta r} \\ & - \frac{1}{r_j} \left\{ \frac{2 \left(\langle \Psi \rangle_{\alpha,j+1} - \langle \Psi \rangle_{\alpha,j-1} \right)}{3 \Delta r} - \frac{\langle \Psi \rangle_{\alpha,j+2} - \langle \Psi \rangle_{\alpha,j-2}}{12 \Delta r} \right\} + \frac{m^2}{r_j^2} \Bigg] = \Psi_j \end{aligned} \tag{3.81}$$

is obtained. In Eq. (3.81), $\langle \Psi \rangle_\alpha$ and Ψ are Fourier transformed in the θ and φ directions, and $\langle \Psi \rangle_{\alpha,j}$ is given by $\langle \Psi \rangle_{\alpha,j} \equiv \langle \Psi \rangle_\alpha (0.5 \Delta r + j \Delta r, m, n)$. Equation (3.81) is solved using the lower-upper (LU) decomposition.

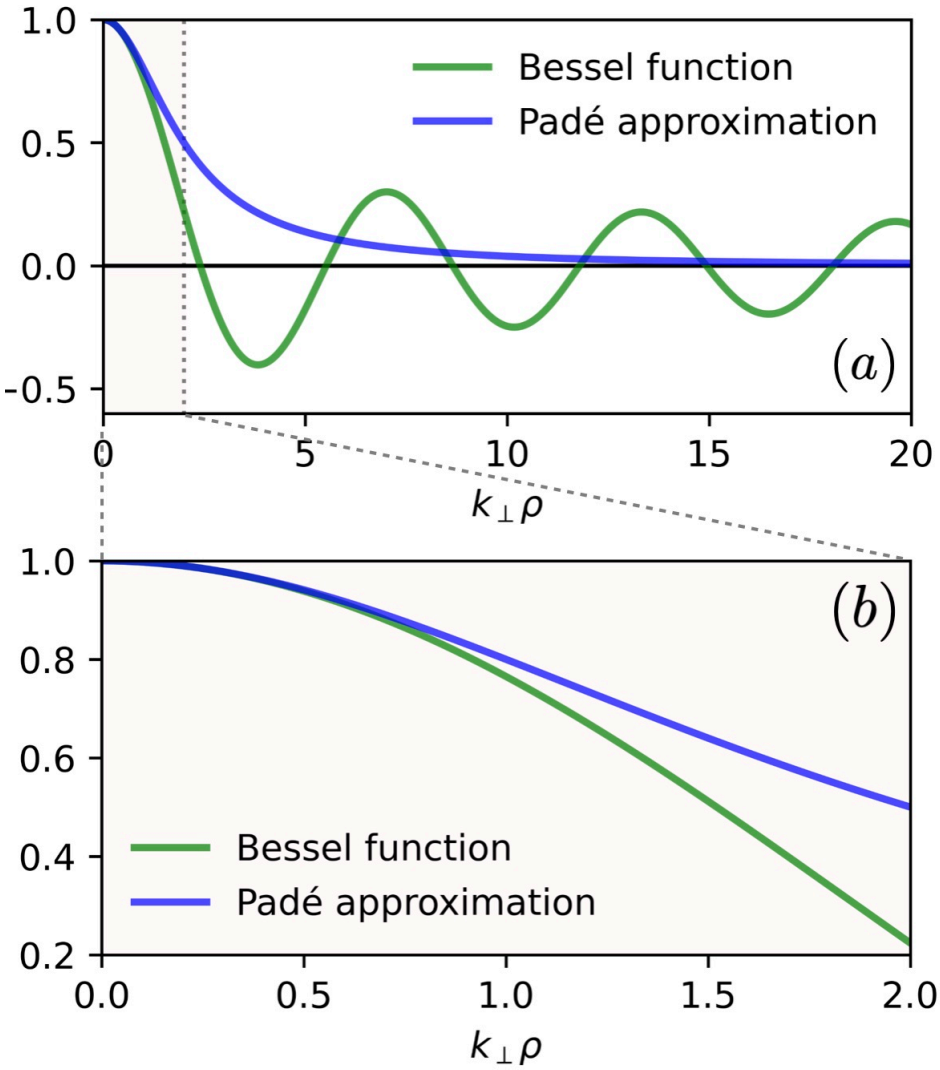

Fig. 3.4: (a) Plot of the Bessel function and its Padé approximation. (b) is the enlarged view of (a).

Another approach is to directly compute the gyrophase averaging by constructing interpolation functions on poloidal cross-sections [130]. Figure 3.5 depicts the Larmor motion centered around a point (r, θ) on a poloidal cross-section. The coordinates $(r_{\mathrm{FLR}}, \theta_{\mathrm{FLR}})$ of a point P on the circular trajectory are represented by

$$r_{\mathrm{FLR}} = \sqrt{r^2 + \rho^2 + 2r\rho\cos(\alpha - \theta)} \tag{3.82}$$

and

$$\theta_{\mathrm{FLR}} = \begin{cases} \arccos\left(\frac{r\cos\theta + \rho\cos\alpha}{r_{\mathrm{FLR}}}\right) & (r\sin\theta + \rho\cos\alpha \geq 0) \\ 2\pi - \arccos\left(\frac{r\cos\theta + \rho\cos\alpha}{r_{\mathrm{FLR}}}\right) & (r\sin\theta + \rho\cos\alpha < 0) \end{cases}, \tag{3.83}$$

respectively. θ_{FLR} is defined such that it does not exceed π. The point P $(r_{\mathrm{FLR}}, \theta_{\mathrm{FLR}})$ typically does not lie on a grid point. Therefore, interpolation is required to determine

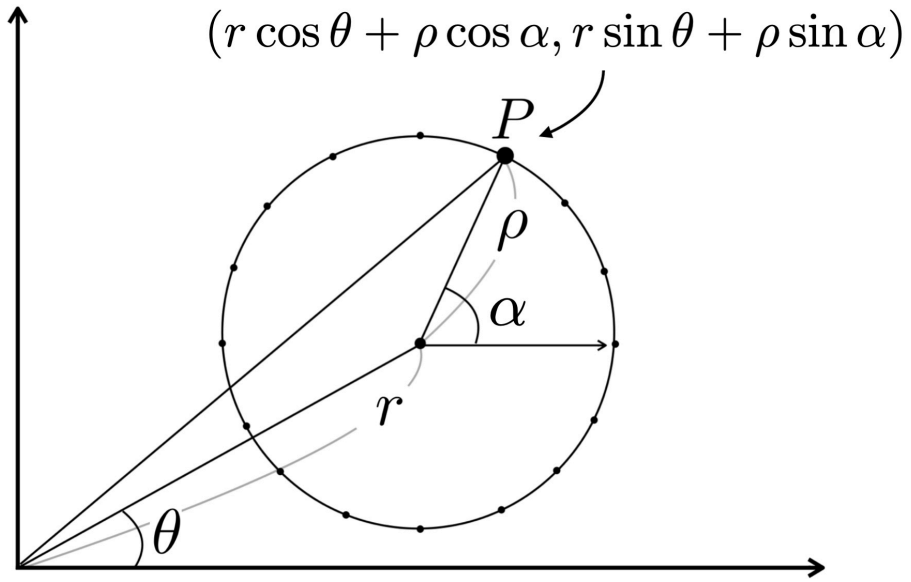

Fig. 3.5: Gyromotion centered around a point (r, θ) on a poloidal cross-section (a modified version of Fig. 3.2 from the reference [130]).

the value of a function at the point. When the discretized points in the r and θ directions are defined as $r_i, \theta_i (i = 1, 2, 3, \cdots)$ in ascending order, $r_{\rm FLR}$ and $\theta_{\rm FLR}$ satisfy

$$r_{[r_{\rm FLR}/\Delta r+2.5]} \leq r_{\rm FLR} \leq r_{[r_{\rm FLR}/\Delta r+2.5]+1} \tag{3.84}$$

and

$$\theta_{[\theta_{\rm FLR}/\Delta\theta+2.5]} \leq \theta_{\rm FLR} \leq \theta_{[\theta_{\rm FLR}/\Delta\theta+2.5]+1}, \tag{3.85}$$

respectively, where $[\cdots]$ is the floor function.

For interpolation, as illustrated in Fig. 3.6, the values of Ψ at the 16 grid points surrounding the point $(r_{\rm FLR}, \theta_{\rm FLR})$, Ψ_i $(i = 1, 2, \ldots, 16)$, are used to determine an interpolation function $F(r, \theta)$, and the value of Ψ at the point $(r_{\rm FLR}, \theta_{\rm FLR})$ is evaluated as $F(r_{\rm FLR}, \theta_{\rm FLR})$. $F(r, \theta)$ is defined by

$$F(r,\theta) = \sum_{i,j=0}^{3} a_{i,j} \left(r - r_{[r_{\rm FLR}/\Delta r+2.5]}\right)^i \left(\theta - \theta_{[\theta_{\rm FLR}/\Delta\theta+2.5]}\right)^j, \tag{3.86}$$

where $a_{i,j}$ $(i, j = 0, 1, 2, 3)$ are real coefficients. By imposing the condition that the interpolation function $F(r, \theta)$ matches Ψ_i $(i = 1, 2, \ldots, 16)$ at the 16 points surrounding the point $(r_{\rm FLR}, \theta_{\rm FLR})$, the coefficients can be determined as follows.

$$\begin{aligned} a_{3,3} = -\frac{1}{36\Delta r^3\Delta\theta^3}\big(&- \Psi_1 + 9\Psi_{10} - 9\Psi_{11} + 3\Psi_{12} + \Psi_{13} - 3\Psi_{14} \\ &+ 3\Psi_{15} - \Psi_{16} + 3\Psi_2 - 3\Psi_3 + \Psi_4 + 3\Psi_5 \end{aligned}$$

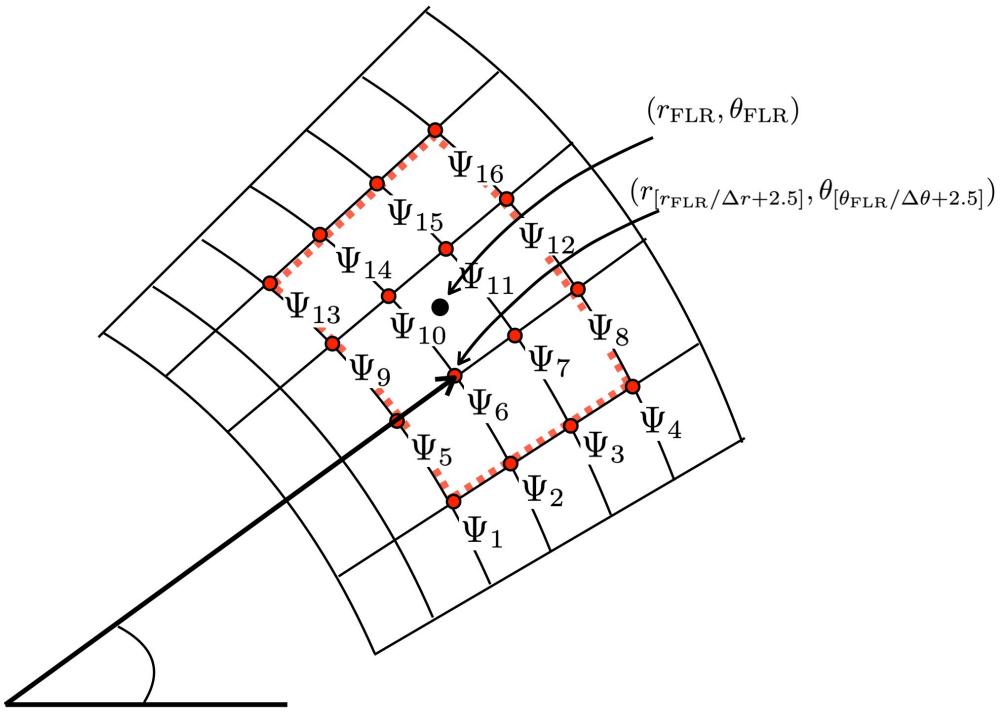

Fig. 3.6: Grid points used for interpolation and the corresponding function values (a modified version of Fig. 3.7 from the reference [130]).

$$- 9\Psi_6 + 9\Psi_7 - 3\Psi_8 - 3\Psi_9\big) \tag{3.87}$$

$$a_{3,2} = -\frac{1}{12\Delta r^3\Delta\theta^2}\big(\Psi_1 - 3\Psi_{10} + 3\Psi_{11} - \Psi_{12} - 3\Psi_2 + 3\Psi_3 - \Psi_4 - 2\Psi_5 + 6\Psi_6 - 6\Psi_7 + 2\Psi_8 + \Psi_9\big) \tag{3.88}$$

$$a_{2,3} = -\frac{1}{12\Delta r^2\Delta\theta^3}\big(\Psi_1 - 6\Psi_{10} + 3\Psi_{11} - \Psi_{13} + 2\Psi_{14} - \Psi_{15} - 2\Psi_2 + \Psi_3 - 3\Psi_5 + 6\Psi_6 - 3\Psi_7 + 3\Psi_9\big) \tag{3.89}$$

$$a_{2,2} = -\frac{1}{4\Delta r^2\Delta\theta^2}\big(-\Psi_1 + 2\Psi_{10} - \Psi_{11} + 2\Psi_2 - \Psi_3 + 2\Psi_5 - 4\Psi_6 + 2\Psi_7 - \Psi_9\big) \tag{3.90}$$

$$a_{3,1} = -\frac{1}{36\Delta r^3\Delta\theta}\big(-2\Psi_2 - 18\Psi_{10} + 18\Psi_{11} - 6\Psi_{12} - \Psi_{13} + 3\Psi_{14} - 3\Psi_{15} + \Psi_{16} + 6\Psi_2 - 6\Psi_3 + 2\Psi_4 - 3\Psi_5 + 9\Psi_6 - 9\Psi_7 + 3\Psi_8 + 6\Psi_9\big) \tag{3.91}$$

$$a_{1,3} = -\frac{1}{36\Delta r\Delta\theta^3}\big(-2\Psi_1 - 9\Psi_{10} + 18\Psi_{11} - 3\Psi_{12} + 2\Psi_{13} + 3\Psi_{14}$$

$$
\begin{aligned}
&- 6\Psi_{15} + \Psi_{16} - 3\Psi_2 + 6\Psi_3 - \Psi_4 + 6\Psi_5 \\
&+ 9\Psi_6 - 18\Psi_7 + 3\Psi_8 - 6\Psi_9\big)
\end{aligned} \tag{3.92}
$$

$$
a_{3,0} = -\frac{1}{6\Delta r^3}\big(\Psi_5 - 3\Psi_6 + 3\Psi_7 - \Psi_8\big) \tag{3.93}
$$

$$
a_{0,3} = -\frac{1}{6\Delta\theta^3}\big(3\Psi_{10} - \Psi_{14} + \Psi_2 - 3\Psi_6\big) \tag{3.94}
$$

$$
\begin{aligned}
a_{2,1} = -\frac{1}{12\Delta r^2\Delta\theta}\big(&2\Psi_1 + 12\Psi_{10} - 6\Psi_{11} + \Psi_{13} - 2\Psi_{14} + \Psi_{15} \\
&- 4\Psi_2 + 2\Psi_3 + 3\Psi_5 - 6\Psi_6 + 3\Psi_7 - 6\Psi_9\big)
\end{aligned} \tag{3.95}
$$

$$
\begin{aligned}
a_{1,2} = -\frac{1}{12\Delta r\Delta\theta^2}\big(&2\Psi_1 + 3\Psi_{10} - 6\Psi_{11} + \Psi_{12} + 3\Psi_2 - 6\Psi_3 \\
&+ \Psi_4 - 4\Psi_5 - 6\Psi_6 + 12\Psi_7 - 2\Psi_8 + 2\Psi_9\big)
\end{aligned} \tag{3.96}
$$

$$
a_{2,0} = -\frac{1}{2\Delta r^2}\big(-\Psi_5 + 2\Psi_6 - \Psi_7\big) \tag{3.97}
$$

$$
a_{0,2} = -\frac{1}{2\Delta\theta^2}\big(-\Psi_{10} - \Psi_2 + 2\Psi_6\big) \tag{3.98}
$$

$$
\begin{aligned}
a_{1,1} = -\frac{1}{36\Delta r\Delta\theta}\big(&- 4\Psi_1 + 18\Psi_{10} - 36\Psi_{11} + 6\Psi_{12} - 2\Psi_{13} - 3\Psi_{14} \\
&+ 6\Psi_{15} - \Psi_{16} - 6\Psi_2 + 12\Psi_3 - 2\Psi_4 - 6\Psi_5 \\
&- 9\Psi_6 + 18\Psi_7 - 3\Psi_8 + 12\Psi_9\big)
\end{aligned} \tag{3.99}
$$

$$
a_{1,0} = -\frac{1}{6\Delta r}\big(2\Psi_5 + 3\Psi_6 - 6\Psi_7 + \Psi_8\big) \tag{3.100}
$$

$$
a_{0,1} = -\frac{1}{6\Delta\theta}\big(-6\Psi_{10} + \Psi_{14} + 2\Psi_2 + 3\Psi_6\big) \tag{3.101}
$$

$$
a_{0,0} = \Psi_6 \tag{3.102}
$$

By substituting $(r_{\mathrm{FLR}}, \theta_{\mathrm{FLR}})$ which is obtained from Eqs. (3.82) and (3.83) into Eq. (3.86),

$$
F\left(r_{\mathrm{FLR}}, \theta_{\mathrm{FLR}}\right) = \sum_{n=1}^{16} c_n \Psi_n \tag{3.103}
$$

is obtained. The coefficients c_n $(n = 1, 2, \cdots, 16)$ can be determined by substituting all equations from (3.87) to (3.102) into Eq. (3.86) as follows.

$$\begin{aligned} c_1 = &\frac{1}{36}x_d^3y_d^3 - \frac{1}{12}x_d^3y_d^2 - \frac{1}{12}x_d^2y_d^3 + \frac{1}{4}x_d^2y_d^2 + \frac{1}{18}x_d^3y_d + \frac{1}{18}x_dy_d^3 \\ &- \frac{1}{6}x_d^2y_d - \frac{1}{6}x_dy_d^2 + \frac{1}{9}x_dy_d \end{aligned} \tag{3.104}$$

$$\begin{aligned} c_2 = &\frac{1}{12}x_d^3y_d^3 + \frac{1}{4}x_d^3y_d^2 + \frac{1}{6}x_d^2y_d^3 - \frac{1}{2}x_d^2y_d^2 - \frac{1}{6}x_d^3y_d + \frac{1}{12}x_dy_d^3 \\ &+ \frac{1}{3}x_d^2y_d - \frac{1}{4}x_dy_d^2 + \frac{1}{6}x_dy_d - \frac{1}{6}y_d^3 + \frac{1}{2}y_d^2 - \frac{1}{3}y_d \end{aligned} \tag{3.105}$$

$$\begin{aligned} c_3 = &\frac{1}{12}x_d^3y_d^3 - \frac{1}{4}x_d^3y_d^2 - \frac{1}{12}x_d^2y_d^3 + \frac{1}{4}x_d^2y_d^2 + \frac{1}{6}x_d^3y_d - \frac{1}{6}x_dy_d^3 \\ &- \frac{1}{6}x_d^2y_d + \frac{1}{2}x_dy_d^2 - \frac{1}{3}x_dy_d \end{aligned} \tag{3.106}$$

$$c_4 = -\frac{1}{36}x_d^3y_d^3 + \frac{1}{12}x_d^3y_d^2 - \frac{1}{18}x_d^3y_d + \frac{1}{36}x_dy_d^3 - \frac{1}{12}x_dy_d^2 + \frac{1}{18}x_dy_d \tag{3.107}$$

$$\begin{aligned} c_5 = &-\frac{1}{12}x_d^3y_d^3 + \frac{1}{6}x_d^3y_d^2 + \frac{1}{4}x_d^2y_d^3 - \frac{1}{2}x_d^2y_d^2 + \frac{1}{12}x_d^3y_d - \frac{1}{6}x_dy_d^3 \\ &- \frac{1}{4}x_d^2y_d + \frac{1}{3}x_dy_d^2 + \frac{1}{6}x_dy_d - \frac{1}{6}x_d^3 + \frac{1}{2}x_d^2 - \frac{1}{3}x_d \end{aligned} \tag{3.108}$$

$$\begin{aligned} c_6 = &\frac{1}{4}x_d^3y_d^3 - \frac{1}{2}x_d^3y_d^2 - \frac{1}{2}x_d^2y_d^3 + x_d^2y_d^2 - \frac{1}{4}x_d^3y_d - \frac{1}{4}x_dy_d^3 \\ &+ \frac{1}{2}x_d^2y_d + \frac{1}{2}x_dy_d^2 + \frac{1}{4}x_dy_d + \frac{1}{2}x_d^3 - x_d^2 - \frac{1}{2}x_d \\ &+ \frac{1}{2}y_d^3 - y_d^2 - \frac{1}{2}y_d + 1 \end{aligned} \tag{3.109}$$

$$\begin{aligned} c_7 = &-\frac{1}{4}x_d^3y_d^3 + \frac{1}{2}x_d^3y_d^2 + \frac{1}{4}x_d^2y_d^3 - \frac{1}{2}x_d^2y_d^2 + \frac{1}{4}x_d^3y_d + \frac{1}{2}x_dy_d^3 \\ &- \frac{1}{4}x_d^2y_d - x_dy_d^2 - \frac{1}{2}x_dy_d - \frac{1}{2}x_d^3 + \frac{1}{2}x_d^2 + x_d \end{aligned} \tag{3.110}$$

$$\begin{aligned} c_8 = &\frac{1}{12}x_d^3y_d^3 - \frac{1}{6}x_d^3y_d^2 - \frac{1}{12}x_d^3y_d - \frac{1}{12}x_dy_d^3 + \frac{1}{6}x_dy_d^2 + \frac{1}{12}x_dy_d \\ &+ \frac{1}{6}x_d^3 - \frac{1}{6}x_d \end{aligned} \tag{3.111}$$

$$\begin{aligned} c_9 = &\frac{1}{12}x_d^3y_d^3 - \frac{1}{12}x_d^3y_d^2 - \frac{1}{4}x_d^2y_d^3 + \frac{1}{4}x_d^2y_d^2 - \frac{1}{6}x_d^3y_d + \frac{1}{6}x_dy_d^3 \\ &+ \frac{1}{2}x_d^2y_d - \frac{1}{6}x_dy_d^2 - \frac{1}{3}x_dy_d \end{aligned} \tag{3.112}$$

$$c_{10} = -\frac{1}{4}x_d^3y_d^3 + \frac{1}{4}x_d^3y_d^2 + \frac{1}{2}x_d^2y_d^3 - \frac{1}{2}x_d^2y_d^2 + \frac{1}{2}x_d^3y_d + \frac{1}{4}x_dy_d^3 - x_d^2y_d - \frac{1}{4}x_dy_d^2 - \frac{1}{2}x_dy_d - \frac{1}{2}y_d^3 + \frac{1}{2}y_d^2 + y_d \tag{3.113}$$

$$c_{11} = \frac{1}{4}x_d^3y_d^3 - \frac{1}{4}x_d^3y_d^2 - \frac{1}{4}x_d^2y_d^3 + \frac{1}{4}x_d^2y_d^2 - \frac{1}{2}x_d^3y_d - \frac{1}{2}x_dy_d^3 + \frac{1}{2}x_d^2y_d + \frac{1}{2}x_dy_d^2 + x_dy_d \tag{3.114}$$

$$c_{12} = -\frac{1}{12}x_d^3y_d^3 + \frac{1}{12}x_d^3y_d^2 + \frac{1}{6}x_d^3y_d + \frac{1}{12}x_dy_d^3 - \frac{1}{12}x_dy_d^2 - \frac{1}{6}x_dy_d \tag{3.115}$$

$$c_{13} = -\frac{1}{36}x_d^3y_d^3 + \frac{1}{12}x_d^2y_d^3 + \frac{1}{36}x_d^3y_d - \frac{1}{18}x_dy_d^3 - \frac{1}{12}x_d^2y_d + \frac{1}{18}x_dy_d \tag{3.116}$$

$$c_{14} = -\frac{1}{12}x_d^3y_d^3 - \frac{1}{6}x_d^2y_d^3 - \frac{1}{12}x_d^3y_d - \frac{1}{12}x_dy_d^3 + \frac{1}{6}x_d^2y_d + \frac{1}{12}x_dy_d + \frac{1}{6}x_d^3 - \frac{1}{6}y_d \tag{3.117}$$

$$c_{15} = -\frac{1}{12}x_d^3y_d^3 + \frac{1}{12}x_d^2y_d^3 + \frac{1}{12}x_d^3y_d + \frac{1}{6}x_dy_d^3 - \frac{1}{12}x_d^2y_d - \frac{1}{6}x_dy_d \tag{3.118}$$

$$c_{16} = \frac{1}{36}x_d^3y_d^3 - \frac{1}{36}x_d^3y_d - \frac{1}{36}x_dy_d^3 + \frac{1}{36}x_dy_d \tag{3.119}$$

x_d and y_d are defined as

$$x_d \equiv \frac{r_{\rm FLR} - r_{[r_{\rm FLR}/\Delta r+2.5]}}{\Delta r} \quad \text{and} \quad y_d \equiv \frac{\theta_{\rm FLR} - \theta_{[\theta_{\rm FLR}/\Delta\theta+2.5]}}{\Delta\theta}, \tag{3.120}$$

respectively. For the electrostatic model, since x_d and y_d do not vary with time, c_n ($n = 1, 2, \cdots, 16$) remain constant. In GKNET, each core only possesses a portion of the information in the r and θ directions. Therefore, it is not guaranteed that a core has all the values of a function at the grid points around a point $(r_{\rm FLR}, \theta_{\rm FLR})$. Therefore, in advance, the cores receive the values at the grid points corresponding to the maximum gyro radius $\rho_{\rm max} \simeq \sqrt{2\mu_{\rm max}/(1 - a_0/R_0)}$ from other cores, and the the poloidal cross-sections one core handles are extended. For partially ionized impurities with large mass, the gyro radius becomes large, which increases communication between cores and makes the calculations more time-consuming.

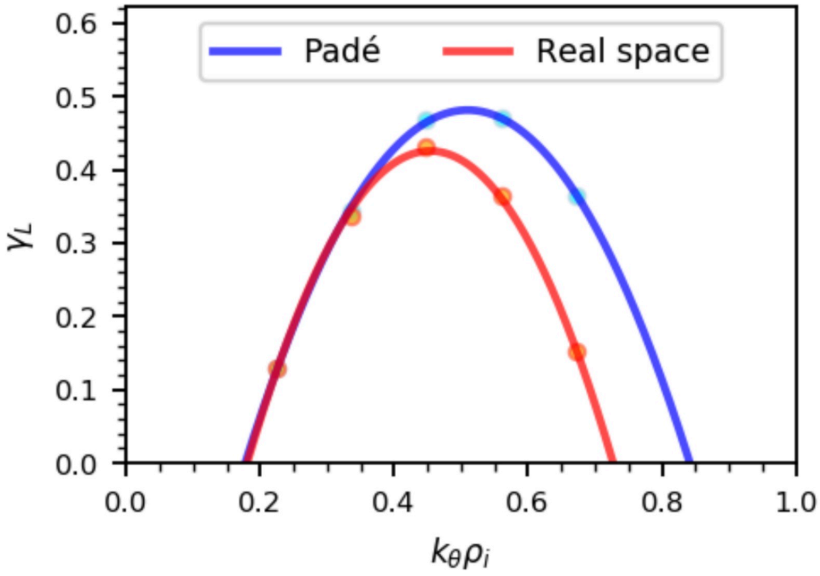

Fig. 3.7: Linear growth rate of the tITG mode with Padé approximation and with real space evaluation.

Figure 3.7 shows the linear growth rate of the tITG mode for the case where the Padé approximation is used and the case where the real space interpolation method is used. In the long wavelength region, the linear growth rates of both cases are consistent. This is consistent with the result in Fig. 3.4, that the Padé approximation is valid in the long wavelength limit. However, in high wavenumber region, the linear growth rate is different between the two cases and the mode number for which the linear growth rate has a maximum value is also different. The previous study has shown that evaluating the FLR effect in real space interpolation method gives more reasonable results [130].

3.3.2 Velocity space integration

The integral in velocity space appears on the right-hand side of the gyrokinetic Poisson equation Eq. (3.24). The $v_\parallel$ direction is discretized in equidistant intervals in the same way as in the real space, and the integral in the direction is computed by the rectangle rule. On the other hand, in the μ direction, since there is no need to differentiate in that direction, it is discretized non-uniformly to allow high-precision integration with fewer grid points. Specifically, it is discretized using the points obtained by applying an affine transformation to the zeros of the Legendre polynomial, and the integration is computed using the Gauss-Legendre quadrature. In this section, we derive the Gauss-Legendre formula as implemented in GKNET.

Orthogonal polynomials are a sequence of polynomials $\{P_n(b)\}_{n=0}^{\infty}$ that satisfy $\deg P_n = n$ and exhibit an orthogonal relationship

$$\mathcal{L}[P_n(b)P_m(b)] = \lambda_n \delta_{n,m}, \quad \lambda_n \neq 0 \tag{3.121}$$

for any given $n, m \in \mathbb{N}_0$ where $\mathcal{L}$ is a linear functional from $\mathbb{C}[b]$ to $\mathbb{C}$ [131]. It can be readily proven that orthogonal polynomials can also be defined as a sequence of polynomials that satisfy a three-term recurrence relation

$$P_n(b) = (\alpha_n b + \beta_n) P_{n-1}(b) - \gamma_n P_{n-2}(b). \tag{3.122}$$

$P_{-1}(b)$ is equal to 0. $\alpha_n, \beta_n, \gamma_n \in \mathbb{C}$ are given by

$$\begin{cases} \alpha_n = \dfrac{\mu_n}{\mu_{n-1}} & (3.123) \\ \beta_n = -\dfrac{\alpha_n \mathcal{L}[bP_{n-1}(b)P_{n-1}(b)]}{\lambda_{n-1}} & (3.124) \\ \gamma_n = \dfrac{\alpha_n \mathcal{L}[bP_{n-1}(b)P_{n-2}(b)]}{\lambda_{n-2}} = \dfrac{\alpha_n \lambda_{n-1}}{\alpha_{n-1}\lambda_{n-2}} = \dfrac{\mu_n \mu_{n-2} \lambda_{n-1}}{\mu_{n-1}^2 \lambda_{n-2}} & (3.125) \end{cases}$$

where μ_n is the leading coefficient of $P_n(b)$. In the case of $b \neq c$, from Eqs. (3.122) and (3.125), we obtain

$$S_n - S_{n-1} = \frac{1}{\lambda_{n-1}} (b-c) P_{n-1}(b) P_{n-1}(c), \tag{3.126}$$

where S_n is defined as

$$S_n \equiv \frac{1}{\alpha_n \lambda_{n-1}} \left\{ P_n(b) P_{n-1}(c) - P_{n-1}(b) P_n(c) \right\}. \tag{3.127}$$

By summing from $n = 1$ to $n = N$ and substituting Eq. (3.123),

$$\sum_{n=0}^{N-1} \frac{P_n(b) P_n(c)}{\lambda_n} = \frac{\mu_{N-1}}{\mu_N \lambda_{N-1}} \frac{P_N(b) P_{N-1}(c) - P_{N-1}(b) P_N(c)}{b-c} \tag{3.128}$$

is derived. It is known that $P_n(b)$ $(n \geq 1)$ has n zeros within the domain and the zeros of $P_m(b)$ $(m > n)$ exist between any zeros of $P_n(b)$. Hence, we can take the zeros of $P_N(b)$ as b_i $(i = 1, 2, \cdots, N)$. By substituting $b = b_j, c = b_k (j \neq k)$ into Eq. (3.128), we obtain

$$\sum_{n=0}^{N-1} \frac{P_n(b_j) P_n(b_k)}{\lambda_n} = 0. \tag{3.129}$$

By substituting $b = b_k$ into Eq. (3.128) and then taking the limit $c \to b_k$,

$$\sum_{n=0}^{N-1} \frac{\{P_n(b_k)\}^2}{\lambda_n} = \frac{\mu_{N-1}}{\mu_N \lambda_{N-1}} P_{N-1}(b_k) P_N'(b_k) \equiv \frac{1}{a_k} \tag{3.130}$$

is derived. From Eqs. (3.129) and (3.130), the Lagrange interpolation coefficients are obtained as

$$L_k^{(N-1)}(b) \equiv a_k \sum_{n=0}^{N-1} \frac{P_n(b_k) P_n(b)}{\lambda_n} = \begin{cases} 1, & b = b_j \quad (j \neq k) \\ 0, & b = b_k \end{cases}. \tag{3.131}$$

The interpolation formula $g_N(b)$ using N sample points of a function $g(b)$ is represented as

$$g_N(b) = \sum_{k=1}^{N} g(b_k) L_k^{(N-1)}(b). \tag{3.132}$$

The integral in the direction of μ for a function $g(\mu)$ is approximated as

$$I = \int_0^{L_\mu} g(\mu) d\mu, \tag{3.133}$$

where L_μ is a cut-off velocity. For Eq. (3.133), by applying the transformation $\mu = (b+1)L_\mu/2$ and performing the Lagrange interpolation Eq. (3.132), it can be expressed as

$$I = \frac{L_\mu}{2} \int_{-1}^{1} g(b) db \simeq \frac{L_\mu}{2} \int_{-1}^{1} g_N(b) db = \sum_{n=0}^{N-1} \left\{ \sum_{k=1}^{N} \frac{L_\mu}{2} a_k P_n(b_k) g(b_k) \right\} \frac{1}{\lambda_n} \int_{-1}^{1} P_n(b) db. \tag{3.134}$$

We consider the Legendre polynomials as orthogonal polynomials $\{P_n(b)\}_{n=0}^{\infty}$. The Legendre polynomials are orthogonal with respect to the $L2$ norm over the closed interval $[-1, 1]$. From the perspective of the three-term recurrence relation, they correspond to the case where $\alpha_n = (2n-1)/n$, $\beta_n = 0$, and $\gamma_n = (n-1)/n$, satisfying

$$bP_n(b) = (2n-1)bP_{n-1}(b) - (n-1)P_{n-2}(b). \tag{3.135}$$

In this case, from

$$\int_{-1}^{1} P_n(b) db = \frac{1}{\mu_0} \int_{-1}^{1} P_n(b) P_0(b) db = \frac{\lambda_0}{\mu_0} \delta_{n,0}, \tag{3.136}$$

Eq. (3.134) becomes

$$I = \sum_{k=1}^{N} \frac{L_\mu}{2} a_k g(b_k). \tag{3.137}$$

Upon using

$$w_k \equiv \frac{L_\mu}{2} a_k \quad \text{and} \quad \mu_k \equiv \frac{L_\mu}{2} b_k + \frac{L_\mu}{2}, \tag{3.138}$$

Eq. (3.137) can be rewritten as

$$I = \sum_{k=1}^{N} w_k g(\mu_k). \tag{3.139}$$

Equation (3.139) is used in the μ direction integration in GKNET. The positions of the zeros b_k and the weights a_k are precomputed and are stored in a text file. In GKNET, this file is read, the values are loaded into arrays, and the integration is then performed using the arrays. a_k satisfies

$$a_k = \frac{\mu_N \lambda_{N-1}}{\mu_{N-1} P_{N-1}(b_k) P'_N(b_k)} = \frac{2}{(1-b_k^2)\, P'_N(b_k)^2} = \frac{2\,(1-b_k^2)}{\left(N P_{N-1}(b_k)\right)^2}, \tag{3.140}$$

derived from Eq. (3.130),

$$\lambda_N = \frac{2}{2N+1}, \qquad \mu_N = \prod_{k=1}^{N} \frac{2k-1}{k}, \tag{3.141}$$

and

$$\left(1-x^2\right) P_n'(x) = nP_{n-1}(x) - nxP_n(x). \tag{3.142}$$

We precompute a_k using Eq. (3.140).

The Gauss-Legendre formula Eq. (3.139) using N sample points provides an exact integration value, barring rounding errors, when $g(\mu)$ is a polynomial of at most $2N-1$ degrees. Assuming $g(\mu)$ is a polynomial of degree $2N-1$ or lower, upon transforming with $\mu = (b+1)L_\mu/2$ and then dividing by $P_N(b)$, with the quotient being $Q(b)$ and the remainder being $R(b)$, we obtain

$$g(b) = P_N(b)Q(b) + R(b). \tag{3.143}$$

Upon integrating Eq. (3.143) and given that $Q(b)$ is a polynomial of at most degree$N-1$, it can be expressed as

$$\frac{L_\mu}{2}\int_{-1}^{1} g(b)db = \frac{L_\mu}{2}\int_{-1}^{1} P_N(b)Q(b)db + \frac{L_\mu}{2}\int_{-1}^{1} R(b)db = \frac{L_\mu}{2}\int_{-1}^{1} R(b)db. \tag{3.144}$$

On the other hand,

$$\sum_{k=1}^{N} w_k g(b_k) = \sum_{k=1}^{N} w_k P_N(b_k)Q(b_k) + \sum_{k=1}^{N} w_k R(b_k) = \sum_{k=1}^{N} w_k R(b_k). \tag{3.145}$$

Since $R(b)$ is a polynomial of degree $N-1$ or lower, Eq. (3.144) and Eq. (3.145) are equivalent. This indicates that when $g(\mu)$ is a polynomial of at most $2N-1$ degrees, Eq. (3.139) provides an exact integration value, excluding rounding errors.

3.3.3 Algorithm

The field solver algorithm in GKNET differs between the adiabatic electron model Eq. (3.25) and the hybrid electron model Eqs. (3.26), (3.27). This is because, in the case of the adiabatic electron model, it is necessary to evaluate the flux-surface averaged electrostatic potential. When it is approximated as $\langle\phi\rangle_f \simeq \langle\phi\rangle_{\theta,\varphi}$, it has been confirmed that the collisionless damping of zonal modes cannot be accurately simulated. $\langle\Psi\rangle_{\theta,\varphi}$ represents the average of Ψ in the θ and φ directions. It is necessary to evaluate $\langle\phi\rangle_f$ without approximation.

First, we describe the field solver algorithm in the adiabatic electron model for the case of a pure plasma. Since $n_0 = n_{0i} = n_{0e}$ in the case, dividing both sides of the equation by $n = n_i = n_e$ yields

$$\mathcal{D}\phi + \frac{1}{T_\mathrm{e}}\left(\phi - \langle\phi\rangle_f\right) = \frac{\rho_i}{n}, \tag{3.146}$$

where $\mathcal{D}$ and ρ_s are defined as

$$\mathcal{D} \equiv -\frac{\partial^2}{\partial r^2} - \left(\frac{1}{r} + \frac{1}{n}\frac{\partial n}{\partial r}\right)\frac{\partial}{\partial r} - \frac{1}{r^2}\frac{\partial^2}{\partial \theta^2} \tag{3.147}$$

and

$$\rho_s \equiv \left\langle \iint \delta f_s \, B^*_{\parallel s} \, dv_\parallel d\mu \right\rangle_{\alpha s}, \tag{3.148}$$

respectively. The right-hand side of Eq. (3.146) is computed using the methods explained in the previous two sections, concerning the gyrophase averaging and velocity space integration. Equation (3.146) cannot be solved directly because $\langle\phi\rangle_f$ on the left-hand side is not known. In the adiabatic electron model, ϕ is obtained by the algorithm illustrated in Fig. 3.8.

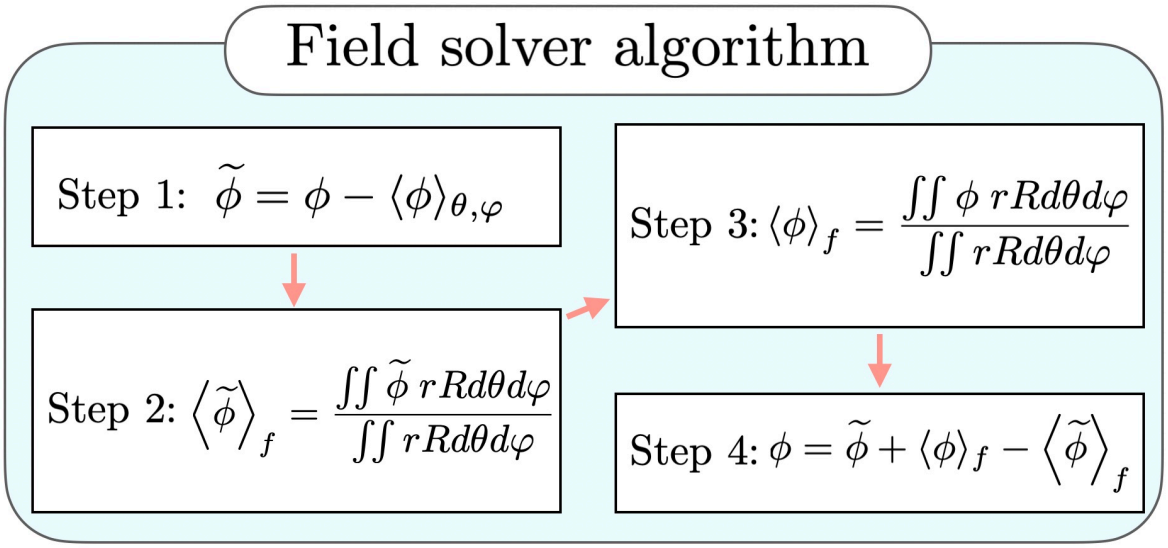

Fig. 3.8: Field solver algorithm in the adiabatic electron model.

In Step 1, $\widetilde{\phi} \equiv \phi - \langle\phi\rangle_{\theta,\varphi}$ is determined. By taking the θ, φ average of Eq. (3.146), and since $\langle\langle\phi\rangle_f\rangle_{\theta,\varphi} = \langle\phi\rangle$,

$$\mathcal{D}\langle\phi\rangle_{\theta,\varphi} + \frac{1}{T_\mathrm{e}}\left(\langle\phi\rangle_{\theta,\varphi} - \langle\phi\rangle_f\right) = \frac{1}{n}\langle\rho_i\rangle_{\theta,\varphi} \tag{3.149}$$

is obtained. By subtracting Eq. (3.149) from Eq. (3.146), we obtain

$$\mathcal{D}\widetilde{\phi} + \frac{\widetilde{\phi}}{T_e} = \frac{\widetilde{\delta n}}{n}, \tag{3.150}$$

where $\widetilde{\delta n}$ is defined as

$$\widetilde{\delta n} \equiv \rho_i - \langle\rho_i\rangle_{\theta,\varphi}\,. \tag{3.151}$$

Since $\langle\phi\rangle_f$ does not appear in Eq. (3.150) and $\widetilde{\delta n}$ is known, $\widetilde{\phi}$ can be determined. To solve Eq. (3.150), $\widetilde{\delta n}$ is discrete Fourier transformed in both the θ and φ directions. For the discrete Fourier transformation, the pencil decomposition [132], which divides the processor grid into two dimensions, is used. We employ the software package P3DFFT [133] for this purpose.

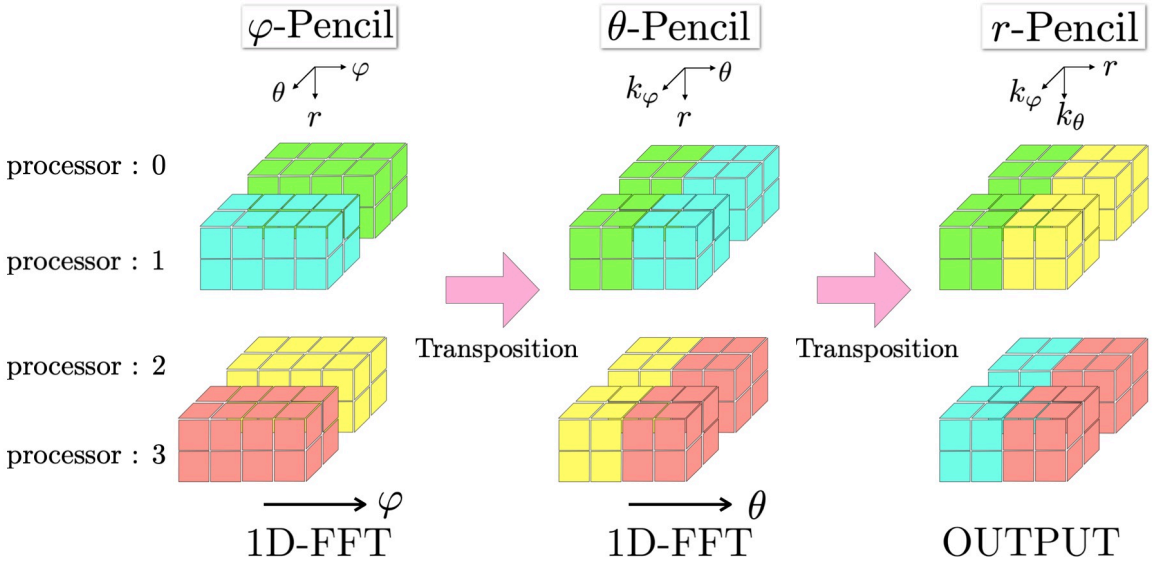

Fig. 3.9: An example of a 2D Fourier transform using the Pencil decomposition.

Figure 3.9 illustrates the algorithm for fast Fourier transformation in the θ and φ directions using P3DFFT, when four processors are employed. Upon inputting the real number array data which is φ-oriented pencil, the 1D fast Fourier transformation is first performed in the φ direction. After arranging the data from φ- to θ-oriented pencils by an all-to-all exchange, a fast Fourier transformation is performed in the θ direction. After transposing the data from θ- to r-oriented pencils by calling MPI_ALLTOALL, the complex array is outputted. By performing the discrete Fourier transformation, only the differential operator in the r direction remains in Eq. (3.150). By discretizing Eq. (3.147) using a fourth-order central difference,

$$\frac{\widetilde{\phi}_{j-2} - 16\widetilde{\phi}_{j-1} + 30\widetilde{\phi}_j - 16\widetilde{\phi}_{j+1} + \widetilde{\phi}_{j+2}}{12\Delta r^2} - \left(\frac{4}{3}\frac{\widetilde{\phi}_{j+1} - \widetilde{\phi}_{j-1}}{2\Delta r} - \frac{1}{3}\frac{\widetilde{\phi}_{j+2} - \widetilde{\phi}_{j-2}}{4\Delta r}\right)\left(\frac{1}{r_j} - \frac{1}{L_{n,j}}\right) + \frac{m^2}{r_j^2}\widetilde{\phi}_j + \frac{\widetilde{\phi}_j}{T_{e,j}} = \frac{\widetilde{\delta n_j}}{n_j} \tag{3.152}$$

is obtained. At the boundary $j = 1, 2$, when m is even, from $\phi_1 = \phi_0,\ \phi_2 = \phi_{-1}$, Eq. (3.152) is

$$\frac{14\widetilde{\phi}_1 - 15\widetilde{\phi}_2 + \widetilde{\phi}_3}{12\Delta r^2} + \left(\frac{2}{3}\widetilde{\phi}_1 - \frac{3}{4}\widetilde{\phi}_2 + \frac{1}{12}\widetilde{\phi}_3\right)\left(\frac{1}{r_1} - \frac{1}{L_{n,1}}\right) + \frac{m^2}{r_1^2}\widetilde{\phi}_1 + \frac{\widetilde{\phi}_1}{T_{e,1}} = \frac{\widetilde{\delta n}_1}{n_1} \tag{3.153}$$

for $j = 1$ and

$$\frac{-15\widetilde{\phi}_1 + 30\widetilde{\phi}_2 - 16\widetilde{\phi}_3 + \widetilde{\phi}_4}{12\Delta r^2} + \left(\frac{7}{12}\widetilde{\phi}_1 - \frac{2}{3}\widetilde{\phi}_3 + \frac{1}{12}\widetilde{\phi}_4\right)\left(\frac{1}{r_2} - \frac{1}{L_{n,2}}\right) + \frac{m^2}{r_2^2}\widetilde{\phi}_2 + \frac{\widetilde{\phi}_2}{T_{e,2}} = \frac{\widetilde{\delta n}_2}{n_2} \tag{3.154}$$

for $j = 2$. On the other hand when m is odd, from $\phi_1 = -\phi_0,\ \phi_2 = -\phi_{-1}$, Eq. (3.152) is

$$\frac{46\widetilde{\phi}_1 - 17\widetilde{\phi}_2 + \widetilde{\phi}_3}{12\Delta r^2} + \left(-\frac{2}{3}\widetilde{\phi}_1 - \frac{7}{12}\widetilde{\phi}_2 + \frac{1}{12}\widetilde{\phi}_3\right)\left(\frac{1}{r_1} - \frac{1}{L_{n,1}}\right) + \frac{m^2}{r_1^2}\widetilde{\phi}_1 + \frac{\widetilde{\phi}_1}{T_{e,1}} = \frac{\widetilde{\delta n}_1}{n_1} \tag{3.155}$$

for $j = 1$ and

$$\frac{-17\widetilde{\phi}_1 + 30\widetilde{\phi}_2 - 16\widetilde{\phi}_3 + \widetilde{\phi}_4}{12\Delta r^2} + \left(\frac{3}{4}\widetilde{\phi}_1 - \frac{2}{3}\widetilde{\phi}_3 + \frac{1}{12}\widetilde{\phi}_4\right)\left(\frac{1}{r_2} - \frac{1}{L_{n,2}}\right) + \frac{m^2}{r_2^2}\widetilde{\phi}_2 + \frac{\widetilde{\phi}_2}{T_{e,2}} = \frac{\widetilde{\delta n}_2}{n_2} \tag{3.156}$$

for $j = 2$. The left-hand side of Eq. (3.152) is an $N_r \times N_r$ square matrix, where N_r represents the number of grid points in the radial direction. The system of equations is solved using the LU decomposition. Since the matrix is a banded matrix, computational costs can be significantly reduced by employing the calculation method illustrated in Fig. 3.10.

Figure 3.10 shows the algorithm of the LU decomposition for the case of $N_r = 6$. The element of the matrix in the i-th row and j-th column is denoted by a_{ij}. The blue squares indicate the calculation for the lower left triangular matrix, while the red squares represent the computation for the upper right triangular matrix. The numbers written inside the circles located at the upper right of each square represent the values of the loop variable. By proceeding with forward elimination as in Fig. 3.10, LU decomposition can be achieved efficiently. The obtained $\widetilde{\phi}$ is transformed back to the real space using the inverse Fourier transformation with the P3DFFT. In Step 2, the flux-surface average of $\widetilde{\phi}$ is computed. It is obtained from equation

$$\left\langle \widetilde{\phi} \right\rangle_f = \frac{\iint \widetilde{\phi} r R\, d\theta d\varphi}{\iint r R\, d\theta d\varphi} = \frac{1}{(2\pi)^2 R_0} \iint \widetilde{\phi} R\, d\theta d\varphi. \tag{3.157}$$

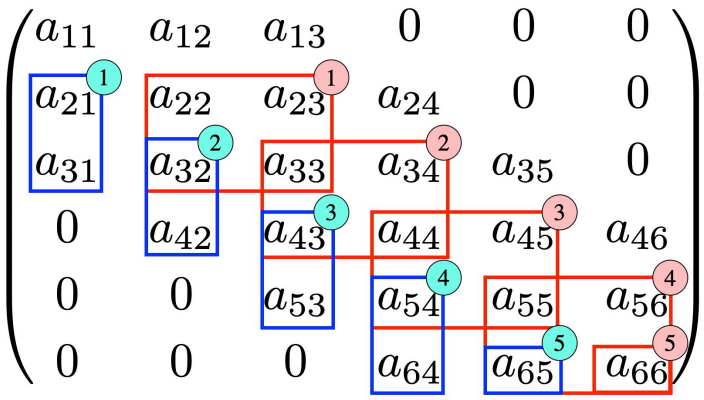

Fig. 3.10: Algorithm for the LU decomposition for a 6×6 matrix. Blue squares represent the computation of the lower triangular matrix, while red squares indicate the computation of the upper triangular matrix.

In Step 3, we find the flux-surface averaged electrostatic potential $\langle\phi\rangle_f$. By substituting $\left\langle\widetilde{\phi}\right\rangle_f = \langle\phi\rangle_f - \langle\phi\rangle_{\theta,\varphi}$ into Eq. (3.149), we obtain

$$\mathcal{D}\langle\phi\rangle_f = \frac{1}{n}\langle\rho_i\rangle_{\theta,\varphi} + \mathcal{D}\left\langle\widetilde{\phi}\right\rangle_f + \frac{\left\langle\widetilde{\phi}\right\rangle_f}{T_e}. \tag{3.158}$$

All the terms on the right-hand side of Eq. (3.158) are known. Thus, by discretizing as in Eq. (3.152) and using the LU decomposition, $\langle\phi\rangle_f$ can be determined. Finally, in Step 4, using $\left\langle\widetilde{\phi}\right\rangle_f = \langle\phi\rangle_f - \langle\phi\rangle_{\theta,\varphi}$ and $\widetilde{\phi} = \phi - \langle\phi\rangle_{\theta,\varphi}$, the electrostatic potential is determined from

$$\phi = \widetilde{\phi} + \langle\phi\rangle_f - \left\langle\widetilde{\phi}\right\rangle_f. \tag{3.159}$$

In the hybrid electron model, the gyrokinetic Poisson equation can be solved more directly compared to the adiabatic electron model since it does not contain $\langle\phi\rangle_f$. We consider hydrogen plasma with impurities ($s = z$). In this case, $n_{0e} \neq n_{0i}$. Upon Fourier transforming Eqs. (3.24), (3.26), and (3.27) and subsequently discretizing them, we obtain

$$\begin{aligned}
&\left(\frac{n_{0i}}{n_{0e}}n_{i,j} + \frac{n_{0z}}{n_{0e}}\frac{m_z}{m_i}n_{z,j}\right)\frac{\phi_{j-2} - 16\phi_{j-1} + 30\phi_j - 16\phi_{j+1} + \phi_{j+2}}{12\Delta r^2} \\
&- \frac{n_{0i}}{n_{0e}}\left[\frac{4}{3}\frac{\phi_{j+1} - \phi_{j-1}}{2\Delta r} - \frac{1}{3}\frac{\phi_{j+2} - \phi_{j-2}}{4\Delta r}\right]\left(\frac{n_{i,j}}{r_j} + \frac{4}{3}\frac{n_{i,j+1} - n_{i,j-1}}{2\Delta r} - \frac{1}{3}\frac{n_{i,j+2} - n_{i,j-2}}{4\Delta r}\right) \\
&- \frac{n_{0z}}{n_{0e}}\frac{m_z}{m_i}\left[\frac{4}{3}\frac{\phi_{j+1} - \phi_{j-1}}{2\Delta r} - \frac{1}{3}\frac{\phi_{j+2} - \phi_{j-2}}{4\Delta r}\right]\left(\frac{n_{z,j}}{r_j} + \frac{4}{3}\frac{n_{z,j+1} - n_{z,j-1}}{2\Delta r} - \frac{1}{3}\frac{n_{z,j+2} - n_{z,j-2}}{4\Delta r}\right) \\
&= \frac{n_{0i}}{n_{0e}}\rho_{i,j} + \frac{n_{0z}}{n_{0e}}\frac{e_z}{e_i}\rho_{z,j} - \rho_{e,j}
\end{aligned} \tag{3.160}$$

for $(m, n) = 0, 0$ and

$$\left(\frac{n_{0i}}{n_{0e}}n_{i,j} + \frac{n_{0z}}{n_{0e}}\frac{m_z}{m_i}n_{z,j}\right)\frac{\phi_{j-2} - 16\phi_{j-1} + 30\phi_j - 16\phi_{j+1} + \phi_{j+2}}{12\Delta r^2}$$

$$
\begin{aligned}
&-\frac{n_{0i}}{n_{0e}}\left[\frac{4}{3}\frac{\phi_{j+1}-\phi_{j-1}}{2\Delta r}-\frac{1}{3}\frac{\phi_{j+2}-\phi_{j-2}}{4\Delta r}\right]\left(\frac{n_{i,j}}{r_j}+\frac{4}{3}\frac{n_{i,j+1}-n_{i,j-1}}{2\Delta r}-\frac{1}{3}\frac{n_{i,j+2}-n_{i,j-2}}{4\Delta r}\right)\\
&-\frac{n_{0z}}{n_{0e}}\frac{m_z}{m_i}\left[\frac{4}{3}\frac{\phi_{j+1}-\phi_{j-1}}{2\Delta r}-\frac{1}{3}\frac{\phi_{j+2}-\phi_{j-2}}{4\Delta r}\right]\left(\frac{n_{z,j}}{r_j}+\frac{4}{3}\frac{n_{z,j+1}-n_{z,j-1}}{2\Delta r}-\frac{1}{3}\frac{n_{z,j+2}-n_{z,j-2}}{4\Delta r}\right)\\
&+\left(\frac{n_{0i}}{n_{0e}}n_{i,j}+\frac{n_{0z}}{n_{0e}}\frac{m_z}{m_i}n_{z,j}\right)\frac{m^2}{r_j^2}\phi_j+\frac{n_{e,j}}{T_{e,j}}\alpha_{\mathrm{pass}}\phi_j=\frac{n_{0i}}{n_{0e}}\rho_{i,j}+\frac{n_{0z}}{n_{0e}}\frac{e_z}{e_i}\rho_{z,j}-\rho_{e,\mathrm{trap},j}
\end{aligned}
\tag{3.161}
$$

for $(m,n)\neq 0,0$. At the boundary $j=1,2$, when m is even,

$$
\begin{aligned}
&\left(\frac{n_{0i}}{n_{0e}}n_{i,1}+\frac{n_{0z}}{n_{0e}}\frac{m_z}{m_i}n_{z,1}\right)\frac{14\phi_1-15\phi_2+\phi_3}{12\Delta r^2}\\
&+\frac{n_{0i}}{n_{0e}}\frac{1}{\Delta r}\left[\frac{2}{3}\phi_1-\frac{3}{4}\phi_2+\frac{1}{12}\phi_3\right]\left\{\frac{n_{i,1}}{r_1}-\frac{1}{\Delta r}\left(\frac{2}{3}n_{i,1}-\frac{3}{4}n_{i,2}+\frac{1}{12}n_{i,3}\right)\right\}\\
&+\frac{n_{0z}}{n_{0e}}\frac{m_z}{m_i}\frac{1}{\Delta r}\left[\frac{2}{3}\phi_1-\frac{3}{4}\phi_2+\frac{1}{12}\phi_3\right]\left\{\frac{n_{z,1}}{r_1}-\frac{1}{\Delta r}\left(\frac{2}{3}n_{z,1}-\frac{3}{4}n_{z,2}+\frac{1}{12}n_{z,3}\right)\right\}\\
&+\left(\frac{n_{0i}}{n_{0e}}n_{i,1}+\frac{n_{0z}}{n_{0i}}\frac{m_z}{m_i}n_{z,1}\right)\frac{m^2}{r_1^2}\phi_1+\frac{n_{e,1}}{T_{e,1}}\alpha_{\mathrm{pass}}\phi_1=\frac{n_{0i}}{n_{0e}}\rho_{i,1}+\frac{n_{0z}}{n_{0e}}\frac{e_z}{e_i}\rho_{z,1}-\rho_{e,\mathrm{trap},1}
\end{aligned}
$$

is used for $j=1$ and

$$
\begin{aligned}
&\left(\frac{n_{0i}}{n_{0e}}n_{i,2}+\frac{n_{0z}}{n_{0e}}\frac{m_z}{m_i}n_{z,2}\right)\frac{-15\phi_1+30\phi_2-16\phi_3+\phi_4}{12\Delta r^2}\\
&+\frac{n_{0i}}{n_{0e}}\frac{1}{\Delta r}\left[\frac{7}{12}\phi_1-\frac{2}{3}\phi_3+\frac{1}{12}\phi_4\right]\left\{\frac{n_{i,2}}{r_2}-\frac{1}{\Delta r}\left(\frac{7}{12}n_{i,1}-\frac{2}{3}n_{i,3}+\frac{1}{12}n_{i,4}\right)\right\}\\
&+\frac{n_{0z}}{n_{0e}}\frac{m_z}{m_i}\frac{1}{\Delta r}\left[\frac{7}{12}\phi_1-\frac{2}{3}\phi_3+\frac{1}{12}\phi_4\right]\left\{\frac{n_{z,2}}{r_2}-\frac{1}{\Delta r}\left(\frac{7}{12}n_{z,1}-\frac{2}{3}n_{z,3}+\frac{1}{12}n_{z,4}\right)\right\}\\
&+\left(\frac{n_{0i}}{n_{0e}}n_{i,2}+\frac{n_{0z}}{n_{0e}}\frac{m_z}{m_i}n_{z,2}\right)\frac{m^2}{r_2^2}\phi_2+\frac{n_{e,2}}{T_{e,2}}\alpha_{\mathrm{pass}}\phi_2=\frac{n_{0i}}{n_{0e}}\rho_{i,2}+\frac{n_{0z}}{n_{0e}}\frac{e_z}{e_i}\rho_{z,2}-\rho_{e,\mathrm{trap},2}
\end{aligned}
$$

is employed for $j=2$. On the other hand, when m is odd,

$$
\begin{aligned}
&\left(\frac{n_{0i}}{n_{0e}}n_{i,1}+\frac{n_{0z}}{n_{0e}}\frac{m_z}{m_i}n_{z,1}\right)\frac{46\phi_1-17\phi_2+\phi_3}{12\Delta r^2}\\
&+\frac{n_{0i}}{n_{0e}}\frac{1}{\Delta r}\left[-\frac{2}{3}\phi_1-\frac{7}{12}\phi_2+\frac{1}{12}\phi_3\right]\left\{\frac{n_{i,1}}{r_1}-\frac{1}{\Delta r}\left(-\frac{2}{3}n_{i,1}-\frac{7}{12}n_{i,2}+\frac{1}{12}n_{i,3}\right)\right\}\\
&+\frac{n_{0z}}{n_{0e}}\frac{m_z}{m_i}\frac{1}{\Delta r}\left[-\frac{2}{3}\phi_1-\frac{7}{12}\phi_2+\frac{1}{12}\phi_3\right]\left\{\frac{n_{z,1}}{r_1}-\frac{1}{\Delta r}\left(-\frac{2}{3}n_{z,1}-\frac{7}{12}n_{z,2}+\frac{1}{12}n_{z,3}\right)\right\}\\
&+\left(\frac{n_{0i}}{n_{0e}}n_{i,1}+\frac{n_{0z}}{n_{0i}}\frac{m_z}{m_i}n_{z,1}\right)\frac{m^2}{r_1^2}\phi_1+\frac{n_{e,1}}{T_{e,1}}\alpha_{\mathrm{pass}}\phi_1=\frac{n_{0i}}{n_{0e}}\rho_{i,1}+\frac{n_{0z}}{n_{0e}}\frac{e_z}{e_i}\rho_{z,1}-\rho_{e,\mathrm{trap},1}
\end{aligned}
$$

is used for $j=1$ and

$$
\left(\frac{n_{0i}}{n_{0e}}n_{i,2}+\frac{n_{0z}}{n_{0e}}\frac{m_z}{m_i}n_{z,2}\right)\frac{-17\phi_1+30\phi_2-16\phi_3+\phi_4}{12\Delta r^2}
$$

$$+\frac{n_{0i}}{n_{0e}}\frac{1}{\Delta r}\left[\frac{3}{4}\phi_1-\frac{2}{3}\phi_3+\frac{1}{12}\phi_4\right]\left\{\frac{n_{i,2}}{r_2}-\frac{1}{\Delta r}\left(\frac{3}{4}n_{i,1}-\frac{2}{3}n_{i,3}+\frac{1}{12}n_{i,4}\right)\right\}$$

$$+\frac{n_{0z}}{n_{0e}}\frac{m_z}{m_i}\frac{1}{\Delta r}\left[\frac{3}{4}\phi_1-\frac{2}{3}\phi_3+\frac{1}{12}\phi_4\right]\left\{\frac{n_{z,2}}{r_2}-\frac{1}{\Delta r}\left(\frac{3}{4}n_{z,1}-\frac{2}{3}n_{z,3}+\frac{1}{12}n_{z,4}\right)\right\}$$

$$+\left(\frac{n_{0i}}{n_{0e}}n_{i,2}+\frac{n_{0z}}{n_{0e}}\frac{m_z}{m_i}n_{z,2}\right)\frac{m^2}{r_2^2}\phi_2+\frac{n_{e,2}}{T_{e,2}}\alpha_{\text{pass}}\phi_2=\frac{n_{0i}}{n_{0e}}\rho_{i,2}+\frac{n_{0z}}{n_{0e}}\frac{e_z}{e_i}\rho_{z,2}-\frac{n_{0e}}{n_{0i}}\rho_{e,\text{trap},2}$$

is employed for $j=2$.

Chapter 4

Gyrokinetic entropy balances and dynamics

4.1 Entropies in nonlinear and nonequilibrium plasma

4.1.1 Thermodynamic entropy

In thermodynamics, the thermodynamic relations are described in the Pfaffian form. When a system can be described by only two state variables, it always possesses an integrating factor; however, for systems with three or more state variables, this is not necessarily the case. For a Pfaffian equation with three or more state variables, the existence of an integrating factor implies the presence of points in a certain neighborhood that cannot be reached along the solution. This signifies that within a vicinity of a thermally equilibrated state, there exist states that cannot be reached from the state through adiabatic processes [10]. This is called the Carathéodory principle. This is equivalent to the second law of thermodynamics and the principle of entropy increase. In thermodynamics, entropy is defined as heat (which is not a state variable) divided by thermodynamic temperature.

We assume that the heat δQ that transfers energy during a process, depends on n state variables $\boldsymbol{X} = (X_1, X_2, \cdots, X_n)$. δQ can be expressed as

$$\delta Q = \sum_{i=1}^{n} Y_i dX_i \tag{4.1}$$

using $\boldsymbol{Y} = (Y_1, Y_2, \cdots, Y_n)$, which a vector function of $\boldsymbol{X}$. The adiabatic condition $\delta Q = 0$ implies that the system can only reach states in directions orthogonal to $\boldsymbol{Y}$, and according to the principle of Carathéodory, there always exists states that are inaccessible. This implies that in the case where a state on the surface $Z(X_1, X_2, \cdots, X_n)$ spanned by vectors orthogonal to $\boldsymbol{Y}$ transitions to a state on the surface located dZ away, δQ is necessary. Using an integrating denominator $t(\neq 0)$ for any arbitrary $\boldsymbol{X}$,

we obtain

$$dZ = \frac{\delta Q}{t}. \tag{4.2}$$

To prove that the integrating factor is solely a function of temperature, we consider the composite system of the two systems. When the heat $\delta Q^{(1)}$ is provided to one system and the heat $\delta Q^{(2)}$ to another, the total heat $\delta Q^{(3)}$ is given by $\delta Q^{(3)} = \delta Q^{(1)} + \delta Q^{(2)}$. From Eq. (4.2), $\delta Q^{(i)} = t^{(i)} dZ^{(i)}$ $(i = 1, 2, 3)$ is satisfied. Let $t^{(i)}$ depend on the a parameter θ that is common to $\{t^{(i)}\}_{i=1,2,3}$. From

$$dZ^{(3)} = \frac{t^{(1)}}{t^{(3)}} dZ^{(1)} + \frac{t^{(2)}}{t^{(3)}} dZ^{(2)}, \tag{4.3}$$

it is evident that $Z^{(3)}$ is a function of $Z^{(1)}$ and $Z^{(2)}$. Therefore, $t^{(1)}/t^{(3)}$ and $t^{(2)}/t^{(3)}$ are independent of θ and

$$\frac{1}{t^{(1)}} \frac{\partial t^{(1)}}{\partial \theta} = \frac{1}{t^{(2)}} \frac{\partial t^{(2)}}{\partial \theta} = \frac{1}{t^{(3)}} \frac{\partial t^{(3)}}{\partial \theta} \tag{4.4}$$

is satisfied. Upon integrating the function that depends solely on θ:

$$g(\theta) \equiv \frac{\partial}{\partial \theta} \log t^{(i)}, \tag{4.5}$$

we obtain

$$t^{(i)} = T(\theta) F^{(i)} \left(Z^{(i)} \right), \tag{4.6}$$

where, θ_0 is a constant, $F^{(i)}(Z^{(i)})$ represents an integration constant, and $T(\theta)$ is defined as

$$T(\theta) \equiv \exp \left\{ \int_{\theta_0}^{\theta} g(\theta) d\theta \right\}. \tag{4.7}$$

When we consider the parameter θ as empirical temperature defined by phenomena such as the volumetric expansion of mercury, the function $T(\theta)$ depending solely on θ can also be interpreted as temperature. By definition, $T(\theta) > 0$ is trivial. Since T is defined by $g(\theta)$ common to all systems, it is independent of the properties of a system. Substituting Eq. (4.6) into Eq. (4.2), we obtain

$$F^{(i)} \left(Z^{(i)} \right) dZ^{(i)} = \frac{\delta Q^{(i)}}{T(\theta)}. \tag{4.8}$$

The right-hand side of the equation is named thermodynamic entropy,

$$dS^{(i)} \equiv \frac{\delta Q^{(i)}}{T(\theta)}. \tag{4.9}$$

From this definition, the additivity of thermodynamic entropy is evident. It is worth noting that the thermodynamic entropy is defined by the difference between states. According to the third law of thermodynamics, entropy becomes zero at absolute zero. Following this, we determine the zero point of it.

In information theory, entropy is characterized by the Shannon-Khinchin axioms. Let Δ_n be an n dimensional simplex

$$\Delta_n = \left\{ (f_1, \cdots, f_n) \in \mathbb{R} \middle| f_i \geq 0, \sum_{i=1}^{n} f_i = 1 \right\}. \tag{4.10}$$

The Shannon-Khinchin axioms are the following four requirements imposed on the function $S(f_1, \cdots, f_n)$. (I) For any $n \in \mathbb{N}$, the function S is continuous with respect to $(f_1, \cdots, f_n) \in \Delta_n$. (II) For any $n \in \mathbb{N}$, the function S attains its maximum value with $f_i = 1/n$ $(i = 1, \cdots, n)$. In other words, for any $f_1, \cdots, f_n \in \Delta_n$,

$$S(f_1, \cdots, f_n) \leq S\left(\frac{1}{n}, \cdots, \frac{1}{n}\right) \tag{4.11}$$

is satisfied. (III) The following equality holds.

$$S(f_{11}, \cdots, f_{nm_n}) = S(f_1, \cdots, f_n) + \sum_{i=1}^{n} f_i \, S\left(\frac{f_{i1}}{f_i}, \cdots, \frac{f_{im_i}}{f_i}\right), \tag{4.12}$$

where $f_{ij} \geq 0$ and $f_i = \sum_{j=1}^{m_i} f_{ij}$ $(\forall i = 1, \cdots, n, \forall j = 1, \cdots, m_i)$. (IV) For any $(f_1, \cdots, f_n) \in \Delta_n$,

$$S(f_1, \cdots, f_n, 0) = S(f_1, \cdots, f_n) \tag{4.13}$$

is satisfied. The function satisfying these conditions is uniquely determined as

$$S(f_1, \cdots, f_n) = -\lambda \sum_{i=1}^{n} f_i \log f_i, \tag{4.14}$$

where λ is a positive constant. This is referred to as the Shannon entropy. In the Γ space, let the number of microscopic states be denoted by W. Assuming that each of these states occurs with equal probability, f_i is given by $f_i = 1/W$. By choosing λ such that $\lambda = k_B$, from the equation, we obtain

$$S = k_B \log W. \tag{4.15}$$

While the statistical entropy is derived from the Shannon entropy, the converse is, of course, also possible. We assume a discrete probability distribution f_i follows the Boltzmann distribution at energy E_i. By using the partition function Z, f_i can be represented as $f_i = e^{-\beta E_i}/Z$. Therefore, from

$$\overline{E} = \sum_i f_i E_i = -\frac{f_i}{\beta}(\log f_i + \log Z) \tag{4.16}$$

and the Helmholtz free energy

$$F = -\frac{1}{\beta} \log Z, \tag{4.17}$$

$$
\begin{aligned}
S &= \frac{\overline{E} - F}{T} \\
&= \frac{1}{T\beta} \left\{ \sum_i f_i (\log f_i + \log Z) + \log Z \right\} \\
&= -k_B \sum_i f_i \log f_i
\end{aligned}
$$

is derived.

The fluid definition of entropy density is [190]

$$
s = n \log \left(\frac{T^{3/2}}{n} \right). \tag{4.18}
$$

The corresponding entropy flux is given as $\boldsymbol{J}_s = s\boldsymbol{V} + \boldsymbol{Q}/T$ where $\boldsymbol{Q}$ is the heat flux. From Eq. (1.72) and the energy equation

$$
\frac{3}{2}\frac{dp}{dt} + \frac{5}{2} p \nabla \cdot \boldsymbol{V} + \boldsymbol{\pi} : \nabla \boldsymbol{V} + \nabla \cdot \boldsymbol{Q} = 0, \tag{4.19}
$$

we obtain the time evolution equation for the entropy density in the fluid model [190],

$$
\frac{\partial s}{\partial t} + \nabla \cdot \boldsymbol{J}_s = \sigma, \tag{4.20}
$$

where π and

$$
\sigma \equiv -\frac{\boldsymbol{\pi} : \nabla \boldsymbol{V}}{T} - \frac{\boldsymbol{Q} \cdot \nabla T}{T^2} \tag{4.21}
$$

are the viscosity tensor and entropy generation rate, respectively. A more refined entropy density equation was derived by Gürcan and colleagues [134]. They first derived the time evolution equation for the two-point correlation function $\langle \delta f_1 \delta f_2 \rangle = \langle \delta f(x_1, v_1) \delta f(x_2, v_2) \rangle$ from the drift kinetic equation. By taking moments of the equation, they derived the Guyer-Krumhansl constitutive relation

$$
\tau \frac{\partial Q}{\partial t} + \tau \frac{\partial}{\partial r} \Gamma_Q + \chi \frac{\partial T}{\partial r} + Q = 0, \tag{4.22}
$$

where $\Gamma_Q \equiv -(\lambda^2/\tau)(\partial Q/\partial r)$ is the flux of heat flux, χ is the heat diffusivity, τ is the mean response time of the heat flux to the changes in temperature gradient、λ is the flux penetration length which represents the cross-correlation length between the flux and the gradient. These parameters are nonlinear functions of the turbulence intensity. In the limit $\lambda \to 0$, Eq. (4.22) converges to the Maxwell-Cattaneo relation

$$
\tau \frac{\partial Q}{\partial t} + \chi \frac{\partial T}{\partial r} + Q = 0. \tag{4.23}
$$

Furthermore, in the limit $\tau \to 0$, the equation reduces to Fourier's law

$$
Q = -\chi \frac{\partial T}{\partial r}. \tag{4.24}
$$

Fourier's law Eq. (4.24) means that the heat flux responds instantaneously and locally to changes in the temperature gradient. On the other hand, the Guyer-Krumhansl relation indicates that the heat flux responds non-locally to changes in the temperature gradient with the response time τ. The solution of Eq. (4.22) is

$$Q(r,t) = -\iint \chi \mathcal{K}(t,t',r,r') \frac{\partial T(t',r')}{\partial r'} dr' dt', \tag{4.25}$$

where

$$\mathcal{K}(t,t',r,r') = \frac{\sqrt{\tau}}{2\lambda\sqrt{\pi(t-t')}} \exp\left\{ -\frac{\tau(r-r')^2}{4\lambda^2(t-t')} - \frac{1}{\tau}(t-t') \right\} \quad (t > t'). \tag{4.26}$$

These describe the global nature of the heat flux. From Eq.(4.22), the heat transport equation

$$\frac{\partial T}{\partial r} + \frac{\partial Q}{\partial r} = 0, \tag{4.27}$$

and the extended Sackur-Tetrode equation

$$\frac{\partial s}{\partial t} = \frac{\partial}{\partial t} \log T - \frac{\tau Q}{\chi T^2} \frac{\partial Q}{\partial t}, \tag{4.28}$$

we obtain [134]

$$\frac{\partial s}{\partial t} + \frac{\partial J_s}{\partial r} = \frac{Q^2}{\chi T^2} - \Gamma_Q \frac{\partial}{\partial r} \left(\frac{\tau Q}{\chi T^2} \right), \tag{4.29}$$

where the entropy flux J_s is given by $J_s = Q/T - (\tau Q/\chi T^2)\Gamma_Q$.

In an adiabatically isolated system, the entropy flux at the boundary is zero. Hence, from Eqs. (4.20) and (4.29), the entropy production rate is zero in a steady state. On the other hand, in a open system which a steady heat flux flows into and out of from the outside, the entropy production rate does not become zero even when the time variation of entropy is zero. In this paper, such a state is referred to as a quasi-steady state.

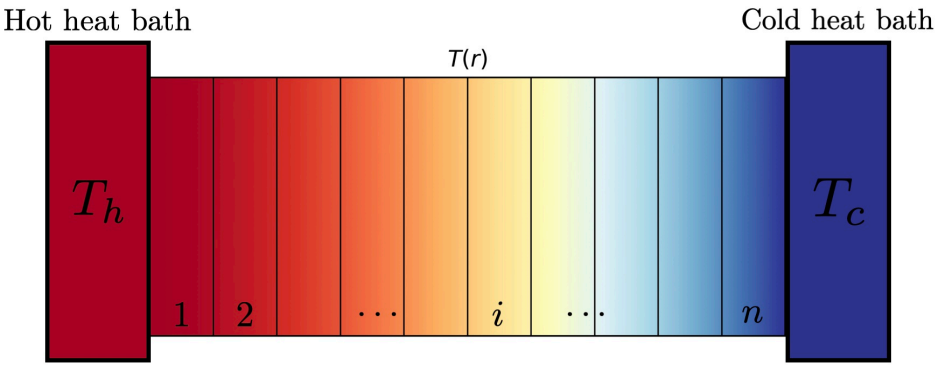

Fig. 4.1: Simple model of temperature profile in quasi-steady state for magnetically confined plasma.

We calculate the entropy production rate in the simple composite system shown in Fig. 4.1 under a quasi-steady state. T_h and T_c represent the temperature at the magnetic axis and at the edge, respectively. The plasma is divided into n subsystems, with the temperature of the hotter side of the subsystem i ($1 \leq i \leq n$) denoted by T_{i-1} and that of the cooler side denoted by T_i. $T_0 = T_h$ and $T_n = T_c$ are established. In a quasi-steady state, the entropy of the subsystems remain unchanged. The entropy generation of the subsystem is given by

$$\frac{Q}{T_{i-1}} - \frac{Q}{T_i} = \sigma_i, \quad (1 \leq i \leq n). \tag{4.30}$$

Summing over all subsystems in the equation, we obtain

$$\sum_{i=1}^{n} \sigma_i = \frac{Q}{T_c} - \frac{Q}{T_h}. \tag{4.31}$$

$\sum_{i=1}^{n} \sigma_i$ balances the negative entropy production rate $(1/T_h - 1/T_c)Q$ at the boundaries, and the net entropy production rate for the sum of the subsystems is zero. The entropy production rate of the composite system is given by [136]

$$\dot{s}_{\text{whole}} = \dot{s}_h + \sum_i \dot{s} + \dot{s}_c = Q\frac{T_h - T_c}{T_h T_c} \geq 0, \tag{4.32}$$

where $\dot{s}_h$ and $\dot{s}_c$ represent the entropy production rates of the high-temperature and low-temperature heat baths, respectively. The entropy production rate of the composite system is always larger than zero. The entropy production rate is proportional to the temperature gradient, which is enhanced by the generation of zonal flows. The ordered structures of zonal flows leads to an increase in entropy, representing the degree of disorder. That appears counterintuitive at first glance. To address the problem, the concept of scale separation was proposed [137], suggesting that the formation of macroscopic structures does not influence the entropy generation at microscopic scale. We address this issue through the analysis based on the gyrokinetic theory. In systems far from thermodynamic equilibrium, based on the principle of maximum entropy production which posits that entropy production is maximized to most efficiently alleviate non-equilibrium states [138, 139, 140], at the microscopic scale the most disordered state is realized, while at the macroscopic scale an ordered flow with maximum energy emerges.

4.1.2 Fluctuation entropy

In turbulence transport studies based on the gyrokinetic theory, the fluctuation entropy

$$\delta S = \int \frac{\delta f^2}{2f_0} d^5\boldsymbol{Z} \tag{4.33}$$

is employed. The distribution function f is normalized. From the gyrokinetic Vlasov equation, the gyrokinetic Poisson equation, and suitable approximations, the evolution equation for the fluctuation entropy is derived as [141, 142]

$$\frac{\partial \delta S}{\partial t} = \Gamma - D, \tag{4.34}$$

where Γ and D represent the entropy generation due to heat flux and dissipation, respectively. This equation establishes a direct relationship between transport and dissipation. Due to the high temperatures in fusion plasmas, the collision frequency is exceedingly low. Consequently, the limit where the collision frequency approaches zero might serve as a good approximation. However, from Eq. (4.34), when $D = 0$, we obtain $\partial \delta S/\partial t = \Gamma$. This implies that, even if the electrostatic potential is saturated, the entropy continue to increase indefinitely with time, never reaching saturation. This is referred to as the entropy paradox [143] and was confirmed by Eulerian gyrokinetic simulations of collisionless slab ITG turbulence [144]. The fluctuation entropy δS increases due to the formation of fine-scale structures in the distribution function from phase mixing. The ballistic mode [145] is a kinematic effect observed not only in plasmas but also in neutral gases. We show that the initial density fluctuation decay with time due to phase mixing [22]. For simplicity, let us consider a distribution function $g(x, v, t)$ that satisfies the advection equation

$$\frac{\partial g}{\partial t} + v\frac{\partial g}{\partial x} = \delta(t) g_0. \tag{4.35}$$

The function g_0 represents the initial distribution and is given by

$$g_0(x, v) = \frac{(n_0 + \tilde{n})}{\sqrt{2\pi v_T^2}} e^{-v^2/(2v_T^2)} = \frac{n_0}{\sqrt{2\pi v_T^2}} e^{-v^2/(2v_T^2)} + \tilde{n}(0). \tag{4.36}$$

The solution to Eq. (4.35) is

$$g(x, v, t) = \frac{1}{\sqrt{2\pi v_T^2}} \Big(n_0 + \tilde{n}\, e^{ik(x - vt)} \Big) e^{-v^2/(2v_T^2)}. \tag{4.37}$$

Equation (4.37) indicates that the wavenumber $k_v = kt$ in the velocity space increases with time. From Eq. (4.37), the density fluctuation is given by

$$\tilde{n}(t) = \tilde{n}(0)\, e^{-k^2 v_T^2 t^2/2}, \tag{4.38}$$

which signifies that the initial density fluctuation decays with time.

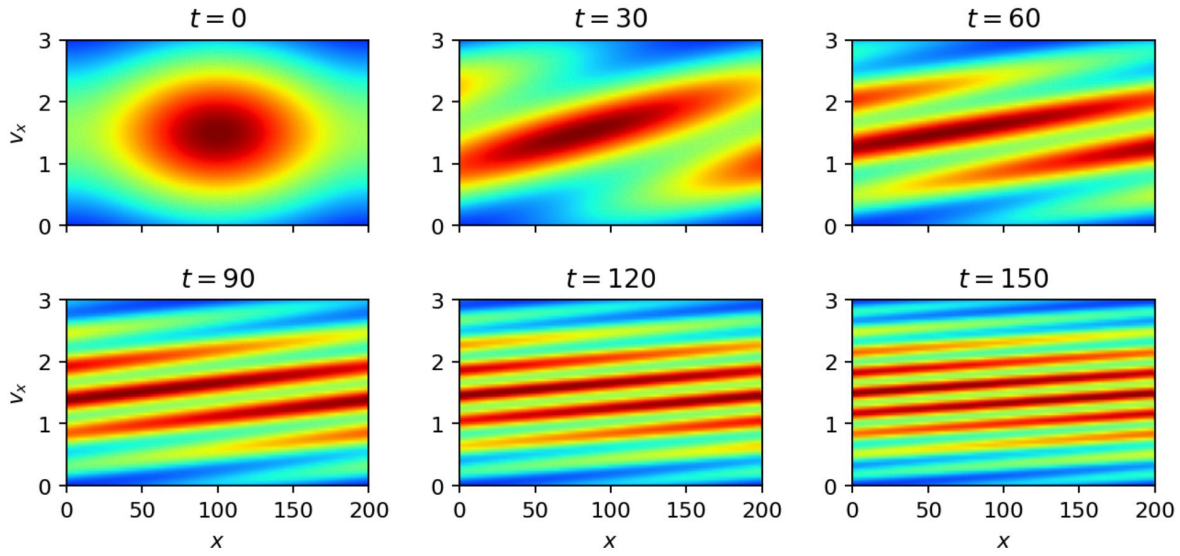

Fig. 4.2: Temporal evolution of the distribution function satisfying Eq. (4.39).

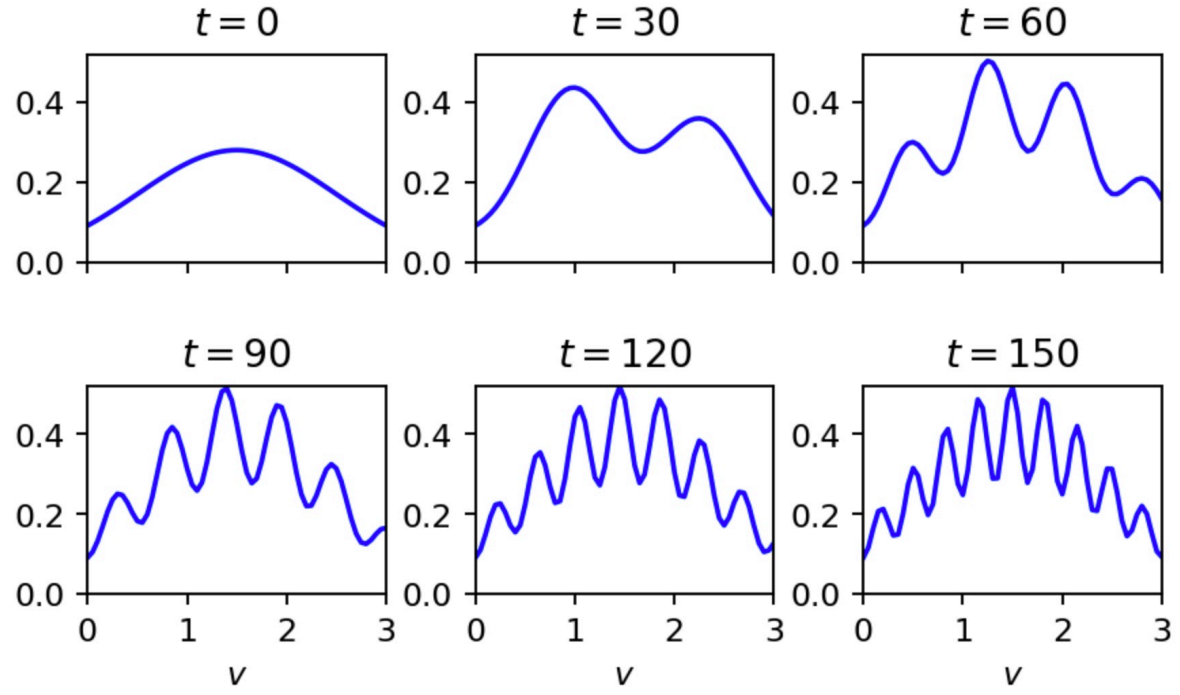

Fig. 4.3: Plot of the cross-section at $x = 0$ in Fig. 4.2.

Figures 4.2 and 4.3 illustrate the formation of fine-scale structures in the distribution function due to phase mixing. These figures are obtained by numerically solving the advection equation

$$\frac{\partial h(x,v,t)}{\partial t} + 4v\frac{\partial h(x,v,t)}{\partial x} = 0, \tag{4.39}$$

describing the evolution of a distribution function $h(x,v,t)$, with a given initial distribution

$$h(x,v,0) = \frac{1}{\sqrt{2\pi}} e^{-(v-1.5)^2/2} \left\{ 1 + 0.3\cos\left(\frac{2\pi(x-100)}{100} \right) \right\}. \tag{4.40}$$

The numerical scheme employed is the CIP-CSL2 scheme [146, 147]. As time progresses, the structures become more refined, and when k_v becomes equal to the wavenumber corresponding to the grid width, the distribution function reverts to the initial one. The fluctuation entropy can be interpreted as one of the f-divergences, specifically the Pearson divergence [148]. Due to the formation of fine-scale structures, the distance from the reference distribution f_0 increases, leading to an increase in δS.

The ballistic mode can also be interpreted as entropy transfer in the Hermite space. The equation describing entropy transfer is derived from the normalized gyrokinetic Vlasov equation for the slab model,

$$\frac{\partial}{\partial t}\delta f_k + i\Theta v_\parallel k_y \delta f_k - \sum_{k'+k''=k} \boldsymbol{b}\cdot(\boldsymbol{k}'\times\boldsymbol{k}'')\psi_{k'}\delta f_{k''} = -ik_y\psi_k\left[1+(v_\parallel^2-1-k_\perp^2)\frac{\eta}{2}+\Theta v_\parallel\right]f_0 + C_{\mathrm{coll}}(\delta f_k), \tag{4.41}$$

where $\psi_k \equiv \phi_k \exp(k_\perp^2\rho^2/2)$ and Θ represents the angle formed between the magnetic field and e_z. We multiply both sides of Eq. (4.41) by $\delta f_k^*/f_0$ and integrate them, and then the real parts are taken. δf_k can be expressed as

$$\delta f_k(v_\parallel) = \sum_{n=0}^{\infty} \widehat{\delta f}_{k,n} H_n(v_\parallel) f_0(v_\parallel), \tag{4.42}$$

where $H_n(v_\parallel)$ is the n-th order Hermite polynomial and is defined as

$$H_n(v_\parallel) = (-1)^n e^{v_\parallel^2/2}\frac{d^n}{dv_\parallel^n}e^{-v_\parallel^2/2}. \tag{4.43}$$

Due to the orthogonality of the Hermite polynomials

$$\int H_m(v_\parallel)H_n(v_\parallel)e^{-v_\parallel^2/2}dv_\parallel = n!\sqrt{2\pi}\delta_{m,n}, \tag{4.44}$$

the first term on the left-hand side of Eq. (4.41) becomes

$$\sum_k \int dv_\parallel \frac{|\delta f_k|^2}{2f_0} = \sum_k\sum_n \frac{1}{2}n!\left|\widehat{\delta f}_{k,n}\right|^2. \tag{4.45}$$

This equation indicates that the fluctuation entropy can be expressed as an infinite series of velocity moments. From equation

$$\int H_n(v_\parallel)H_m(v_\parallel)v_\parallel e^{-v_\parallel^2/2}dv_\parallel = n!\sqrt{2\pi}\delta_{n-1,m} + (n+1)!\sqrt{2\pi}\delta_{n+1,m}, \tag{4.46}$$

the second term on the left-hand side of Eq. (4.41) is

$$\int \sum_k i\Theta v_\parallel k_y \frac{|\delta f_k|^2}{f_0}dv_\parallel = \int \sum_k\sum_n\sum_m i\Theta k_y v_\parallel \widehat{\delta f}_{k,n}\widehat{\delta f}_{-k,n}H_n(v_\parallel)H_m(v_\parallel)\frac{1}{\sqrt{2\pi}}e^{-v_\parallel^2/2}dv_\parallel$$

$$= \sum_k \sum_m \sum_n i\Theta k_y \widehat{\delta f}_{k,n} \widehat{\delta f}_{-k,n} \left\{ n!\delta_{n-1,m} + (n+1)!\delta_{n+1,m} \right\}$$
$$= -\sum_k \sum_n i\Theta k_y \left\{ n!\widehat{\delta f}_{k,n-1} \widehat{\delta f}^*_{k,n} + (n+1)!\widehat{\delta f}_{k,n} \widehat{\delta f}^*_{k,n+1} \right\}. \tag{4.47}$$

The first term on the right-hand side of Eq. (4.47) represents transfer from the $n-1$th order to the nth order, while the second term signifies transfer from the nth order to the $n-1$th order. The Lenard-Bernstein model [149]

$$C_{\rm coll}(\delta f_k) = \nu \frac{\partial}{\partial v_\parallel} \left(v_\parallel + \frac{\partial}{\partial v_\parallel} \right) \delta f_k = \frac{\nu}{\sqrt{2\pi}} \widehat{\delta f}_{k,n} e^{-v_\parallel^2/2} \left(\frac{\partial^2 H_n}{\partial v_\parallel^2} + v_\parallel \frac{\partial H_n}{\partial v_\parallel} \right) \tag{4.48}$$

is used here as the collision model. From $\partial H_n/\partial v_\parallel = v_\parallel H_n - H_{n+1}$, the collision term in the equation becomes

$$-\sum_k \sum_n \sum_m \int \frac{n\nu}{\sqrt{2\pi}} \widehat{\delta f}_{k,n} \widehat{\delta f}^*_{k,m} H_n H_m e^{-v_\parallel^2/2} dv_\parallel = \sum_k \sum_n -n\nu n! \left| \widehat{\delta f}_{k,n} \right|^2. \tag{4.49}$$

In summary, we obtain [150]

$$\frac{d}{dt} \left[\delta S_n + \delta_{n,0} \sum_k |\delta\phi_k|^2 \left\{ 2 - \Gamma_0(k_\perp^2) \right\} \right] = J_{n-1/2} - J_{n+1/2} + \delta_{n,2}\eta Q - 2\nu n \delta S_n, \tag{4.50}$$

where

$$\delta S_n = \sum_k \frac{1}{2} n! \left| \widehat{\delta f}_{k,n} \right|^2, \tag{4.51}$$

$$J_{n-1/2} = \sum_k \Theta k_y n! \, {\rm Im} \left(\widehat{\delta f}_{k,n-1} \widehat{\delta f}^*_{k,n} \right), \tag{4.52}$$

and

$$J_{n+1/2} = \sum_k \Theta k_y (n+1)! \, {\rm Im} \left(\widehat{\delta f}_{k,n} \widehat{\delta f}^*_{k,n+1} \right). \tag{4.53}$$

Entropy is transferred to higher order δS_n by the transfer functions $J_{n-1/2}$ and $J_{n+1/2}$. This is consistent with the decay of the initial density fluctuation shown in Eq. (4.38). It is noteworthy that the dissipation term $-2\nu n \delta S_n$ is proportional to n. No matter how small the collision frequency is, when n increases due to the ballistic mode, the dissipation effect becomes non-negligible. The entropy paradox is due to the fact that the collision frequency is zero. It was reported that the entropy paradox is resolved and a quasi-steady state is achieved when the collision frequency is not zero in the Eulerian gyrokinetic simulations for the slab ITG mode turbulence [150]. In this case, Eq. (4.34) shows that $\Gamma = D$ is satisfied. The relationship implies that the entropy production due to the heat flux Γ is determined by a different mechanism from the entropy production due to the collision D, and D is determined such that $\Gamma = D$. If

the causal relationship were reversed, no entropy would be generated by the heat flux in the collisionless case, which is clearly erroneous [143]. The fluctuation entropy is used as an important benchmark for steady state [19]. In studies using the flux-tube Eulerian code GYRO [151], the flux-tube Eulerian code GKV [152], and the global PIC code ORB5 [153], the entropy balance equation was calculated, confirming that a quasi-steady state is achieved. On the other hand, from the drift kinetic equation and adiabatic electron approximation, under the assumption that the initial distribution function is the Maxwellian, Kosuga *et al.* derived the time evolution equation for the fluctuation entropy [154]

$$\frac{\partial \delta S}{\partial t} = \int d^3\boldsymbol{z} \Bigg[\Big\{ \frac{n}{TL_T} Q - \frac{n}{v_T^2} \langle \tilde{V}_r \tilde{V}_\perp \rangle \frac{\partial}{\partial r} \langle V_\perp \rangle - \frac{n}{v_T^2} \langle \tilde{V}_r \tilde{V}_\parallel \rangle \frac{\partial}{\partial r} \langle V_\parallel \rangle + \frac{1}{T} \langle \tilde{J}_\parallel \tilde{E}_\parallel \rangle \Big\} + \int d^3\boldsymbol{v} \frac{\langle \delta f C_{\mathrm{coll}}(\delta f) \rangle}{\langle f \rangle} \Bigg], \tag{4.54}$$

where $\langle \tilde{V}_r \tilde{\boldsymbol{V}} \rangle \equiv n^{-1} \int d^3\boldsymbol{v} \left(\boldsymbol{v} - \langle \boldsymbol{V} \rangle \right) \langle \tilde{V}_r \delta f \rangle$ and $\langle \tilde{J}_\parallel \tilde{E}_\parallel \rangle \equiv e \int d^3\boldsymbol{v} \left(v_\parallel - \langle V_\parallel \rangle \right) (\delta \tilde{E}_\parallel)$. From Eq. (4.54), the lowest order entropy production rate

$$\sigma^{(0)} = n\chi L_T^{-2} - \frac{n\gamma_{ZF}}{(q_r v_T)^2} \left(\frac{\partial}{\partial r} \langle V_E \rangle \right)^2 \tag{4.55}$$

and the first order entropy production rate

$$\sigma^{(1)} = \frac{n\chi_\varphi}{v_T^2} \left(\frac{\partial}{\partial r} \langle V_\parallel \rangle \right)^2 - \frac{n\Pi_{r\parallel}^2}{v_T^2 \chi_\varphi} \tag{4.56}$$

in the case of ITG turbulence are obtained. γ_{ZF} χ_φ, and $\Pi_{r\parallel}$ are the linear growth rate of zonal flow, momentum diffusion coefficient, and residual stress, respectively. The first term on the right-hand side of Eq. (4.55) is the entropy production rate due to profile relaxation, which is always positive, and the second term is the entropy destruction rate due to zonal flow generation, which is always negative. The first term on the right-hand side of Eq. (4.56) is the entropy production rate due to viscous heating, which is always positive, and the second term is the entropy destruction rate due to intrinsic toroidal rotation generation, which is always negative. These equations suggest that even in the case of no collisions $D = 0$, $\partial \delta S / \partial t = 0$ is satisfied if $\sigma^{(0)} = \sigma^{(1)} = 0$ due to the generation of zonal flows and intrinsic toroidal rotation.

Fluctuation entropy transfer is frequently used as a method to investigate nonlinear interactions in plasma turbulence. This is because the fluctuation entropy is conserved even in systems where energy is not conserved, allowing us to investigate the entropy transfer between modes from the three-wave interaction term.

From entropy transfer analysis, it was observed that in the case of the ITG turbulence, radial low wavenumber components are transferred to high wavenumber components via zonal flows, resulting in reduced heat transport [155]. Conversely, for the

ETG turbulence, the rate of zonal flow generation is lower, thus diminishing the effect. For the ITG turbulence in LHD, when the magnetic axis is shifted inward compared to the standard configuration, the transfer from low wavenumber components to high wavenumber components is enhanced, leading to turbulence suppression and an improved confinement performance [156]. It was elucidated that zonal flows driven by the TEM turbulence meditate the entropy transfer of the ETG modes from low to high radial wavenumber regions [157], and the turbulence at electron scale reduces the entropy transfer from turbulent modes to zonal modes [158].

It is noted that besides the linear phase mixing, there exists nonlinear phase mixing that at spatial scales smaller than the Larmor radius, drives the structure formation of $f(v_\perp)$ more rapidly than parallel phase mixing drives $f(v_\parallel)$. In the inertial range in electrostatic turbulence, $k_\perp^{-10/3}$ scaling was theoretically predicted [159]. This prediction was corroborated by simulations using AstroGK [160] and observed experimentally using MPX (magnetized plasma experiment) device which is a mirror linear plasma device [161].

4.2 Gyrokinetic entropy balances

4.2.1 Simulation settings

The relationship between the thermodynamic entropy and the fluctuation entropy remains unclear to this day. Furthermore, a thermodynamic entropy equation corresponding to the balance equation for the fluctuation entropy Eq. (4.34) has not yet been derived. Full-f gyrokinetic simulations are essential for research on these issues. This is because, in the local flux-tube model that fixes the background temperature gradient, it is not possible to evaluate the thermodynamic entropy associated with profile relaxation. It is anticipated that the results concerning entropy production at constant heat flux, discussed in the previous section, are reproduced in simulations using the fixed-flux model. In full-f gyrokinetic simulations, poloidal flows include not only zonal flow but also mean radial electric field. Therefore, we can accurately evaluate the correlation between poloidal flows and entropy production. There are two conflicting research findings regarding this correlation. One suggests that poloidal flow leads to a larger temperature gradient, resulting in increased entropy production [137]. The other posits that entropy decreases due to the ordered structure introduced by the poloidal flow. We aim to elucidate which of these findings is true [154].

We perform flux-driven full-f gyrokinetic simulations. Due to the necessity of longe time computation until the background profile reaches equilibrium, we employ the adiabatic electron model to reduce computational costs. We use the Maxwellian as the initial distribution function. The Maxwellian maximizes entropy under the

condition that the Hamiltonian is constant. This is referred to as the maximum entropy principle and can be readily proven by solving the constrained maximization problem using Lagrange multipliers [142].

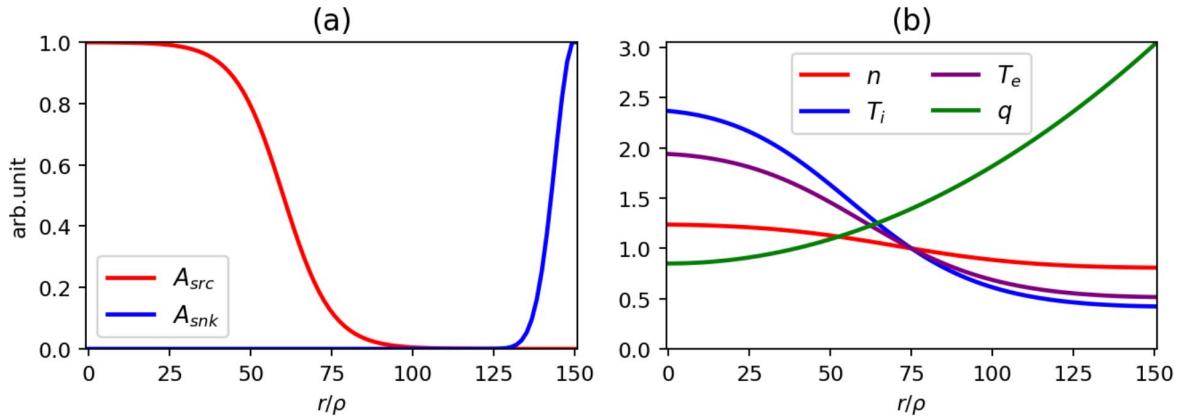

Fig. 4.4: (a) Radial profile for source term and sink term. (b) Radial profile for density, ion temperature, electron temperature, and safety factor at initial time.

Fig. 4.4(a) shows the radial profile of energy source and sink. These are given by

$$A_{\mathrm{src}}(r) = \frac{1}{2}\left[1 + \tanh\left(-\frac{x - 0.4a_0}{0.1a_0}\right)\right] \tag{4.57}$$

and

$$A_{\mathrm{snk}}(r) = \exp\left\{-\frac{(x - a_0)^2}{0.5a_0}\right\}. \tag{4.58}$$

The timescale for the energy source is $\tau_{\mathrm{src}}^{-1} = 0.01$, which means that the input power is 2 MW. The time scale parameter of the energy sink is determined to satisfy the energy balance, $\tau_{\mathrm{snk}}^{-1} = 0.1$. Figure 4.4(b) represents the radial profiles of density, ion temperature, electron temperature, and safety factor at initial time, given respectively by

$$n(r) = \exp\left\{-\frac{\mathcal{T}}{L_n}\tanh\left(\frac{x - 0.5a_0}{\mathcal{T}}\right)\right\}, \tag{4.59}$$

$$T_s(r) = \exp\left\{-\frac{\mathcal{T}}{L_{Ts}}\tanh\left(\frac{x - 0.5a_0}{\mathcal{T}}\right)\right\}, \tag{4.60}$$

and

$$q(r) = q_a\left(\frac{x}{a_0}\right)^2 + q_b, \tag{4.61}$$

where

$$\mathcal{T} \equiv \Delta r \exp\left\{-\left(\frac{x - 0.5a_0}{2a_0}\right)^2\right\}, \tag{4.62}$$

$\Delta r = 0.3a_0$, $q_a = 2.18$, and $q_b = 0.85$. At $r_s = 0.5a_0$, $R/L_n = 2.22$, $R/L_{Ti} = 9$, $R/L_{Te} = 6.92$, $q \simeq 1.4$, $\hat{s} \simeq 0.78$. Except for the ion temperature profile, they do not change with time. Simulations are performed using the minor radius $a_0 = 150\rho_i$ and the inverse aspect ratio $a_0/R_0 = 0.36$. The gyrokinetic equations are computed in a 1/4 wedge torus by taking velocity spaces $v_\parallel = -5v_{Ti} \sim 5v_{Ti}$ and $v_\perp = -5v_{Ti} \sim 5v_{Ti}$ on grids $(N_r, N_\theta, N_\varphi, N_{v_\parallel}, N_\mu) = (96, 192, 48, 96, 16)$.

4.2.2 Entropy density equations

By expanding the entropy density $s^{(\mathrm{all})} = -f_i \log f_i$, we can obtain both the first-order entropy density $s^{(1)} \equiv -\delta f_i(1 + \log f_{0i})$ and the second-order entropy density $s^{(2)} \equiv -\delta f_i^2/(2f_{0i})$ [162]. The gyrocenter phase-space integral of the second-order entropy density is equal to opposite sign of the fluctuation entropy δS given by Eq. (4.33). In other words, the second-order entropy represents the discrepancy between the reference distribution f_0 and the distribution function f. The second-order entropy can also be interpreted as a kinetic extension of turbulent energy. The equation for the second-order entropy and the equation for zonal flow shear have the same structure as a predator-prey model [154]. The fluctuation entropy plays the same role of turbulent intensity. On the other hand, the first-order entropy is linked to the thermodynamic entropy. Integrating the first-order entropy density over velocity space yields

$$S^{(1)} \equiv \iint s^{(1)} \mathcal{J} dv_\parallel d\mu = \frac{3}{2}\frac{\delta P_i}{T_i} - \delta n_i \left(1 + \frac{1}{2}\log\frac{n_i^2}{2\pi T_i^3}\right), \tag{4.63}$$

where ion pressure fluctuation δP_i and ion density fluctuation δn_i are defined as

$$\delta P_i = \frac{1}{3}\iint \delta f_i \, (v_\parallel^2 + 2\mu B)\mathcal{J} dv_\parallel d\mu, \quad \text{and} \quad \delta n_i = \iint \delta f_i \mathcal{J} dv_\parallel d\mu, \tag{4.64}$$

respectively. In the adiabatic electron model, since $\delta n_i \simeq 0$, it follows that $S^{(1)} \simeq 3\delta P_i/(2T_i)$. This means that the first-order entropy represents the entropy change due to profile relaxation.

The time evolution equations for the entropy density $s^{(\mathrm{all})}$, first-order entropy density $s^{(1)}$, and second-order entropy density $s^{(2)}$ can be derived by multiplying the ion gyrokinetic Vlasov equation

$$\frac{\partial f_i}{\partial t} + v^i \frac{\partial f_i}{\partial z^i} = S_{\mathrm{snk}} + S_{\mathrm{src}} + C_{\mathrm{coll}} \tag{4.65}$$

by $\Upsilon^{(\mathrm{all})} \equiv -\mathcal{J}(1+\log f_i)$, $\Upsilon^{(1)} \equiv -\mathcal{J}(1+\log f_{0i})$, and $\Upsilon^{(2)} \equiv -\mathcal{J}\delta f_i/f_{0i}$, respectively. Here, $\boldsymbol{z} = (\boldsymbol{R}, v_\parallel)$ and $\boldsymbol{v} = (\{\boldsymbol{R}, H\}, \{v_\parallel, H\})$. The entropy density equation is

$$\mathcal{J}\frac{\partial s^{(\mathrm{all})}}{\partial t} = -\frac{\partial}{\partial z^i}\left(\mathcal{J} v^i s^{(\mathrm{all})}\right) + S_{\mathrm{snk}}^{(\mathrm{all})} + S_{\mathrm{src}}^{(\mathrm{all})} + C_{\mathrm{coll}}^{(\mathrm{all})}. \tag{4.66}$$

Equation (**??**) represents the continuity equation for the entropy density. When the right-hand side of Eq. (4.65) is zero, the entropy is conserved. The first-order entropy density equation and the second-order entropy density equation are

$$\mathcal{J}\frac{\partial s^{(1)}}{\partial t} = -\frac{\partial}{\partial z^i}\left(\mathcal{J}v^i s^{(1)}\right) + (1+\log f_{0i})\mathcal{J}v^i\frac{\partial f_{0i}}{\partial z^i} + \alpha + S^{(1)}_{\rm snk} + S^{(1)}_{\rm src} + C^{(1)}_{\rm coll} \tag{4.67}$$

and

$$\mathcal{J}\frac{\partial s^{(2)}}{\partial t} = -\frac{\partial}{\partial z^i}\left(\mathcal{J}v^i s^{(2)}\right) + \frac{1}{2}\mathcal{J}v^i\left(\frac{\delta f_i}{f_{0i}}\right)^2\frac{\partial f_{0i}}{\partial z^i} - \alpha + S^{(2)}_{\rm snk} + S^{(2)}_{\rm src} + C^{(2)}_{\rm coll}, \tag{4.68}$$

respectively, where $\psi^{(s)} \equiv \psi\Upsilon^{(s)}$ ($\psi = S_{\rm snk}$, $S_{\rm src}$, $C_{\rm coll}$, $s =$ all, 1, 2) and α is defined as

$$\alpha \equiv -\delta f_i \mathcal{J}v^i\frac{\partial}{\partial z^i}\left(\log f_{0i}\right). \tag{4.69}$$

C is included in both Eqs. (4.67) and (4.68) and represents the interaction between the first- and second-order entropy. In this study, this term is referred to as the interaction term between the first- and second- order entropy, or simply the interaction term. As can be seen from the presence of the interaction term, the mth-order entropy density equation also contains terms other than mth-order, exhibiting a hierarchical structure reminiscent of the BBGKY hierarchy. This arises from the fact that the distribution function f_i encompasses both the transport scale f_{0i} and the fluctuation scale δf_i. It is worth noting that Eqs. (4.67) and (4.68) are obtained without approximation. The second term on the right-hand side of Eq. (4.68) represents the interaction term between the second-order entropy density and the third-order entropy density $(1/6)(\delta f_i^3/f_{0i}^2)$. In general, mth-order entropy can be defined as

$$s^{(m)} = \begin{cases} -f_{0i}\log f_{0i} & (\text{for } m=0) \\ -\delta f_i(1+\log f_{0i}) & (\text{for } m=1) \\ \left(\dfrac{1}{m}-\dfrac{1}{m-1}\right)\zeta^m f_{0i} & (\text{for even } m \text{ and } m\geq 2) \\ \left(\dfrac{1}{m-1}-\dfrac{1}{m}\right)\zeta^m f_{0i} & (\text{for odd } m \text{ and } m\geq 3) \end{cases}, \tag{4.70}$$

where $\zeta \equiv \delta f_i/f_{0i}$. By multiplying Eq. (4.65) by

$$\Upsilon^{(m)} = \begin{cases} -\mathcal{J}(1+\log f_{0i}) & (\text{for } m=0,1) \\ -\mathcal{J}\dfrac{1}{m-1}\zeta^{m-1} & (\text{for even } m \text{ and } m\geq 2) \\ \mathcal{J}\dfrac{1}{m-1}\zeta^{m-1} & (\text{for odd } m \text{ and } m\geq 3) \end{cases}, \tag{4.71}$$

we obtain the mth-order entropy density equation

$$\text{for } m=0: \quad \mathcal{J}\frac{ds^{(0)}}{dt} = S^{(0)}_{\text{src}} + S^{(0)}_{\text{snk}} + C^{(0)}_{\text{coll}}, \tag{4.72}$$

$$\text{for } m=1: \quad \mathcal{J}\frac{ds^{(0)}}{dt} + \mathcal{J}\frac{ds^{(1)}}{dt} + \mathcal{J}\zeta\frac{df_{0i}}{dt} = S^{(1)}_{\text{src}} + S^{(1)}_{\text{snk}} + C^{(1)}_{\text{coll}}, \tag{4.73}$$

$$\text{for even } m \text{ and } m \geq 2: \quad \mathcal{J}\frac{ds^{(m)}}{dt} - \mathcal{J}\left(\frac{1}{m-1}\zeta^{m-1} + \frac{1}{m}\zeta^{m}\right)\frac{df_{0i}}{dt} = S^{(m)}_{\text{src}} + S^{(m)}_{\text{snk}} + C^{(m)}_{\text{coll}}, \tag{4.74}$$

$$\text{for odd } m \text{ and } m \geq 3: \quad \mathcal{J}\frac{ds^{(m)}}{dt} + \mathcal{J}\left(\frac{1}{m-1}\zeta^{m-1} + \frac{1}{m}\zeta^{m}\right)\frac{df_{0i}}{dt} = S^{(m)}_{\text{src}} + S^{(m)}_{\text{snk}} + C^{(m)}_{\text{coll}}, \tag{4.75}$$

where $\psi^{(m)} \equiv \psi\Upsilon^{(m)}$ ($\psi = S_{\text{snk}}, S_{\text{src}}, C_{\text{coll}}$). Equation (4.73) is identical to Eq. (4.67). The second term on the left-hand side of the mth-order entropy density equations Eq. (4.74) and Eq. (4.75) represents the interaction with the $m-1$th-order entropy density, while the third term represents the interaction with the $m+1$th-order entropy density. When the interaction term between the mth-order entropy and the $m+1$th-order entropy is positive in the mth-order entropy density equation, it is necessarily negative in the $m+1$th-order entropy density equation, and vice versa. Therefore, the interaction terms do not produce a net entropy.

4.2.3 Entropy production and dissipation

First, we investigate the interaction between the thermodynamic entropy (first-order entropy) and the fluctuation entropy (second-order entropy). By integrating α over both the time and gyrocenter phase space, we obtain

$$\int_0^t \int \alpha r R d^5\boldsymbol{z} dt = \int_0^t \int r R \mathcal{J} d^5\boldsymbol{z} dt \left(\frac{\delta f_i v_r}{L_n} - \frac{3}{2}\frac{\delta f_i v_r}{L_{Ti}} + \frac{v^2}{2T_i}\frac{\delta f_i v_r}{L_{Ti}} + \delta f_i v_r \frac{\mu}{T_i}\frac{\partial B}{\partial r} + \delta f_i \left\{ v_\parallel, H \right\} \frac{v_\parallel}{T_i} + \delta f_i v_\theta \frac{\mu}{T_i}\frac{\partial B}{\partial \theta} \right). \tag{4.76}$$

Figure 4.5 shows the time evolution of each tem on the right-hand side of Eq. (4.76). The third term is at least 6.6 times larger than the other terms. Since the third term corresponds to the heat flux, the interaction term can be approximated as entropy change due to heat flux.

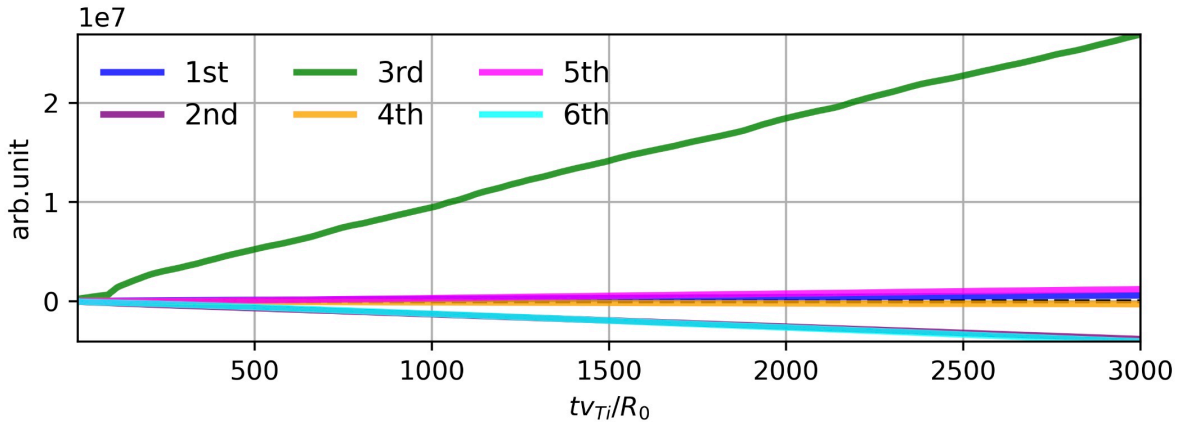

Fig. 4.5: Time evolution of each tem on the right-hand side of Eq. (4.76).

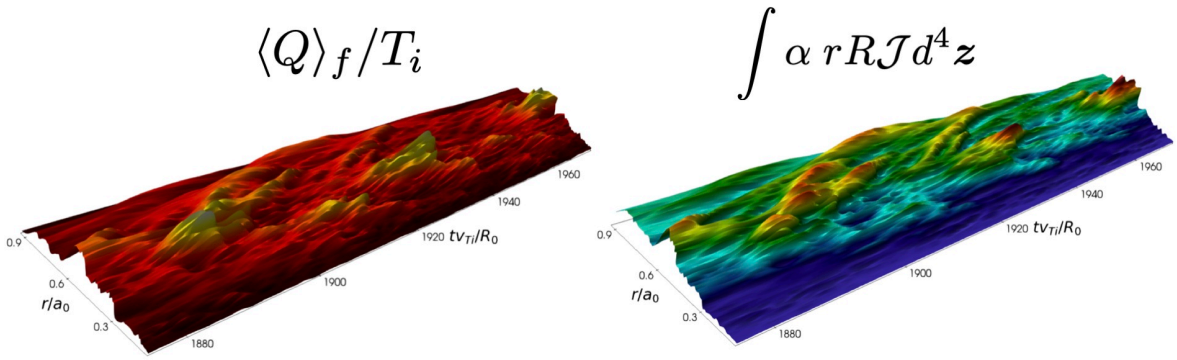

Fig. 4.6: Temporal and spatial profile of turbulent heat flux divided by temperature and interaction term.

As shown in Fig. 4.6, the spatiotemporal structures of the turbulent heat flux divided by temperature and the interaction term are similar. This further supports the approximation that the interaction term corresponds to the entropy change due to the heat flux. The turbulent heat flux is given by

$$Q(r,\theta,\varphi) = \int (v_{E,r} - v_{E,r,n=0}) \left(\frac{1}{2} v_\parallel^2 + \mu B \right) f \mathcal{J} dv_\parallel d\mu, \tag{4.77}$$

where $v_{E,r,n=0}$ represents the $n = 0$ component of the $E \times B$ drift, which contributes to neoclassical transport. The fact that the interaction term represents the entropy change due to heat flux indicates that the background profile and turbulence are interacting through the heat flux.

Figure 4.7 shows the time evolution of each term in Eqs. (4.67) and (4.68) integrated in the gyrocenter phase space. The second terms on the right-hand sides of Eqs. (4.67) and (4.68) are nearly zero, and therefore are not plotted in the figure. For large $|v_\parallel|$ and/or large μ, f_0 is almost zero. As a result, it is extremely difficult to

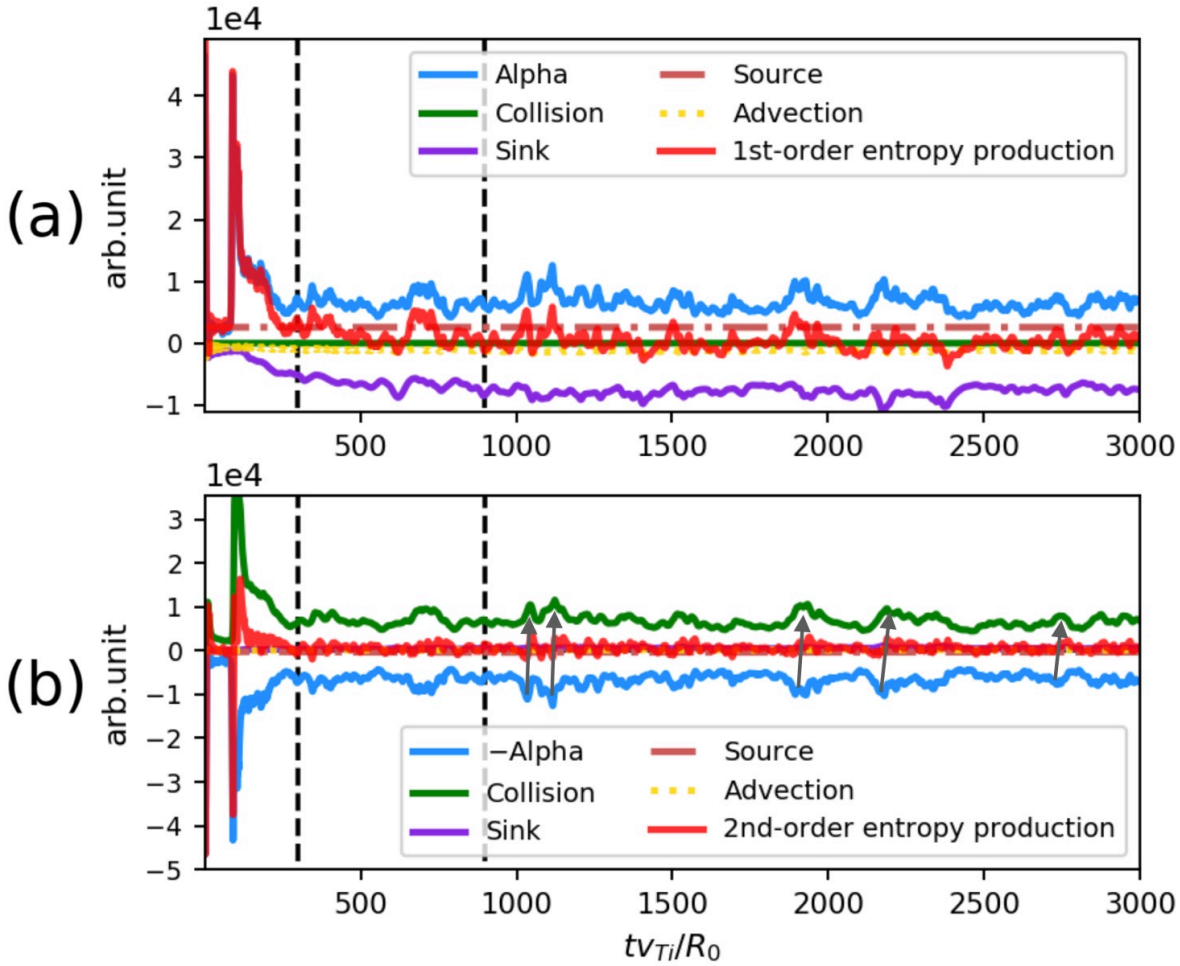

Fig. 4.7: Temporal evolution of each term in the first- and second-order entropy equation. The vertical black lines ($tv_{Ti}/R_0 = 300$ and $tv_{Ti}/R_0 = 900$) represent the time it takes for the first- and second-order entropies to reach the quasi-steady state, respectively.

compute numerically the terms including $\delta f/f_0$, such as the second-order entropy. For small $L_{v_\parallel}$ and small L_μ, direct computation of these terms becomes feasible. However, in this case, the conservation laws are violated and unphysical entropy oscillations are observed. Moreover, the potential structure and turbulent heat flux cannot be accurately evaluated [142]. In this study, we assume that the entropy of the third order and beyond is sufficiently small. By subtracting the first-order entropy $S^{(1)}$ from the entropy $S^{(\mathrm{all})}$, we compute the second-order entropy $S^{(2)} = S^{(\mathrm{all})} - S^{(1)}$. The fact that the interaction between the second-order entropy and the third-order entropy is small supports this assumption.

The first-order entropy density is of the first order, while the second-order entropy density is of the second order. However, as shown in Fig. 4.7, the production rates of the first-order and second-order entropies are of the same order. This is understood as follows. For simplicity, the radial direction is divided into two regions: the region with

a smaller radius has a temperature denoted as T_h, and the region with a larger radius has a temperature denoted as T_c. When there is a pressure change δP_i due to profile relaxation, from Eq. (4.63), the change in the first-order entropy is

$$\delta \mathcal{S}^{(1)} = -\frac{3}{2}\frac{\delta P_i}{T_h} + \frac{3}{2}\frac{\delta P_i}{T_c} = \frac{3}{2}\delta P_i \left(\frac{T_h - T_c}{T_h T_c}\right) > 0. \tag{4.78}$$

As indicated by Eq. (4.78), integrating the first-order entropy radially leads to a cancellation of increases and decreases in entropy. Consequently, the production rate of the first-order entropy becomes of the same order as that of the second-order entropy.

Figure 4.7(a) suggests that first-order entropy is not changed by collisions. This is due to the fact that velocity integral of the collision term $C^{(1)}_{\rm coll} = C_{\rm coll}\Upsilon^{(1)}$ in the first-order entropy density equation is analytically almost zero. To show this, we compute

$$\iint C^{(1)}_{\rm coll} B dv_\parallel d\mu = -\iint (1 + \log f_{0i}) \left[C_T(f_i) + \mathcal{P} f_{0i}\right] B dv_\parallel d\mu. \tag{4.79}$$

The first term on the right-hand side of Eq. (4.79) is

$$\iint (1 + \log f_{0i}) C_T(f_i) B dv_\parallel d\mu = \left\{1 + \frac{1}{2}\log\left(\frac{n^2}{2\pi T_i^3}\right)\right\} a - \frac{1}{2T_i} c. \tag{4.80}$$

From

$$\iint a F(x) f_{0i} \log f_{0i} B dv_\parallel d\mu = \frac{1}{2}\log\left(\frac{n^2}{2\pi T_i^3}\right) a, \tag{4.81}$$

$$\iint b G(x,\xi) f_{0i} \log f_{0i} B dv_\parallel d\mu = 0, \tag{4.82}$$

and

$$\iint c H(x) f_{0i} \log f_{0i} B dv_\parallel d\mu = -\frac{1}{2T_i} c, \tag{4.83}$$

the second term on the right-hand side is

$$\iint (1 + \log f_{0i}) \mathcal{P} f_{0i} B dv_\parallel d\mu = -\left\{1 + \frac{1}{2}\log\left(\frac{n^2}{2\pi T_i^3}\right)\right\} a + \frac{1}{2T_i} c. \tag{4.84}$$

Therefore, $\iint C^{(1)}_{\rm coll} B dv_\parallel d\mu = 0$. In general, when a collision operator conserves density and energy, the first-order entropy is not changed by the collision term. It is noted that it is in the collision theory only that the change in the first-order entropy by collision is strictly zero. In the gyrokinetic theory, because the Jacobian is $B^*_\parallel = B + v_\parallel \boldsymbol{b}\cdot\nabla\times\boldsymbol{b}$, not B, the first-order entropy change due to collision is not strictly zero. Figure 4.7 indicates that while the second-order entropy reaches a steady state at $tv_{Ti}/R_0 \sim 300$, it takes $900R_0/v_{Ti}$ for the background profile to achieve equilibrium.

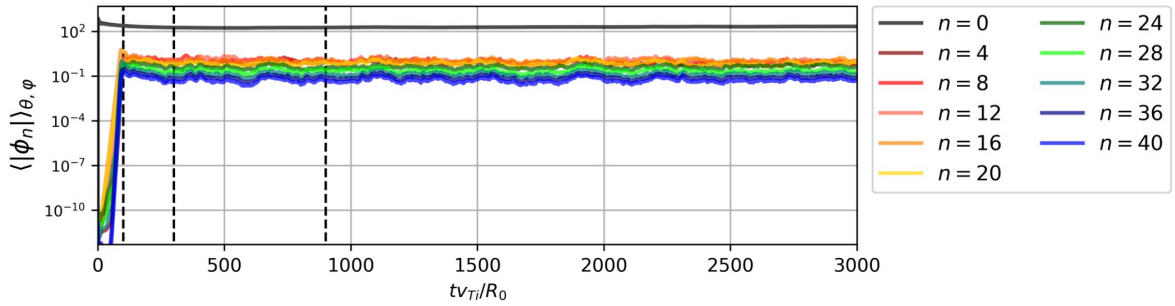

Fig. 4.8: Time evolution of electrostatic potential for each toroidal mode number. The black vertical lines represent $tv_{Ti}/R_0 = 100, 300$ and 900, respectively.

As shown in Fig. 4.8, the linear instability saturates at $tv_{Ti}/R_0 \sim 100$. The second-order entropy reaches the steady state after nonlinear saturation. This result is consistent with the results of GKV simulations [155]. The time it takes for the first- and second-order entropies to reach the steady state corresponds to the time it takes for the background profile and turbulence to reach that, respectively. Thus, the time difference can be interpreted as the difference between the timescale of transport and that of turbulence. Even in the quasi-steady state, the first-order and second-order entropy exhibit differences.

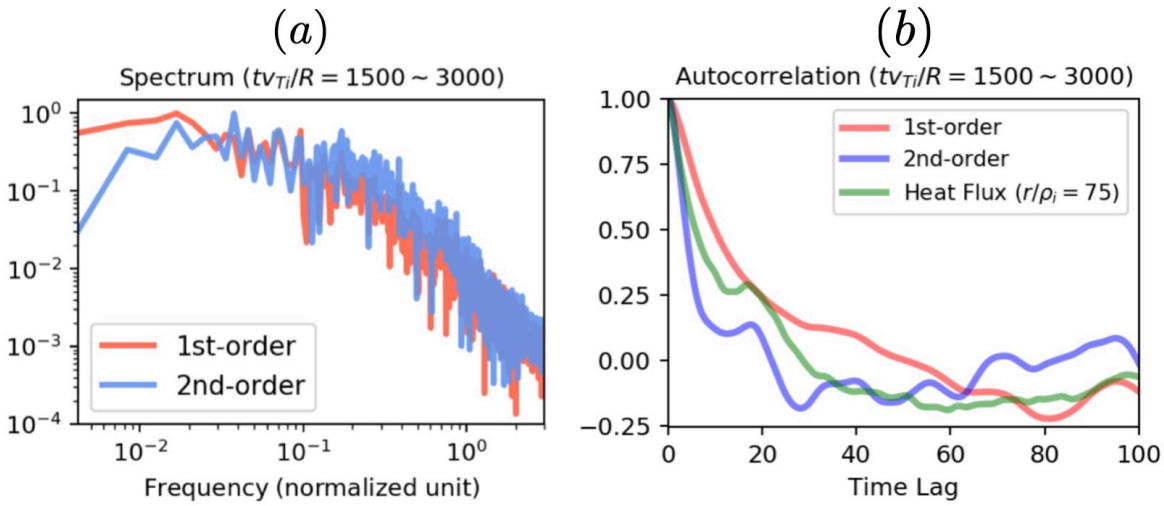

Fig. 4.9: Frequency spectra of the first-order and second-order entropy generation rates (a) and their autocorrelation functions (b) in the quasi-steady state.

The probability density distribution (PDF) of the first-order entropy production rate and that of the second-order entropy production rate in the quasi-steady state ($tv_{Ti}/R_0 = 1500 \sim 3000$) are close to Gaussian. The standard deviation of the PDF of the first-order entropy is about twice as large as that of the second-order entropy,

with their skewness being nearly identical. Figure 4.9 shows the frequency spectrum and autocorrelation function of the first-order entropy production rate and the second-order entropy production rate in the quasi-steady state. High-frequency components of the second-order entropy production rate are larger than that of the first-order entropy production rate. This is consistent with the fact that the timescale for turbulence is faster than that for transport. The autocorrelation function of second-order entropy production rate decreases more rapidly than that of first-order entropy production rate. Interestingly, the autocorrelation function of the heat flux is close to the average of the autocorrelation functions for the first-order and second-order entropy production rates. This might reflect that the heat flux arises from the interaction between the background profile and turbulence.

From Fig. 4.7, the first-order entropy balance equation and the second-order entropy balance equation can be approximated as

$$\frac{\partial \mathcal{S}^{(1)}}{\partial t} = \int \alpha r R d^5 \boldsymbol{z} + \int \left(S_{\rm src}^{\rm (all)} + S_{\rm snk}^{\rm (all)} \right) r R d^5 \boldsymbol{z} = \Gamma - E \tag{4.85}$$

and

$$\frac{\partial \mathcal{S}^{(2)}}{\partial t} = - \int \alpha r R d^5 \boldsymbol{z} + \int C_{\rm coll}^{\rm (all)} r R d^5 \boldsymbol{z} = -\Gamma + D, \tag{4.86}$$

respectively, where $\Gamma \equiv \int \alpha r R d^5 \boldsymbol{z}$, $E \equiv -\int \left(S_{\rm src}^{\rm (all)} + S_{\rm snk}^{\rm (all)} \right) r R d^5 \boldsymbol{z}$, and $D \equiv \int C_{\rm coll}^{\rm (all)} r R d^5 \boldsymbol{z}$ represent the entropy production rates due to heat flux, energy input and output, and collisional dissipation, respectively. Equation (4.85) means that $\mathcal{S}^{(1)}$ changes depending on the thermodynamic terms, such as the heat source and sink terms. Equation (4.86) is equivalent to Eq. (4.33) and means that $\mathcal{S}^{(2)}$ changes depending on kinematic terms, such as the collision term. In some previous studies [19, 144, 150, 155, 156, 157, 158], it is seen that the fluctuation entropy balance equation contains a term representing the time derivative of the square of the potential, $dW_{\boldsymbol{k}_\perp}/dt = d/dt[\mathrm{Re}\langle(1 - \Gamma_0 + (T_i/T_e))|\phi_{\boldsymbol{k}_\perp}|^2\rangle - (T_i/T_e)|\langle\phi_{\boldsymbol{k}_\perp}\rangle|^2\delta_{k_y,0}]/2$. This term is included within the interaction term of Eq. (4.86). To explicitly represent $dW_{\boldsymbol{k}_\perp}/dt$, one must substitute the continuity equation and quasi-neutrality condition into the interaction term. As in Eq. (4.33), D in Eq. (4.86) is determined by Γ. $-\Gamma$ can be interpreted as the entropy change due to phase mixing that forms fine-scale structures. As indicated by the arrows in Fig. 4.7(b), after the formation of fine-scale structures, entropy increases due to the irreversible process of collisional dissipation.

Figure 4.10 depicts $C_{\Gamma D}$, $C_{\mathcal{S}^{(1)}\Gamma}$, and $C_{\mathcal{S}^{(1)}\mathcal{S}^{(2)}}$. They are the cross-correlation functions (CCF) of Γ and D, $\partial\mathcal{S}^{(1)}/\partial t$ and Γ, and $\partial\mathcal{S}^{(1)}/\partial t$ and $\partial\mathcal{S}^{(2)}/\partial t$, respectively. For

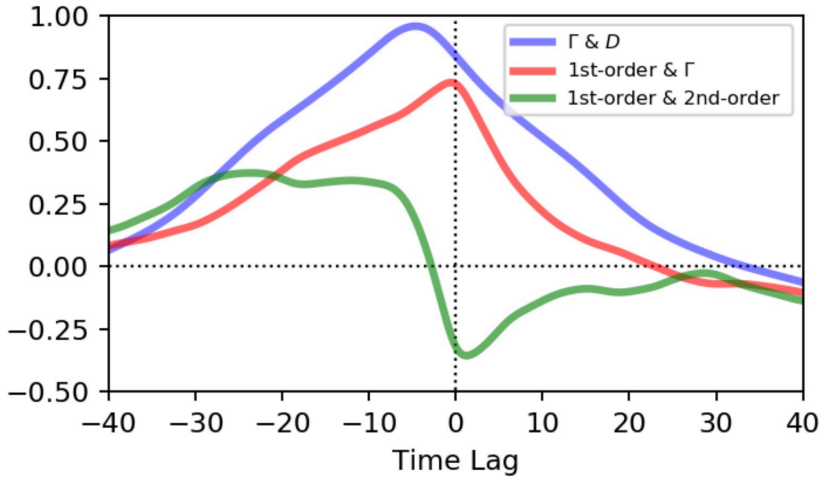

Fig. 4.10: Cross-correlation function between interaction term Γ and collision term D (blue), between first-order entropy production and Γ (red), and between first- and second-order entropy production (green).

time series $X(t)$ and $Y(t)$, their cross-correlation function is given by

$$C_{XY}(\tau) = \sum_t X(t+\tau)Y(t), \tag{4.87}$$

where τ is a time lag.

$C_{\Gamma D}$ reaches its peak at $\tau = -4.65R_0/v_{Ti}$. This suggests that fine-scale structures form without dissipation for $4.65R_0/v_{Ti}$. $C_{\mathcal{S}^{(1)}\Gamma}$ indicates that the first-order entropy production rate and the entropy generation due to heat flux increase simultaneously. As indicated by Eq. (4.86), $\partial S^{(2)}/\partial t$ is determined by $-\Gamma$ and D. Reflecting this, $C_{\mathcal{S}^{(1)}\mathcal{S}^{(2)}}$ takes its maximum value at $\tau = -23.65R_0/v_{Ti}$. This suggests that on average it takes $23.65R_0/v_{Ti}$ for the fine-scale structures to dissipate due to collisions.

The figure is a schematic diagram of the first-order entropy balance equation and of the second-order entropy balance equation. Figure 4.11 is a schematic diagram of the first- and second-order entropy balance equation. In the quasi-steady state, Eq. (4.85) illustrates the entropy balance between the energy source/sink and the heat flux (interaction term). On the other hand, Eq. (4.86) indicates the entropy balance between the collisional dissipation and the phase mixing (interaction term). The interaction term does not produce net entropy, which means that the energy input/output term and collision term are balanced. In other words, the quasi-steady state is achieved by profile formation in real space and structural dissipation in velocity space.

Given a constant positive Γ, in the absence of collisions $D = 0$, Eq. (4.86) indicates that the second-order entropy continues to decrease indefinitely. This is the same as the

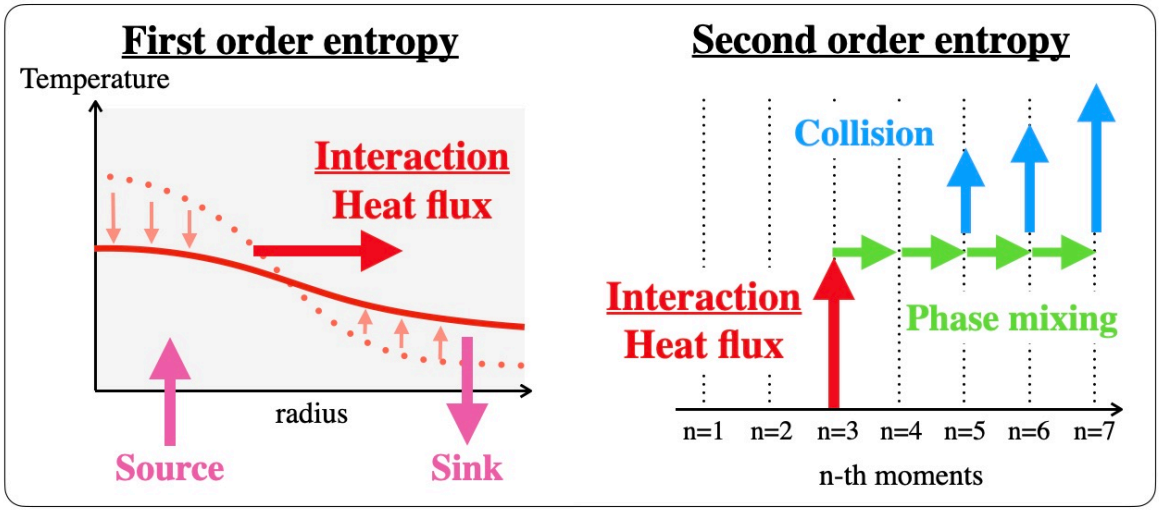

Fig. 4.11: Schematic diagram of first- and second-order entropy balance equations.

conventional entropy paradox. Given a constant positive Γ, in the absence of energy sources and sinks $E = 0$, the equations show that first-order entropy continues to increase indefinitely. This is a new type of entropy paradox. D and E are determined by Γ, and $\Gamma = E = D$ is satisfied in a quasi-steady state. Kosuga *et al.* pointed out the existence of a steady state where the entropy production due to profile relaxation and the entropy destruction due to zonal flow generation balance each other, satisfying $\Gamma = 0$ [154]. This corresponds to the trivial steady state of the fluctuation entropy satisfying $\Gamma = D = 0$ [144]. For the case of $\Gamma = 0$, the temperature gradient becomes infinitely large, and thus the first-order entropy does not reach a steady state. Therefore, this particular steady state is unlikely to be observed in reality.

Net entropy is generated in velocity space, and turbulence in real space does not contribute to entropy production directly. Therefore, even when there are ordered flows like zonal flows in real space, they do not lead to a reduction in entropy. The turbulence suppression by zonal flows is anticipated to lead to the generation of entropy. Moreover, from the entropy balance equation where $D = E$, it is inferred that the entropy production is independent of collision frequency. To verify these hypotheses, we conduct simulations for cases with collision frequencies of $\nu_\star = 0.2$ and $\nu_\star = 0.05$.

Figure 4.12 shows the time evolution of the main terms in the first- and second-order entropy balance equations for $\nu_\star = 0.2$ and $\nu_\star = 0.05$. It can be seen that when the collision frequency is high, the first-order entropy become smaller, even though the entropy production due to heat flux become larger. This is explained by the collisional

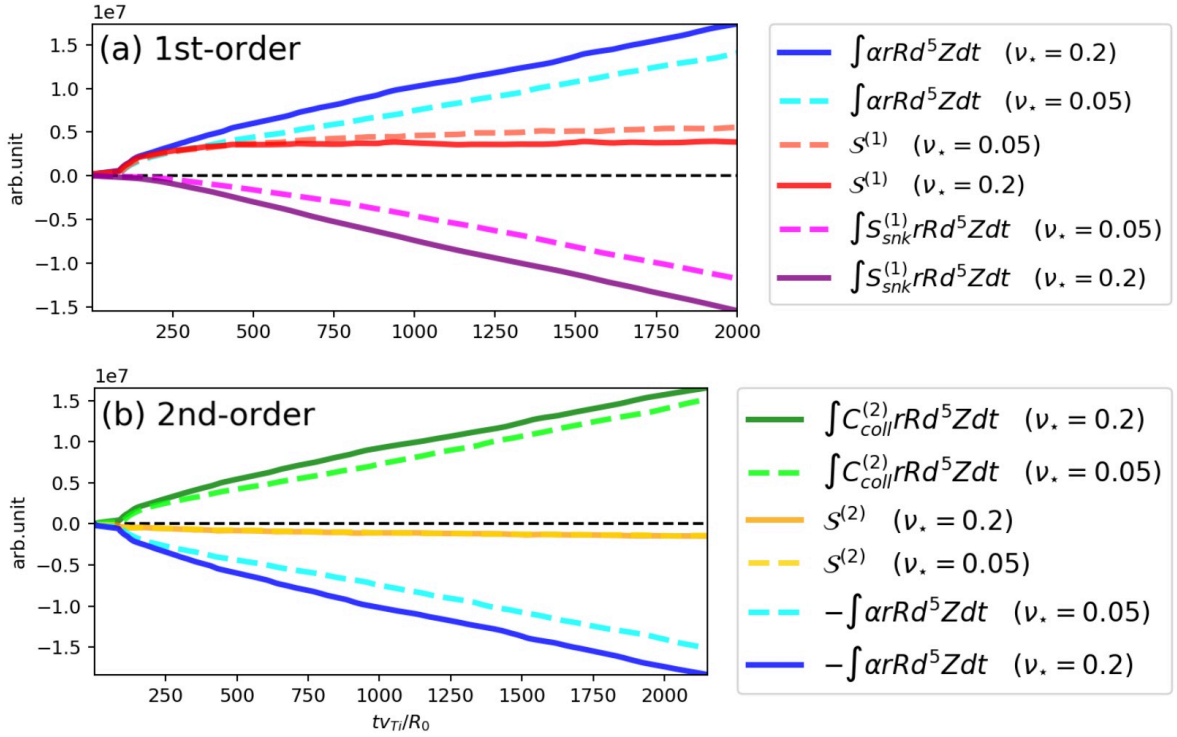

Fig. 4.12: Time evolution of the main terms in the first-order (a) and second-order (b) entropy balance equations.

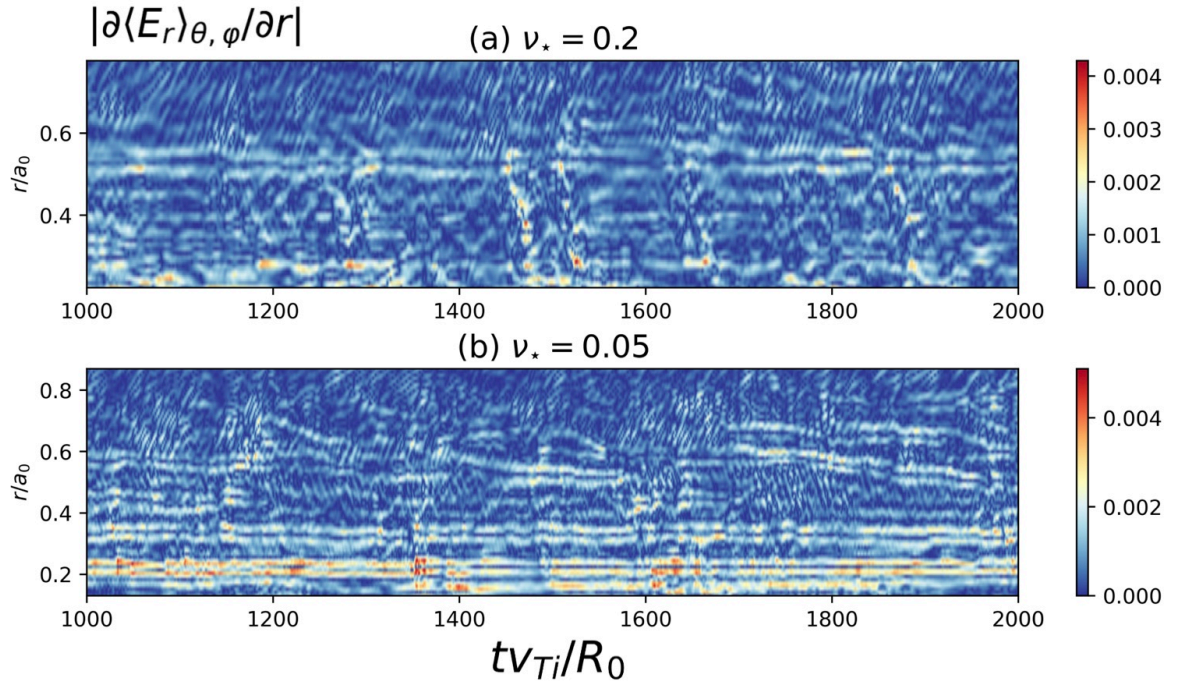

Fig. 4.13: Spatiotemporal evolutions of the absolute value of radial electric field shear for $\nu_\star = 0.2$ and $\nu_\star = 0.05$.

damping of zonal flow. As illustrated in Fig. 4.13, The high collision frequency results in a reduction in both zonal flow and poloidal flow shear. Consequently, with increased

collision frequency, the turbulence suppression effect due to the poloidal flow shear becomes weaker, leading to an enhanced heat flux and associated interaction term. When the heat flux is large, the time required for the sink term to reach a quasi-steady state is reduced. As a result, the first-order entropy reaches a steady state more rapidly. Therefore, in cases with a higher collision frequency, the first-order entropy is smaller. On the other hand, the second-order entropy does not depend on the collision frequency. This is because the more entropy is reduced by fine-scale structure formation, the more entropy is produced by collisional dissipation. The second-order entropy might be dependent on the driving source of turbulence.

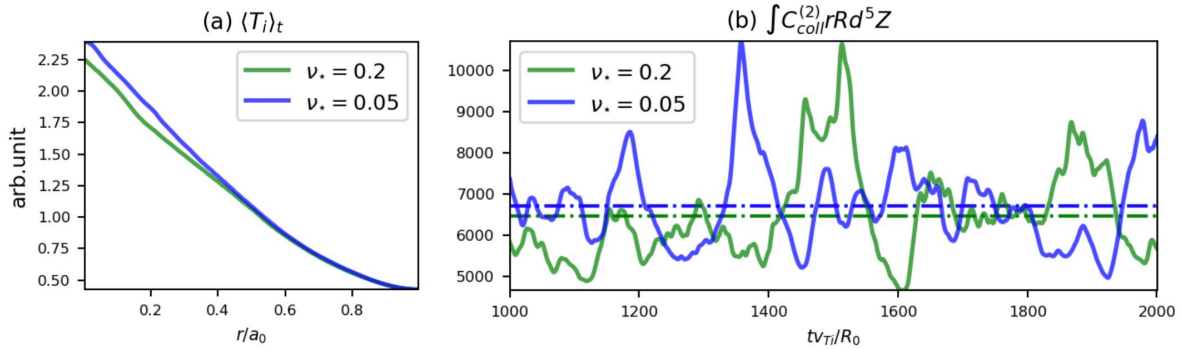

Fig. 4.14: (a) Time-averaged ion temperature profiles and (b) temporal evolutions of D for $\nu_\star = 0.2$ and $\nu_\star = 0.05$

Figure 4.14(a) shows the radial profile of the ion temperature, averaged over $tv_{Ti}/R = 1000 \sim 2000$. The temperature gradient is larger when the collision frequency is smaller. Particularly for $r/a_0 < 0.5$, the improvement is pronounced. The figure indicates the formation of the large radial electric field shear in that region, suggesting that the large temperature gradient is formed due to turbulence suppression. Figure 4.14(b) illustrates that for $\nu_\star = 0.05$, despite the collision frequency being 4 times smaller than that in the case of $\nu_\star = 0.2$, the entropy production is larger. This indicates that entropy production is not dependent on the collision frequency but is reliant on the temperature gradient. In other words, ordered flows such as zonal flows can significantly increase entropy production. Yoshida and Mahajan also pointed out that zonal flows lead to a significant increase in entropy generation, based on their analytical results using the heat engine model of the plasma boundary layer [137]. They proposed that while zonal flows are generated on a macroscopic scale, entropy is produced on a microscopic scale. On the other hand, our results suggest that entropy production is not explained by scale separation. We demonstrate that entropy is produced in velocity space, and that flows in real space do not directly contribute to entropy production.

In the local gyrokinetic model, the fluctuation entropy balance equation Eq. (4.86) is assumed to be locally satisfied. To validate this assumption, we vary the radial integration range and calculate the temporal evolution of the terms in the second-order entropy balance equation. The results are presented in Fig. 4.15. As the integral range becomes smaller, the contribution from the advection term becomes larger. Locally, the advection term is one order of magnitude larger than the other terms. This suggests that turbulence is not simply dissipated locally. In other words, Eq. (4.86) does not hold locally. This might be due to heat avalanches, necessitating a global analysis of turbulent transport.

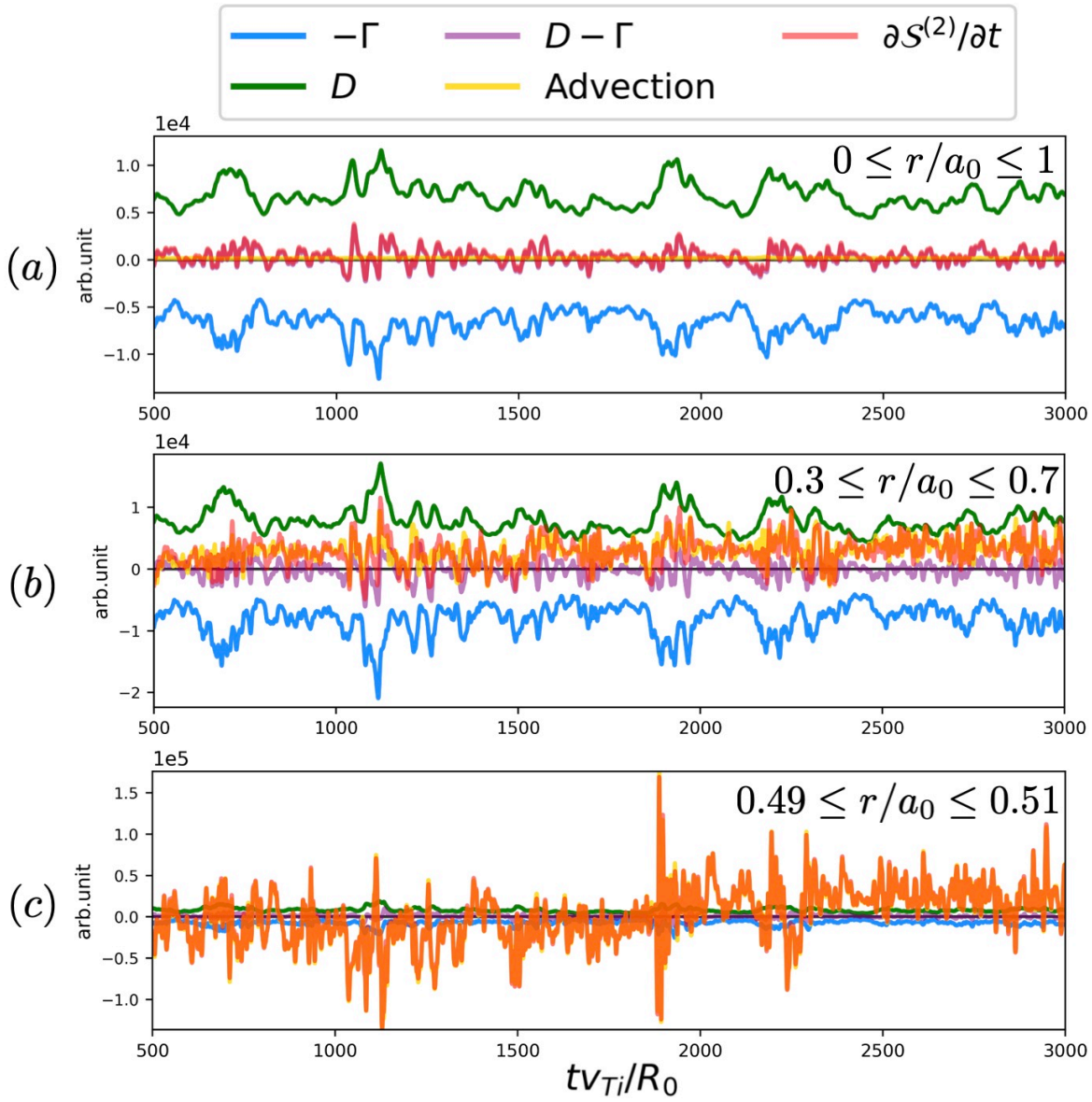

Fig. 4.15: Temporal evolution of the terms in the second-order entropy balance equation for radial integration ranges of $0 \leq r/a_0 \leq 1$ (a), $0.3 \leq r/a_0 \leq 0.7$ (b), and $0.49 \leq r/a_0 \leq 0.51$ (c).

4.3 Gyrokinetic entropy dynamics

4.3.1 Nonlocal heat transport

Figure 4.15 suggests that turbulent transport exhibits global rather than local characteristics. The non-local nature of turbulent transport is evaluated by the kernel (generalized diffusivity) $\mathcal{K}_r$ in

$$Q(r) = -\int \mathcal{K}_r(r, r')\frac{\partial T}{\partial r'}dr'. \tag{4.88}$$

GYSELA and XGC-1 simulation results show that it is represented by the Cauchy-Lorentz distributuion [163]

$$\mathcal{K}_r(r, r') = \frac{\Lambda}{\pi}\frac{\Delta/2}{(\Delta/2)^2 + |r - r'|^2}. \tag{4.89}$$

Λ is a parameter that represents the turbulence intensity and is proportional to $\langle\phi^2\rangle_r\sqrt{\langle R/L_T\rangle_r - R/L_{Tc}}$. Δ is a nonlocality parameter, which is larger than the turbulence autocorrelation length. This indicates that turbulent transport exhibits nonlocality. Δ corresponds to the avalanche size and $E \times B$ staircase width. $E \times B$ staircase is a quasi-regular shear flow pattern. At scales smaller than Δ, transport is dominated by avalanches. The temperature profile becomes corrugated due to heat avalanche jam, leading to the formation of $E \times B$ staircase from the radial force balance Eq. (1.129) [164].

Turbulent transport exhibits long-range correlations not only in space but also in time. The long-time correlation of time series data can be evaluated by the Hurst exponent [165]. The Hurst exponent for time series data $\{X_i\}_{i=1}^N$ is calculated from the rescaled range (R/S) statistic as follows [166]. We construct a subset of the time series data, $\{X_i\}_{i=t+1}^{t+n}$, $t, n \in \mathbb{N}$, and utilize it to generate a new dataset, $\{Y_i\}_{i=t+1}^{t+n}$, where $Y_{t+i} \equiv X_i - \overline{X(t,n)}$, $\overline{X(t,n)} \equiv \sum_{i=1}^n X_{t+i}/n$. The standard deviation of $\{X_i\}_{i=t+1}^{t+n}$ is obtained from $S(t,n) = \sqrt{\sum_{i=1}^n Y_{t+i}^2}$. From $\{Y_i\}_{i=t+1}^{t+n}$, we generate a new dataset, $\{Z_i\}_{i=t+1}^{t+n}$, where $Z_{t+i} \equiv \sum_{k=1}^i Y_{t+k}$. The adjusted range $R(t,n)$ is defined as

$$R(t,n) \equiv \max\{Z_{t+1}, Z_{t+2}, \cdots, Z_{t+n}\} - \min\{Z_{t+1}, Z_{t+2}, \cdots, Z_{t+n}\}. \tag{4.90}$$

The average of $R(t,n)/S(t,n)$ can be expressed as

$$\overline{\frac{R(n)}{S(n)}} = Cn^H, \tag{4.91}$$

where C is a constant and H represents the Hurst exponent with a range of 0 to 1. When $X_1, X_2, \cdots, X_N$ are mutually independent, $H = 0.5$ from the central limit

theorem. For time series data exhibiting long memor, $H > 0.5$ is observed. Simulation results from GKNET indicate that for turbulent heat transport, $H \simeq 0.7$ [167].

It is believed that models based on self-organized criticality (SOC) can explain features of turbulent transport such as long-range correlations in time and space as well as the critical temperature gradient depicted in Fig. 1.11 [168, 169, 170, 171]. Dynamical systems with SOC spontaneously maintain a critical state without the need for external interventions [172, 173, 174]. A commonly used model to represent SOC is the sandpile model [175, 176]. When sand is continuously dropped onto a sandpile, the pile accumulates until it reaches a point where the sand starts to flow downward. Consequently, the sandpile doesn't grow infinitely tall, but instead achieves a statistically steady state. The sandpile model is a cellular automaton that simulates this dynamics. Instead of steadily releasing energy, the system accumulates it and releases a burst of energy once a critical threshold is exceeded. The similarities between turbulent heat transport and the sandpile model are summarized in Tab. 4.1 [176].

Tab. 4.1: Analogies between turbulent heat transport and sandpile model [176].

Turbulent transport	Sandpile model
Turbulent eddy	Cell
Critical gradient for instability	Critical sandpile slope
Local eddy-induced transport	Number of grains moved
Total energy	Total number of grains
Background fluctuations	Random rain of grains
Turbulent heat flux	Sand flux
Mean temperature profile	Average slope of sandpile
Transport event	Avalanche
Electric field shear	Wind shear

Figure 4.16 shows the frequency spectrum of turbulent heat flux at $r = 75.8\rho_i$. The spectrum has three characteristic frequency regions that appear in the frequency spectrum of systems with SOC [175, 176]. The low frequency range where the power spectrum is proportional to ω^0 corresponds to large avalanche events that release stored energy all at once and exhibits a long-time correlation. The frequency of such large avalanches is proportional to the input energy. This is because the time it takes to re-establish the significant temperature gradient after the catastrophic bursts is

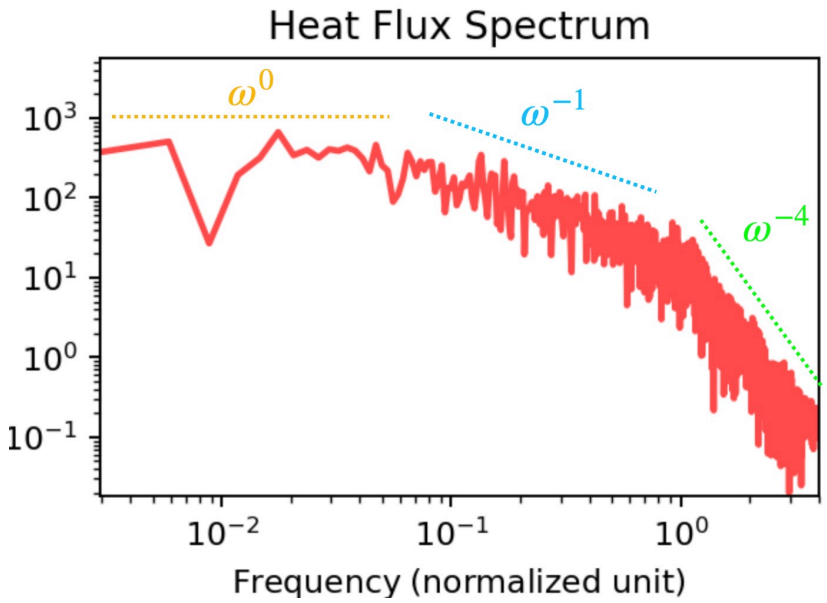

Fig. 4.16: Frequency spectrum of turbulent heat flux at $r = 75.8\rho_i$.

proportional to the energy source. The intermediate frequency domain is related to the overlapping avalanches. This suggests the lack of characteristic scale for the avalanches [177]. The high frequency range which is proportional to A corresponds to small scale avalanches that do not interact with each other. Similar frequency spectra was reported in many previous studies. The heat flux spectra in the global fluid code [177], GT5D [118], GYSELA [178], GENE[179], and GKNET [180] suggest that turbulent heat transport has the properties of SOC. The ion saturation current spectrum observed in the stellarator device W7-AS [181], the frequency spectrum of electron temperature fluctuations in the tokamak device DIII-D [182], the spectra of the floating potential and density fluctuations in the TEXTOR [183], the frequency spectra of density fluctuations in both Tore Supra and Castor Tokamak [184], and the frequency spectrum of electron temperature fluctuations in the HL-2A tokamak [185] are all consistent with the theoretical predictions of SOC. This is noteworthy because it implies that despite the differences in device configuration (e.g., stellarators versus tokamaks) and diagnostics, the underlying turbulent transport mechanisms share commonalities which can be captured by the concepts of SOC, which could provide a unifying framework to understand intermittent, avalanche-like transport in fusion devices. In HL-2A, an increase in the temporal and spatial correlation lengths was observed after supersonic molecular beam injection (SMBI) [185]. This indicates an enhanced SOC, leading to an increase in inward heat avalanches, thereby raising the core temperature. This contributes to confinement improvement.

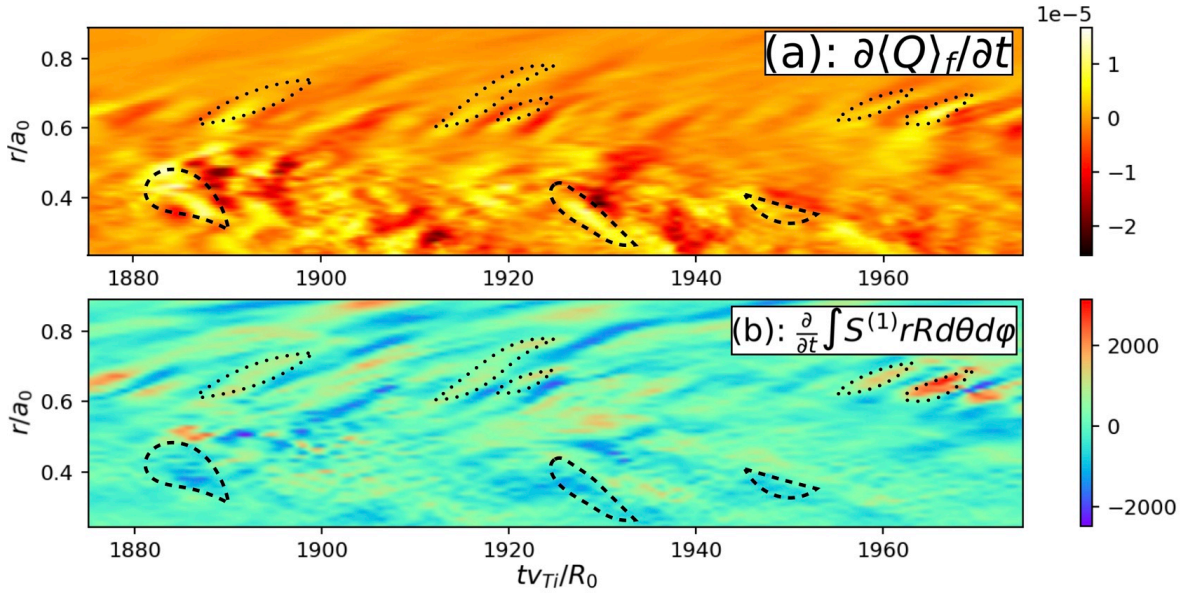

Fig. 4.17: Spatiotemporal evolution of time derivative of (a) flux-surface averaged turbulent heat flux and (b) first-order entropy.

4.3.2 Entropy advection

Figure 4.17(a) shows the spatiotemporal evolution of the time derivative of the flux-surface averaged turbulent heat flux. The dotted circles and the dashed circles represent outward and inward intermittent heat avalanches, respectively. Figure 4.17(b) shows the spatiotemporal evolution of the first-order entropy production. In this section, when evaluating entropy, we employ the Maxwellian based on the density and temperature that are time-averaged in the steady state as the initial distribution. Consequently, Fig. 4.17(b) illustrates the extent to which the pressure has deviated from the steady-state profile. The dynamics of entropy are dominated by entropy advection, and the time derivative of entropy is almost equivalent to the advective term. From Fig. 4.17(b), it can be observed that the bumps of the temperature profile propagate with the outward heat avalanches, while the voids of the temperature profile propagate with the inward heat avalanches.

Figure 4.18 provides an illustration of the propagation of bump and void. The bump propagates outwardly because the temperature gradient at the outer front exceeds the critical gradient. Conversely, the void propagates inwardly because temperature gradient at the inner front is larger than the critical gradient. In the model based on the theory of SOC, both bump and void have identical probability distributions

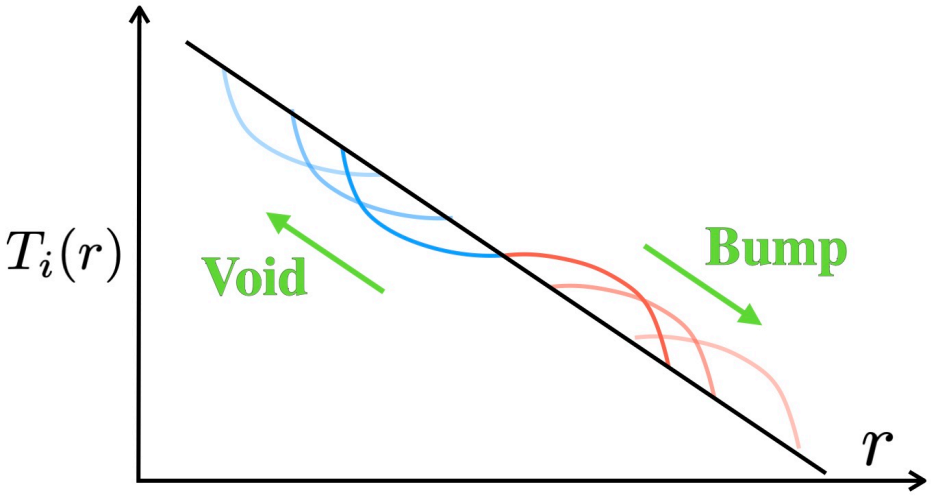

Fig. 4.18: Schematic diagrams of avalanche propagation.

owing to symmetry. However, in real plasmas, the symmetry is broken by the mean radial electric field [186, 187]. From the radial force balance Eq. (1.129), the radial electric field shear $\partial E_r/\partial r$ is proportional to the curvature of the temperature profile. As illustrated in Fig. 4.18, the bump has a negative temperature curvature, while the void has a positive temperature curvature. Therefore, the bump and void induce negative and positive radial electric field shears, respectively. When the background radial electric field shear is positive, the presence of a bump leads to a reduction in the shear, whereas the presence of a void results in an increased shear. Therefore, only the bump propagates outward. Conversely, when the background radial electric field shear is negative, the presence of a bump enhances the absolute value of the shear, while the presence of a void diminishes the absolute shear value. Hence, only the void propagates inwardly. In this manner, the symmetry between bumps and voids is broken. The background radial electric field shear, as shown by Eqs. (4.60) and (1.129), is negative for $r/a_0 < 0.5$ and positive for $r/a_0 > 0.5$. Figure 4.17(b) illustrates that for $r/a_0 < 0.5$, the voids propagate, whereas for$r/a_0 > 0.5$, the bumps propagate. This is consistent with the symmetry-breaking avalanche theory.

Figure 4.19(a) shows the CCFs of the first-order entropy production rate and the interaction term in the inward avalanche region at $r/a_0 = 0.4$ and in the outward avalanche regions at $r/a_0 = 0.6$ and $r/a_0 = 0.7$. Figure 4.19(a) represents the local counterpart of the red line in Fig. 4.10. Figure 4.10 indicates that the first-order entropy production rate and the interaction term are in-phase, while Fig. 4.19(a) demonstrates that there is a time lag between their increases or decreases. This represents a delay in the heat flux response to changes in the temperature profile. The

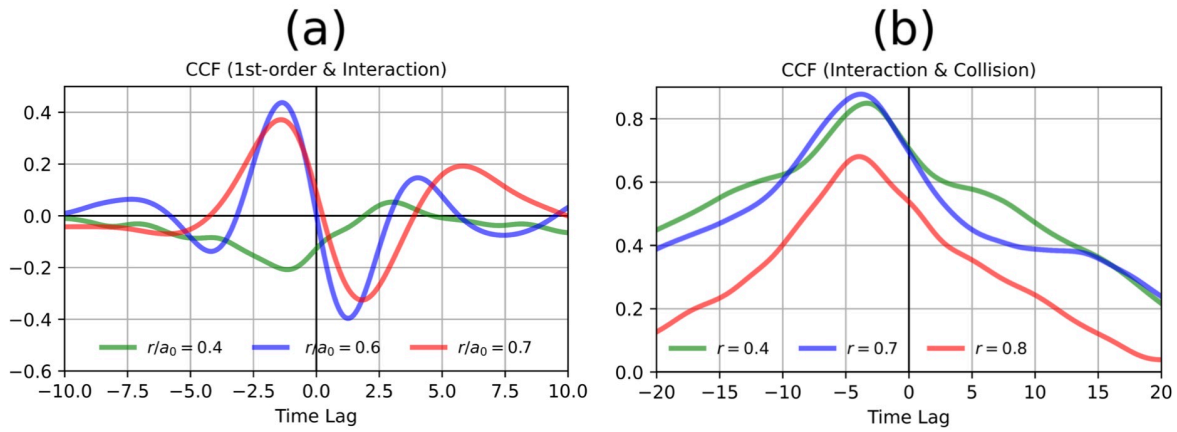

Fig. 4.19: (a) CCFs between first-order entropy production and interaction term and (b) CCFs between interaction and collision term.

heat flux increases approximately $tv_{Ti}/R_0 \sim 1.4$ after the temperature rises. It is noteworthy that this time lag is of the same order as the inverse of the linear growth rate of the tITG mode. The first-oder entropy production rate is positive for bumps and negative for voids, hence their signs of the CCTs are opposite.

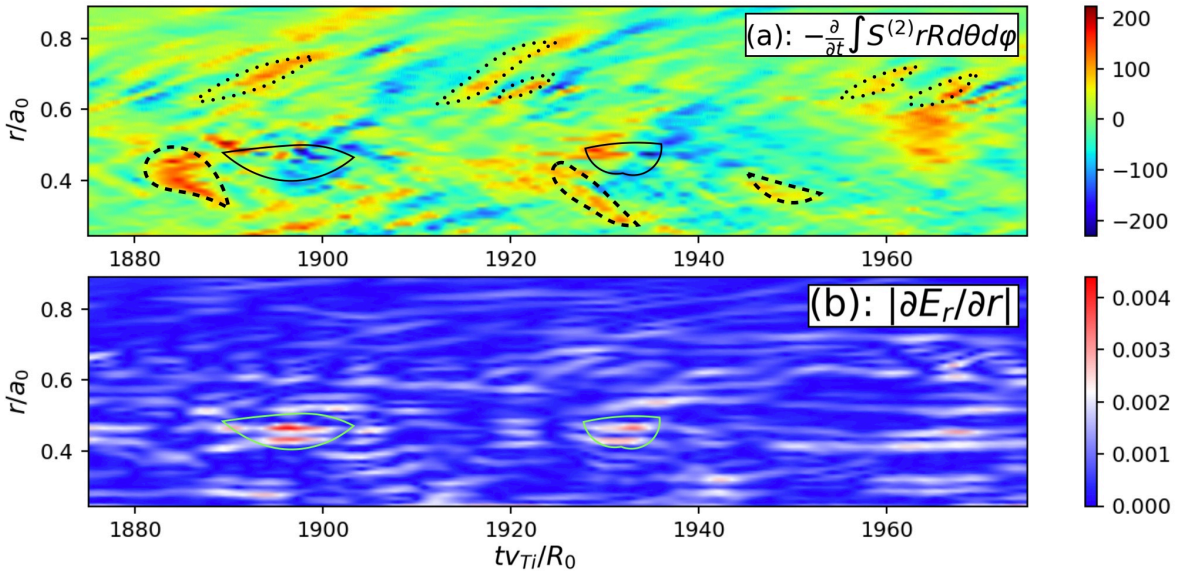

Fig. 4.20: Spatiotemporal evolution of (a) fluctuation entropy production and (b) the absolute value of electric field shear.

Figure 4.20 shows the spatiotemporal evolution of the fluctuation entropy and the absolute values of the radial electric field shear. It can be seen that the turbulence propagates with the heat avalanches. This result is consistent with the simulation results for the collisionless slab ITG turbulence [162]. The first-order and second-order

entropies are in-phase in the outward avalanche region, while they are out-of-phase in the inward avalanche region. This relationship markedly differs from the one shown by the green line in Fig. 4.10. In Fig. 4.20(a), the solid circles represent regions where the fluctuation entropy significantly changes from positive to negative, implying a substantial reduction in turbulence intensity. FromFig. 4.20(b), it can be observed that in these areas, the shear flow is four times the average value. This means that the turbulence is suppressed by the strong shear flow. Figure 4.19(b) depicts the local CCFs between the interaction term and the collision term. Its global counterpart is represented by the blue line in Fig. 4.10. From Fig. 4.19(b), it is seen that the relationship indicating the dissipation of fine-scale structures holds true locally as well and is independent of the direction of the avalanches. However, locally, the contribution from the entropy advection is more significant than that from the entropy production due to dissipation.

Chapter 5

Effects of magnetic island on profile formation

5.1 Magnetic island and plasma turbulence

Magnetic fusion devices such as tokamaks and stellarators confine high-temperature plasmas by nested flux surfaces. Due to perturbations with tearing parity, the topology of magnetic fields changes, leading to the formation of a magnetic island [188]. It is noteworthy that even instabilities such as the ITG mode, which only have twisting parity in the linear regime, can generate tearing parity through nonlinear parity mixing [189]. A magnetic island structure can be understood from the discussion presented below [190].

In a coordinate system (χ, θ, ζ), a magnetic field can be described as

$$\boldsymbol{B}(\chi, \theta, \zeta) = \nabla\zeta \times \nabla\psi(\chi, \theta, \zeta) + \nabla\chi \times \nabla\theta, \tag{5.1}$$

where χ and ψ respectively represent the toroidal and poloidal magnetic flux divided by 2π, θ and ζ are generalized angles for the poloidal and toroidal directions, respectively. Equation (5.1) is the Clebsch representation of the magnetic field, and it always satisfies $\nabla \cdot \boldsymbol{B} = 0$. The equations for the magnetic field lines,

$$\frac{d\chi}{d\zeta} = \frac{B^{\chi}}{B^{\zeta}} = \frac{\boldsymbol{B} \cdot \nabla\chi}{\boldsymbol{B} \cdot \nabla\zeta} \tag{5.2}$$

and

$$\frac{d\theta}{d\zeta} = \frac{B^{\theta}}{B^{\zeta}} = \frac{\boldsymbol{B} \cdot \nabla\theta}{\boldsymbol{B} \cdot \nabla\zeta}, \tag{5.3}$$

can be expressed

$$\frac{d\chi}{d\zeta} = -\frac{\partial\psi}{\partial\theta}, \qquad \frac{d\theta}{d\zeta} = \frac{\partial\psi}{\partial\chi} \tag{5.4}$$

by using

$$\nabla\psi(\chi, \theta, \zeta) = \frac{\partial\psi}{\partial\chi}\nabla\chi + \frac{\partial\psi}{\partial\theta}\nabla\theta + \frac{\partial\psi}{\partial\zeta}\nabla\zeta \tag{5.5}$$

and

$$\nabla\chi \times \nabla\theta \cdot \nabla\zeta = \frac{1}{\sqrt{g}}. \tag{5.6}$$

Equation (5.4) is equivalent to the Hamilton's canonical equations. θ, χ, ζ, and ψ correspond to the position, momentum, time, and Hamiltonian in Hamiltonian mechanics, respectively. In the case of an axisymmetric tokamak, the magnetic field does not depend on ζ, therefore $d\psi/d\zeta = 0$. This corresponds to the Hamiltonian being independent of time in Hamiltonian mechanics. If ψ depends only on χ, then from Eq. (5.4), the solution is $(\psi, \theta) = (\psi_0, \theta_0 + \zeta/q)$, where ψ_0 and θ_0 are constant, and $q = d\chi/d\psi$ is the safety factor. $\theta = \theta_0 + \zeta/q$ indicates that when q is a rational number, the magnetic field line returns to the poloidal angle θ_0, and when q is an irrational number, it does not return to θ_0. Instabilities like resistive [191, 192] and neoclassical [193, 194] tearing modes lead to magnetic field fluctuations at a rational surface $q(\chi_s) = q_s = m_0/n_0$. In tokamaks, the reduction of bootstrap current due to magnetic islands induces their growth. However, in stellarators, due to the negative magnetic shear, the decrease in bootstrap current causes magnetic islands to shrink [195]. The perturbed part of ψ can be approximated as

$$\delta\psi\left(\chi,\ \theta - \frac{\zeta}{q_s}\right) = \sum_l \delta\psi_{lm_0,ln_0} e^{il(m_0\theta - n_0\zeta)}, \tag{5.7}$$

implying that the Hamiltonian is completely integrable. On transforming θ into $\alpha = \theta - \zeta/q_s$, Eq. (5.1) becomes

$$\begin{aligned}\boldsymbol{B} &= \nabla\zeta \times \left(\nabla\psi - \frac{1}{q_s}\nabla\chi\right) + \nabla\chi \times \nabla\alpha \\ &= \nabla\zeta \times \nabla\psi_h + \nabla\chi \times \nabla\alpha.\end{aligned}$$

The Hamiltonian after the transformation ψ_h is defined as

$$\psi_h(\chi, \alpha) = \psi(\chi, \alpha) - \frac{1}{q_s}\chi. \tag{5.8}$$

Because of the discussion near the rational surface, we can substitute $\chi = \chi_s + \xi$ and obtain [190]

$$\psi_h(\xi, \alpha) = -\frac{1}{2q_s^2}\left.\frac{dq}{d\chi}\right|_{\chi=\chi_s} \xi^2 + \delta\psi(\chi_s, \alpha). \tag{5.9}$$

When the magnetic field perturbation $\delta\psi(\chi_s, \alpha)$ is proportional to $\cos(m\alpha)$, Eq. (5.9) is equivalent to the pendulum Hamiltonian. As illustrated in Fig. 5.1, the magnetic island structure can be seen from the orbits in phase space.

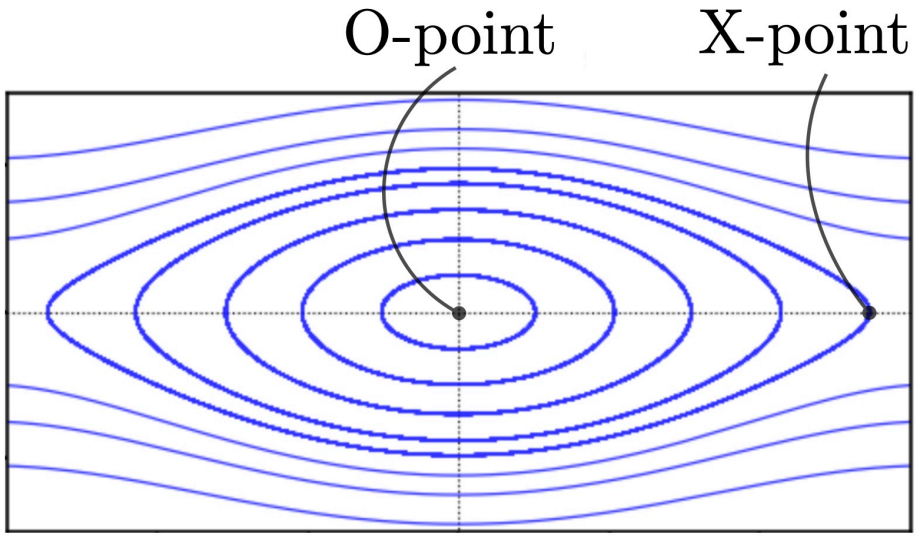

Fig. 5.1: Magnetic island structure

Magnetic islands have traditionally been believed to degrade plasma performance. This is because magnetic islands possess a radial component, and there is a potential for the background profiles to be flattened due to the parallel streaming, which is faster than the $\boldsymbol{E} \times \boldsymbol{B}$ drift. This characteristic profiles have been confirmed in numerous experiments to have a significant impact on turbulence and confinement. In LHD, the impact of an $(m, n) = (1, 1)$ static magnetic island generated by external perturbation coils on the ion temperature profile and poloidal flow was investigated [196]. Similar to the electron temperature profile, the ion temperature profile is flattened inside the magnetic island. Furthermore, because the poloidal flow becomes zero inside the magnetic island, a poloidal flow shear was observed at the boundaries of the magnetic island. Experiments on HL-2A showed that the flow inside the magnetic island is nearly zero with minimal density fluctuation, while at the boundary of the magnetic island, there is a large flow shear and large density fluctuation [199]. Similar results was obtained in experiments on J-TEXT [198]. In DIII-D experiments, a reduction in turbulent fluctuations was observed at the O-point of the neoclassical tearing mode islands [200]. In the experiments on LHD, when the magnetic island width exceeds 15% to 20% of the plasma radius, the poloidal flow within the magnetic island no longer remains zero and the direction of the poloidal flow reverses across the island [196]. Similarly, in KSTAR, a reversal of the poloidal flows direction across the $(m, n) = (2, 1)$ magnetic island induced by an external resonant magnetic perturbation (RMP) field was observed [197]. These poloidal flows increase towards the O-point. It was suggested that these reversed flows could suppress turbulence, maintaining a large temperature gradient at the boundaries. Regarding toroidal rotation, it is nearly zero in the $q = 2$ region in KSTAR [197]. In JT-60U experiments, no toroidal rotation was observed inside the magnetic island, while a significant toroidal flow shear was observed at the boundaries

of the island [201]. Significant improvement in ion heat transport inside the magnetic island was observed, with the thermal diffusivity being an order of magnitude smaller than that outside. These results could be related to the formation of the internal transport barrier on the rational surface [202, 203, 204, 205]. In experiments on LHD, when a magnetic island is present, the electron temperature increases significantly after the onset of on-axis electron cyclotron heating (ECH) compared with the case without the magnetic island [206]. The foot point of the electron ITG was observed to move outward in conjunction with the movement of the magnetic island (rational surface) in experiments conducted on Heliotron-J [207].

The impact of magnetic islands on plasma turbulence and associated turbulent transport has been investigated using gyrokinetic simulations. δf ITG turbulence simulations by ORB5 were conducted with the introduction of an $(m, n) = (3, 2)$ magnetic island [208, 209]. They assumed the adiabatic electron approximation and, for simplicity, ignored the $n = m = 0$ mode. Outside the O-point region, despite the high temperature gradient due to the flattened temperature profile within the magnetic island, the heat flux is small. Instead, it was found to be larger near the X-point region. This is attributed to turbulence vortices being torn apart outside the O-point region by the $n = 2$ mode generated by inverse cascade, similar to the turbulence suppression by zonal flows. ITG turbulence simulations in the presence of an $(m, n) = (2, 1)$ magnetic island using GTC also demonstrated that the turbulence is considerably weakened inside the magnetic island, and the particle and heat fluxes peak near the X-point [210]. The dynamics of electrons was computed from the drift-kinetic equation. In the simulations, only five toroidal modes were considered: the zonal mode $(m, n) = (0, 0)$, the mode same as the magnetic island $(m, n) = (2, 1)$, and the high n modes $(m, n) = (10 \sim 30, 9), (10 \sim 30, 10), (10 \sim 30, 11)$. It is believed that the turbulence is suppressed due to the flow shear from a vortex mode formed by nonlinear coupling. The vortex mode, which is a mesoscale turbulent vortex with the same toroidal and poloidal mode numbers as the magnetic island, was reported in simulations by the flux-tube code GKW [211, 212, 213]. Kinetic electron dynamics was retained in the simulations. The flow shear induced by the vortex mode not only suppresses turbulence and enhances the temperature gradient at the magnetic island boundary but also inhibits turbulent advection from the X-point to the O-point. It was pointed out that the presence of the turbulence inside the magnetic island originates from drift-direction advection and is not due to turbulent diffusion [214]. On the other hand, as the magnetic island width W increases, radial heat transport due to the vortex mode increases, competing with the heat transport by the parallel streaming. The dependence of the turbulent transport and profile on the island width was examined in greater detail by the flux-tube code GENE [215]. It demonstrated that when the

island width exceeds $W_t \simeq 33\rho_i$, the temperature profiles is flattened and the vortex mode appears. Furthermore, when $W > W_t$, it was found that the radial electric field shear is proportional to W and the turbulent particle and heat fluxes decrease by an order of $1 \sim 2$.

These simulation results shed light on the impacts of a magnetic island on microturbulence. On the other hand, since the studies were based on δf gyrokinetic simulations, there was insufficient discussion of the influence of magnetic islands and the vortex mode on background profiles. It is important to investigate the influence, because variations in the background profiles are likely to influence the dynamics of the vortex mode. Additionally, it was reported that the mean radial electric field, originating from the large temperature gradient at the boundaries of a magnetic island, exerts a significant influence on turbulence [216]. In this study, initially, neoclassical simulations using the full-f PIC code XGC1 were performed to self-consistently compute the evolution of gyrokinetic ions and drift kinetic electrons, determining the background profiles. It was found that the flow due to the mean radial electric field is large at the O-point and small at the X-point. By using the obtained background profiles, linear gyrokinetic simulations were performed by the δf PIC code gKPSP. In this code, the evolution of gyrokinetic ions and bounce-averaged electrons is solved. The simulation results indicate that the shearing rate due to the mean radial electric field across the O-point of the island is close to the maximum linear growth rate of the TEM, suggesting that the majority of modes are suppressed by the flow shear. Therefore, the large electron temperature gradient is maintained. This result suggests that the flow shear has the potential to suppress turbulence in the vicinity of magnetic islands, regardless of the existence of a vortex mode. From these points of view, full-f simulations are urgently required in which the background profiles and turbulence are solved self-consistently.

5.2 Numerical method

5.2.1 Velocities and forces

In this study, the $(m, n) = (2, 1)$ static parallel vector potential fluctuation

$$\delta A_{\parallel} = \frac{I_a r^2 B_0}{R} h(r) \cos(2\theta - \varphi) \tag{5.10}$$

is introduced as in previous studies [216, 210]. $h(r) \equiv \exp\left[-(r - I_b\rho_i)^2/(I_c\rho_i^2)\right]$ is the dimensionless radial profile for the vector potential fluctuation. $I_a = 0.003$, $I_b = 108.6$, $I_c = 289.7$, are the dimensionless parameters for the intensity, center position, radial extent of the fluctuation, respectively. As indicated by the star in Fig. 5.2(a), $q(I_b) = 2$.

Magnetic island width is $W \simeq 22\rho_i \sim 5\text{cm}$, evaluated by

$$W = \sqrt{\frac{8qI_aI_b^2}{\hat{s}}}\rho_i. \tag{5.11}$$

This width is the same as in the reference literature [210]. Figure 5.2(b) represents the contour plot of the vector potential fluctuation given by Eq. (5.10). The magnetic island width is much larger than the typical turbulent vortices, and the vector potential fluctuation is symmetrical.

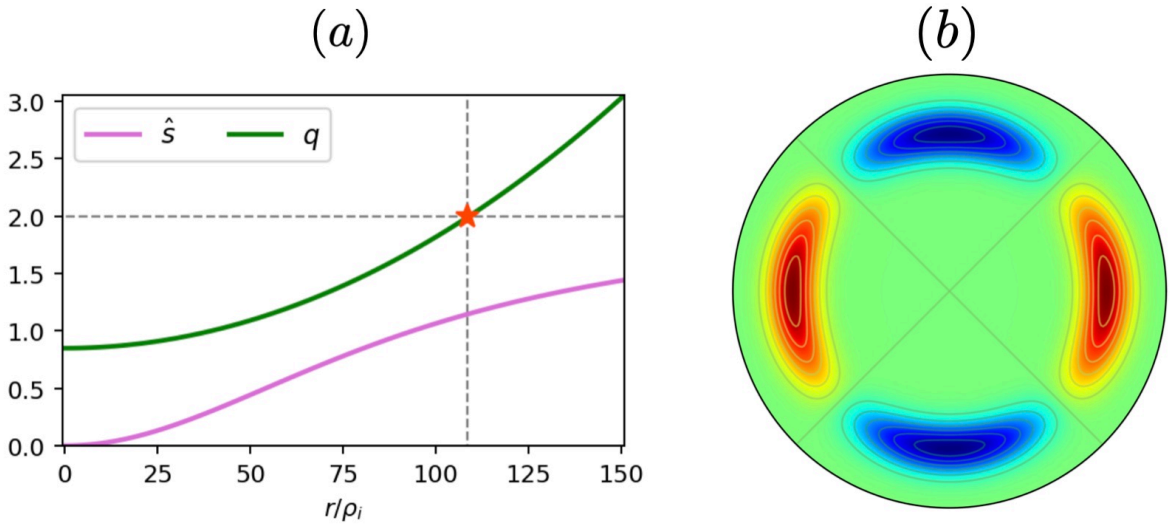

Fig. 5.2: (a) Radial profiles of safety factor and magnetic shear. The center of the magnetic island is also shown. (b) Contour plot of the vector potential fluctuation.

The magnetic field $\boldsymbol{B}$ is derived from $\boldsymbol{B} = \nabla \times \boldsymbol{A}$ such that

$$\begin{cases} B_r &= -2I_a \dfrac{r}{R}\, e^{-\frac{(r-I_b)^2}{I_c}} \sin(2\theta - \varphi) \\ B_\theta &= \dfrac{r}{qR} - 2I_a \dfrac{r}{R}\, e^{-\frac{(r-I_b)^2}{I_c}} \cos(2\theta - \varphi) + 2\,(r - I_b)\, \dfrac{I_a}{I_c} \dfrac{r^2}{R}\, e^{-\frac{(r-I_b)^2}{I_c}} \cos(2\theta - \varphi)\,. \\ B_\varphi &= \dfrac{R_0}{R} \end{cases} \tag{5.12}$$

Since the vector potential fluctuation and the corresponding magnetic field fluctuation are zero at $r = 0$, the numerical scheme which enables us to avoid numerical errors at the singularity can be used without modifications. The magnetic field has the finite radial component, which is not present in the axisymmetric tokamak field. This can potentially lead to the relaxation of the profiles within the magnetic island due to motion along the field. Furthermore, the magnetic field has φ dependence, and the φ

derivative is not zero. In the presence of the magnetic island, from Eqs. (3.8) $\sim$ (3.11), the ion velocities and forces in each direction are given as

$$\begin{aligned} v_{0x} = &\left(v_\parallel^2 + \mu B\right) \frac{\partial}{\partial \theta} \left(R b_\varphi - R_0\right) - \left(v_\parallel^2 + \mu B\right) \frac{\partial}{\partial \varphi}(r b_\theta) + v_\parallel \frac{\partial}{\partial \theta} \left(\delta A_\parallel\right) \\ &+ \mu \frac{\partial}{\partial \varphi}(r b_\theta B) - \mu \frac{\partial}{\partial \theta} \left(B R b_\varphi - R_0\right), \end{aligned} \tag{5.13}$$

$$\begin{aligned} v_{1x} = &\frac{\partial}{\partial \varphi} \left(\langle \phi \rangle_{\alpha i} r b_\theta\right) - \frac{\partial}{\partial \theta} \left(\langle \phi \rangle_{\alpha i} R b_\varphi - \langle \phi \rangle_{\alpha i, r=0} R_0\right) \\ &+ \langle \phi \rangle_{\alpha i} \frac{\partial}{\partial \theta} \left(R b_\varphi - R_0\right) - \langle \phi \rangle_{\alpha i} \frac{\partial}{\partial \varphi}(r b_\theta), \end{aligned} \tag{5.14}$$

$$\begin{aligned} v_{0y} = &-v_\parallel \frac{\partial}{\partial r} \left(R A_\varphi - R_0\right) - \left(v_\parallel^2 + \mu B\right) \frac{\partial}{\partial r}(R b_\varphi - R_0) \\ &+ \left(v_\parallel^2 + \mu B\right) \frac{\partial b_r}{\partial \varphi} - \mu \frac{\partial}{\partial \varphi}(B b_r) + \mu \frac{\partial}{\partial r}(B R b_\varphi - R_0), \end{aligned} \tag{5.15}$$

$$\begin{aligned} v_{1y} = &\frac{\partial}{\partial r} \left(\langle \phi \rangle_{\alpha i} R b_\varphi - \langle \phi \rangle_{\alpha i, r=0} R_0\right) - \langle \phi \rangle_{\alpha i} \frac{\partial}{\partial r}(R b_\varphi - R_0) \\ &- \frac{\partial}{\partial \varphi}(\langle \phi \rangle_{\alpha i} b_r) + \langle \phi \rangle_{\alpha i} \frac{\partial b_r}{\partial \varphi}, \end{aligned} \tag{5.16}$$

$$\begin{aligned} v_{0z} = &v_\parallel \frac{\partial}{\partial r}(r A_\theta) + \left(v_\parallel^2 + \mu B\right) \frac{\partial}{\partial r}(r b_\theta) - \mu \frac{\partial}{\partial r}(r b_\theta B) \\ &- \left(v_\parallel^2 + \mu B\right) \frac{\partial b_r}{\partial \theta} + \mu \frac{\partial}{\partial \theta}(b_r B), \end{aligned} \tag{5.17}$$

$$v_{1z} = -\frac{\partial}{\partial r} \left(\langle \phi \rangle_{\alpha i} r b_\theta\right) + \langle \phi \rangle_{\alpha i} \frac{\partial}{\partial r}(r b_\theta) + \frac{\partial}{\partial \theta} \left(\langle \phi \rangle_{\alpha i} b_r\right) - \langle \phi \rangle_{\alpha i} \frac{\partial b_r}{\partial \theta}, \tag{5.18}$$

$$\begin{aligned} v_{0v_\parallel} = &-\mu \frac{\partial}{\partial \theta} \left(\delta A_\parallel\right) \frac{\partial B}{\partial r} + \mu \frac{\partial}{\partial r}(R A_\varphi - R_0) \frac{\partial B}{\partial \theta} - \mu \frac{\partial}{\partial r}(r A_\theta) \frac{\partial B}{\partial \varphi} \\ &- v_\parallel \mu \frac{\partial}{\partial r} \left[B \left\{ \frac{\partial}{\partial \theta}(R b_\varphi - R_0) - \frac{\partial}{\partial \varphi}(r b_\theta) \right\}\right] \\ &- v_\parallel \mu \frac{\partial}{\partial \theta} \left[B \left\{ \frac{\partial b_r}{\partial \varphi} - \frac{\partial}{\partial r}(R b_\varphi - R_0) \right\}\right] - v_\parallel \mu \frac{\partial}{\partial \varphi} \left[B \left\{ \frac{\partial}{\partial r}(r b_\theta) - \frac{\partial b_r}{\partial \theta} \right\}\right], \end{aligned} \tag{5.19}$$

and

$$v_{1v_\parallel} = -\frac{\partial}{\partial \theta} \left(\delta A_\parallel\right) \frac{\partial \langle \phi \rangle_{\alpha i}}{\partial r} + \frac{\partial}{\partial r} \left(R A_\varphi - R_0\right) \frac{\partial \langle \phi \rangle_{\alpha i}}{\partial \theta} - \frac{\partial}{\partial r}(r A_\theta) \frac{\partial \langle \phi \rangle_{\alpha i}}{\partial \varphi}$$

$$
\begin{aligned}
&- v_\parallel \frac{\partial}{\partial r}\left[\langle\phi\rangle_{\alpha i}\left\{\frac{\partial}{\partial\theta}(Rb_\varphi - R_0) - \frac{\partial}{\partial\varphi}(rb_\theta)\right\}\right] \\
&- v_\parallel \frac{\partial}{\partial\theta}\left[\langle\phi\rangle_{\alpha i}\left\{\frac{\partial b_r}{\partial\varphi} - \frac{\partial}{\partial r}(Rb_\varphi - R_0)\right\}\right] - v_\parallel \frac{\partial}{\partial\varphi}\left[\langle\phi\rangle_{\alpha i}\left\{\frac{\partial}{\partial r}(rb_\theta) - \frac{\partial b_r}{\partial\theta}\right\}\right].
\end{aligned} \tag{5.20}
$$

The Vlasov solver for the case with the magnetic island is the same as that for the axisymmetric tokamak magnetic field.

5.2.2 Calculation of flux surface average

In the absence of a magnetic island, the flux-surface average of ϕ is given by

$$
\langle\phi\rangle_f = \frac{\displaystyle\int_0^{2\pi}\int_0^{2\pi} \phi\, rRd\theta d\varphi}{\displaystyle\int_0^{2\pi}\int_0^{2\pi} rRd\theta d\varphi}. \tag{5.21}
$$

By expanding ϕ as

$$
\phi = \sum_{m,n} \phi_{m,n}\, e^{i(m\theta - n\varphi)} \tag{5.22}
$$

and substituting it into Eq. (5.21), we obtain

$$
\langle\phi\rangle_f = \phi_{0,0} + \frac{r}{R_0}\mathrm{Re}[\phi_{1,0}]. \tag{5.23}
$$

The equation (5.23) indicates that flux-surface averaged quantities are represented by the zonal mode and its sidebands. The second term on the right-hand side arises due to toroidal effects. Fig. 5.3(a) shows the contour plots of the flux-surface averaged electrostatic potential calculated by Eq. (3.158). In poloidal cross-sections, magnetic surfaces are represented by countless circles with the same center and the $m = 0$ mode is dominant. The $m = 1$ mode is small because it cancels out between the high field side surface and the low field side surface.

When the magnetic field structure is varied by a vector potential fluctuation, the calculation of the flux-surface average becomes challenging. Without it, it is impossible to solve the gyrokinetic Poisson equation, both in the adiabatic electron model and in the hybrid electron model. This is because even in the hybrid electron model, the adiabatic response is assumed for $(m, n) \neq (0, 0)$ passing electrons. It has been pointed out that without appropriately considering the electron response, the vortex mode does not appear [209]. Therefore, in the presence of a magnetic island, $\langle\phi\rangle_f \simeq \phi_{(m,n)=(0,0)}$ is not valid. To address this issue, several methods have been developed to date [217],

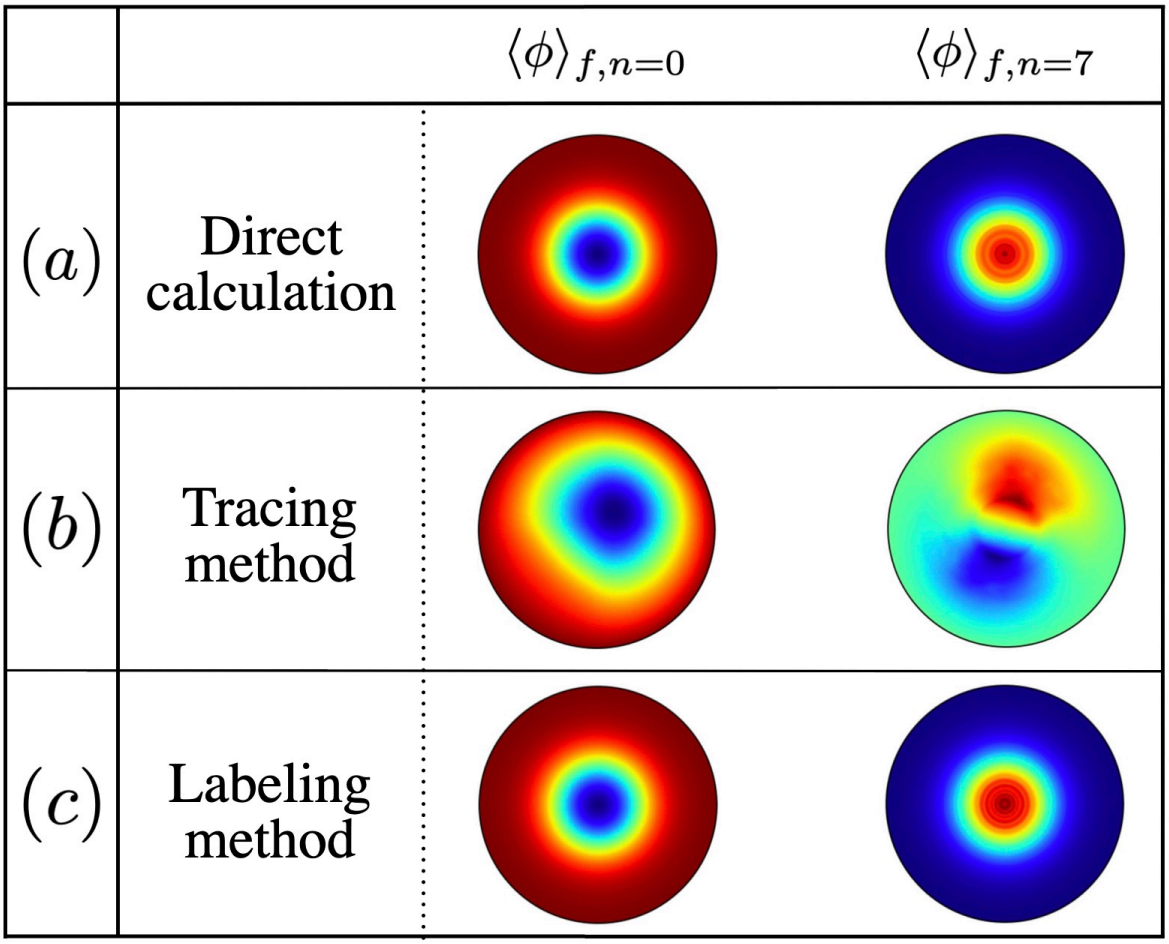

Fig. 5.3: Contour plots of the flux-surface averaged electrostatic potential calculated from Eq. (3.158) (a), using the tracing method (b), and using the labeling method (c).

however, to our knowledge, no standard method has been established. Therefore, in this study, we develop a new method for calculating the flux-surface average. First, we verify whether the results obtained by applying the methods in the absence of a magnetic island match with Fig. 5.3(a).

A method called the tracing method is developed as an intuitive and accurate approach. This method consists of the following three steps.

1. The equations for the magnetic field lines

$$\begin{cases} \dfrac{dr}{d\varphi} = 0 \\ \dfrac{d\theta}{d\varphi} = \dfrac{R}{qR_0} \end{cases} \tag{5.24}$$

   are calculated using all real-space grid points as initial values, and the coordinates of intersections with each poloidal cross-section are computed.

2. The coordinates calculated in step 1 are not on the nodes, thus interpolation

functions are used to determine their values from the values at neighboring grid points.

3. The flux-surface averaged value at each grid point is obtained by summing all values along the magnetic field line from that point and dividing by the total number.

The equations for the magnetic field lines need to be computed $N_r \times N_\theta \times N_\varphi$ times, which is time-consuming. However, since steps 1 and 2 only need to be performed once, the effective computation time can be reduced to virtually zero. The equations are solved using the Runge-Kutta method. At the grid number N_φ, the CFL condition may not be satisfied or the accuracy may degrade. Therefore, we compute the magnetic field line equations using the grid number $4N_\varphi$ in the toroidal direction. The flux-surface averaged electrostatic potential obtained by the tracing method shown in Fig. 5.3(b) significantly differs from that presented in Fig. 5.3(a). This is attributed to memory limit constraints. In the tracing method, due to the time-consuming nature of repeatedly solving the magnetic field line equations and loading the computational results, interpolation coefficients are stored in memory. However, due to the necessity of storing all the intersections between the magnetic field lines originating from every grid point and all poloidal cross-sections, as well as the interpolation coefficients, the memory usage exceeds its limit. For instance, in the case of the Cray XC50, only 2GB per process can be utilized. For instance, if we trace the magnetic field lines for 500 toroidal rotations and use a 4-point interpolation, it requires memory on the order of terabytes. Therefore, it is not feasible to trace the magnetic field lines for more than 1000 toroidal rotations due to the memory constraint. Figure 5.4 indicates that tracing for about 100 laps is insufficient to construct a flux surface. Instead, approximately 1000 rotations are necessary to properly form the flux surfaces. The reason for the incorrect results shown in Fig. 5.3(b) is considered to be the overestimation of low poloidal number modes due to the insufficient formation of the flux surfaces.

We improve the tracing method and develop a new method called the labeling method consisting of the following three steps.

1. By calculating the equations of the magnetic field lines with different initial values in the radial and poloidal directions, we obtain the coordinates of the points constituting the flux surfaces on poloidal planes. Each magnetic field line is traced 3000 laps in the toroidal direction to construct the flux surface.

2. The distance between the 3D discretized grid points in real space and the points obtained in step 1 is calculated, and then the grid points are grouped according

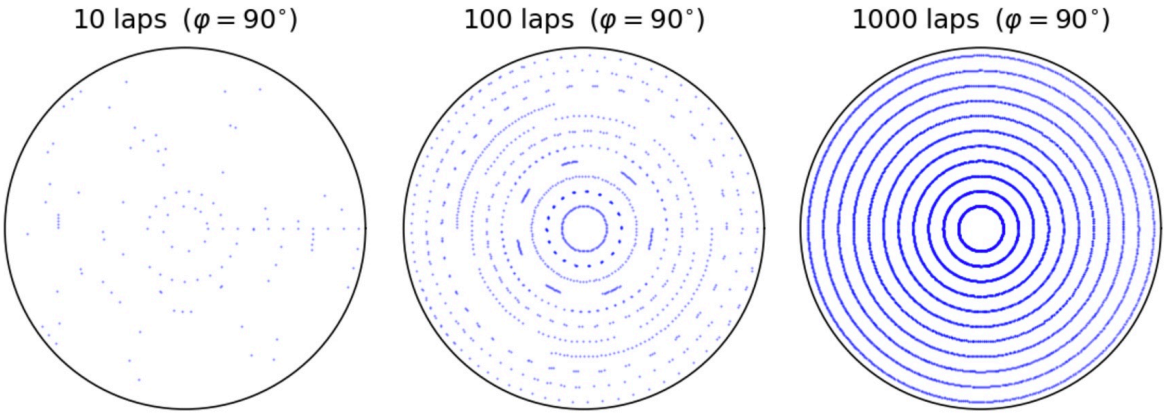

Fig. 5.4: Poincaré plots at $\varphi = 90$ in the absence of magnetic islands. From left to right, the plots represent the magnetic field line trajectories after 10, 100, and 1000 toroidal rotations, respectively.

to the magnetic field line that minimizes the distance. The maximum number of groups is the number of initial values when solving the equations of the magnetic field lines.

3. We take the average for each group.

Similar to the tracing method, since steps 1 and 2 need only be performed once initially, the effective computational time is essentially zero. When there is no magnetic island, there is no gap between the grid points and magnetic flux surfaces. From Fig. 5.3, it is evident that the labeling method provides a good approximation. However, it is noted that the labeling method cannot fully reproduce the flux-surface average given by Eq. (5.23). Due to the same grid number on the high magnetic field side and low magnetic field side, the $(m, n) = (1, 0)$ mode disappears with the flux-surface averaging. This issue comes from perceiving a flux surface as points rather than as a face. To achieve accurate calculations of the $(m, n) = (1, 0)$ mode, improvements to the method are necessary.

The equations of the magnetic field lines in the presence of the magnetic island are given by

$$\begin{cases} \dfrac{dr}{d\varphi} = -2I_a \dfrac{rR}{R_0} h(r) \sin(2\theta - \varphi) \\ \dfrac{d\theta}{d\varphi} = \dfrac{R}{qR_0} - 2I_a \dfrac{R}{R_0} h(r) \cos(2\theta - \varphi) \\ \qquad\quad + 2(r - I_b \rho_i) \dfrac{I_a}{I_c} \dfrac{rR}{\rho_i^2 R_0} h(r) \cos(2\theta - \varphi) \end{cases} . \tag{5.25}$$

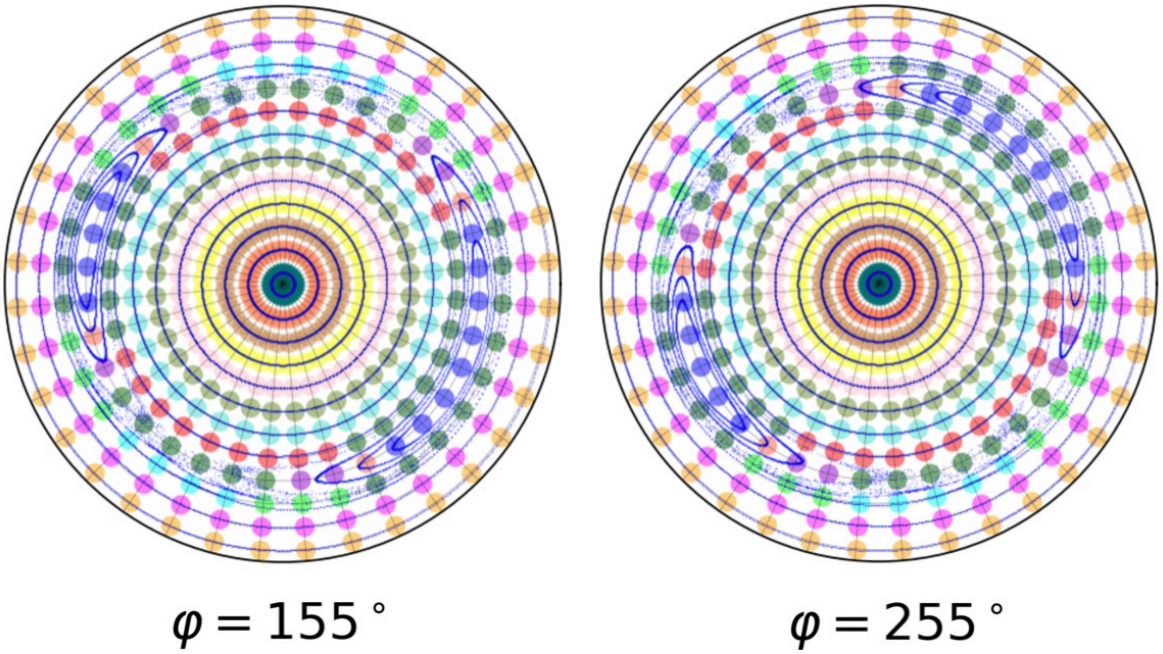

Fig. 5.5: Grouped grid point in the poloidal plane at $\varphi = 155°$ and $\varphi = 255°$.

Figure 5.5 shows an example of grouped real space grid points calculated by the labeling method, where points of the same color represent the same groups (the flux surfaces), and the small blue dots are the numerical solutions of Eq. (5.25). For clarity, the low-resolution case $(N_r, N_\theta, N_\varphi) = (12, 36, 36)$ is shown. The distance between flux surfaces and grid points reaches its maximum at the O-point and is given by $\sqrt{r^2\Delta\theta^2 + \Delta r^2}\rho_i/2$. It becomes smaller as the grid size decreases. For the parameters used in this study, $(N_r, N_\theta, N_\varphi) = (96, 160, 144)$, The largest gap is calculated to be $1.07\rho_i$.

Figure 5.6(a) represents the Poincaré map obtained by tracing the magnetic field lines for 3000 laps in the toroidal direction. It is noteworthy that the magnetic field is asymmetric in the poloidal direction and possesses ergodic regions. This comes from a toroidal effect. For $(N_r, N_\theta, N_\varphi) = (80, 160, 160)$, the result of calculating the flux-surface average of

$$\phi = \sum_{m=-79}^{m=79} \sum_{n=0}^{79} 100 \cos(m\theta - n\varphi) \tag{5.26}$$

using the labeling method is also shown in 5.6(a). Not only does the $(m, n) = (2, 1)$ mode have a relatively large value, but due to the toroidal effect, several modes other than the $(m, n) = (2, 1)$ harmonics have finite small values. On the other hand, if the toroidal effect is ignored, as shown in Fig. 5.6(b), only the $(m, n) = (2, 1)$ harmonic

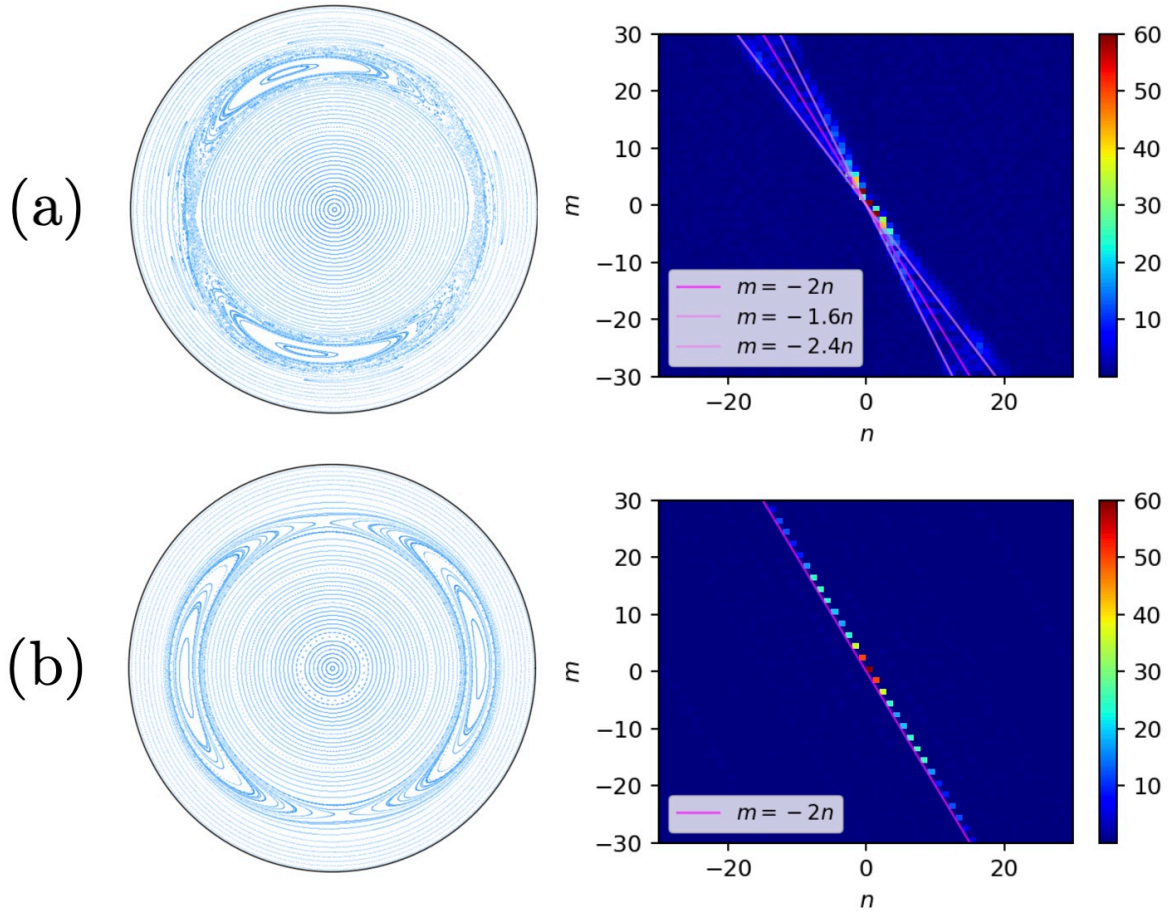

Fig. 5.6: Magnetic field structures and mode components of the flux-surface average, in the presence of the magnetic island (a) and in the case of the simplified magnetic island (b).

modes are non-zero. In this case, the magnetic field is given by

$$\begin{cases} \dfrac{dr}{d\varphi} = -2I_a r h(r)\sin(2\theta-\varphi) \\ \dfrac{d\theta}{d\varphi} = \dfrac{1}{q} - 2I_a h(r)\cos(2\theta-\varphi) \\ \qquad\qquad + 2(r-I_b\rho_i)\dfrac{I_a}{I_c}\dfrac{r}{\rho_i^2}h(r)\cos(2\theta-\varphi) \end{cases} . \tag{5.27}$$

However, this approximation breaks the Gauss's law for magnetism $\nabla\cdot\boldsymbol{B}=0$ and the phase space volume conservation $\partial/\partial\boldsymbol{R}\cdot(\mathcal{J}d\boldsymbol{R}/dt)+\partial/\partial v_\parallel\left(\mathcal{J}dv_\parallel/dt\right)=0$, which are required for the Morinishi scheme. In order to avoid numerical noise caused by small amplitude modes due to the toroidal effects, only the main modes $(m,n)=(0,0),(2,1),(4,2)$ are extracted by a numerical filter. It is applied only to flux-surface averaged values.

5.3 Effects of magnetic island on profiles and turbulence

5.3.1 Profile flattening

We conduct neoclassical transport simulations in the presence of the magnetic island. The simulations are performed for a tokamak with $a_0 = 150\rho_i$ and $a_0/R_0 = 0.36$. Although wedge torus configurations are often used to save computational cost in full-f simulations, such an approximation cannot be adopted in this study because the magnetic island with $n = 1$ is introduced. $L_{v_\parallel}$ and L_μ are the same as those in the previous chapter. The grid numbers used in the simulations are $(N_r, N_\theta, N_\varphi, N_{v_\parallel}, N_\mu) = (96, 160, 144, 80, 16)$. The initial density and temperature gradients at $r = 0.5a_0$ are $(R/L_n, R/L_{Ti}, R/L_{Te}) = (3, 3, 3)$ and below the linear instability threshold for the toroidal ITG mode. Their radial profiles are given by Eqs. (4.59) and (4.60).

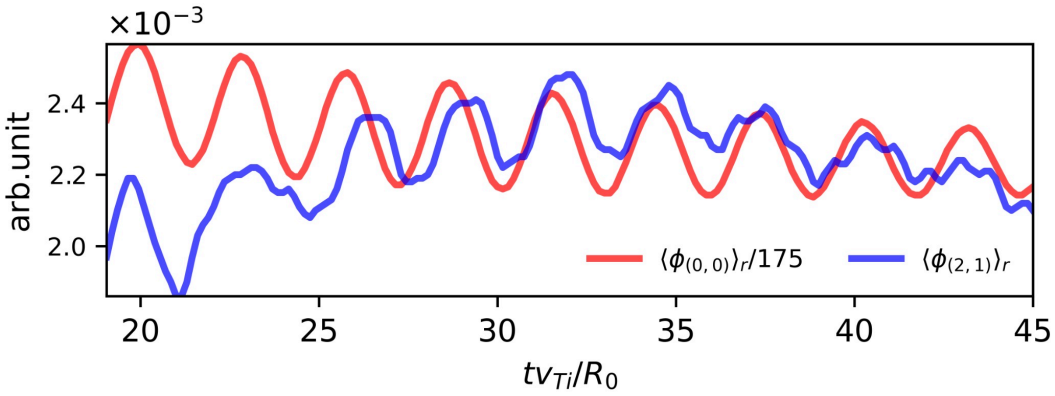

Fig. 5.7: Temporal evolution of radial average of $\phi_{0,0}$ and $\phi_{2,1}$

Figure 5.7 shows that the $(0, 0)$ and $(2, 1)$ components of the electrostatic potential oscillate at the same frequency $\omega R_0/v_{Ti} = 2.17$. This frequency corresponds to that of the GAM. This result is consistent with the simulation results obtained by GTC in the presence of the $(2, 1)$ magnetic island [210]. The $(0, 0)$ and $(2, 1)$ electrostatic potentials are phase-shifted by $\pi/2$ from the $(1, 0)$ electrostatic potential. The electric field that gives rise to the polarization current to counteract the diamagnetic current caused by the $(1, 0)$ pressure fluctuation is phase-shifted by $\pi/2$ with respect to the $(1, 0)$ electrostatic potential. This suggests that the $(2, 1)$ electrostatic potential originates from the electric field responsible for generating the polarization current. The result suggests a connection with the synchronization of the GAM and magnetic field fluctuations observed in HL-2A [218]. This oscillation of $\phi_{2,1}$ does not appear unless

the flux-surface average is accurately computed. Without using the labeling method, the gyroknetic Poisson equation is computed in the same manner as in the absence of a magnetic island. In the case, the $(2, 1)$ electric field is underestimated, and the $(0, 0)$ electric field is increased instead. As as result, the $(2, 1)$ electric field does not involve with the GAM dynamics. A GAM oscillation with a long period and a small damping rate, which originates from the magnetic field structure of the island, was theoretically predicted and confirmed in simulations using GKW [213]. However, it it not observed in our simulations. This might be attributed more to globality or island width than to differences in electron response or the radial force balance. This is because it is not observed even in GTC simulations using a drift kinetic electron model.

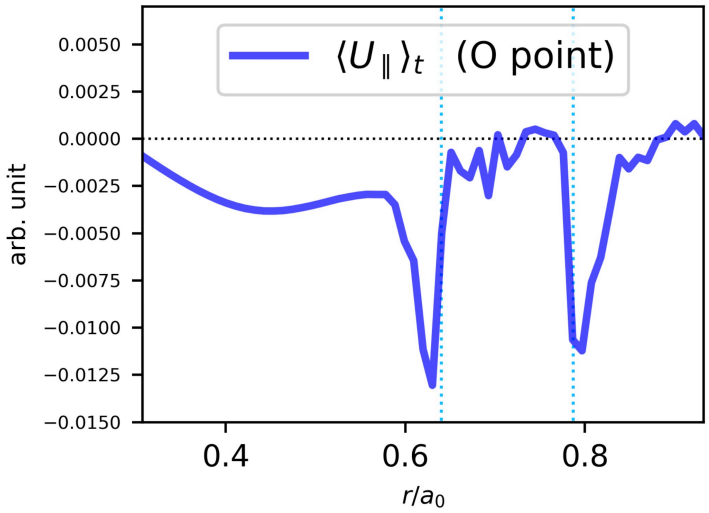

Fig. 5.8: Radial profile of time averaged parallel flow at the O-point.

Figure 5.8 shows the radial profile of time averaged parallel flow. Inside the magnetic island, the flow is zero, and a large flow shear is observed at the boundaries of the island. It is considered that the flow is formed to satisfy the radial force balance. This result is consistent with the experimental findings in JT-60U where the toroidal flow inside the magnetic island is zero and the large flow shear is formed at the boundaries [201].

Figure 5.9 shows the time averages of (a) the ion density profile and (b) the ion temperature profile at the X-point and O-point. The light blue dotted lines indicate the boundaries of the magnetic island. (V) indicates the case where only the gyrokinetic Vlasov equation is computed, and (V + P) indicates the case where the gyrokinetic

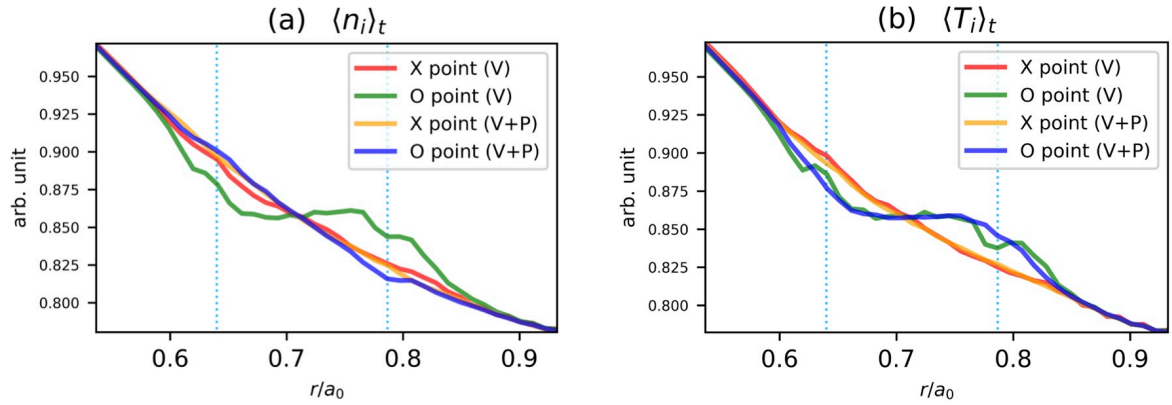

Fig. 5.9: Time averaged radial profiles of (a) ion density and (b) ion temperature at the X-point and O-point.

Vlasov equation and the gyrokinetic Poisson equation are solved self-consistently. Profile corrugation of the density and temperature might be due to the ergodic region due to the toroidal effects. When only the gyrokinetic Vlasov equation is computed with the electrostatic potential being zero, both the density and temperature profiles are flattened at the O-point. On the other hand, when solving particle motion and field self-consistently, only the temperature profile becomes flat at the O-point, while the density profile remains almost unchanged from the initial state. It is noteworthy that this is brought about by the mean electric field rather than by trapped particles. While previous studies have focused on trapped particles hindering the flattening of the density profile at the O-point, it is a novel result that the mean electric field plays this role.

In order to investigate the mechanism of this phenomenon, we examine the force balance in the direction parallel to the magnetic field. This is because the flattening of the profiles is brought about by the motion along the magnetic field. Multiplying the gyrokinetic Vlasov equation by $v_\parallel B^*_\parallel/m_i$, integrating it over vecoity apace, and averaging it over the poloidal and toroidal directions, without any approximations, we obtain the parallel force balance equation,

$$\begin{aligned} -\frac{\partial}{\partial t}\langle nU_\parallel\rangle_{\theta,\varphi} = \frac{1}{m_i}\frac{\partial}{\partial r}\langle p_\parallel b_r\rangle_{\theta,\varphi} + \frac{\partial}{\partial r}\langle n\Pi_{\parallel,E\times B,r}\rangle_{\theta,\varphi} + \frac{\partial}{\partial r}\langle n\Pi_{\parallel,\nabla B,r}\rangle_{\theta,\varphi} \\ - \langle nA_{Er}\rangle_{\theta,\varphi} - \langle nA_{E\theta}\rangle_{\theta,\varphi} - \langle nA_{E\varphi}\rangle_{\theta,\varphi} + \langle nA_{\nabla B}\rangle_{\theta,\varphi} \\ + A_{\mathrm{snk}}\tau^{-1}_{\mathrm{snk}}\langle nU_\parallel\rangle_{\theta,\varphi} \end{aligned} \tag{5.28}$$

where we define the fluid quantities as follows;

$$nU_\parallel = \iint v_\parallel f_i \frac{B^*_\parallel}{m_i} dv_\parallel d\mu, \tag{5.29}$$

$$n\Pi_{\parallel,E\times B,r} = \iint v_\parallel \frac{c}{m_i}\left(\boldsymbol{E}\times\boldsymbol{b}\right)_r f_i dv_\parallel d\mu, \tag{5.30}$$

$$p_{\parallel} = m_i \iint v_{\parallel}^2 f_i \frac{B_{\parallel}^*}{m_i} dv_{\parallel} d\mu, \tag{5.31}$$

$$n\Pi_{\parallel,\nabla B,r} = \iint v_{\parallel} \frac{c}{m_i e} \left\{ \boldsymbol{b} \times \left(m_i v_{\parallel}^2 \boldsymbol{b} \cdot \nabla \boldsymbol{b} + \mu \nabla B \right) \right\}_r f_i dv_{\parallel} d\mu, \tag{5.32}$$

$$nA_{Er} = \iint \frac{e}{m_i^2} B_r^* E_r f_i dv_{\parallel} d\mu, \tag{5.33}$$

$$nA_{E\theta} = \iint \frac{e}{m_i^2} B_\theta^* E_\theta f_i dv_{\parallel} d\mu, \tag{5.34}$$

$$nA_{E\varphi} = \iint \frac{e}{m_i^2} B_\varphi^* E_\varphi f_i dv_{\parallel} d\mu, \tag{5.35}$$

$$nA_{\nabla B} = \iint \frac{\mu}{m_i^2} \boldsymbol{B}^* \cdot \nabla B f_i dv_{\parallel} d\mu. \tag{5.36}$$

$$\tag{5.37}$$

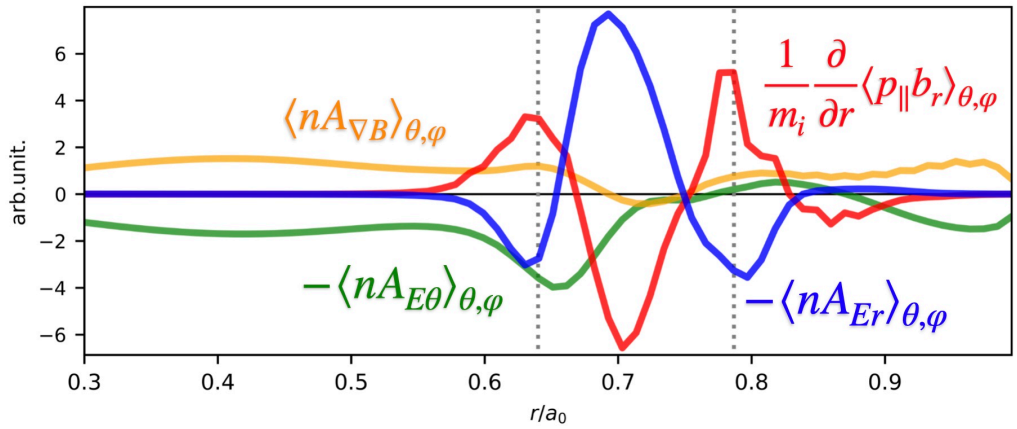

Fig. 5.10: Time-averaged radial profiles of the main terms in the parallel force balance equation.

Figure 5.10 shows the radial profiles of the main terms in the parallel force balance equation. The other terms are very small and can be ignored. It is found that, in the steady state, inside the magnetic island,

$$\frac{1}{m_i} \frac{\partial}{\partial r} \langle p_{\parallel} b_r \rangle_{\theta,\varphi} = \langle nA_{Er} \rangle_{\theta,\varphi} \tag{5.38}$$

is satisfied, while outside the island,

$$\langle nA_{\nabla B} \rangle_{\theta,\varphi} = \langle nA_{E\theta} \rangle_{\theta,\varphi} \tag{5.39}$$

is met. $(1/m_i)(\partial/\partial r)\langle p_{\parallel} b_r \rangle_{\theta,\varphi}$ in Eq. (5.38) is derived from the term representing the ion parallel streaming in the gyrokinetic Vlasov equation and is zero in the absence of

magnetic islands because $b_r = 0$. When only the gyrokinetic Vlasov equation is solved, the parallel momentum is driven by this term, leading to the flattening of the density profile. On the other hand, when the gyrokinetic Poisson equation is also calculated self-consistently, the force balances with the force due to the mean radial electric field $\langle nA_{Er}\rangle_{\theta,\varphi}$, preventing the density profile from becoming flat. This does not imply a balance between the parallel energy flux due to parallel streaming and that due to the mean radial electric field and the temperature profile is flattened at the O-point. It is noteworthy that $(1/m_i)(\partial/\partial r)\langle p_\parallel b_r\rangle_{\theta,\varphi}$ is determined primarily by the temperature gradient rather than the density gradient. This is because the primary component of b_r is $(m, n) = (2, 1)$, and when it is coupled with the density gradient that has only $(0, 0)$ component, the poloidal and toroidal average of the coupling is quite small.

The gradients within a magnetic island is deeply associated with the stability of the neoclassical tearing mode (NTM), a large-scale MHD instability that set a limit to achievable pressure. When the pressure gradient inside a magnetic island decreases, the bootstrap current decreases, leading to reinforce the NTM growth. The primary contribution to the bootstrap current comes from the density gradient, accounting for approximately 65% [219]. Therefore, the question of whether the magnetic island flattens the density profile is of importance for the realization of commercial fusion energy, and has been the subject of research. It was shown that when a small magnetic island rotates at a frequency close to the ion diamagnetic frequency, the density gradient becomes zero inside the magnetic island. Conversely, when it rotates at a frequency close to the electron diamagnetic frequency, the density gradient is preserved [220]. When the island width exceeds the radial correlation length of turbulence, it was observed that the density gradient no longer depends on the rotation frequency of the island, and the density profile relaxes [221]. Simulation results from GTC revealed that in the banana region, while the density profile is flattened on the high field side, on the low field side, the density gradient is preserved due to trapped particles [222]. It was also shown that in the plateau region, the density profile is flattened, and in the collisional region, a small density gradient exists due to collisional transport across the magnetic island. The simulation results from GENE indicate that the density gradient at the O-point shows little dependence on the width of the magnetic island and, while it relaxes, it does not flatten as much as the temperature gradients [215]. Some believe that the density profile within a magnetic island should be flattened. In Ref [210], the electrostatic potential was turned off until a flat density profile was attained, and then they performed self-consistent gyrokinetic simulations. On the other hand, the results of the neoclassical simulations using XGC1, and HL-2A experiment results indicate that the density profile is not flattened at the O-point [216, 199]. It is speculated that the trapped particles maintain a steep density profile at the O-point

in the reference [215]. We consider that the observed flattening of the density profile in previous studies is due to the neglect of the mean radial electric field, namely, the use of the δf gyrokinetic model. When one takes into account the the mean electric field, the force arising from the radial electric field is balanced by the force due to the parallel streaming, maintaining the density gradient within the magnetic island. The destabilizing effect for a magnetic island is smaller than that observed in previous studies.

5.3.2 Statistical analysis for turbulent vortices

We conducted turbulence simulations in the presence of the magnetic island and performed statistical analysis of the turbulent vortices. The input power is 2 MW, and the initial background profiles are such that at $r = 0.5a_0$, $(R/L_n, R/L_{Ti}, R/L_{Te}) = (2.22, 6.92, 6.92)$. The temperature profile is flattened by parallel streaming, and at the inner boundary of the magnetic island, R/L_{Ti} exceeds 9.5. Therefore, as illustrated in Fig. 5.11, there exists modes that arise at the boundary of the island. Figure 5.11 shows the contour plots of the $n = 22$ electrostatic potential at $tv_{Ti}/R_0 = 60$, where the black line represents the inner boundary of the magnetic island. In the presence of the island, the maximum value of the temperature gradient is larger and the time to nonlinear saturation is shortened. In the linear phase, the electrostatic potential is dominated by the $n = 0$ and $n = 1$ components. This is attributed to the radial force balance.

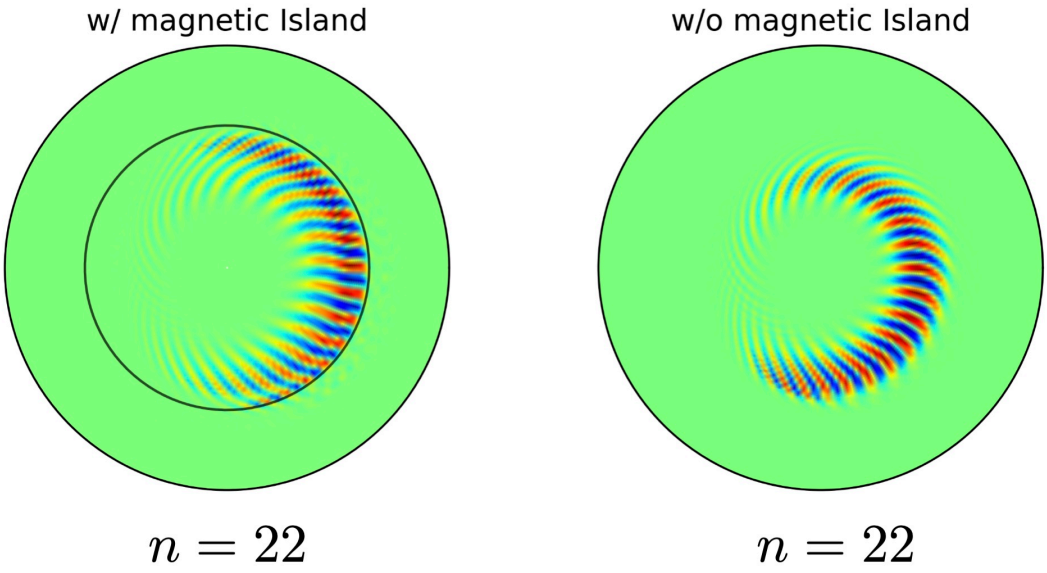

Fig. 5.11: Electrostatic potential structure in the presence and absence of the magnetic island.

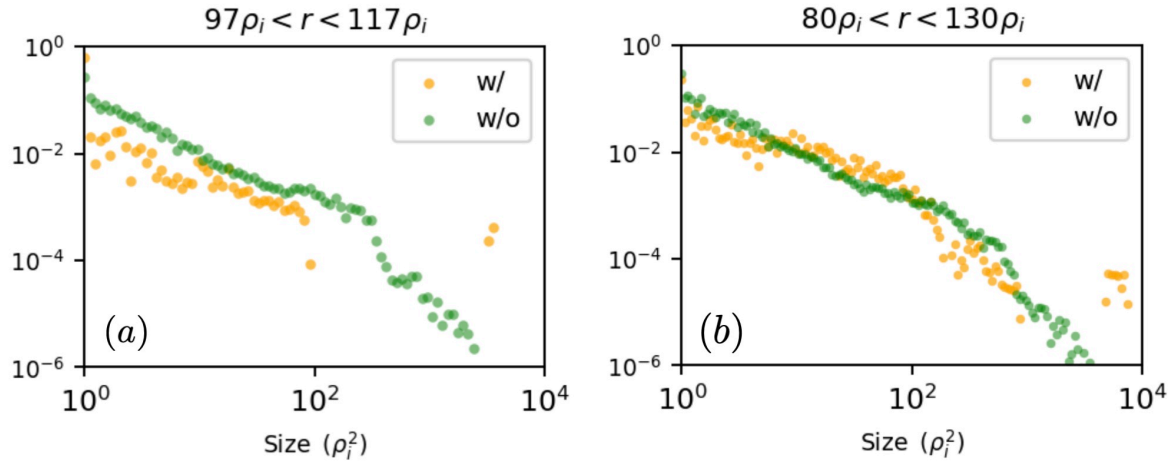

Fig. 5.12: (a) Size PDF of the electrostatic potential inside the magnetic island and (b) size PDF in the magnetic island and its vicinity.

Figures 5.12(a) and 5.12(b) show the size probability distribution function (PDF) of the electrostatic potential within the magnetic island ($97\rho_i < r < 117\rho_i$) and the size PDF of the magnetic island and its surroundings ($80\rho_i < r < 130\rho_i$), respectively. The size PDF represents the distribution of the area of the turbulent vortices in the poloidal cross-sections, with the detailed algorithm described in Appendix A. While the turbulent vortices inherently possess a three-dimensional structure, the size PDF analysis assumes that the two-dimensional turbulent vortices in each poloidal cross-section are independent of those in other poloidal cross-sections. From Figs. 5.12(a) and 5.12(b), it is found that in the presence of the magnetic island, turbulent vortices are sheared, leading to an increase in smaller vortices and a decrease in relatively larger ones. Moreover, mesoscale turbulent vortices, which did not exist when there was no magnetic island, are also observed. These large vortices correspond to the vortex mode with the same $(2, 1)$ mode as the magnetic island. These vortices drifts in the poloidal direction, thus they are not the electrostatic potential due to the lowest-order force balance. The reason why the vortex mode grows easily within the magnetic island is the same as why zonal flows grow readily in the absence of a magnetic island [73, 83]. Since $k_{\|} = 0$ fluctuations do not produce an electric field along the magnetic field lines, Boltzmann electrons cannot shield these fluctuations, leading to mode growth. Therefore, within the magnetic island, the mode with the same topology as the magnetic island grow nonlinearly. The vortex mode cannot be generated unless adiabatic electrons are properly treated. If one assumes $\langle\phi\rangle_f \simeq \phi_{0,0}$, the vortex mode does not appear. It is considered that turbulent vortices are sheared by the mesoscale flow shear [223], resulting in smaller turbulent vortices inside the magnetic island.

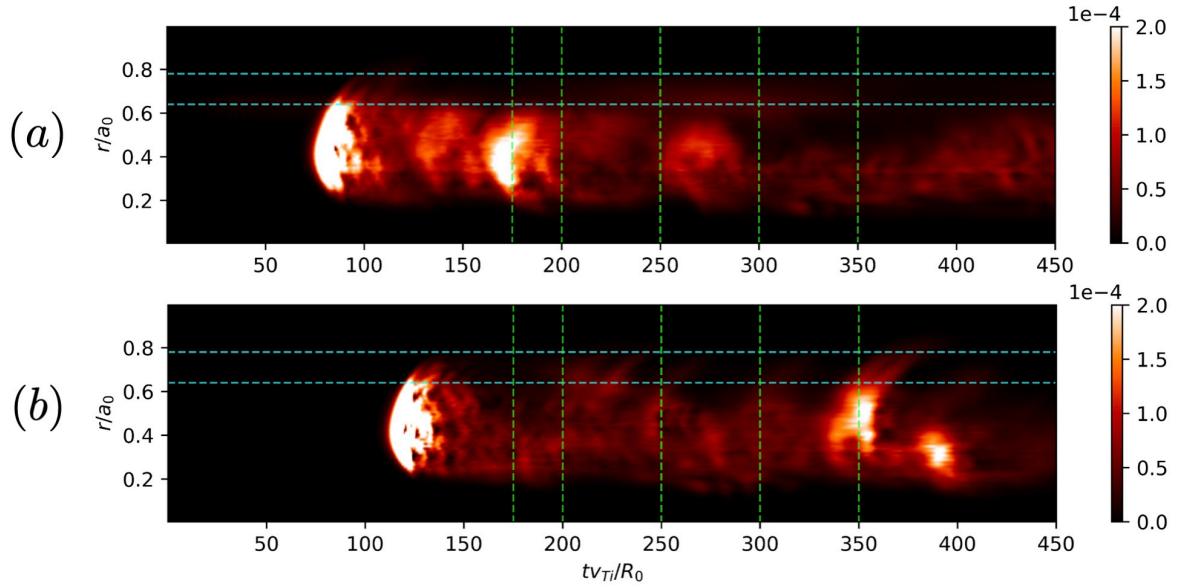

Fig. 5.13: Spatiotemporal evolutions of the turbulent heat flux in (a) the presence and (b) the absence of the magnetic island.

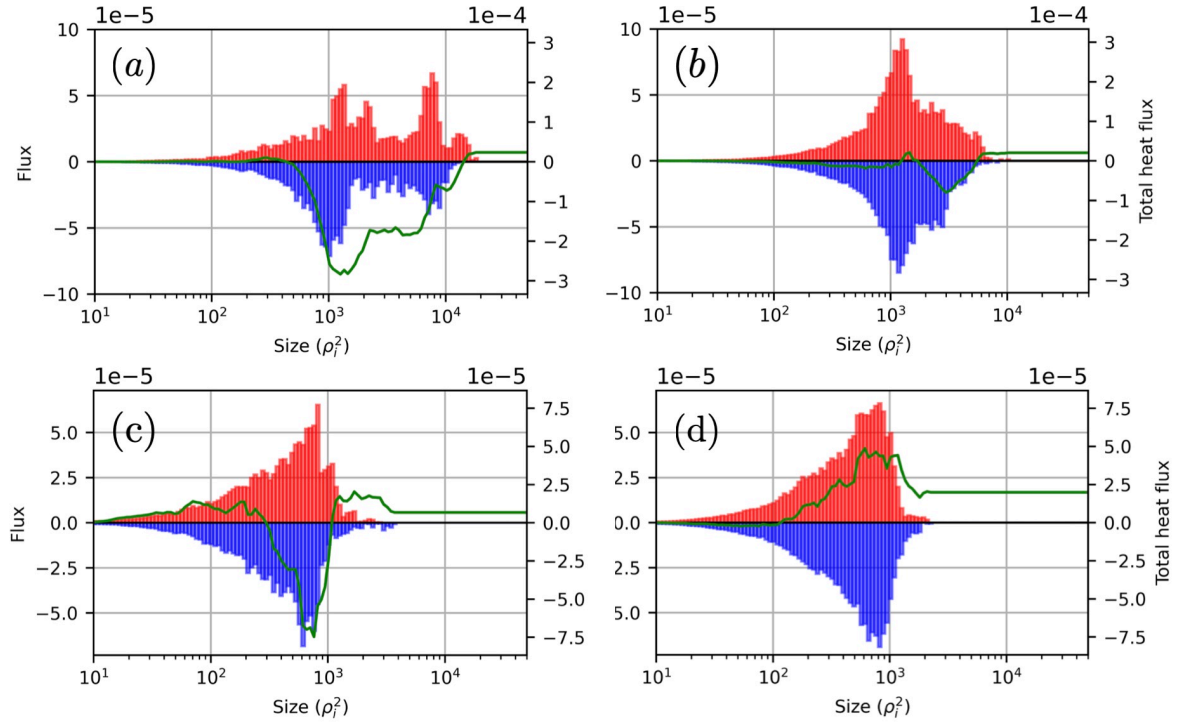

Fig. 5.14: Heat flux contribution for both positive and negative components against the size of eddies, and net cumulative heat flux. (a) and (b) correspond to the case of $\beta = 0.01$, while (c) and (d) correspond to $\beta = 0.05$. (a) and (c) correspond to the case of the presence of the magnetic island, whereas (b) and (d) correspond to its absence.

Figure 5.13 shows the spatiotemporal evolutions of the poloidal and toroidal av-

eraged turbulent heat flux $\langle Q \rangle_{\theta,\varphi}$, both in the presence and absence of the magnetic island. The light blue lines represent the boundaries of the magnetic island. It is observed that heat avalanches do not penetrate the interior of the magnetic island. Additionally, the radial correlation length of the turbulence is small. These phenomena are attributed to the shearing effect of the vortex mode and the flat temperature profile. It is suggested that heat could be dammed at the inner boundary of the magnetic island. Figures 5.14(a) and 5.14(b) respectively depict the averaged heat flux contribution for both positive (red) and negative (blue) components against the size of the turbulent eddies, and the averaged net cumulative heat flux (green) in the presence and absence of the magnetic island for $\beta = 0.01$. The averaged heat flux contribution is evaluated using the heat flux at $tv_{Ti}/R_0 = 175, 200, 250, 300, 350$ which are indicated by the green dashed lines in Fig. 5.13. As shown in Fig A.3, for $\beta = 0.01$, it is possible to reproduce the original net heat flux. In the absence of the magnetic island, the heat flux contribution has a peak only around $10^3\rho_i^2$, however when there is the magnetic island, two peaks are observed around $10^3\rho_i^2$ and $10^4\rho_i^2$. Figure 5.13(a) indicates that $tv_{Ti}/R_0 = 175$ corresponds to a bursting phase, and the averaged heat flux contribution at $tv_{Ti}/R_0 = 175$ is similar to that in Fig.5.14(b). Therefore, the peak around $10^3\rho_i^2$ can be concluded to result from transport burst. On the other hand, the peak around $10^4\rho_i^2$ originates from the mesoscale vortex mode. This does not imply that the vortex mode induces significant radial transport. Due to the small value of β, Fig. 5.14(a) shows the contribution of heat flux from vortices which combine ones with long radial correlation with the vortex mode. Whether the vortex mode produces heat flux or not cannot be determined from Fig. 5.14(a). Figures 5.14(c) and 5.14(d) represent the counterparts for Figs. 5.14(a) と 5.14(b) respectively, for $\beta = 0.05$. The averaged heat flux contribution is similar both with and without the presence of the magnetic island. This implies that the radial heat flux due to the vortex mode is less than 5% of the maximum heat flux caused by the turbulence. In other words, the heat flux due to the vortex mode is not zero, but it is small. In our simulations, the vortex mode contributes to confinement improvement. As indicated in previous studies, there is a possibility that the heat flux due to low n modes increase as the island width is enlarged [209, 211].

5.3.3 Impact of magnetic island on confinement

By setting the input power to 16 MW, we investigate how strong plasma turbulence interacts with the magnetic island and affects confinement performance. The initial ion

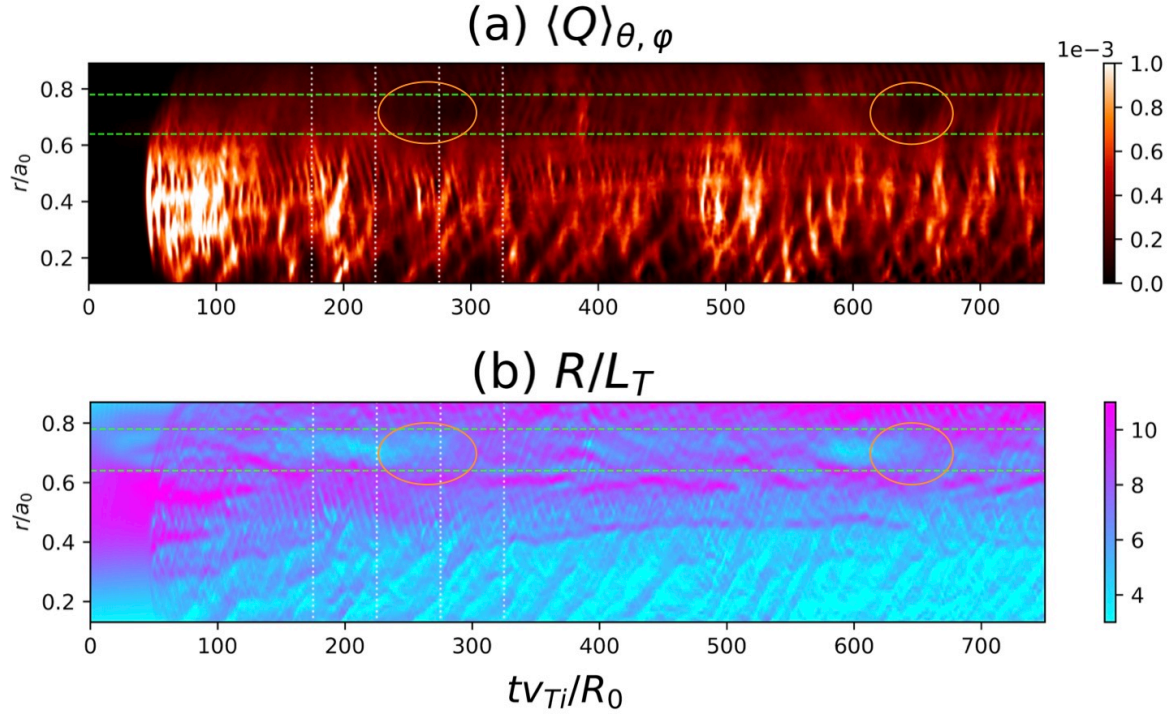

Fig. 5.15: Spatiotemporal evolutions of (a) the turbulent heat flux and (b) the ion temperature gradient length.

temperature gradient length is $R/L_{Ti} = 10$ at $r = 0.5a_0$. Figures 5.15(a) and 5.15(b) show the spatiotemporal evolution of the heat flux $\langle Q \rangle_{\theta,\varphi}$ and ion temperature gradient length R/L_{Ti}, averaged in the poloidal and toroidal directions, respectively. The green dotted lines represent the boundaries of the magnetic island. Figure 5.16(a) displays the temporal evolution of the heat flux averaged within the magnetic island $(\langle Q \rangle_{\theta,\varphi})_{\text{inside}}$, and the heat flux and ion temperature gradient at the inner boundary of the magnetic island, $(\langle Q \rangle_{\theta,\varphi})_{\text{boundary}}$ and $(R/L_{Ti})_{\text{boundary}}$. In Fig. 5.15, the areas enclosed by the orange circle indicate a transport reduction phase. In Fig. 5.16, the corresponding times are shaded in orange. This implies that in the presence of a magnetic island, turbulence transport is periodically suppressed. During the transport reduction phase, the heat diffusion coefficient is confirmed to be less than half compared to the case without a magnetic island. The large temperature gradient at the inner boundary of the island is maintained. It increases just before the transport reduction phase. Figure 5.16(b) shows the temporal evolution of the normalized $\phi_{(2,1)} - \langle \phi_{(2,1)} \rangle_t$ and the temperature gradient length averaged within the magnetic island, demonstrating that they are out of phase. The $(2, 1)$ electrostatic potential is in the vortex mode, growing linearly, and reaches its maximum amplitude just before the transport reduction phase. During the transport reduction phase, the amplitude of the vortex mode monotonically decreases and the temperature gradient inside the magnetic island increases. Figure 5.17 shows the contour plots of the electrostatic potential at $tv_{Ti}/R_0 = 175, 225, 275$

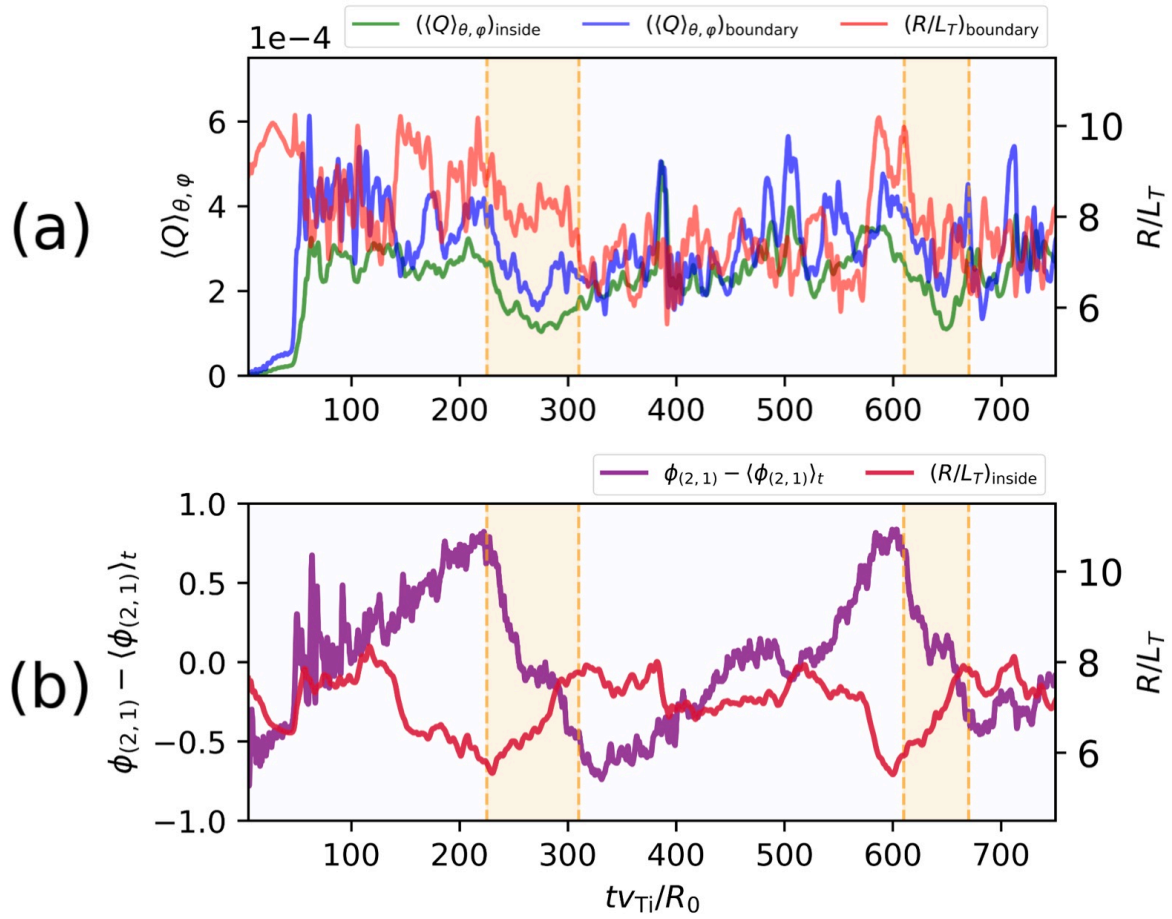

Fig. 5.16: (a) Temporal evolutions of the heat flux averaged inside the island and the heat flux at the inner boundary, and ion temperature gradient length at the inner boundary. (b) Temporal evolutions of the normalized $(m, n) = (2, 1)$ electrostatic potential subtracted by the average and the ion temperature gradient length averaged inside the island.

and 325 on the $\varphi = 3.75°$ poloidal plane. In Fig. 5.15, $tv_{Ti}/R_0 = 175, 225, 275$ and 325 are indicated by the white dotted lines. From Fig. 5.17, similar to Fig. 5.16(b), it can be seen that the vortex mode grows until the transport reduction phase and then decays. It is worth highlighting that while the vortex mode grows, it rotates in the poloidal direction. The direction of the rotation is in line with the electron diamagnetic drift direction, which is opposite to the drift direction of the ITG mode. This implies that the rotation is due to the mean radial electric field. As the vortex mode grows, the temperature gradient inside the magnetic island decreases. Therefore, the drift velocity of the vortex mode also reduces, as shown in Figs. 5.16(b) and 5.17. During the transport reduction phase, as the amplitude of the vortex mode reduces, the structure of the electrostatic potential becomes close to that in the case without a magnetic island, as depicted in the contour plot at $tv_{Ti}/R_0 = 325$ in Fig. 5.17. Therefore, after the transport reduction phase, as shown in Fig. 5.15(a), the heat

avalanche occurs inside the magnetic island. At this time, as shown in Fig. 5.16(a), the heat flux at the inner boundary of the magnetic island and its interior is almost the same.

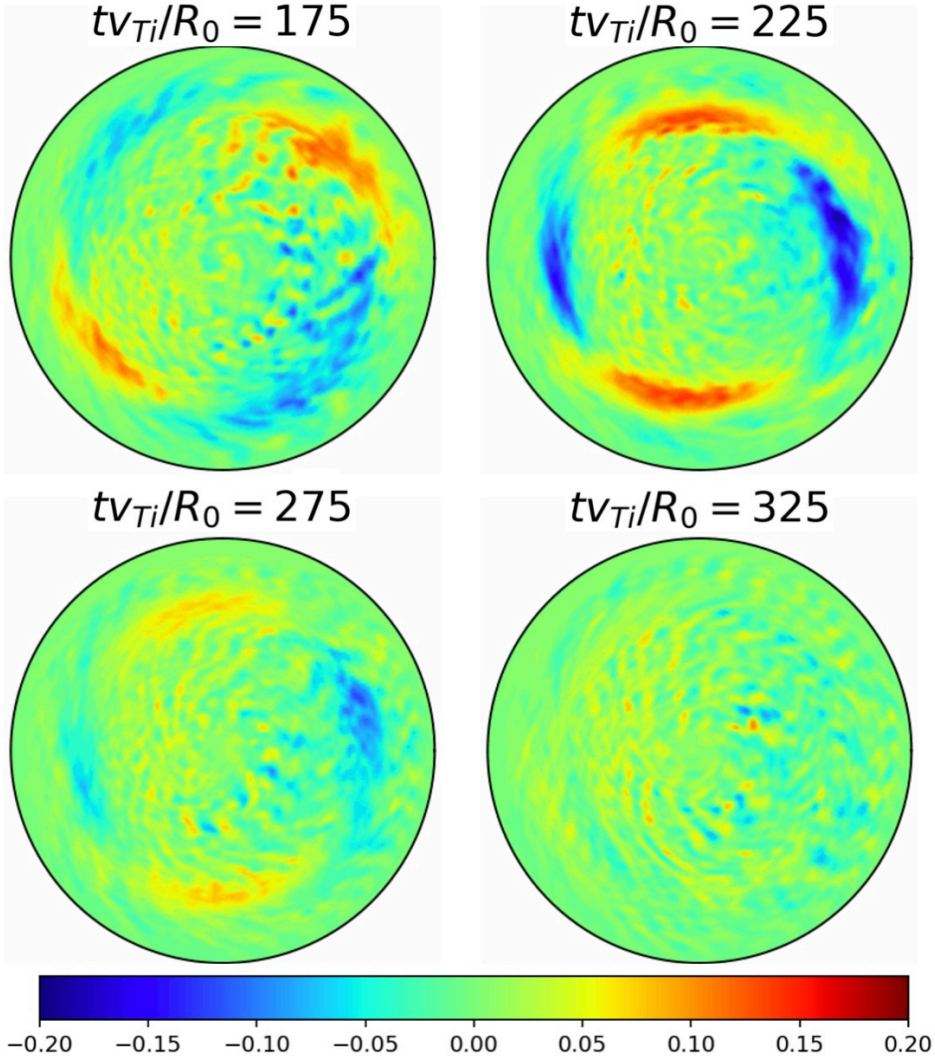

Fig. 5.17: Contour plots of the electrostatic potential at $tv_{Ti}/R_0 = 175, 225, 275$ and 325 on the $\varphi = 3.75°$ poloidal plane.

Using the normalized Hasegawa-Mima equation

$$\left(1 - \nabla^2\right) \frac{\partial \phi}{\partial t} + \left(\frac{\partial}{\partial x} \nabla^2 \phi \frac{\partial \phi}{\partial y} - \frac{\partial}{\partial y} \nabla^2 \phi \frac{\partial \phi}{\partial x} \right) = 0, \tag{5.40}$$

we investigate the mechanism by which the vortex mode linearly grows. We expand ϕ as $\phi = \phi_{k_1}(t)\ e^{i\boldsymbol{k}_1 \cdot \boldsymbol{r}} + \phi_{k_2}(t)\ e^{i\boldsymbol{k}_2 \cdot \boldsymbol{r}} + \phi_{k_3}(t)\ e^{i\boldsymbol{k}_3 \cdot \boldsymbol{r}}$ using Fourier decomposition. For simplicity, we consider only the wave numbers $\boldsymbol{k}_1, \boldsymbol{k}_2$, and $\boldsymbol{k}_3$ $(k_1 < k_2 < k_3)$ that satisfy

the resonance condition $\boldsymbol{k}_1 + \boldsymbol{k}_2 + \boldsymbol{k}_3 = 0$. From Eq. (5.40), we obtain the three-wave interaction equations [224]:

$$\frac{d\phi_{k_1}}{dt} = \Lambda^{k_1}_{k_2,k_3}\phi^*_{k_2}\phi^*_{k_3}, \tag{5.41}$$

$$\frac{d\phi_{k_2}}{dt} = \Lambda^{k_2}_{k_3,k_1}\phi^*_{k_3}\phi^*_{k_1}, \tag{5.42}$$

$$\frac{d\phi_{k_3}}{dt} = \Lambda^{k_3}_{k_1,k_2}\phi^*_{k_1}\phi^*_{k_2}, \tag{5.43}$$

where $\Lambda^{k_p}_{k_q,k_r}$ is defined as

$$\Lambda^{k_p}_{k_q,k_r} \equiv \frac{1}{2}\frac{1}{1+k_p^2}\left(k_{qx}k_{ry} - k_{qy}k_{rx}\right)\left(k_r^2 - k_q^2\right). \tag{5.44}$$

The three-wave interaction equations describe the energy exchange between three waves. Indeed, from Eqs. (5.41), (5.42), and (5.43), we have

$$\frac{d}{dt}(N_{k_3} - N_{k_1}) = 0, \quad \frac{d}{dt}(N_{k_2} + N_{k_3}) = 0, \quad \frac{d}{dt}(N_{k_1} + N_{k_2}) = 0, \tag{5.45}$$

where N_{k_p} is given by

$$N_{k_p} \equiv \mathrm{sgn}\left(k_q^2 - k_r^2\right)\frac{(1+k_p)^2}{k_q^2 - k_r^2}\left|\phi_{k_p}\right|^2. \tag{5.46}$$

At $t = 0$, when the amplitude of the wave with wave number k_3 is large and the amplitudes of other waves are small, $|\phi_{k_3}| \gg |\phi_{k_1}|, |\phi_{k_2}| \simeq 0$, from Eq. (5.43), we get $\phi_{k_3}(t) \simeq \phi_{k_30}$ (constant). From Eqs. (5.41) and (5.42), we obtain

$$\frac{d^2\phi_{k_1}}{dt^2} \simeq \Lambda^{k_1}_{k_2,k_3}\phi^*_{k_30}\frac{d\phi^*_{k_2}}{dt} = \Lambda^{k_1}_{k_2,k_3}\Lambda^{k_2}_{k_3,k_1}\left|\phi_{k_30}\right|^2\phi_{k_1} \tag{5.47}$$

and

$$\frac{d^2\phi_{k_2}}{dt^2} \simeq \Lambda^{k_2}_{k_3,k_1}\phi^*_{k_30}\frac{d\phi^*_{k_1}}{dt} = \Lambda^{k_1}_{k_2,k_3}\Lambda^{k_2}_{k_3,k_1}\left|\phi_{k_30}\right|^2\phi_{k_2}. \tag{5.48}$$

Consequently, in this case, ϕ_{k_1} and ϕ_{k_2} grow exponentially as represented by

$$\phi_{k_1}, \phi_{k_2} \propto \exp\left(\sqrt{\Lambda^{k_1}_{k_2,k_3}\Lambda^{k_2}_{k_3,k_1}}\left|\phi_{k_30}\right| t\right). \tag{5.49}$$

Since the vortex mode grows linearly, it is found that its growth is not due to the decay instability that excites two other waves from a single wave. Conversely, we consider the case where a single wave is excited by two waves. For $\phi_{k1}(0) = 0, \phi_{k_2}(0) = \phi_{k_20}$, and $\phi_{k_3}(0) = \phi_{k_30}$, from Eqs. (5.42) and (5.43), we obtain $\phi_{k_2}(t) = \phi_{k_20}$ and $\phi_{k_3}(t) = \phi_{k_30}$. Thus, from Eq. (5.41), we get

$$\phi_{k_1} = \left(\Lambda^{k_1}_{k_2,k_3}\phi^*_{k_20}\phi^*_{k_30}\right)t. \tag{5.50}$$

This suggests a linear growth of ϕ_{k_1} and is qualitatively consistent with Fig. 5.16(b). Therefore, it can be considered that the vortex mode is excited by two drift waves.

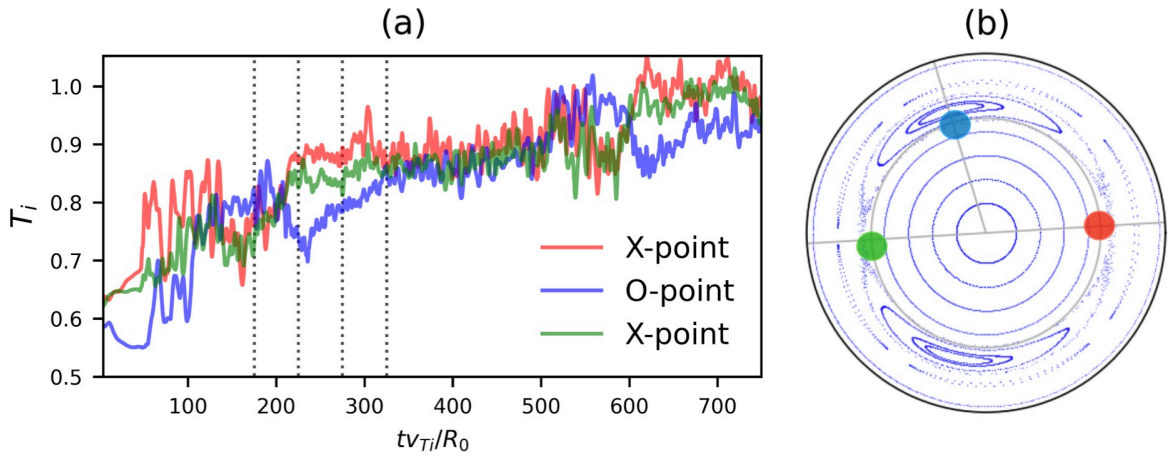

Fig. 5.18: (a) Time evolution of the temperatures at the X-points and the O-point. (b) Poincaré map of magnetic field lines on the $\varphi = 3.75°$ poloidal plane.

Figure 5.18(a) shows the temporal evolution of the ion temperatures at the X-points (red and green) and the O-point (blue). The corresponding locations are indicated on the Poincaré map in Fig. 5.18(b). $tv_{Ti}/R_0 = 175, 225, 275$ and 325 are indicated by the black dotted lines. With the growth of the vortex mode, it can be observed that the temperature rises at the X-points and decreases at the O-points. This suggests that the vortex mode drives the heat flux in the θ direction. This heat flux leads to the reduction in the temperature gradient inside the magnetic island, as observed in Fig. 5.16(b).

The mechanism for the quasi-periodic transport reduction and associated vortex mode dynamics can be described as follows. When the ITG turbulence is driven by ion temperature gradients, non-linear wave coupling leads to the linear growth of the vortex mode inside the island, which has the same topology as the magnetic island (Figs. 5.16(b) and 5.17). With the growth of the vortex mode, the heat transport occurs from the O-point regions to the X-point regions (Fig. 5.18), leading to a reduction in the temperature gradient inside the magnetic island (Figs. 5.15(b) and 5.16(b)). When the temperature gradient becomes sufficiently small, the ITG mode is no longer excited, and the drift velocity of the vortex mode decreases (Fig. 5.17). During the transport reduction phase, both the heat flux and thermal diffusivity decrease inside the island (Figs. 5.15(a) and 5.16(a)). The amplitude of the vortex mode decreases, while the temperature gradient inside the magnetic island increases (Figs. 5.15(b) and 5.16(b)). When the amplitude of the ITG turbulence exceeds that of the vortex mode, the electrostatic potential distribution becomes similar to that in the case without a magnetic island (Fig. 5.17). At this point, the ITG turbulence behaves as if there is no magnetic island, resulting in the heat avalanche inside the magnetic island (Figs.

5.15(a) and 5.16(a)). When the amplitude of the vortex mode is large, heat avalanches cannot penetrate into the interior of the island.

Chapter 6

Impurity transport and profile formation

6.1 Toroidal impurity mode turbulence

6.1.1 Stabilization and destabilization by impurities

It is believed that the accumulation of impurities can degrade confinement performance due to increased radiative losses and fuel dilution. However, when benefits brought by impurities outweigh the adverse effects, the confinement performance can be improved due to impurities. In tokamaks such as Impurity Study Experiment (ISX-B) [225, 226], TXTOR-94 [227, 228], HT-7 [229], DIII-D [230], and TFTR [231, 232], as well as in stellarators like LHD [233, 234, 235], the confinement improvement due to impurity injection was observed. In ISX-B, it was reported that puffing of neon led to an increase in ion and electron temperatures and electron density, with their gradients becoming more large [225]. Without the puffing of neon, the energy confinement time does not depend on the density. However, in the presence of neon, it was found that the energy confinement time increases proportionally with the density [226]. Similarly, in TXTOR-94, it was observed that with neon seeding, there is a rise in radiated power $P_{\rm rad}/P_{\rm tot} > 60\%$, and the enhancement factor increases proportionally with the density [227]. $P_{\rm rad}$ and $P_{\rm tot}$ represent the radiated power and total heating power, respectively. The confinement performance improves beyond the ELM-free H mode, and the density exceeds the Greenwald density limit. Adverse effects on fusion reactivity due to impurity seeding were not observed. This can be attributed to the reduction in sputtering as the edge temperature decreases, and the intrinsic impurities decreases by the amount the neon increases. Furthermore, the Li- and Be-like states of Ne, which are responsible for most of the radiation, have a longer ionization time compared to intrinsic impurities, resulting in the observation of a poloidally symmetric radiating

mantle at the plasma boundary. The radiation can dissipate the energy uniformly over the walls. This high-confinement regime, characterized by the radiating belt and strong density peaking, is referred to as the radiative improved (RI) mode. During the RI mode, the root mean square values of the potential fluctuations, the density fluctuations and poloidal electric field fluctuations decrease by half, and the turbulent particle transport reduces by a factor of 4–7 [228]. The cross-power spectrum of the density and electrostatic potential diminishes across all frequencies. The turbulence suppression in the RI mode does not originate from the $E \times B$ shear but is attributed to the stabilization of the ITG mode due to changes in the ion temperature and density profiles. The initial density peaking is triggered by a reduction in the turbulent particle transport due to a decreased linear growth rate, stemming from the increase in the effective mass and charge [236, 237, 238]. The RI mode by neon puffing was also observed on HT-7 [229]. Both energy and particle confinement improve simultaneously, with the electron density doubling and the profile steepening, and the central electron temperature increases by 1.4 times. A reduction in the turbulence was observed in the core region. In DIII-D, when neon was injected into an L-mode plasma, increases in the confinement performance and neutron rate were observed despite the rise in the radiated power and dilution of bulk ions [230]. The density fluctuation spectrum at $r/a_0 = 0.7$ is reduced by a factor of five due to impurity injection. Notably, for $k_\perp \rho_s > 0.35$, the fluctuation is almost entirely suppressed. Unlike the RI mode, the radial electric field is believed to play a significant role. Impurity seeding reduces the growth rate, resulting in a reduction in the turbulent momentum transport. With the reduced momentum transport, the toroidal rotation increases, leading to an increase in the $E \times B$ shearing rate. The $E \times B$ shearing further suppresses the turbulence. Gyrokinetic simulations confirmed that the shearing rate surpasses the linear growth rate due to the impurity injection. In the TFTR plasma with an input power of 16–22MW, xenon injection leads to a significant increase in the density and ion temperature [231]. The electron density increase due to the impurity gas is not prominent, indicating an enhancement in particle confinement. While impurities cause an increase in radiated power, the change in the electron temperature is small due to the rise in ion-electron equilibration power $q_{ei} \sim n_e^2(T_i - T_e)/T_e^{3/2}$. In TFTR supershots, immediately after xenon puff, an increase in the poloidal velocity near the edge was observed, and the radial electric field increases by a factor of three. With krypton injection, the $E \times B$ shearing rate increases across the entire profile compared to cases without impurity puff [232]. In LHD, high ion temperature plasmas are achieved with the formation of an ion transport barrier due to carbon pellet injection and intensive neutral beam heating [233]. Because the electron and impurity densities have a hollow (outwardly peaked) profile, this high confinement mode is different from the RI mode. When the

electron density exceeds a threshold, the ion temperature rather decreases with increasing the electron density. When the carbon density becomes less than a threshold, a rapid increase in the thermal diffusivity is observed [234]. In a separate experiment, by injecting boron powder, enhancements in ion temperature, electron temperature, stored energy, and confinement time was observed [235]. It was found that the density profile becomes hollow and there is a reduction in recycling and impurity influx from the plasma-facing components. With the injection of boron powder, it was found that the low-frequency components of the turbulence decreases, while the high-frequency components increases. The improvement in confinement is believed to be related to the suppression of the ITG turbulence.

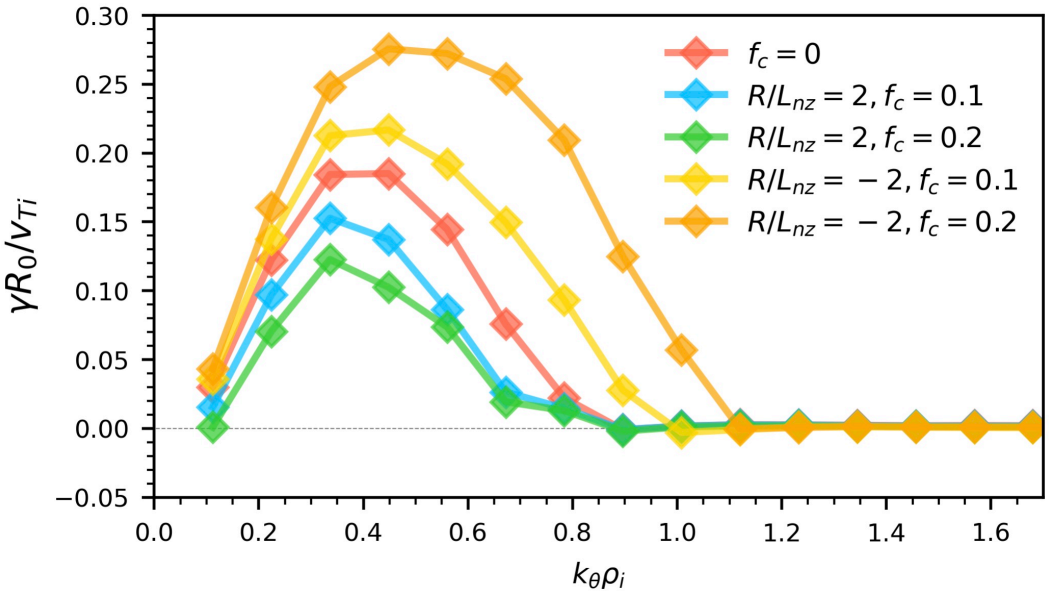

Fig. 6.1: Linear growth rate of the ITG mode in the presence of impurities for $R/L_{Ts} = 6$.

Figure 6.1 shows the linear growth rate of the ITG mode in the presence of fully stripped carbon (C, $A = 12$, $Z = 6$) at a concentration $f_c = Zn_z/n_e = 0.2$. The gradients of the background profiles are given by $(R/L_{Ts}, R/L_{ne}) = (6, 3)$ at $r = 0.5a_0$. In tokamaks, the ITG mode is stabilized when the impurity density has a peaked (inwardly peaked) profile, and conversely, it becomes unstable with a hollow impurity profile. These results are consistent with the findings obtained from numerical computations of gyrokinetic integral equations [237, 239] and gyrokinetic simulation results from GYRO, XGC1, and gKPSP [240, 241]. In addition to the stabilization of the linear ITG mode by a peaked impurity profile, full-f ITG turbulence simulations with adiabatic electron approximation by XGC1 demonstrated that when the impurity

density has a peaked profile, the peak of the turbulence wavenumber spectrum shifts towards the lower wavenumber side, and the turbulence intensity decreases for all wavelengths [240]. Additionally, it was shown that impurities can enhance the $E \times B$ shear. In global δf simulations by gKPSP, the formation of a robust $E \times B$ staircase due to impurities and the consequent suppression of heat transport were reported [241]. The improvement in confinement observed in experiments due to impurity injection can be understood to be driven by a peaked impurity profile. How injected impurities form a peaked profile is an intriguing question. The direction of the turbulent impurity particle flux can vary depending on the background profiles and the instabilities driving the turbulence [243, 244, 245], meaning that injected impurities do not necessarily accumulate at the center. There are reports suggesting that the outward turbulent particle flux can exceed the inward neoclassical transport [252, 242], and that the particle flux can be altered due to the interplay between turbulent and neoclassical transport [246, 247]. In DIII-D, when the ion temperature gradient is large, it has been observed that the impurity density profile becomes hollow due to the strong outward convection of impurities [248, 249]. This outward convective flux is driven by temperature screening.

In this study, we focus on the toroidal impurity mode (tIM). The instability condition for the impurity mode in slab geometry,

$$\frac{n_i}{n_z}\frac{L_{nz}}{L_{ni}} + \frac{Zn_i}{(T_i/T_e)n_e + n_i} < 0, \tag{6.1}$$

was first derived by Coppi *et al.* [250]. The impurity mode, as represented by Eq. (6.1), is characterized by becoming unstable when the density gradient of bulk ions and that of impurities are opposite. In experiments involving argon supersonic molecular beam injection into H-mode plasma in HL-2A, the IM turbulence was observed [251]. In theoretical research, through the analysis based on the gyrokinetic integral equations, it was shown that the tIM becomes more unstable as the impurity concentration and the absolute value of the impurity density gradient increase [236, 237]. Furthermore, the quasi-linear impurity particle flux due to the tIM turbulence was shown to be about an order of magnitude larger than that due to the TEM turbulence [251]. However, nonlinear fluid simulations and nonlinear gyrokinetic simulations for the tIM turbulence have not yet been performed, leading to an incomplete understanding of turbulent transport caused by it. The hollow impurity profiles which could drive the IM were observed in several experiments such as KSTAR [252], HL-2A [253], and LHD [254]. Impurities are not necessarily injected solely for the confinement improvement. They can be used to address issues such as mitigating a large influx of carbon [255] or suppressing edge-localized modes (ELMs) [256]. Additionally, impurities can be introduced for a divertor heat load reduction [257]. Understanding how the injected impurities are transported

by turbulence is an important issue. Therefore, investigating the transport caused by the IM turbulence is meaningful from these perspectives.

6.1.2 Stability analysis and physical mechanism

The instability condition for the tIM can be derived using a fluid model and the adiabatic electron approximation as in Ref. [34]. The density n_s of particle species s can be expressed as the sum of an equilibrium part n_{0s} and a fluctuating part $\tilde{n}_s$. The time evolution of the perturbed density of the particle species s is given by the continuity equation

$$\frac{\partial \tilde{n}_s}{\partial t} + \nabla \cdot \{n_s(\boldsymbol{v}_E + \boldsymbol{v}_{ps})\} = 0, \tag{6.2}$$

where the $E \times B$ drift $\boldsymbol{v}_E$ and the diamagnetic drift $\boldsymbol{v}_{ps}$ are defined by

$$\boldsymbol{v}_E = \frac{\boldsymbol{b} \times \nabla\phi}{B}, \qquad \boldsymbol{v}_{ps} = T_{0s}\frac{\boldsymbol{b} \times \nabla n_s}{q_s n_s B}, \tag{6.3}$$

respectively. For simplicity, the flat temperature profiles are assumed and the inertial drift is neglected. In local slab coordinates (x radial, y poloidal, and z along $\boldsymbol{B}$), $\boldsymbol{b}\times\nabla\phi$ is $(-\partial_y\phi, \partial_x\phi, 0)$. Eq. (6.2) becomes

$$\frac{\partial \tilde{n}_s}{\partial t} - Z_s\tau_s n_{0s} v_{*s}\frac{\partial \Phi}{\partial y} + Z_s\tau_s n_{0s} v_{Ds}\frac{\partial \Phi}{\partial y} + v_{Ds}\frac{\partial \tilde{n}_s}{\partial y} = 0, \tag{6.4}$$

where $\tau_s = T_{0e}/T_{0s}$, $v_{*s} = T_{0s}/(Z_s eBL_{ns})$, $v_{Ds} = T_{0s}/(Z_s eBL_B)$, and $\Phi = e\phi/T_{0e} = (\tilde{n}_i + Z\tilde{n}_z)/n_{0e}$. From Eq. (6.4), we obtain

$$\begin{cases} \dfrac{\partial \tilde{n}_z}{\partial t} - \tau_z f_c v_{*z}\dfrac{\partial \tilde{n}_i}{\partial y} - Z\tau_z f_c v_{*z}\dfrac{\partial \tilde{n}_z}{\partial y} + \tau_z f_c v_{Dz}\dfrac{\partial \tilde{n}_i}{\partial y} + Z\tau_z f_c v_{Dz}\dfrac{\partial \tilde{n}_z}{\partial y} + v_{Dz}\dfrac{\partial \tilde{n}_z}{\partial y} = 0 \\ \dfrac{\partial \tilde{n}_i}{\partial t} - \tau_i f_i v_{*i}\dfrac{\partial \tilde{n}_i}{\partial y} - Z\tau_i f_i v_{*i}\dfrac{\partial \tilde{n}_z}{\partial y} + \tau_i f_i v_{Di}\dfrac{\partial \tilde{n}_i}{\partial y} + Z\tau_i f_i v_{Di}\dfrac{\partial \tilde{n}_z}{\partial y} + v_{Di}\dfrac{\partial \tilde{n}_i}{\partial y} = 0 \end{cases}, \tag{6.5}$$

where $f_c = Zn_{0z}/n_{0e}$ and $f_i = n_{0i}/n_{0e} = (n_{0e} - Zn_{0z})/n_{0e} = 1 - f_c$ represent the impurity concentration and the bulk ion concentration, respectively. Considering plane waves, we get

$$\begin{cases} \left(-\omega - Z\tau_z f_c\omega_{*z} + Z\tau_z f_c\omega_{Dz} + \omega_{Dz}\right)\tilde{n}_z + \left(-\tau_z f_c\omega_{*z} + \tau_z f_c\omega_{Dz}\right)\tilde{n}_i = 0 \\ \left(-Z\tau_i f_i\omega_{*i} + Z\tau_i f_i\omega_{Di}\right)\tilde{n}_z + \left(-\omega - \tau_i f_i\omega_{*i} + \tau_i f_i\omega_{Di} + \omega_{Di}\right)\tilde{n}_i = 0, \end{cases} \tag{6.6}$$

where $\omega_{*s} = v_{*s}k_y$, $\omega_{*i} = v_{Di}k_y$. From the conditions where the density fluctuations of bulk ions and impurities have non-trivial solutions, in the limit $\omega_{Dz} \to 0$, we obtain

$$\begin{aligned} &\omega^2 + \left(\tau_i f_i\omega_{*i} - \tau_i f_i\omega_{Di} - \omega_{Di} + Z\tau_z f_c\omega_{*z}\right)\omega \\ &\quad - Z\tau_z f_c\omega_{*z}\left(-\tau_i f_i\omega_{*i} + \tau_i f_i\omega_{Di} + \omega_{Di}\right) + \tau_z f_c\omega_{*z}\left(-Z\tau_i f_i\omega_{*i} + Z\tau_i f_i\omega_{Di}\right) = 0. \end{aligned} \tag{6.7}$$

The instability condition is equivalent to the discriminant being negative; hence,

$$D \equiv \tau_i^2 f_i^2 \omega_{*i}^2 + Z^2 \tau_z^2 f_c^2 \omega_{*z}^2 + (\tau_i f_i + 1)^2 \omega_{Di}^2 + 2Z\tau_i\tau_z f_i f_c \omega_{*i}\omega_{*z} \\ - 2Z\tau_i\tau_z f_i f_c \omega_{*z}\omega_{Di} + 2Z\tau_z f_c \omega_{*z}\omega_{Di} - 2\tau_i^2 f_i^2 \omega_{*i}\omega_{Di} - 2\tau_i f_i \omega_{*i}\omega_{Di} < 0, \tag{6.8}$$

is derived. In the absence of impurities ($f_c \to 0$), the mode is stable because $D = (\tau_i f_i \omega_{*i} - \tau_i f_i \omega_{Di} - \omega_{Di})^2 > 0$. In this model, because $D = (\tau_i f_i \omega_{*i} + Z\tau_z f_c \omega_{*z})^2 > 0$ without the gradient of the magnetic field ($\omega_{Di} \to 0$), the instability does not occur. This is because the model does not account for the motion parallel to the magnetic field, which plays an important role for the slab IM. When $\omega_{*i}\omega_{Di} < 0$ and $\omega_{*i}\omega_{*z} < 0$, the mode is stable because $D = (\tau_i f_i \omega_{*i} + Z\tau_z f_c \omega_{*z} - \tau_i f_i \omega_{Di})^2 + 2\tau_i f_i \omega_{Di}^2 + \omega_{Di}^2 + 2Z\tau_z f_c \omega_{*z}\omega_{Di} - 2\tau_i f_i \omega_{*i}\omega_{Di} > 0$. When $\omega_{*i}\omega_{Di} < 0$ and $\omega_{*i}\omega_{*z} > 0$, it is also stable because $D = (Z\tau_z f_c \omega_{*z} + \omega_{Di})^2 + \tau_i^2 f_i^2 \omega_{*i}^2 + \tau_i^2 f_i^2 \omega_{Di}^2 + 2\tau_i f_i \omega_{Di}^2 + 2Z\tau_i\tau_z f_i f_c \omega_{*i}\omega_{*z} - 2Z\tau_i\tau_z f_i f_c \omega_{*z}\omega_{Di} - 2\tau_i^2 f_i^2 \omega_{*i}\omega_{Di} - 2\tau_i f_i \omega_{*i}\omega_{Di} > 0$. Therefore, for the mode to grow, the condition $\omega_{*i}\omega_{Di} > 0$ must be satisfied. This is satisfied in the bad curvature region. When $\omega_{*i}\omega_{Di} > 0$, $\omega_{*i}\omega_{*z} > 0$ and $\omega_{Di} > \omega_{*i}$, the mode is stable because $D = (\tau_i f_i \omega_{*i} + Z\tau_z f_c \omega_{*z} - \tau_i f_i \omega_{Di})^2 + \omega_{Di}^2 + 2Z\tau_z f_c \omega_{*z}\omega_{Di} + 2\tau_i f_i (\omega_{Di} - \omega_{*i})\omega_{Di} > 0$. When $\omega_{*i}\omega_{Di} > 0$, $\omega_{*i}\omega_{*z} > 0$ and $\omega_{*i} > \omega_{Di}$, it is also stable because $D = (\tau_i f_i \omega_{*i} - \tau_i f_i \omega_{Di} - \omega_{Di})^2 + Z^2\tau_z^2 f_c^2 \omega_{*z}^2 + 2Z\tau_z f_c \omega_{*z}\omega_{Di} + 2Z\tau_i\tau_z f_i f_c (\omega_{*i} - \omega_{Di})\omega_{*z} > 0$. Therefore, for the mode to be unstable, $\omega_{*i}\omega_{*z} < 0$ must be satisfied. The condition indicates that the density gradients of bulk ions and impurities must be in opposite directions. For these reasons, the instability deserves to be called the tIM.

We consider the background profiles depicted in Fig. 6.2. The gray vertical dashed line indicates $r = r_s = a_0/2$ and the gradients of the temperatures and densities are $(R/L_{Ts}(r_s), R/L_{ne}(r_s),\ R/L_{ni}(r_s), R/L_{nz}(r_s)) = (0, 3, 5.75, -8)$. The introduced impurity is carbon with $f_c(r_s) = 0.2$. The temperatures are normalized by the electron temperature at r_s, $T_{0e} = T_e(r_s)$. Similarly, the densities are normalized by the electron density at r_s, $n_{0e} = n_e(r_s)$. The normalized ion density and impurity density at r_s are 0.80 and about 0.03, respectively. The density gradients are not independent of each other and satisfy

$$\frac{R}{L_{ni}(r)} = \frac{\dfrac{R}{L_{ne}(r)} - f_c(r)\dfrac{R}{L_{nz}(r)}}{1 - f_c(r)}. \tag{6.9}$$

Given the electron density profile and impurity density profile, the ion density profile is determined from Eq. (6.9). The gradient of the electron density and impurity density

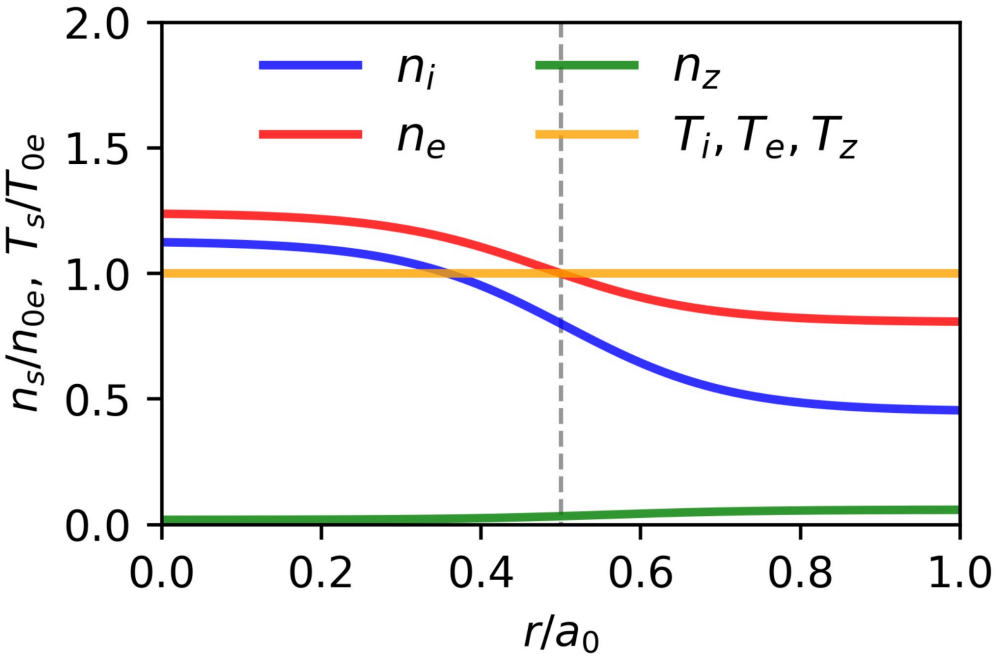

Fig. 6.2: Radial profiles of density n_s and temperature T_s $(s = i, e, z)$. These profiles are also used as the initial ones for the tIM simulations.

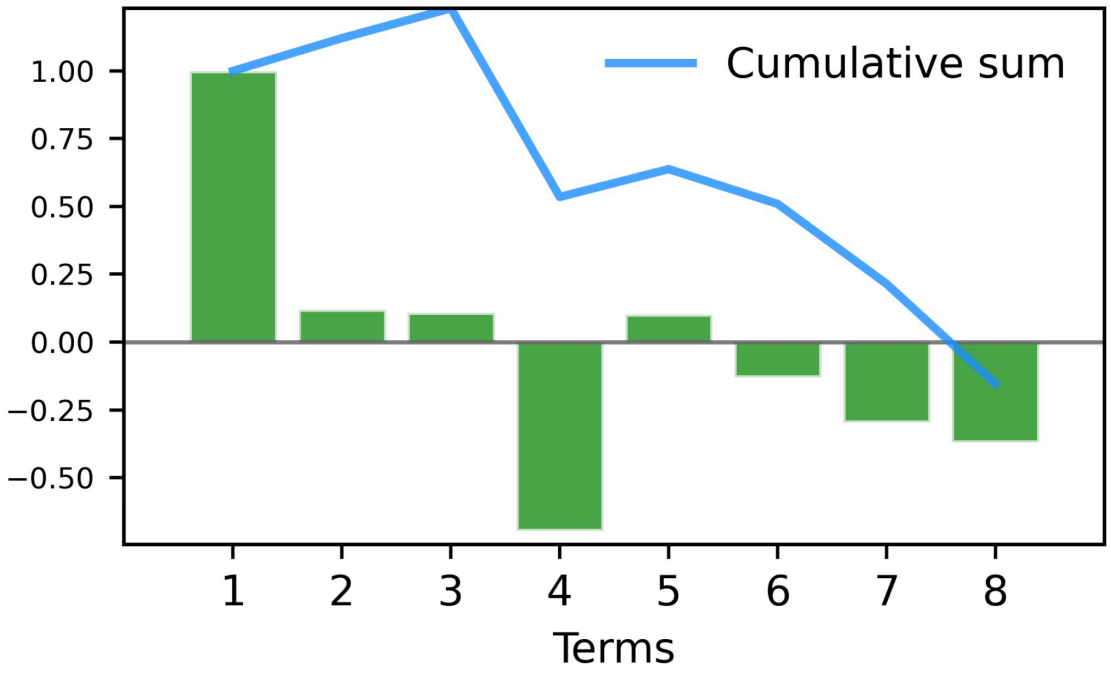

Fig. 6.3: Value of each term on the left-hand side of the instability condition (6.8) normalized by the first term. The blue line represents the cumulative sum. The parameters $(f_c, R/L_{ne}, R/L_{ni}, R/L_{nz}) = (0.2, 3, 5.75, -8)$ shown in Fig. 6.2 are used to evaluate the values.

reaches its maximum value at $r = r_s$, while the gradient of the ion density peaks around $r = 0.55\rho_i$.

Figure 6.3 shows the value of each term in D at r_s normalized by the first term. The blue line represents the cumulative sum. Since the cumulative sum is negative ($D < 0$), the mode is unstable in the profiles shown in Fig. 6.2. Figure 6.3 indicates that the major terms in D are the first, fourth, and eighth terms, therefore D can be approximated as

$$D \simeq \tau_i^2 f_i^2 \omega_{*i}^2 + 2Z\tau_i\tau_z f_i f_c \omega_{*i}\omega_{*z} - 2\tau_i f_i \omega_{*i}\omega_{Di}. \tag{6.10}$$

The second term on the right-hand side of Eq. (6.10) represents the contribution due to the necessary condition $\omega_{*i}\omega_{*z} < 0$. Because it increases with the absolute value of the impurity density gradient $|R/L_{nz}|$ and impurity concentration f_c, as $|R/L_{nz}|$ and f_c increase, the linear growth rate increases. The third term on the right-hand side of Eq. (6.10) represents the contribution from the necessary conditions $\omega_{*i}\omega_{Di} > 0$.

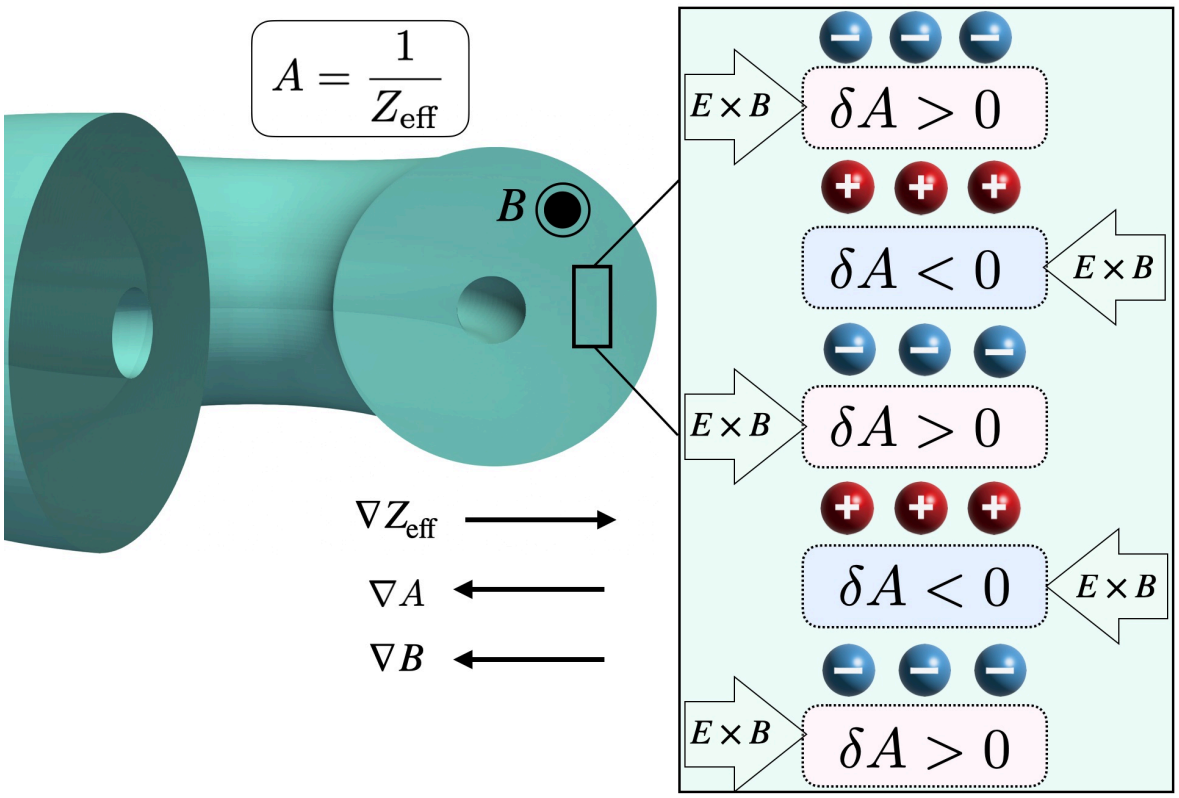

Fig. 6.4: Physical mechanism of the tIM.

We regard the tIM as one of interchange instabilities and consider that it grows through a mechanism similar to the ITG mode depicted in Fig. 1.7. Figure 6.4 shows the physical mechanism of the tIM that we propose. The stability analysis indicates that the bulk ion density must have a peaked profile and the impurity density must have a hollow profile to destabilize the tIM. Therefore, the effective charge Z_{eff} has a

hollow profile. Because the magnetic drift is proportional to $A = 1/Z_{\rm eff}$, regions where the electrostatic potential is positive or negative are created by an effective charge fluctuation δA. The electrostatic potential gradient generates the electric field that creates an $E \times B$ drift. In the bad curvature region, the $E \times B$ drift increases the amplitude of the fluctuation, leading to exponential growth of the mode.

6.1.3 Impurity mode turbulence simulations

We conduct collisionless δf simulations with impurities. The radial profiles of the safety factor and magnetic shear are shown in Fig. 5.2. The time evolution of the perturbed guiding center distribution function is given by the gyrokinetic Vlasov equation

$$\frac{\partial \delta f_s}{\partial t} + v_\parallel \boldsymbol{b} \cdot \nabla \delta f_s - \frac{\mu \boldsymbol{B}_s^*}{m_s B_{\parallel s}^*} \cdot \nabla B \frac{\partial \delta f_s}{\partial v_\parallel} = -\boldsymbol{v}_{ds} \cdot \nabla \delta f_s - \frac{c}{B_{\parallel s}^*} \left[\langle \phi \rangle_{\alpha s}, \delta f_s \right] + \frac{q_s}{T_s} f_{0s} \boldsymbol{v}_{*s} \cdot \nabla \langle \phi \rangle_{\alpha s} - \frac{q_s}{m_s} \langle E^* \rangle_{\alpha s} \frac{\partial f_s}{\partial v_\parallel}, \quad (6.11)$$

where $\langle E^* \rangle_{\alpha s} = -(\boldsymbol{B}_s^*/B_{\parallel s}^*) \cdot \nabla \langle \phi \rangle_{\alpha s}$, $[\langle \phi \rangle_{\alpha s}, \delta f_s] = \boldsymbol{b} \cdot (\nabla \langle \phi \rangle_{\alpha s} \times \nabla \delta f_s) = (B_{\parallel s}^*/c) \boldsymbol{v}_{Es} \cdot \nabla \delta f_s$, $\boldsymbol{v}_{Es} = (c/B_{\parallel s}^*) \boldsymbol{b} \times \nabla \langle \phi \rangle_{\alpha s}$ is the $E \times B$ drift, $\boldsymbol{v}_{ds} = (c/q_s B_{\parallel s}^*) \boldsymbol{b} \times (\mu \nabla B + m v_\parallel^2 \boldsymbol{b} \cdot \nabla \boldsymbol{b})$ is the magnetic drift, $\boldsymbol{v}_{*s} = (c T_s/q_s B_{\parallel s}^*) \boldsymbol{b} \times \nabla \ln f_{0s}$ is the diamagnetic drift. The gyro-averaged electrostatic potential $\langle \phi \rangle_{\alpha s}$ is evaluated by using the Padé approximation $\langle \phi \rangle_{\alpha s} \simeq \phi/(1 + \rho_s^2 k_\perp/4)$ [129]. It is necessary to introduce a source model that prevents relaxation of the equilibrium profiles in order to investigate the steady-state transport in nonlinear global simulations [258, 259]. However, the source term is ignored in the simulations. Decaying turbulence simulations are performed. The electrostatic potential is obtained by solving the gyrokinetic Poisson equation

$$-\nabla_\perp \cdot \frac{\rho_i^2}{\lambda_{Di}^2} \nabla_\perp \phi - \nabla_\perp \cdot \frac{\rho_z^2}{\lambda_{Dz}^2} \nabla_\perp \phi + 4\pi e \tilde{n}_e = 4\pi e \int d^6 \boldsymbol{Z} \mathcal{J}_i \delta^3 \left(\boldsymbol{R} + \boldsymbol{\rho}_i - \boldsymbol{x} \right) \delta f_i + 4\pi Z e \int d^6 \boldsymbol{Z} \mathcal{J}_z \delta^3 \left(\boldsymbol{R} + \boldsymbol{\rho}_z - \boldsymbol{x} \right) \delta f_z. \quad (6.12)$$

For the adiabatic electron model, $\tilde{n}_e$ is given by Eq. (2.96), while for the hybrid electron model, it is given by Eqs. (2.98) and (2.99). The simulations are performed using a 1/4 wedge torus of the minor radius $a_0 = 100\rho_i$ and inverse aspect ratio $a_0/R_0 = 0.36$. The grid numbers are $(N_r, N_\theta, N_\varphi, N_{v_\parallel}, N_\mu) = (64, 256, 64, 96, 16)$ and convergence tests have confirmed that the grid numbers are sufficiently large.

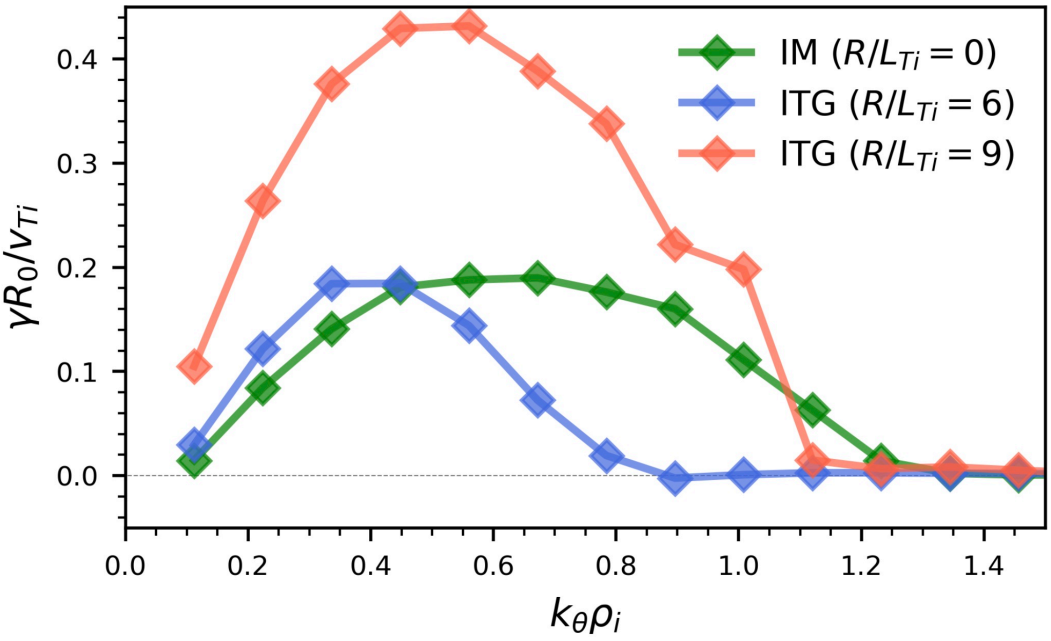

Fig. 6.5: Linear growth rates of the tIM $(R/L_{Ti}, R/L_{nz}) = (0, -8)$, and the ITG modes $(R/L_{Ti} = 6, 9)$.

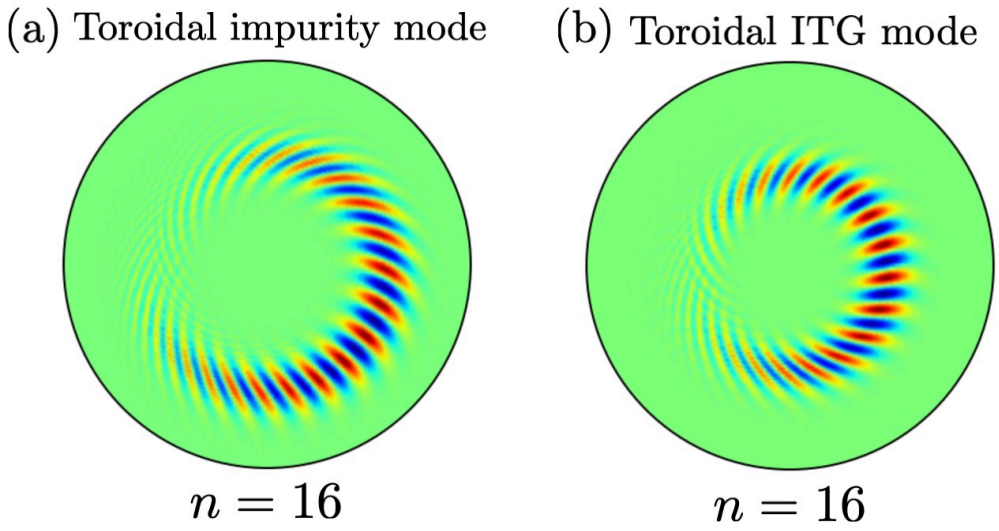

Fig. 6.6: Color map of the $n = 16$ electrostatic potentials for tIM (a) and ITG mode (b).

In this subsection, the adiabatic electron approximation is employed to avoid complications arising from electron dynamics. Figure 6.5 shows the linear growth rates of tIM and the ITG modes. The initial profiles of the simulation of the tIM are given in Fig. 6.2. The simulation of the ITG mode $(R/L_{Ti} = 6)$ corresponds to the $f_c = 0$ case in Fig. 6.1. In cases where the linear growth rates are comparable, the unstable spectrum of the tIM is broader than that of the ITG mode. As the linear growth rate of the ITG mode increases, the unstable spectrum becomes comparable to that of the

tIM. Figure 6.6(a) shows a poloidal cross section of the $n = 16$ electrostatic potential, indicating that a ballooning mode structure is formed. The fact that it is unstable in the bad curvature region is consistent with the results of the stability analysis. The peak of the mode is not at r_s but is shifted outward. It might be attributed to the outward shift of the maximum of the ion density gradient. For comparison, the contour plot of the $n = 16$ electrostatic potential for the ITG mode is shown in Fig. 6.6(b). It is found that the ballooning angles of the tIM and ITG mode are different. Even when the tIM and ITG mode coexist, in linear phase, it is possible to determine which mode is dominant from the ballooning angle.

Figure 6.7 shows the parameter dependences of the linear growth rate of the tIM. The other background parameters are the same as the profiles shown in Fig. 6.2, $(A, Z, f_c, R/L_{Ts}, R/L_{nz},\ R/L_{ni},) = (12, 6, 0.2, 0, -8, 5.75)$. From Figs. 6.7(a) and 6.7(b), it is evident that as f_c and $|R/L_{nz}|$ increase, the linear growth rate also increases. This result is consistent with both the results expected from the stabiliy analysis and the numerical results of the gyrokinetic integral equations [236, 237]. Figure 6.7(c) indicates, consistent with previous studies [237, 251], that the tIM is destabilized by the ion temperature gradient. As depicted in Figs. 6.7(d) と 6.7(e), we find that the impurity temperature gradient destabilizes the tIM, and an increase in the impurity temperature stabilizes the tIM. Figure 6.7(f) shows that the linear growth rates are nearly identical when the impurity is argon $(\mathrm{Ar}, A = 40, Z = 18)$ and when it is tungsten $(\mathrm{W}, A = 184, Z = 40)$. However, there is dependency on the impurity species; the linear growth rates for both are about twice as large as for carbon impurity $(\mathrm{C}, A = 12, Z = 6)$. The difference in the linear growth rates is considered to be due to the FLR effect. The Larmor radii for carbon, argon, and tungsten are $\rho_C \simeq 0.58\rho_i$, $\rho_{Ar} \simeq 0.35\rho_i$, and $\rho_W \simeq 0.34\rho_i$, respectively. The similar linear growth rates between the cases where the impurity is argon and where it is tungsten can be explained by their similar Larmor radii. The smaller linear growth rate when the impurity species is carbon can be attributed to its larger Larmor radius. When the mass of the impurities is the same but with different charges, as illustrated in Fig. 6.7(g), the linear growth rate increases as the charge becomes larger. This is consistent with the results obtained in prior study. It is confirmed that the real frequency of the tIM is slower than that of the ITG mode.

Figure 6.8(a) shows the time evolution of the turbulent ion particle flux $\langle \Gamma_{i\,\mathrm{turb}} \rangle_{f,r}$ and the turbulent impurity particle flux $\langle Z\Gamma_{z\,\mathrm{turb}} \rangle_{f,r}$. $\langle \cdot \rangle_{f,r}$ represents the radial average

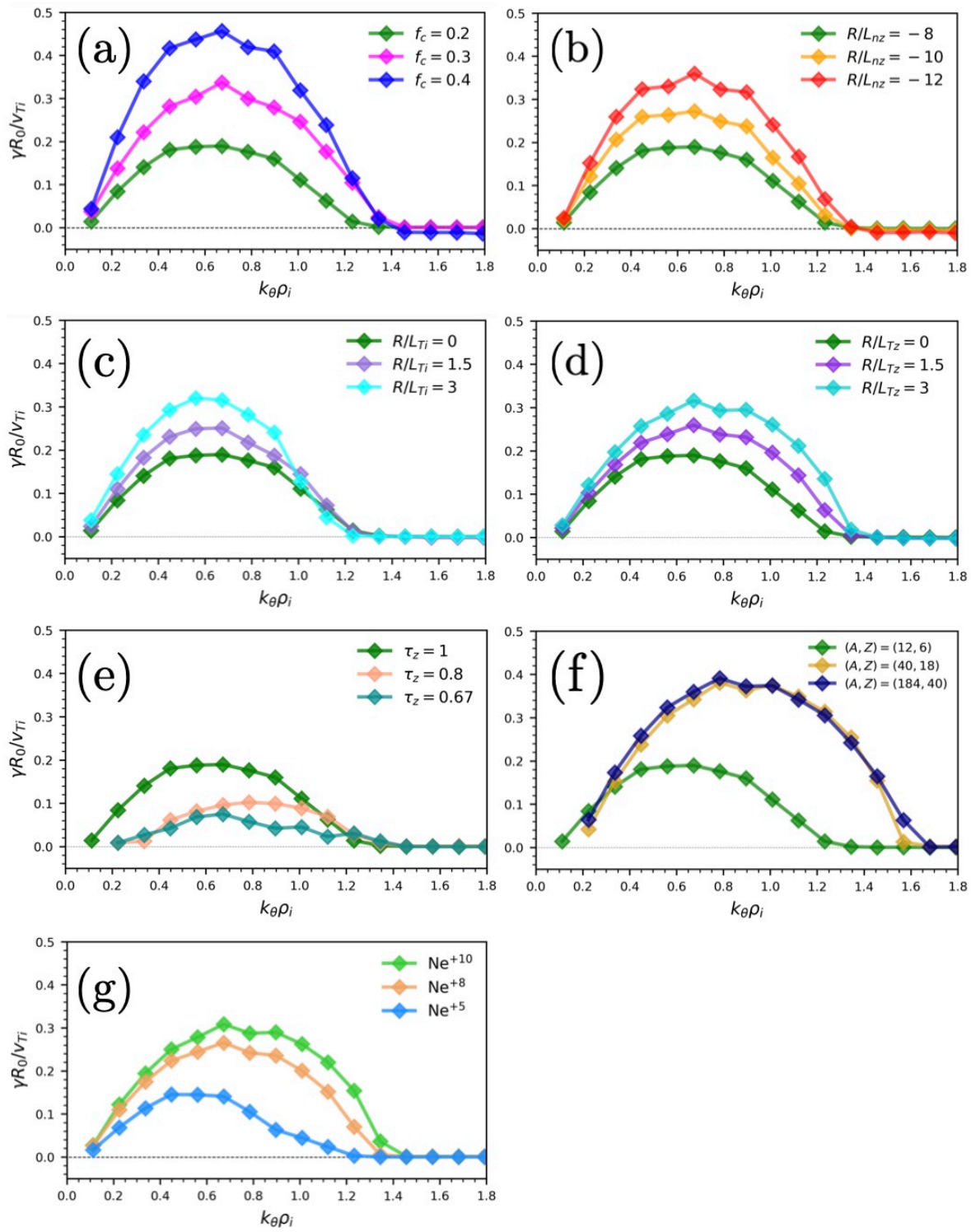

Fig. 6.7: f_c dependence (a), R/L_{nz} dependence (b), R/L_{Ti} dependence (c), R/L_{Tz} dependence (d), τ_z dependence (e), impurity species dependence (f) and impurity charge dependence (g) on the linear growth rate of tIM.

of a flux-surface averaged value. From 6.8(a), it is found that the large outward ion particle flux and inward impurity particle flux occur. Since the tIM turbulence is driven by the negative density gradient of bulk ions and the positive density gradient

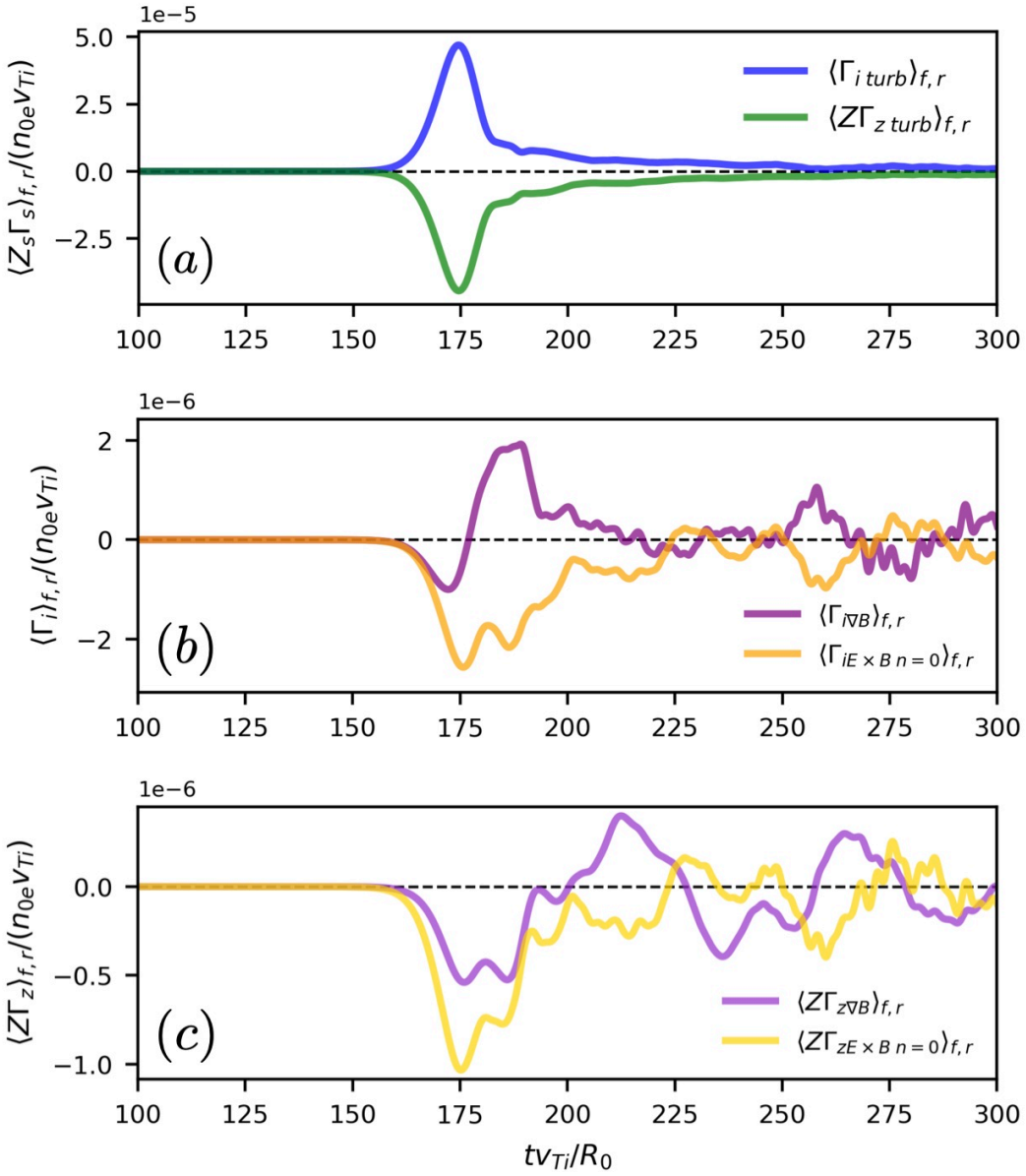

Fig. 6.8: (a) Time evolution of the turbulent particle fluxes of bulk ions and impurities. (b) Time evolution of the ion (b) and impurity (c) particle fluxes due to the magnetic drift and due to the $n = 0$ component of the $E \times B$ drift.

of impurities, it is a reasonable that such turbulent transports are observed. The particle fluxes of bulk ions and impurities are of the same order. On the other hand, the heat flux of bulk ions is two orders of magnitude larger than that of impurities. Figure 6.8(b) shows the time evolution of the ion particle flux due to the magnetic drift $\langle \Gamma_{i\,\nabla B} \rangle_{f,r}$ and that due to the $n = 0$ component of the $E \times B$ drift $\langle \Gamma_{i\,E\times B\,n=0} \rangle_{f,r}$. Figure 6.8(c) depicts the fluxes for the case of impurities. They are an order of magnitude smaller than the turbulent particle flux. $\langle \Gamma_{i\,\nabla B} \rangle_{f,r}$ and $\langle \Gamma_{i\,E\times B\,n=0} \rangle_{f,r}$ are balanced, except for the burst phase. This balance establishes more quickly than the balance between $\langle Z\Gamma_{z\,\nabla B} \rangle_{f,r}$ and $\langle Z\Gamma_{z\,E\times B\,n=0} \rangle_{f,r}$. This is due to the fact that bulk ions reach

equilibrium $\left(\partial\langle\tilde{n}_i\rangle_f/\partial t = -\partial/\partial r\left\{\langle\Gamma_{i\,\nabla B}\rangle_f + \langle\Gamma_{i\,E\times B\,n=0}\rangle_f\right\} = 0\right)$ faster than impurities by the parallel streaming motion that generates the return current since the thermal velocity of bulk ions is larger than that of impurities.

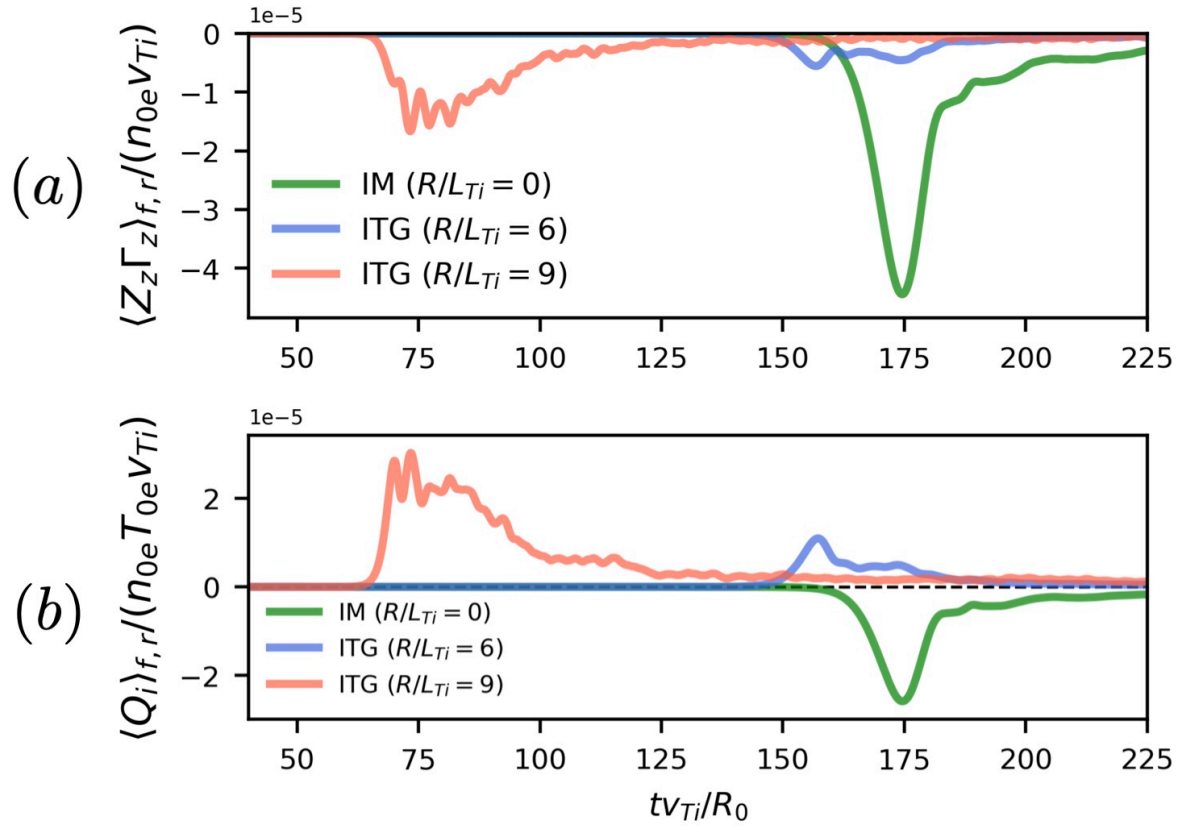

Fig. 6.9: Time evolution of the impurity particle fluxes (a) and the bulk ion heat fluxes (b) due to the tIM turbulence or the ITG turbulences

Figure 6.9(a) shows the temporal evolution of the impurity particle fluxes and the bulk ion heat fluxes due to the tIM turbulence or the ITG turbulences. In the ITG turbulence simulations, the impurity particle flux is evaluated using the trace impurity approximation [260, 261], treating impurities as test particles that do not affect the quasi-neutrality condition. From Figs. 6.5 and 6.9(a), it can be seen that when the linear growth rates of the tIM and the ITG mode are comparable, the impurity particle flux induced by the tIM turbulence is an order of magnitude larger than that induced by the ITG turbulence. Furthermore, even when the linear growth rate of the ITG mode is more than twice that of the tIM, the impurity particle flux due to the ITG turbulence is less than half of that from the tIM turbulence. In the previous study, it was shown that the impurity particle flux due to the tIM turbulence is an order of magnitude larger than that due to the TEM turbulence [251]. The impurity transport due to tIM

turbulence is significantly large, and treating impurities as trace impurities can lead to an underestimation of the impurity transport. Figure 6.9(b) depicts the temporal evolutions of the ion heat flux induced by the tIM turbulence or the ITG turbulences. For a fair comparison, the ion heat flux obtained from the ITG turbulence simulations are multiplied by $n_{0i} = 0.8$ and plotted. Since in the simulations, the presence of impurities has no influence with the quasi-neutrality condition, the ion density is 1.25 times larger than that in the tIM turbulence simulation. The ion heat flux due to the tIM turbulence is found to be negative, indicating an increase in the central ion temperature. A heat flux can be expressed as the sum of a diagonal term proportional to the temperature gradient and an off-diagonal term proportional to the density gradient in a quasilinear limit. In the case of the tIM turbulence, since the absolute value of the off-diagonal term is larger than that of the diagonal term, the ion heat flux becomes negative. Interestingly, when the linear growth rates of the tIM and the ITG mode are comparable, the absolute value of the ion heat flux due to the tIM turbulence is larger than that due to the ITG turbulence, even in the absence of an ion temperature gradient. When the tIM is dominant, the off-diagonal term is very large, implying that the heat flux can be negative even if the ion temperature gradient is not zero. Even when the linear growth rate of the ITG mode is more than twice that of the tIM, the ion heat flux due to the ITG mode turbulence is only 1.17 times larger than that due to the tIM turbulence. It can be said that tIM turbulence can cause significant turbulent heat transport even with a small linear growth rate.

Figure 6.10(a) shows the spatiotemporal evolution of the radial electric field averaged in θ and φ directions. It is found that the large scale and robust radial electric field is formed. Figure 6.10(b) depicts the radial profiles of the change the θ and φ averaged radial electric field $\langle E_r \rangle_{\theta,\varphi}$, the change of the sum of the turbulent particle fluxes $\delta \sum_s \langle Z_s \Gamma_{s,turb} \rangle_f = \delta(\langle \Gamma_{i,turb} \rangle_f + \langle Z \Gamma_{z,turb} \rangle_f)$, and the change of the flux-surface averaged ion heat flux $\delta \langle Q_i \rangle_f$, during time interval $\delta t = 2$ from $t = 165$. From Fig. 6.10(b), it is considered that the radial electric field is generated by the difference in the magnitude of the bulk ion and impurity turbulent particle fluxes. In local flux-tube gyrokinetic simulations, the sum of the turbulent particle fluxes is always zero because the equations are derived using the flute approximation, $k_\parallel / k_\perp \ll 1$. On the other hand, in global gyrokinetic simulations, the sum of particle fluxes is not necessarily zero, as the flute approximation is not strictly valid. By assuming the flute approximation and the limit $a_0/R_0 \to 0$, $\sum_s q_s \Gamma_s = 0$ can be proven as follows. From the turbulent particle

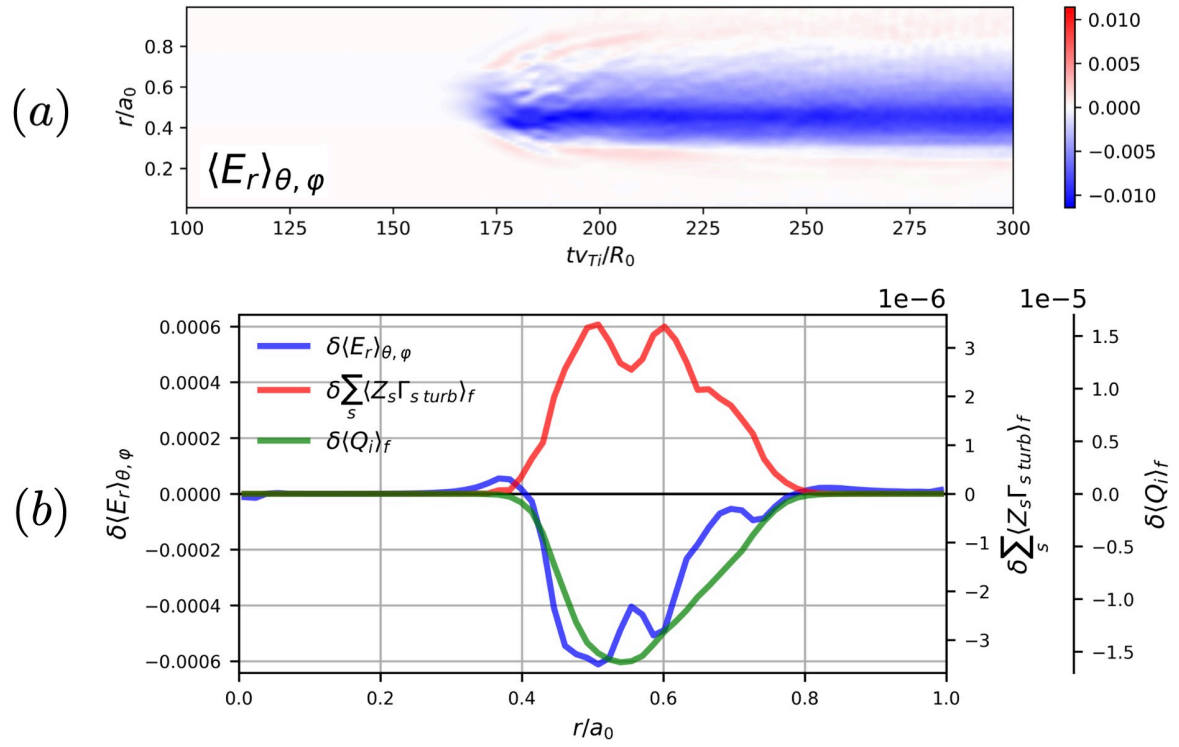

Fig. 6.10: (a) Spatiotemporal evolution of the radial electric field $\langle E_r\rangle_{\theta,\varphi}$. (b) Radial profile of the change of the radial electric field $\delta\langle E_r\rangle_{\theta,\varphi}$ (blue), the change of the sum of the turbulent particle fluxes $\delta\sum_s\langle Z_s\Gamma_{s,turb}\rangle_f$ (red), the change of the ion heat flux $\delta\langle Q_i\rangle_f$ (green).

flux $\Gamma_s = \langle \tilde{n}_s(1/rB)\partial\phi/\partial\theta\rangle_f$ and the Poisson equation $-\nabla_\perp^2\phi = \sum_s q_s\tilde{n}_s$, we obtain

$$\begin{aligned}\sum_s q_s\Gamma_s &= \left\langle \sum_s q_s\tilde{n}_s\frac{1}{rB}\frac{\partial\phi}{\partial\theta}\right\rangle_f = -\left\langle \nabla_\perp^2\phi\frac{1}{rB}\frac{\partial\phi}{\partial\theta}\right\rangle_f \\ &= -\mathrm{Re}\left\langle \sum_{m,k}\left[\left\{\frac{1}{r}\frac{\partial}{\partial r}\left(r\frac{\partial}{\partial r}\right)-\frac{m^2}{r^2}\right\}\hat{\phi}_m\right]\left[\frac{ik}{rB}\hat{\phi}_k\right]e^{i(m+k)\theta}\right\rangle_f \\ &= \mathrm{Re}\,\frac{1}{2\pi}\int\sum_m\left[\left\{\frac{1}{r}\frac{\partial}{\partial r}\left(r\frac{\partial}{\partial r}\right)-\frac{m^2}{r^2}\right\}\hat{\phi}_m\right]\left[\frac{im}{rB}\hat{\phi}_m^*\right]d\varphi. \end{aligned} \tag{6.13}$$

Assuming the flute approximation, we use the eikonal representation,

$$\hat{\phi}_m = \tilde{\phi}_m\, e^{iS/\varepsilon} \quad (\varepsilon \ll 1). \tag{6.14}$$

Because the radial derivative of $\hat{\phi}_m$ can be approximated as

$$\frac{\partial}{\partial r}\hat{\phi}_m = \frac{\partial\tilde{\phi}_m}{\partial r}\,e^{iS/\varepsilon} + \frac{i}{\varepsilon}\frac{\partial S}{\partial r}\tilde{\phi}_m\,e^{iS/\varepsilon} \simeq \frac{i}{\varepsilon}\frac{\partial S}{\partial r}\tilde{\phi}_m\,e^{iS/\varepsilon},$$

The radial derivative term in Eq. (6.13) is

$$\frac{1}{r}\frac{\partial}{\partial r}\left(r\frac{\partial}{\partial r}\right)\hat{\phi}_m = \frac{1}{r}\frac{\partial}{\partial r}\hat{\phi}_m + \frac{\partial^2}{\partial r^2}\hat{\phi}_m \simeq -\frac{1}{\varepsilon^2}\left(\frac{\partial S}{\partial r}\right)^2\hat{\phi}_m. \tag{6.15}$$

Substituting Eq. (6.15) into Eq. (6.13), we get

$$\sum_s q_s \Gamma_s \simeq -\mathrm{Re}\,\frac{1}{2\pi}\int \sum_m \left\{ \frac{1}{\varepsilon^2}\left(\frac{\partial S}{\partial r}\right)^2 + \frac{m^2}{r^2} \right\} \frac{im}{rB} |\hat{\phi}_m|^2 d\varphi = 0. \tag{6.16}$$

The profile of $\delta\langle E_r\rangle_{\theta,\varphi}$ largely overlaps with that of $\delta\langle Q_i\rangle_f$. Therefore, the zonal flow induced by the tIM turbulence is also candidate for generating the electric field [187]. However, since the profile of $\delta\sum_s\langle Z_s\Gamma_{s,turb}\rangle_f$ is closer to that of $\delta\langle E_r\rangle_{\theta,\varphi}$, the electric field could primarily be driven by the difference of the turbulent particle fluxes. It was shown that the radial electric field generated by temperature relaxation due to turbulence transport is about 1/3 compared to that by zonal flow [187]. Therefore, a similar profile of the change of the radial electric field would likely be observed in the case of full-f simulations.

The radial electric field can explain the dynamics of $\langle\Gamma_{i\,\nabla B}\rangle_f$ in the burst phase when $\langle\Gamma_{i\,\nabla B}\rangle_f$ and $\langle\Gamma_{i\,E\times B\,n=0}\rangle_f$ are not balanced as shown in Fig. 6.8(b). The $E\times B$ drift due to the radial electric field $E_r < 0$ induces up-down asymmetric density fluctuations $\tilde{n}_i \propto -E_r \sin\theta$, which couples with the magnetic drift $v_{D,r} \propto -\sin\theta$, leading to $\langle\Gamma_{i\,\nabla B}\rangle_f \simeq \langle\tilde{n}_i v_{D,r}\rangle_f \propto E_r\langle\sin^2\theta\rangle_f < 0$ [247]. The dynamics of $\langle Z\Gamma_{z\,\nabla B}\rangle_f$ are also explained by the same mechanism.

6.1.4 Coexistence of impurity mode and ITG mode

In the previous subsection, it was shown that the tIM becomes unstable even without temperature gradients, leading to an inward impurity particle flux and an inward ion heat flux due to the tIM turbulence. We investigate whether these fluxes are observed in the presence of temperature gradients and a hollow impurity profile. Because an ion temperature gradient drives the ITG mode, the presence of a negative ion temperature gradient and a positive impurity density gradient causes the ITG mode and the tIM to be unstable simultaneously. The mode with a higher linear growth rate becomes dominant mode. As shown in Fig. 6.1, when the impurity density profile is hollow, the linear growth rate of the ITG mode increases. It is inferred that the ITG mode dominates when the ion temperature gradient is large and the tIM dominates when it is small.

We perform simulations for the case with small temperature gradients $R/L_{Ts} = 4$ (Case A), and the case with large temperature gradients $R/L_{Ts} = 6$ (Case B). Figure 6.11 shows the density, temperature, and pressure profiles of bulk ions (a) and

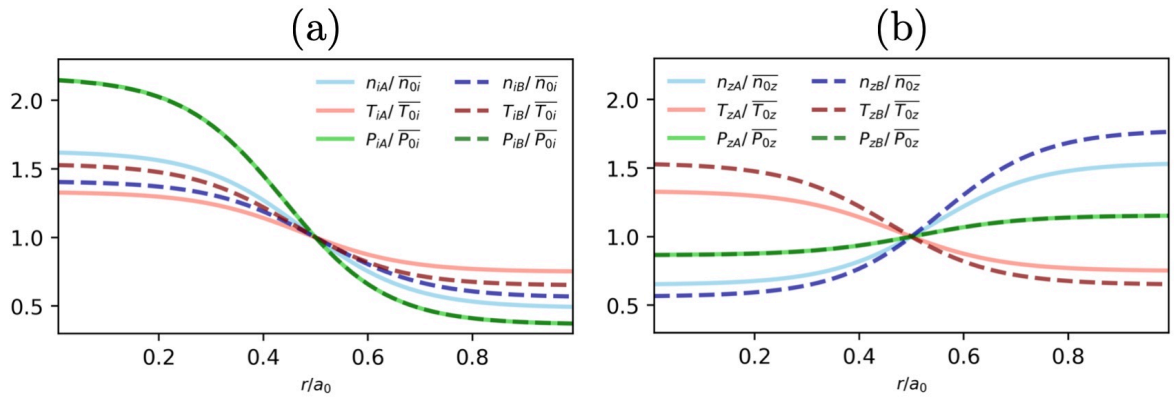

Fig. 6.11: Density, temperature, and pressure profiles of bulk ions (a) and impurities (b). The solid and dashed lines represent the profiles for Case A and Case B, respectively.

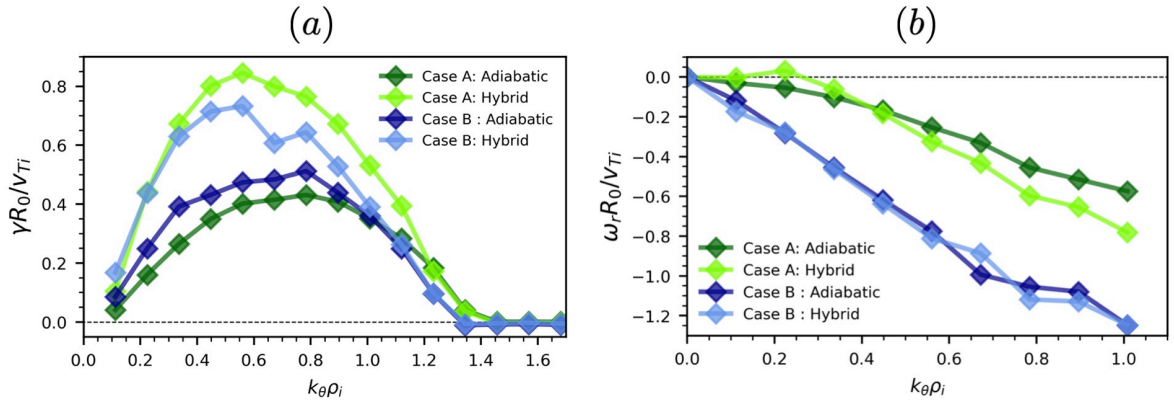

Fig. 6.12: Linear growth rate (a) and real frequency (b) for Case A and Case B in adiabatic electron model or hybrid electron model.

impurities (b) in Case A and Case B. In both cases, the pressure of bulk ions and that of impurities are the same. The ion density gradient in Case A is larger compared to that in Case B. On the other hand, the impurity density gradient in Case A is smaller than that in Case B. Figure 6.12 shows the linear growth rate (a) and real frequency (b) for Case A and Case B in the adiabatic electron model or hybrid electron model. The linear growth rates are similar for Case A and Case B. In both cases, for the hybrid electron model, the wavenumber at which the linear growth rate peaks becomes lower, but the unstable spectra are not changed by the dynamics of electrons. The modes in Case A is more destabilized by the non-adiabatic motion of electrons. Since the real frequency of the tIM is smaller than that of the ITG mode, it is found that the dominant mode is the tIM for Case A and the ITG mode for Case B. We have also confirmed the dominant modes by the difference in the ballooning angles between the tIM and ITG mode. The real frequency does not change significantly due to electron dynamics, but in Case A, at $k_\theta \rho_i \sim 0.25$, the real frequency is positive (in the direction of the electron

diamagnetic drift). For the tIM, the effect of electron motion might be significant in the low wavenumber range. Due to the destabilizing effect of impurities, in the adiabatic electron model for Case B, despite the ion temperature gradient being $R/L_{Ti} = 6$, the linear growth rate is larger than that in the case shown in Fig. 6.5, where there are no impurities and is the temperature gradient $R/L_{Ti} = 9$. The turbulent thermal diffusivity is larger in Case B, while the ion heat flux is larger in the pure ITG mode case.

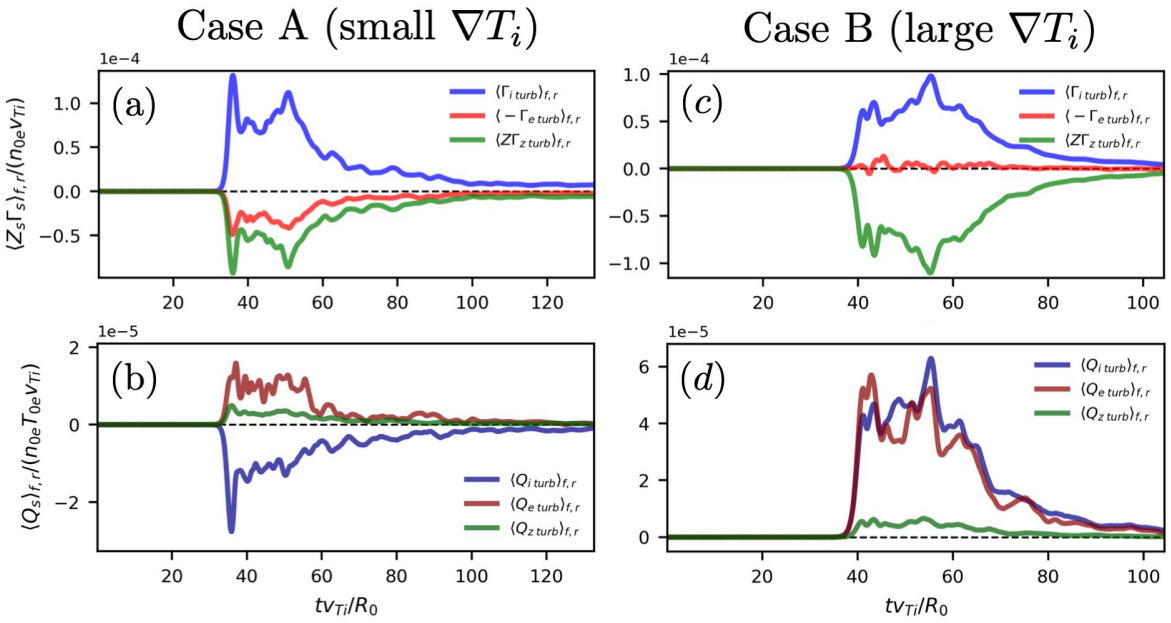

Fig. 6.13: Time evolution of the turbulent particle fluxes (a) and turbulent heat fluxes (b) for Case A. Time evolution of the turbulent particle fluxes (c) and turbulent heat fluxes (d) for Case B.

Figure 6.13(a) and (b) show the time evolution of the turbulent particle fluxes and turbulent heat fluxes for Case A in the hybrid electron model, respectively. Since the particle fluxes and heat fluxes are qualitatively similar in both the adiabatic electron model and the hybrid electron model, figures are only provided for the case of the hybrid electron model. It can be seen that the tIM turbulence generates the outward ion particle flux, the outward electron particle flux and the inward impurity particle flux. A notable result is that the ion heat flux is negative in Fig. 6.13(b), despite the presence of the ion temperature gradient. This increases the ion core temperature and ion temperature gradient. The absolute value of the ion heat flux is greater than the sum of the outward impurity and electron heat fluxes, thus the net heat flux is negative. If a multi-species collision operator is implemented, the temperatures of the electron and impurity would increase by thermal equipartition. In the quasi-steady

state, the temperature profiles could be more peaked than the initial ones. This result indicates that when the dominant mode changes from the ITG mode to the tIM by injecting impurities into a L-mode plasma, the energy confinement could be improved.

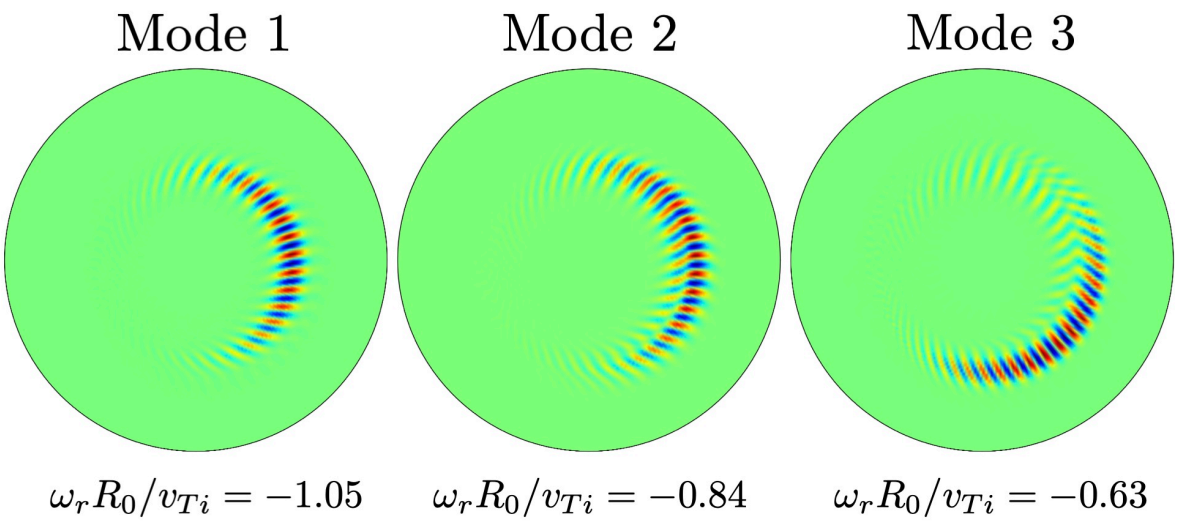

Fig. 6.14: Eigenmodes and frequencies of the $n = 28$ electrostatic potential in the linear phase of Case B.

Figure 6.13(c) and (d) show the time evolution of the turbulent particle fluxes and turbulent heat fluxes for Case B in the hybrid electron model, respectively. It can be seen that the large inward impurity transport occurs even though the dominant mode is the ITG mode. The impurity transport is larger than in the case of the pure ITG mode with a nearly identical linear growth rate. However, even though in Case B the absolute value of the impurity density gradient is larger than that in Case A, since the dominant mode is the ITG mode, the impurity particle flux is smaller. The large inward impurity transport comes from a subdominant tIM. The presence of the subdominant tIM can be confirmed using dynamic mode decomposition (DMD) [262, 263, 264]. The details are discussed in Appendix B. Figure 6.14 shows the frequency and corresponding eigenmodes of the $n = 28$ electrostatic potential in the linear phase. The real frequency of Mode 1 is consistent with that shown in Fig. 6.12(b). In other words, Mode 1 is the most unstable ITG mode. Mode 2 can also be identified as the ITG mode from its positive ballooning angle and relatively large frequency. A notable result is Mode 3. It has a negative ballooning angle and a relatively small real frequency, indicating that it is the tIM. The result indicates the presence of the subdominant tIM in the shadow of the dominant ITG mode. The contribution rates of Mode 1, Mode 2, and Mode 3 are 62.2%, 22.6%, and 8.5%, respectively, which means that only three modes can reproduce 93.3% of the original electrostatic potential dynamics.

When the temperature gradients are large, as seen in Fig. 6.13(d), the large outward ion and electron heat fluxes occur. In this case, unlike Case A, impurity injection does not improve energy confinement immediately. However, it is possible that even for large temperature gradients, if the impurity density gradient is sufficiently large, the dominant mode might change to the tIM.

The results indicate that not only neoclassical impurity transport but also the transport by the tIM turbulence contributes to the inward impurity flux. Once the impurity density evolve into a peaked profile, the tIM turbulence and ITG turbulence are both suppressed, and the confinement performance is improved.

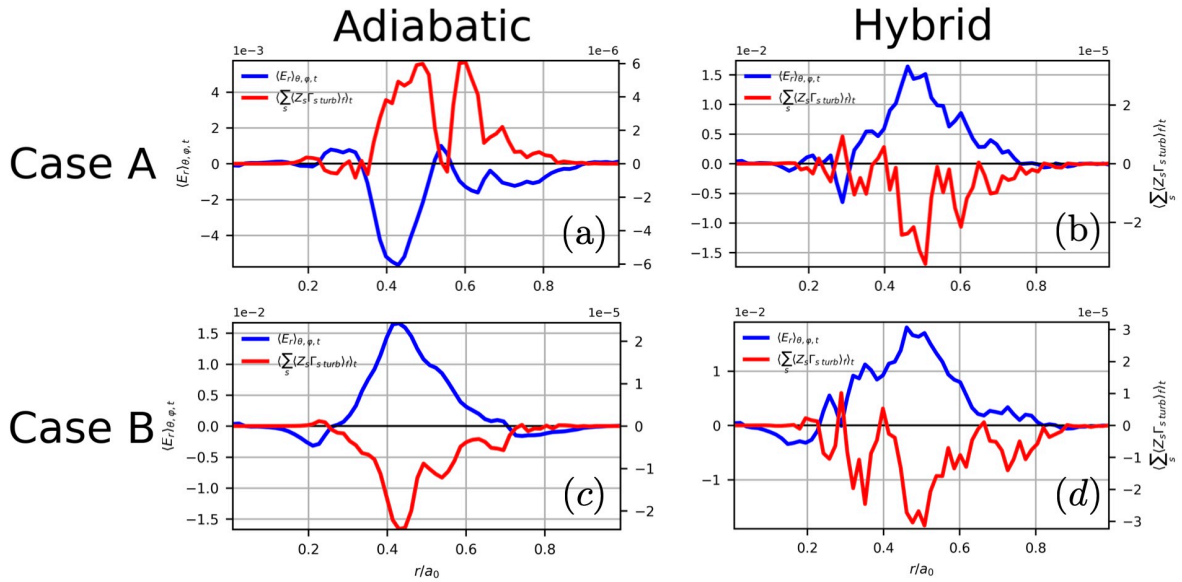

Fig. 6.15: Radial profiles of the θ, φ and time averaged radial electric field $\langle E_r \rangle_{\theta,\varphi,t}$ (blue) and the time average of the sum of the turbulent particle fluxes $\langle \sum_s \langle Z_s \Gamma_{s,turb} \rangle_f \rangle_t$ (red).

Figure 6.15 shows the radial profile of the θ, φ and time averaged radial electric field $\langle E_r \rangle_{\theta,\varphi,t}$ and the time average of the sum of the turbulent particle fluxes $\langle \sum_s \langle Z_s \Gamma_{s,turb} \rangle_f \rangle_t$ for Case A and Case B. Figs. (a) and (b) correspond to the case of the adiabatic electron model, while Figs. (b) and (d) correspond to the case of the hybrid electron model. The averaging is taken over $\delta t = 50$. Because the $\langle E_r \rangle_{\theta,\varphi,t}$ profile and the $\langle \sum_s \langle Z_s \Gamma_{s,turb} \rangle_f \rangle_t$ profile are similar, it can be inferred that the robust radial electric field is generated not by zonal flow due to the Reynolds stress, but by the non-ambipolar turbulent particle fluxes. For the cases where the adiabatic electron model are employed, the directions of the electric field are opposite between Case A where the tIM is dominant and Case B where the ITG mode is dominant. It can also be

seen that the absolute value of $\langle E_r \rangle_{\theta,\varphi}$ in Case B is larger than that in Case A because $\sum_s \langle Z_s \Gamma_{s,turb} \rangle_f$ in Case B is larger than that in Case A. For Case A in the adiabatic electron model, $\sum_s \langle Z_s \Gamma_{s,turb} \rangle_f$ is positive and $\langle E_r \rangle_{\theta,\varphi}$ is negative since the absolute value of the ion particle flux is larger. These results are consistent with the pure tIM turbulence simulation results shown in Fig. 6.10(b). However, in the case of the hybrid electron model, since $\Gamma_{e,turb} > \Gamma_{i,turb} + Z\Gamma_{z,turb}$, $\sum_s \langle Z_s \Gamma_{s,turb} \rangle_f$ becomes negative and $\langle E_r \rangle_{\theta,\varphi}$ becomes positive. This result also supports the idea that the radial electric field is generated by the sum of the turbulent particle fluxes. In Case B, the electron particle flux is smaller compared to that of ions or impurities. In both the adiabatic electron model and the hybrid electron model, $\sum_s \langle Z_s \Gamma_{s,turb} \rangle_f$ is negative and $\langle E_r \rangle_{\theta,\varphi}$ is positive. These results are similar to those of the full-f ITG turbulence simulation in a previous study. In Ref [247], the positive electric field $E_r > 0$ is driven by $\Gamma_{D,turb} - \Gamma_{e,turb} < 0$ where $\Gamma_{D,turb}$ and $\Gamma_{e,turb}$ are the turbulent particle flux of deuterium and electrons, respectively.

6.2 Fuel supply and impurity exhaust by ITG and TEM turbulence

6.2.1 Impurity exhaust by heating

When turbulence cannot be sufficiently suppressed by impurities, impurity accumulation causes dilution of fuel ions and radiation cooling, thus degrading plasma performance. In order to deal with the problem, turbulent impurity transport is being actively studied, because impurity density profiles observed experimentally cannot be reproduced by the neoclassical transport theory alone, and turbulent transport plays an important role. It was reported that the diffusivity and convective velocity observed in DIII-D can be modeled as a linear combination of the turbulent and neoclassical transport [249]. If only the contribution from neoclassical transport are considered, it was found that the impurity density profiles become either substantially more peaked or extremely hollow compared to the measured impurity profiles. Similarly, it was reported that with only neoclassical transport, the impurity density profiles become much more peaked compared to the measured impurity profiles in W7-X [265]. In this experiment, it was determined that the turbulent diffusion is 1–2 orders of magnitude larger than the neoclassical diffusion. To avoid impurity accumulation, it is necessary to control turbulence and drive a strong outward impurity particle flux. In KSTAR, by heating the L-mode plasma with the electron cyclotron resonance heating (ECH), it was observed that impurities are expelled and the impurity density profile becomes hollow [252]. The ECH effect is most pronounced with on-axis heating and diminishes

as the heating positions move outward. The impurity transport due to the ECH is attributed to the increase in the diffusivity and convection velocity, and the change in the direction of the convection from inward to outward in the core region. The turbulent transport is 1–2 orders of magnitude larger than the neoclassical transport. According to linear simulations, the instability is the TEM, and the outward convection could be due to the parallel compression pinch [266]. Similarly, in EAST, it was observed that with on-axis ECH, in the core region the diffusion coefficient increases and the convective velocity changes from negative to positive, and the central molybdenum density decreases to 1/5 compared to that before the ECH [242]. Since the neoclassical transport is an order of magnitude smaller than the turbulent transport, it is believed that the relaxation of the molybdenum density profile is caused by the TEM turbulence. These results suggest that heating can control turbulent impurity transport and the associated impurity density profile. However, in EAST, due to the ECH, not only the impurity density but also the electron density decreases across the entire plasma radii. Since fusion power increases with densities, it is desirable for turbulent particle flux of fuel ions and electrons to be inward. In DEMO-class reactors, fuel supply is challenging because fuel pellets only reaches 80–90% of the small radius. From this perspective, an inward turbulent ion particle flux is ideal. In this section, we study how turbulent particle fluxes are changed by heating in order to investigate how to achieve both fuel supply and impurity exhaust.

6.2.2 Differences between numerical methods

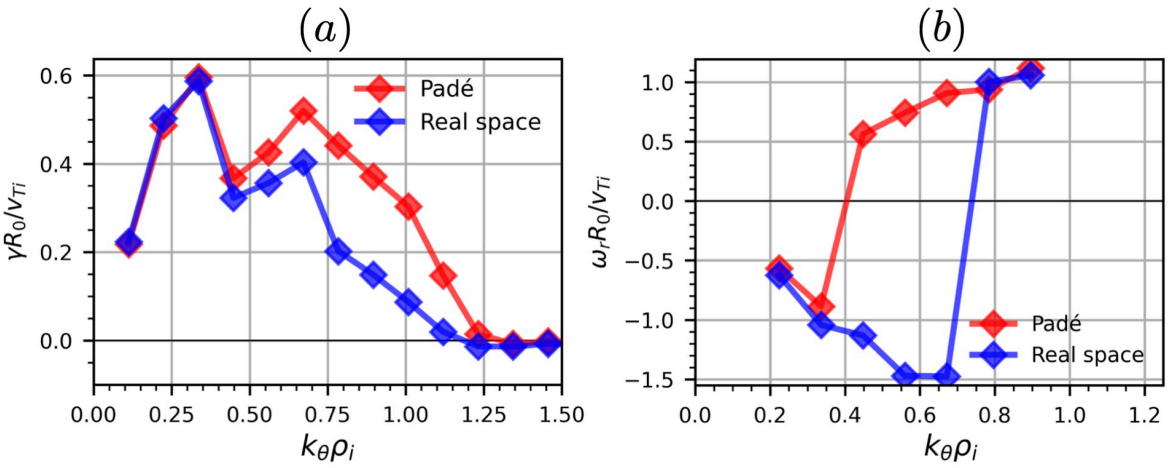

Fig. 6.16: Linear growth rate (a) and real frequency (b) for the case with the Padé approximation and with the real space solver.

When conducting simulations with the hybrid electron model, where both the ITG

mode and TEM become unstable, one must be cautious as the results could vary depending on computation methods for gyro-phase averaging. As mentioned in Subsection 3.3.1, in GKNET, gyro-phase averaging can be calculated in two ways: using the Padé approximation and by interpolation in real space. Figure 6.16 represents the linear growth rate and real frequency for the initial gradients $(R/L_{Ti}, R/L_{Te}, R/L_{ns}) = (10, 10, 2.22)$, comparing results from the Padé approximation and the real space solver. The impurity concentration is zero and the grid numbers are $(N_r, N_\theta, N_\varphi, N_{v_\parallel}, N_\mu) = (64, 256, 64, 96, 16)$. A positive real frequency represents the rotation in the electron diamagnetic drift direction, while a negative real frequency indicates rotation in the ion diamagnetic drift direction. As shown in Fig. **??**, using the Padé approximation tends to overestimate the high wavenumber components of the linear growth rate. Using the Padé approximation, the TEM is dominant from $k_\theta \rho_i \sim 0.4$, whereas when employing the real space solver, the ITG mode is dominant up to $k_\theta \rho_i \sim 0.8$. This result suggests that the contributions of the ITG mode and TEM to turbulent transport vary depending on numerical methods for gyro-phase averaging.

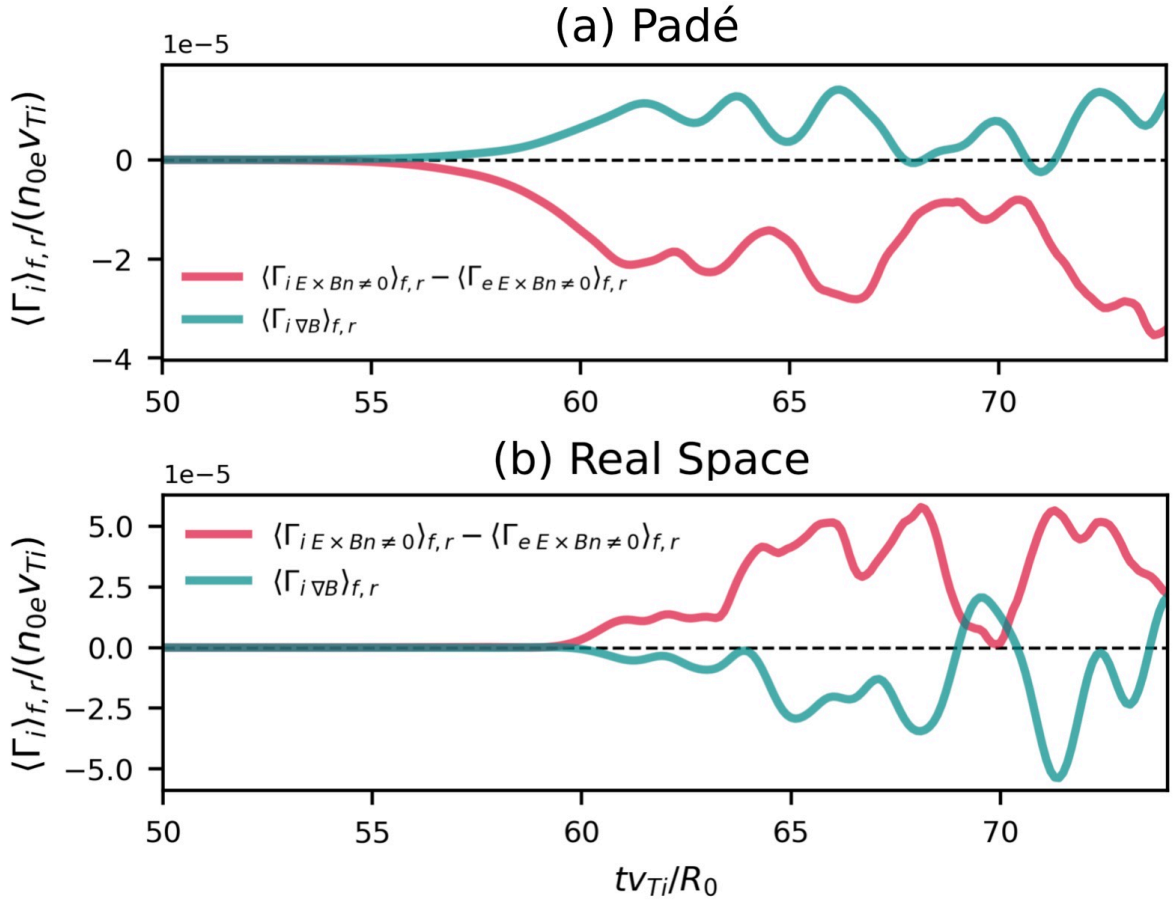

Fig. 6.17: Time evolution of the sum of the turbulent particle fluxes and the particle flux due to the magnetic field drift for the case with the Padé approximation (a) and the case with the real space solver (b).

Figure 6.17 shows the temporal evolution of the sum of the turbulent particle fluxes $\sum_s \langle Z_s \Gamma_{s,turb} \rangle_{f,r} = \langle \Gamma_{i\,E\times B\,n\neq 0} \rangle_{f,r} - \langle \Gamma_{e\,E\times B\,n\neq 0} \rangle_{f,r}$ and the particle flux due to the magnetic drift $\langle \Gamma_{i\,\nabla B} \rangle_{f,r}$ in the case with Padé approximation and with the real-space solver. With the Padé approximation, the turbulent electron particle flux is larger, with $\sum_s \langle Z_s \Gamma_{s,turb} \rangle_{f,r}$ being negative, leading to the formation of a positive radial electric field. On the other hand, for the case with the real space solver, the turbulent ion particle flux is larger, with $\sum_s \langle Z_s \Gamma_{s,turb} \rangle_{f,r}$ being positive, resulting in the formation of a negative radial electric field. A radial electric field induces an up-down asymmetric density fluctuation and $\langle \Gamma_{i\,\nabla B} \rangle_{f,r}$ is increased. When using the Padé approximation compared to when using the real space solver, the sign of the formed radial electric field is reversed. Consequently, $\langle \Gamma_{i\,\nabla B} \rangle_{f,r}$ also has the opposite direction. These differences can be attributed to the overestimation of the TEM in the high wavenumber region by the Padé approximation, especially when the linear growth rates of the ITG mode and TEM are comparable. In this section, we employ the real space solver. In situations where the linear growth rates of the ITG mode and TEM significantly differ, or when only a single mode becomes unstable, although the linear growth rate and real frequency are overestimated by the Padé approximation, the turbulent transport qualitatively remains unchanged regardless of computational methods used for gyro-phase averaging.

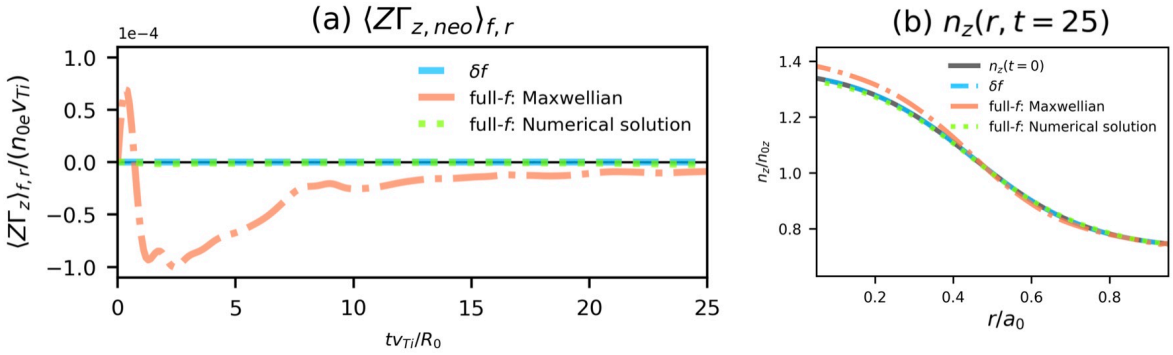

Fig. 6.18: Time evolution of the neoclassical impurity transport (a) and the impurity density profile at $tv_{Ti}/R_0 = 25$ (b) in the δf simulation and the full-f simulations where the initial distribution function is the Maxwellian and the numerical solution of the gyrokinetic Vlasov equation.

Figures 6.18(a) and 6.18(b) show the temporal evolution of the neoclassical impurity transport $\langle Z\Gamma_{z,neo} \rangle_{f,r} = \langle Z\Gamma_{z\,\nabla B} \rangle_{f,r} + \langle Z\Gamma_{z\,E\times B\,n=0} \rangle_{f,r}$ and the radial profile of the

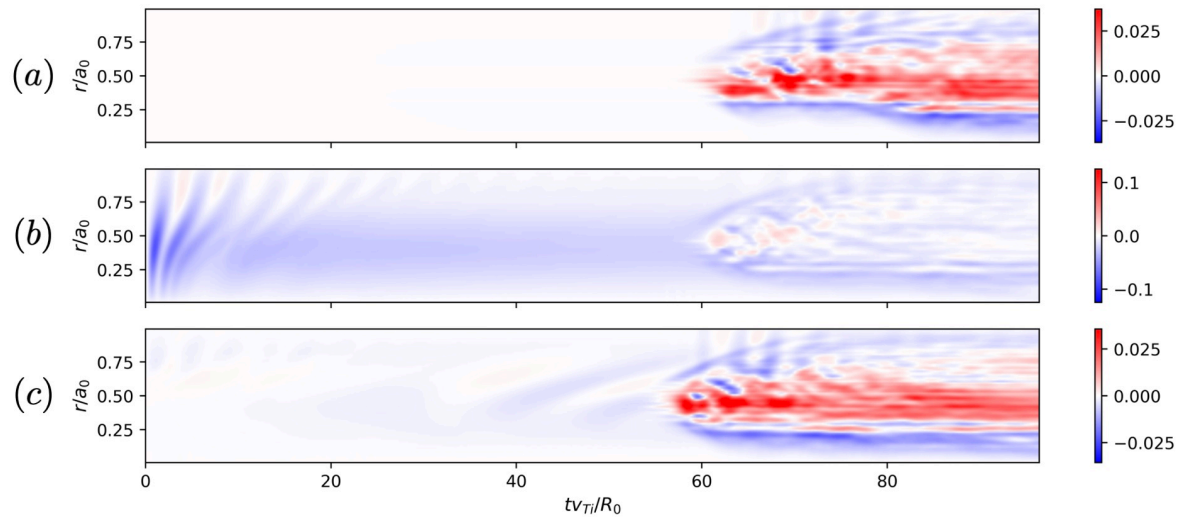

Fig. 6.19: Spatiotemporal evolution of the radial electric field in the case of the δf simulation (a) and the full-f simulations where f_0 is the Maxwellian (b) and the numerical solution of the gyrokinetic Vlasov equation (c).

impurity density at $tv_{Ti}/R_0 = 25$, respectively. The gradients of the initial profiles are $(R/L_{Ti}, R/L_{Te}, R/L_{ns}) = (10, 3, 3)$ and the ITG mode is excited. In the δf simulation, during the linear phase, $\langle Z\Gamma_{z,neo}\rangle_{f,r}$ is zero. On the other hand, in the full-f simulation with the initial distribution f_0 as the Maxwellian, the neoclassical impurity particle flux during the linear phase is about twice as large as the turbulent impurity particle flux. Consequently, the impurity density profile becomes more peaked. The large neoclassical impurity transport can be attributed to the large radial electric field resulting from the initial distribution function not satisfying the gyrokinetic Vlasov equation, and it is considered to be unphysical. When using the numerical solution of the gyrokinetic Vlasov equation as the initial distribution function, as shown in Fig. 6.18, no significant neoclassical impurity transport occurs, and the density profile does not become peaked. The neoclassical impurity particle flux is 2 orders of magnitude smaller than that when using the Maxwellian as f_0. Figure 6.19 depicts the spatiotemporal evolution of the radial electric field $\langle E_r\rangle_{\theta,\varphi}$ for each case. In the full-f simulation using the numerical solution of the gyrokinetic Vlasov equation as the initial distribution function, the structure of the radial electric field resembles that in the δf simulation. In contrast, the results from the full-f simulation using the Maxwellian as the initial distribution function show that the radial electric field is an order of magnitude larger and its structure differs from the other cases. In this case, due to the large Doppler shift frequency, the ITG mode drifts in the direction of the electron diamagnetic drift. In this section, when conducting full-f simulations, we use the numerical solution of the gyrokinetic Vlasov equation as the initial distribution function to avoid numerical impurity accumulation. The larger linear growth rate in the full-f simulation when

using the numerical solution as the initial distribution function compared to that in the δf simulation, is attributed to the mean radial electric field satisfying the radial force balance. Due to the Doppler shift frequency canceling with the real frequency, the ballooning angle decreases, leading to an enhanced linear growth rate [92].

6.2.3 Global gyrokinetic simulation results

The turbulent particle fluxes in the ITG and TEM turbulence have been studied using the fluid model [243] and the gyrokinetic model [267, 268], and a quasilinear particle flux can be expressed as

$$R\frac{\Gamma_s}{n_s} = D_s\frac{R}{L_{ns}} + D_{Ts}\frac{R}{L_{Ts}} + RV_s. \tag{6.17}$$

The transport coefficients D_s, D_{Ts} and the convective velocity V_s are functions of the temperature and density gradients. The second term in Eq. (6.17) represents the thermodiffusion and is expected to be dominant as a result of heating because it is proportional to the temperature gradient. In the presence of impurities, there are degrees of freedom in the particle fluxes as $\Gamma_e \simeq \Gamma_i + Z\Gamma_z$. Therefore, for example, when Γ_e is negative, it does not necessarily imply that Γ_i and Γ_z are also negative.

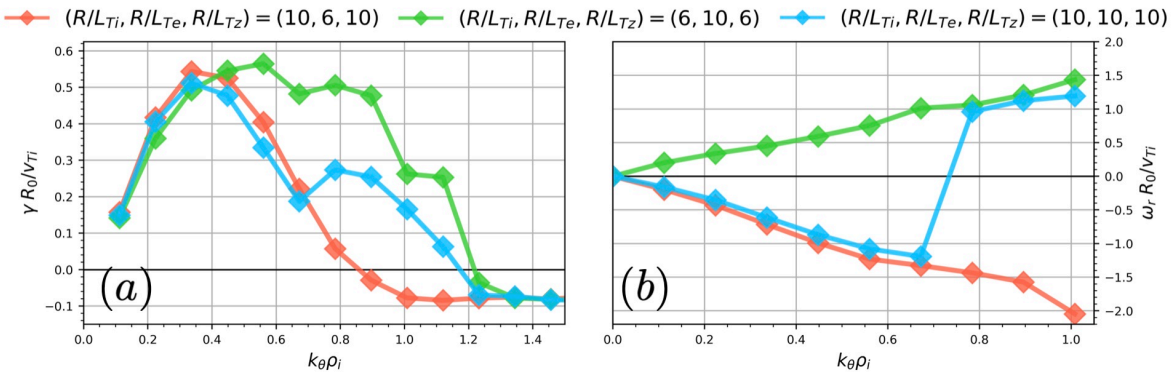

Fig. 6.20: Linear growth rate (a) and real frequency (b) for the cases of $(R/L_{Ti}, R/L_{Te}, R/L_{Tz}) = (10, 6, 10), (6, 10, 6), (10, 10, 10)$.

To investigate the changes in particle fluxes due to heating, we conduct global δf gyrokinetic simulations using the hybrid electron model for cases of ion heating $(R/L_{Ti}, R/L_{Te}, R/L_{Tz}) = (10, 6, 10)$, electron heating $(R/L_{Ti}, R/L_{Te}, R/L_{Tz}) = (6, 10, 6)$, and ion and electron heating $(R/L_{Ti}, R/L_{Te}, R/L_{Tz}) = (10, 10, 10)$. A 1/4 wedge torus with $a_0 = 100$ and $a_0/R = 0.36$ is employed and the grid numbers are $(N_r, N_\theta, N_\varphi, N_{v_\parallel}, N_\mu) = (80, 256, 64, 96, 16)$. The initial density gradients are $(R/L_{ni},$

$R/L_{ne}, R/L_{nz}) = (3, 3, 3)$, and the normalized collision frequency is $\nu_\star = 0.025$. The mass ratio is $\sqrt{m_i/m_e} = 10$ to reduce computational time. Figure 6.20(a) and 6.20(b) show the linear growth rate and real frequency. It can be seen that the ITG mode is dominant for ion heating $(R/L_{Ti}, R/L_{Te}, R/L_{Tz}) = (10, 6, 10)$, while the TEM is dominant for electron heating $(R/L_{Ti}, R/L_{Te}, R/L_{Tz}) = (10, 10, 10)$. In the case of ion and electron heating $(R/L_{Ti}, R/L_{Te}, R/L_{Tz}) = (10, 10, 10)$, the ITG mode is dominant in the low wavenumber region and the TEM is dominant in the high wavenumber region, with the linear growth rate in the low wavenumber region being larger than that in the high wavenumber region. In the case of electron heating, the linear growth rate is the highest. On the other hand, when both ions and electrons are heated, the linear growth rate is the lowest.

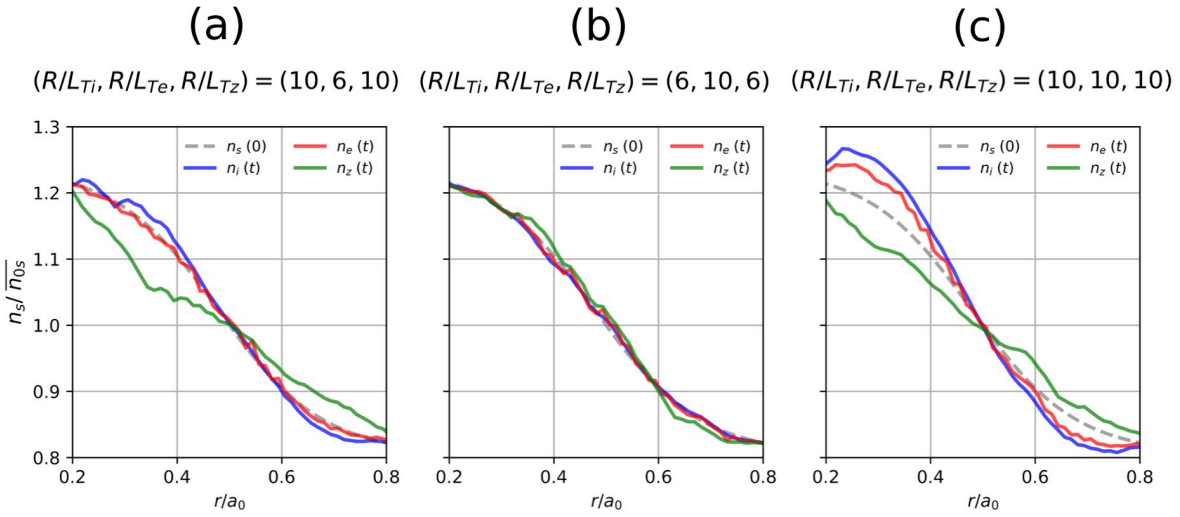

Fig. 6.21: Radial profiles of the bulk ion, electron, impurity densities for $(R/L_{Ti}, R/L_{Te}, R/L_{Tz}) = (10, 6, 10), (6, 10, 6)$, and $(10, 10, 10)$.

Figure 6.21 shows the flux-surface averaged radial profiles of the bulk ion, electron, and impurity density at $tv_{Ti}/R_0 = 90$ after nonlinear saturation, which are normalized by $n_{0i} = 0.8$, $n_{0e} = 1$, and $n_{0z} = 0.33$, respectively. In the case of ion heating, the inward bulk ion transport and outward impurity transport occur, which are roughly balanced $(\Gamma_i + Z\Gamma_z \simeq 0)$. The bulk ion particle flux is negative because the thermodiffusion pinch is dominant. In the absence of impurities, $\Gamma_i \simeq \Gamma_e$ is satisfied and the bulk ion and electron density profile become peaked. However, in the presence of impurities, while the bulk ion density profile becomes peaked, the electron density profile changes little, and the impurity density profile relaxes instead. In the case of electron heating, the negative electron particle flux and the negative bulk ion particle flux are balanced $(\Gamma_i \simeq \Gamma_e)$, and the impurity transport is much smaller than that in other cases. When

the electron density gradient is large and the density gradient driven TEM is dominant, the first term in Eq. (6.17) becomes dominant, so the bulk ion and electron particle fluxes are outward, which leads to particle pump-out. In this case, the impurity particle flux is also outward and the impurity density profile is relaxed. In the case of ion and electron heating, the particle pinch of bulk ions and electrons that is about one order of magnitude larger than that in the other cases results in density peaking, as shown in Fig. 6.21(c). Because the absolute value of the particle flux of bulk ions is larger than that of electrons, the impurity is exhausted outward ($Z\Gamma_z \simeq \Gamma_e - \Gamma_i > 0$). The maximum impurity particle flux in the case of ion and electron heating is about 2.4 times larger than that in the case of ion heating.

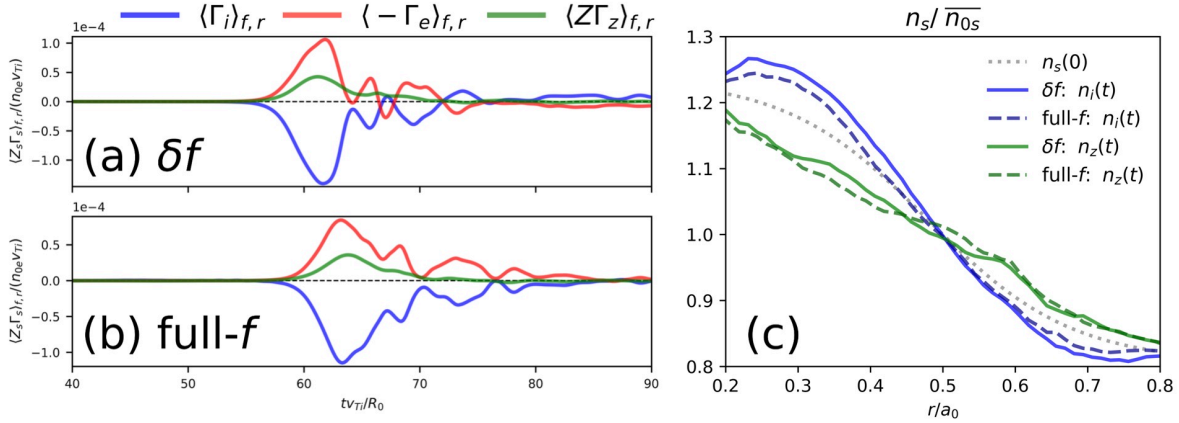

Fig. 6.22: Temporal evolution of the bulk ion, electron, and impurity particle fluxes in the δf simulation (a) and the full-f simulation (b). (c) Radial density profile of bulk ions and impurities for the δf and full-f simulations.

Figures 6.22(a) and 6.22(b) depict the temporal evolution of the bulk ion, electron, and impurity particle fluxes for the ion and electron heating case, as obtained from the δf and full-f simulations, respectively. Due to the Doppler shift frequency, the linear growth rate and turbulence intensity in the full-f simulation are smaller than those in the δf simulation. In the full-f simulation, the large inward bulk ion and electron particle fluxes, as well as the large outward impurity particle flux, are observed. These results are qualitatively consistent with those obtained from the δf simulation. The neoclassical particle fluxes are an order of magnitude smaller than the turbulent particle fluxes. Since electrons have a smaller mass and a shorter time to reach equilibrium, $\langle -\Gamma_{e\,\nabla B}\rangle_{f,r} = \langle -\Gamma_{e\,E\times B\,n=0}\rangle_{f,r}$ is satisfied. As a result, the net electron neoclassical particle flux is nearly zero. On the other hand, due to the larger mass of the impurities, the inward neoclassical particle flux occurs. However, since the turbulent impurity

particle flux is much larger, the impurity density profile is relaxed. Figure 6.22(c) shows the radial profile of the bulk ion and impurity densities at $tv_{Ti}/R_0 = 90$ in the δf and full-f simulations. In both cases, the ion density is peaked and the impurity density is relaxed. The bulk ion density profile in the δf simulation is more peaked than in the full-f simulation. This is attributed to the initial bulk ion density and its gradient being smaller in the full-f simulation compared to those in the δf simulation. The initial distribution function in the full-f simulation is a numerical solution of the gyrokinetic Vlasov equation. Therefore, before conducting the full-f simulation, it is necessary to perform a neoclassical simulation with the electrostatic potential being zero and the initial distribution function as Maxwellian. Due to the neoclassical particle transport, the bulk ion density relaxes, leading to a smaller gradient of the initial bulk ion density in the full-f simulation.

When only the electron temperature gradient is large, the TEM becomes dominant. In this case, neither the particle pinch in bulk ions nor outward impurity transport occurs. When only the ion temperature gradient is large, the ITG turbulence drives a small inward bulk ion particle flux and an outward impurity particle flux. In this case, since the electron temperature gradient is relatively small, the bulk ion particle flux and the impurity particle flux are balanced, resulting in the small electron particle flux. When both ion and electron temperature gradients are large, the large particle pinch occurs for both bulk ions and electrons, along with the large outward impurity transport. The dominant mode in this case is also the ITG mode. To achieve both fuel supply and impurity exhaust, it is essential that the dominant mode is the ITG mode and there is a large electron temperature gradient. We investigate whether the electron pinch occurs as a result of the influence of the electron temperature gradient on the ITG turbulence or if it occurs due to other effects of the electron temperature gradient.

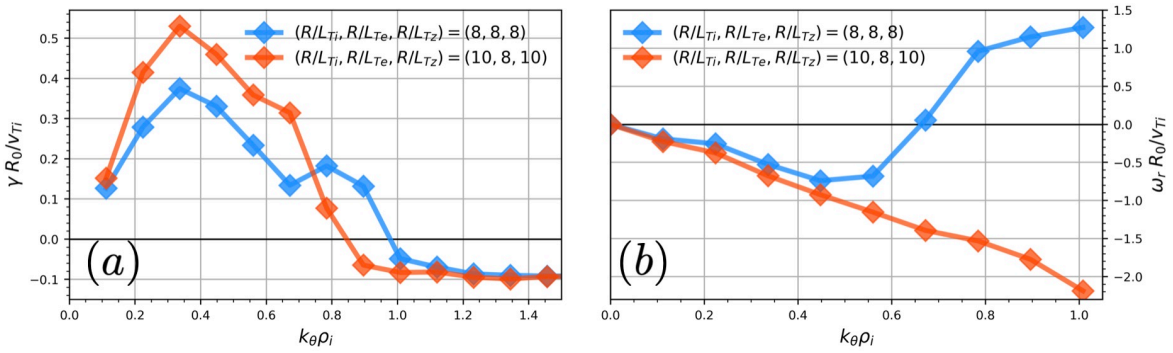

Fig. 6.23: Linear growth rate (a) and real frequency (b) for the cases of $(R/L_{Ti}, R/L_{Te}, R/L_{Tz}) = (8, 8, 8), (10, 8, 10)$.

Figures 6.23(a) and 6.23(b) show the linear growth rate and the real frequency for the cases of $(R/L_{Ti}, R/L_{Te}, R/L_{Tz}) = (8, 8, 8)$ and $(R/L_{Ti}, R/L_{Te}, R/L_{Tz}) = (10, 8, 10)$, respectively. The case of $(R/L_{Ti}, R/L_{Te}, R/L_{Tz}) = (8, 8, 8)$ corresponds to the case where both ions and electrons are heated. In the low wavenumber region, the ITG mode is dominant, while in the high wavenumber region, the TEM is dominant. The linear growth rate of the ITG mode is larger. The case of $(R/L_{Ti}, R/L_{Te}, R/L_{Tz}) = (10, 8, 10)$ corresponds to a situation where ion heating is further applied from the case of $(R/L_{Ti}, R/L_{Te}, R/L_{Tz}) = (8, 8, 8)$. Due to the large ion temperature gradient, the ITG mode is dominant across the entire spectrum. In both cases, the electron temperature gradient is $R/L_{Te} = 8$. If a large electron pinch is induced by the ITG turbulence, one would expect the electron particle flux, along with the inward bulk ion and outward impurity particle fluxes, to be larger in the case of $(R/L_{Ti}, R/L_{Te}, R/L_{Tz}) = (10, 8, 10)$. However, Fig. 6.24 indicates that the particle fluxes in the case of $(R/L_{Ti}, R/L_{Te}, R/L_{Tz}) = (8, 8, 8)$ is larger than those in the case of $(R/L_{Ti}, R/L_{Te}, R/L_{Tz}) = (10, 8, 10)$. This result suggests that even when the temperature gradients and linear growth rate are large, the particle fluxes are smaller. This implies that a significant electron pinch is not necessarily driven by the ITG turbulence only.

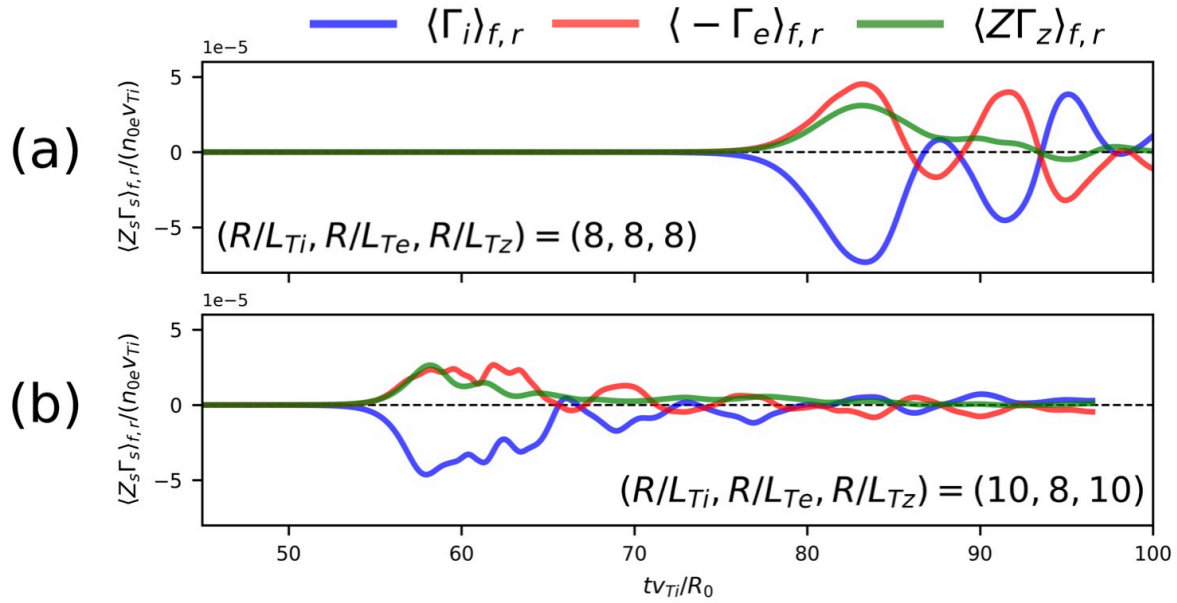

Fig. 6.24: Temporal evolution of the bulk ion, electron, and impurity particle fluxes for $(R/L_{Ti}, R/L_{Te}, R/L_{Tz}) = (8, 8, 8)$ (a) and $(R/L_{Ti}, R/L_{Te}, R/L_{Tz}) = (10, 8, 10)$ (b)

.

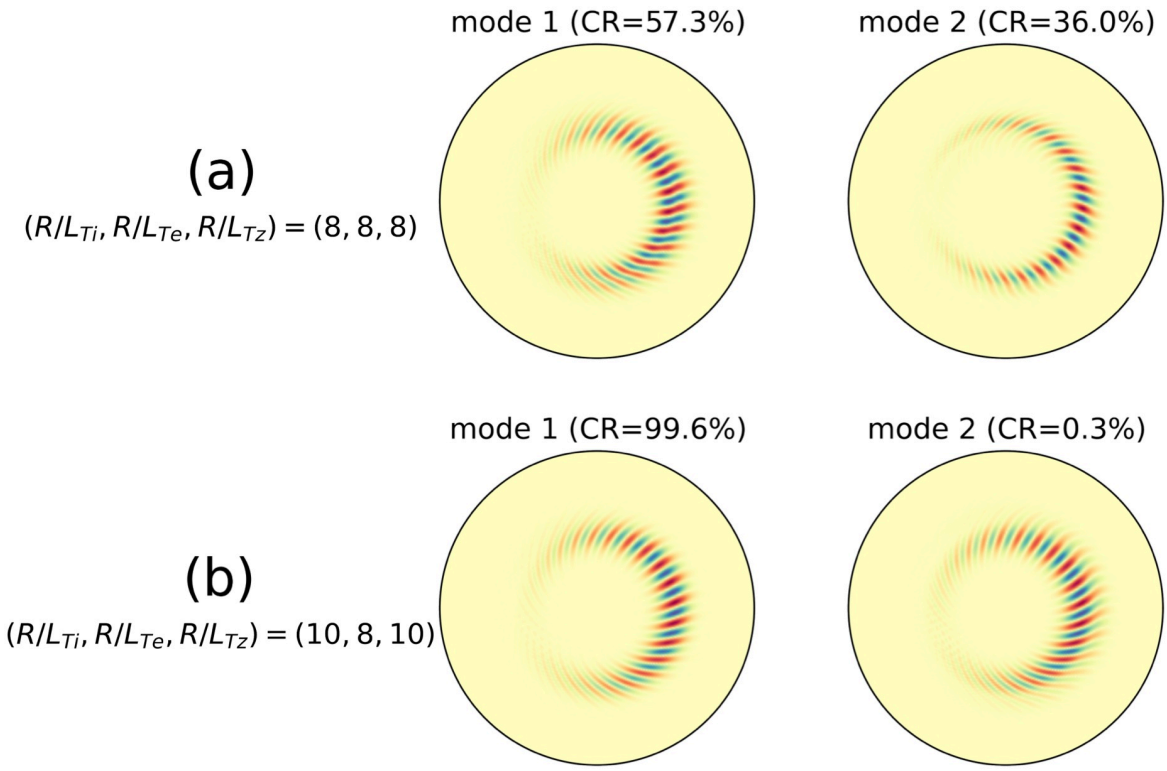

Fig. 6.25: Eigenmodes of the $n = 20$ electrostatic potential the cases of $(R/L_{Ti}, R/L_{Te}, R/L_{Tz}) = (8, 8, 8)$ (a) and $(R/L_{Ti}, R/L_{Te}, R/L_{Tz}) = (10, 8, 10)$ (b)
.

We propose the hypothesis that a significant electron pinch in cases dominated by the ITG mode is also driven by a subdominant TEM. Figure 6.25 shows the eigenmodes of the $n = 20$ electrostatic potential in the linear phase, as obtained by DMD, along with their contribution rates. For the case of $(R/L_{Ti}, R/L_{Te}, R/L_{Tz}) = (10, 8, 10)$, it can be seen that the eigenmode with the largest contribution rate corresponds to the ITG mode and is dominat. On the other hand, for the case of $(R/L_{Ti}, R/L_{Te}, R/L_{Tz}) = (8, 8, 8)$, the second largest contributing eigenmode corresponds to the TEM, and its contribution rate is relatively large. It is worth noting that in this case, the second eigenmode corresponds to the TEM, even for $n = 12$, where the linear growth rate of the ITG mode is the largest. Based on this hypothesis, it can be concluded that the ratio of ITG turbulence intensity to TEM turbulence intensity is crucial for simultaneously achieving fuel supply and impurity exhaust. For the case of $(R/L_{Ti}, R/L_{Te}, R/L_{Tz}) = (10, 8, 10)$, despite the large free energy and turbulence intensity, the small particle fluxes can be explained by the intensity of the ITG turbulence being much larger than that of the TEM turbulence, which did not induce the large electron pinch. From these results, it is suggested that in order to induce a large inward particle transport of bulk ions and electrons and a large outward particle transport of impurities, it is necessary to heat both ions and electrons and maintain an appropriate ratio of the amplitudes

of the ITG mode and the TEM.

Chapter 7

Summary

7.1 Gyrokinetic entropy balances and dynamics

The first-order entropy density equation and the second-order entropy density equation were derived from the gyrokinetic Vlasov equation. The first-order entropy corresponds to thermodynamic entropy. It can be approximated as $S^{(1)} \simeq 3\delta P_i/(2T_i)$, representing the entropy change associated with profile relaxation. On the other hand, the second-order entropy corresponds to the fluctuation entropy and is related to the turbulence intensity. The first-order entropy and the second-order entropy interact through the interaction term α. The simulations revealed that α corresponds to the entropy change due to the heat flux. This implies that the temperature profile in real space and the fluctuations in velocity space interact via the heat flux. From the temporal evolution of the first-order entropy equation, it was found that the entropy production due to the heat flux Γ and the entropy destruction due to the energy input/output $-E$ are balanced. The collision term has little influence on the first-order entropy which is primarily determined the thermodynamic terms. From the temporal evolution of the second-order entropy equation, it was found that the entropy production due to the collisonal dissipation D and the entropy destruction due to the phase mixing $-\Gamma$ are balanced. This entropy balance is consistent with previous studies and suggests that D is determined by Γ. The causality is also demonstrated through the CCF analysis. In the absence of collisions $D = 0$, even when the electrostatic potential is saturated, the second-order entropy decreases due to $-\Gamma$ infinitely. This is the entropy paradox that has been confirmed in previous studies. We identified a new type of entropy paradox wherein the first-order entropy increases to infinity in the absence of energy input/output $E = 0$. This implies that E and D are essential for the system to reach a quasi-steady state. The second-order entropy reaches a steady state more quickly than the first-order entropy. However, it takes a longer time than the turbulence saturation time. In the quasi-steady state, the second-order entropy fluctuates

and its autocorrelation function decays, more rapidly.

The relationship between flow and entropy production is often a subject of debate. Some argue that when ordered flows like zonal flows exists, entropy, which evaluates degree of disorder, should decrease. On the other hand, since entropy is correlated with the temperature gradient, there are those who believe that the zonal flows could lead to an increase in entropy. The entropy balances indicate that entropy is generated by D rather than Γ. This means that the net entropy is produced in velocity space, and turbulence and flows in real space do not directly contribute to entropy generation. It is expected that entropy production rate increases due to the zonal flows. In order to verify this, simulations were performed at different collision frequencies. The simulation results indicate that entropy production rate correlates with the flow shear and increases as confinement performance improves.

On the whole, the second-order entropy is determined by $-\Gamma$ and D. However, it became clear that locally, the second-order entropy is dominated by the advective term. This implies that the turbulence exhibits non-local dynamics, which was not previously shown in previous local gyrokinetic simulations. The fluctuation entropy production rate propagates radially together with the heat avalanches. The positive first-order entropy production rate corresponds to bumps, while the negative one corresponds to voids. The bumps propagate with the outward avalanches, and the voids propagate with the inward avalanches. This is consistent with the symmetry-breaking avalanche theory. Overall, since the first-order entropy production rate increases by the entropy change due to the heat flux, $\partial \mathcal{S}^{(1)}/\partial t$ and Γ are in-phase. Locally, however, due to the time lag for the heat flux to respond to change in the temperature profile, Γ increases after the rise in $\partial \mathcal{S}^{(1)}/\partial t$. The time delay is on the same order as the inverse of the linear growth rate. The relationship between Γ and D holds locally. D increases after an increase in Γ. Locally, the entropy change due to the entropy advection is more significant than the entropy increase from the collisional dissipation.

7.2 Effects of magnetic island on profile formation

In order to investigate the effects of magnetic islands on turbulent transport and profile formation, we performed neoclassical and turbulent simulations with a $(m, n) = (2, 1)$ static magnetic island. When magnetic islands are present, the computation of the flux-surface average is challenging. Consequently, even for the adiabatic electron model or the hybrid electron model, solving the electrostatic gyrokinetic Poisson equation is difficult. To address this issue, we developed a novel algorithm called the labeling method. The method consists of three steps: (1) calculating the equations for the magnetic field lines, (2) grouping the 3D real space grid points, and (3) taking the average

for each group. In the absence of magnetic islands, all grid points are located on the magnetic surfaces, and the flux-surface average computed using the labeling method closely matches that of the precise calculation. When a magnetic island is present, it was confirmed that, in addition to the $(0,0)$ component, the $(2,1)$ harmonics have a large value. With the implementation of the labeling method, we were able to reproduce the previously reported results where the $(0,0)$ electrostatic potential $\phi_{(0,0)}$ and the $(2,1)$ electrostatic potential $\phi_{(2,1)}$ oscillate at the GAM frequency. $\phi_{(0,0)}$ and $\phi_{(2,1)}$ are out of phase with $\phi_{(1,0)}$ by $\pi/2$. Therefore, it is considered that the oscillation of $\phi_{(2,1)}$ originates from an electric field that produces the polarization current, balancing the diamagnetic current.

In the neoclassical simulation, it was found that when only the gyrokinetic Vlasov equation is computed while the electrostatic potential is zero, the ion temperature and density profiles are flattened at the O-point, however when both the gyrokinetic Vlasov equation and the gyrokinetic Poisson equation are self-consistently solved, although the temperature profile is flattened at the O-point, the density profile is not flattened. From the numerical calculation of the parallel force balance equation which is derived from the gyrokinetic Vlasov equation, it was found that inside the magnetic island, $(1/m_i)(\partial/\partial r)\left\langle p_\parallel b_r\right\rangle_{\theta,\varphi} = \langle nA_{Er}\rangle_{\theta,\varphi}$ is satisfied. $(1/m_i)(\partial/\partial r)\left\langle p_\parallel b_r\right\rangle_{\theta,\varphi}$ represents the force derived from parallel streaming, and $\langle nA_{Er}\rangle_{\theta,\varphi} \equiv \left\langle \iint (e/m_i^2) B_r^* E_r f_i dv_\parallel d\mu \right\rangle_{\theta,\varphi}$ is the force due to the mean radial electric field. When the electrostatic potential is zero, the parallel momentum is driven by $(1/m_i)(\partial/\partial r)\left\langle p_\parallel b_r\right\rangle_{\theta,\varphi}$, causing the density profile to relax. On the other hand, when the gyrokinetic Vlasov equation and the gyrokinetic Poisson equation are self-consistently solved, $(1/m_i)(\partial/\partial r)\left\langle p_\parallel b_r\right\rangle_{\theta,\varphi}$ balances with the force due to the radial electric field, preventing the density profile from becoming flat. The issue of whether the gradients of the profiles inside the magnetic island relax is of importance because it greatly influences the stability of the NTM and the associated confinement performance. In previous studies, it has been pointed out that the density gradient inside the magnetic island is maintained due to the presence of trapped particles and collisional transport. The finding that the density profile does not relax due to the force from the radial electric field is novel. The destabilizing effects due to magnetic islands cannot be adequately evaluated unless the evolution of the background profiles is also computed self-consistently. In previous studies, this effect could have been overestimated.

The turbulence simulation was conducted for the input power of 2 MW, and the size PDF was calculated. Inside the magnetic island, it was observed that the turbulence vortices are smaller than in the absence of a magnetic island. Moreover, around the periphery of the magnetic island, the turbulent vortices are torn apart, leading to an increase in the number of small vortices, and it was also noted that there is a decrease

in the relatively large vortices. This is believed to be due to the shearing effects of the mesoscale vortex mode, which has the same mode numbers as the magnetic island. The area of the vortex mode is larger than that of the turbulence vortices. For $\beta = 0.05$, the distribution of positive and negative heat fluxes with respect to the size is similar in cases with and without the magnetic island. That is, the vortex mode does not significantly contribute to the radial heat flux.

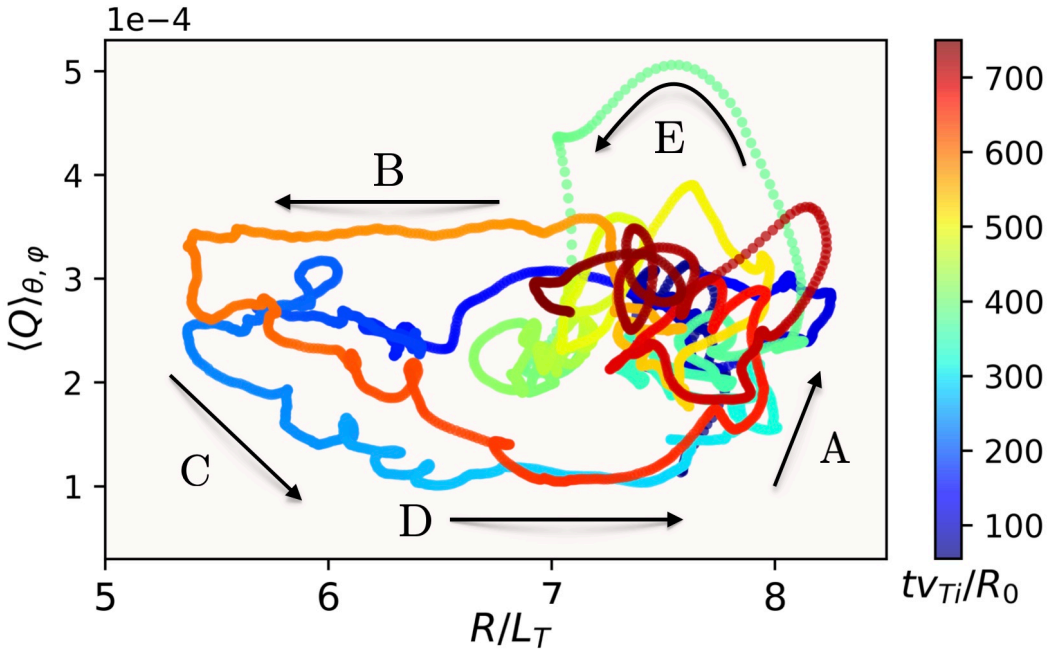

Fig. 7.1: Hysteresis of the turbulent heat flux and temperature gradient length averaged inside the magnetic island.

The results of the flux-driven ITG turbulence simulation where the input power is 16 MW revealed a quasi-periodic transport reduction due to the interaction between the temperature profile and the vortex mode. Figure 7.1 shows the Lissajous plot of the turbulent heat flux and the temperature gradient length averaged inside the magnetic island. The color bar represents the time from $tv_{\mathrm{Ti}}/R_0 = 55$ when the ITG linear mode saturates. The hysteresis loop reflects a predator–prey relationship between the vortex mode and the temperature gradient. The ITG turbulence is driven by the temperature gradient in phase A in Fig. 7.1. Subsequently, the vortex mode grows linearly due to the nonlinear coupling of drift waves. By an analytical analysis based on the Hasegawa-Mima equation, it was confirmed that the vortex mode is excited by two waves. In phase B, the heat transport from the O-point regions to the X-point region occurs, leading to a reduction in the temperature gradient within the magnetic island. It is in antiphase with the amplitude of the vortex mode. The vortex mode

drifts due to the mean electric field, and its drift velocity decreases with the relaxation of the temperature gradient. In phases C and D, because of the shearing effects of the vortex mode and the small temperature gradient, the heat flux and thermal diffusion coefficient inside the magnetic island are reduced. As the temperature gradient becomes small, the amplitude of the vortex mode decreases. When it becomes smaller than the amplitude of the turbulence, the turbulent structure becomes similar to that in the absence of a magnetic island. In phase E, because the vortex mode is absent and there are no shearing effects, the heat avalanche occurs inside the magnetic island. This result suggests that the mean electric field alone is not sufficient to reduce the turbulent heat flux and that the vortex mode is essential for transport reduction.

In this study, a internal transport barrier was not observed. This might be due to the introduction of the relatively small magnetic island $W \simeq 22\rho_i$. In previous study, it has been pointed out that when the island width W exceeds the threshold width $W_t \simeq 33\rho_i$, the flow shear increases proportionally to W. Therefore, by introducing larger magnetic islands, there is a possibility that a internal transport barrier could be formed.

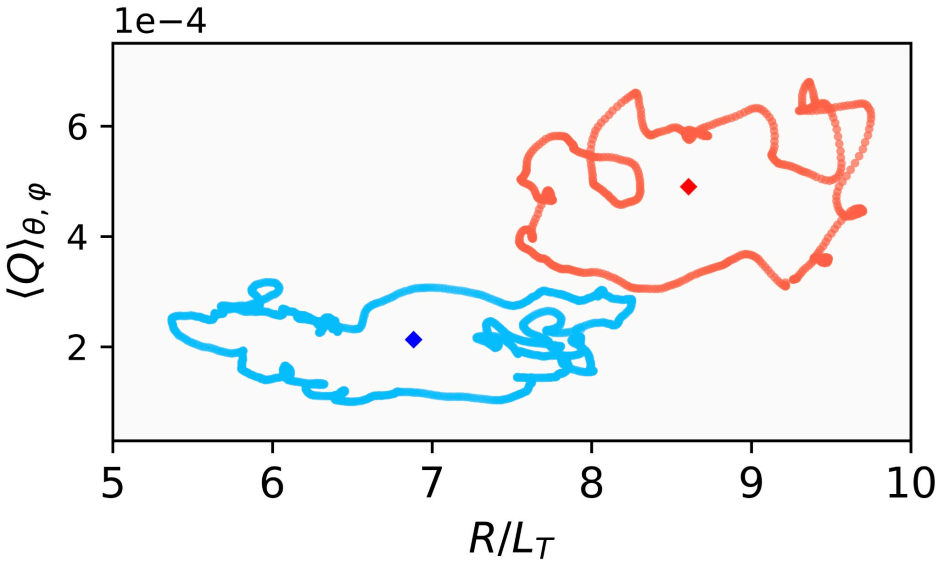

Fig. 7.2: Hysteresis loops for the input powers of 16 MW (blue) and 64 MW (red).

Another approach to form a transport barrier is to increase the input power. Fig. 7.2 shows the Lissajous plots for the input powers of 16 MW and 64 MW. As shown in Fig. 7.2, as the heating power increases, the center of the hysteresis loop shifts to the right. Hence, if the heating is sufficiently strong, a transport barrier could be formed by the positive feedback loop where the temperature gradient increases, leading to the larger mean electric field that suppresses the turbulence, further increasing the temperature gradient.

7.3 Impurity transport and profile formation

In order to investigate the characteristics of the tIM and turbulent transport driven by the tIM turbulence, the stability analysis and gyrokinetic simulations were performed for a hollow impurity density profile.

The stability analysis using a simple fluid model indicates that $\omega_{*i}\omega_{*z} < 0$ and $\omega_{*i}\omega_{Di} > 0$ must be satisfied for the tIM to grow. This condition implies that the ion density gradient is in the opposite direction to the impurity density gradient and is in the same direction as the magnetic field gradient. These are satisfied in the bad curvature region. The results of the stability analysis showed that as $|R/L_{nz}|$ and f_c increase, the linear growth rate of the tIM increases. These dependences were confirmed by the linear gyrokinetic simulations. We proposed the physical mechanism for the tIM similar to an interchange instability. In this model, the tIM is driven by the effective charge gradient, and the instability occurs when the effective charge gradient and magnetic field gradient are in the opposite direction. This condition is satisfied in the bad curvature region when the impurity density has a hollow profile.

The simulations for the tIM were conducted in the absence of temperature gradients. Despite the real frequency of the tIM being in the ion diamagnetic drift direction, it was found that the ballooning angle of the tIM is negative. Furthermore, compared to the case of the pure ITG mode, the ballooning structure is larger, and the center of the mode shifts outward. From the nonlinear global gyrokinetic simulations of the tIM turbulence, it was revealed that the tIM turbulence drives the large inward impurity transport and the large outward ion heat transport. When the linear growth rates of the tIM and the ITG mode are comparable, the impurity transport due to the tIM turbulence is an order of magnitude larger than that due to the ITG turbulence. Furthermore, even when the linear growth rate of the ITG mode is more than twice that of the tIM, the impurity particle flux due to the tIM turbulence is more than twice as large as that due to the ITG turbulence. The previous study showed that the impurity particle flux due to the TEM turbulence is an order of magnitude smaller than that due to the tIM turbulence. It is found that the impurity transport due to tIM turbulence is significant. When the linear growth rates of the tIM and the ITG mode are comparable, despite the absence of a temperature gradient, the absolute value of the ion heat flux due to the tIM turbulence is larger than that due to the ITG turbulence. This indicates a substantial contribution from the off-diagonal terms to the heat flux. Moreover, it was found that the turbulent transport due to the tIM turbulence does not significantly change qualitatively due to the dynamics of electrons.

A robust negative radial electric field was found to form. The profiles of variations in $\langle E_r \rangle_{\theta,\varphi}$ and $\sum_s \langle Z_s \Gamma_{s,turb} \rangle_f$ are similar, indicating that $\sum_s \langle Z_s \Gamma_{s,turb} \rangle_f$ contributes significantly to the formation of this electric field. It is noted that unlike local gy-

rokinetic simulations, in global gyrokinetic simulations, the flute approximation is not strictly valid; thus, the ambipolar condition is not satisfied. In regions where the radial electric field is formed, the turbulence intensity is high, so the contribution from zonal flows may not be negligible.

Due to their lighter mass compared to impurities, the ion density profile reaches a quasi-steady-state faster than the impurity density profile. Therefore, $\langle \Gamma_{i\,\nabla B} \rangle_f$ and $\langle \Gamma_{i\,\boldsymbol{E}\times\boldsymbol{B},n=0} \rangle_f$ are balanced earlier. During the burst phase, this balance is not established. The dynamics of $\langle \Gamma_{i\,\nabla B} \rangle_f$ and $\langle Z\Gamma_{z\,\nabla B} \rangle_f$ in this phase are consistent with the theory of the enhanced neoclassical transport and can be explained by the formation of the negative radial electric field.

For the small temperature gradients, the linear growth rate of the tIM is larger than that of the ITG mode, indicating that the tIM is dominant. Because the contribution from the off-diagonal term proportional to the ion density gradient is large, the inward ion heat flux occurs despite the presence of the negative ion temperature gradient. The inward ion heat flux is greater than the sum of the outward heat flux of impurities and electrons, resulting in the net heat flux directed inward. This result suggests that if the dominant mode changes from the ITG mode to the tIM by impurity injection, the central temperatures and the temperature gradients could increase. For the adiabatic electron model, since $\Gamma_{i,turb} + Z\Gamma_{z,turb} > 0$, a negative radial electric field arises, but the electric field is small due to the minor difference in the turbulent particle fluxes. In the case of the hybrid electron model, $\Gamma_{i,turb} - \Gamma_{e,turb} + Z\Gamma_{z,turb} < 0$, leading to the formation of a positive radial electric field. The direction of a radial electric field changes the direction of the particle transport due to the magnetic drift. In turbulent transport caused by tIM turbulence, the dynamics of electrons play a crucial role, suggesting that they cannot be ignored.

In the presence of the large temperature gradients, the dominant mode is the ITG mode. In contrast to the case where the tIM is dominant, the large outward ion and electron heat fluxes were observed. It was revealed that the large impurity transport is generated by the subdominant tIM even when the ITG mode is dominant. By applying DMD to the time series data of the electrostatic potential in the linear phase, the subdominant mode was detected. Although the contribution rate of the subdominant mode is only 8.5%, it plays a significant role in transport. The electron particle transport is smaller compared to the ion and impurity particle transports, $|\Gamma_{i,turb}|, |Z\Gamma_{z,turb}| \gg |\Gamma_{e,turb}|$. For both the adiabatic electron model and the hybrid electron model, since $\Gamma_{i,turb} + Z\Gamma_{z,turb} < 0$, a positive radial electric field is formed.

In the presence of a hollow impurity density profile, the large turbulent impurity transport occurs regardless of the dominant mode. If the impurity density becomes a peaked profile by the turbulent and neoclassical impurity flux, the tIM and the ITG

mode are stabilized. as future work, we plan to investigate the statistical properties of turbulent transport by performing gradient-driven δf simulations with a source term. We also plan to verify impurity profile peaking and associated turbulence suppression due to the turbulent and neoclassical impurity transport by performing flux-driven full-f simulations.

We explored control methods to simultaneously achieve fuel supply and impurity exhaust through heating when a peaked impurity density profile is present. When only electrons are heated, the temperature gradient driven TEM becomes dominant. In this case, the particle fluxes are small, the density profiles hardly change, and the initial density gradients are preserved. On the other hand, when only ions are heated, the ITG mode becomes dominant, and the inward bulk ion particle flux and the outward impurity particle flux are observed. $\Gamma_i + Z\Gamma_z \simeq 0$ holds, and the electron particle flux is 5–6 times smaller than the bulk ion and impurity particle fluxes. The impurity density profile relaxes, while the bulk ion and electron density profiles remain largely unchanged. When both ions and electrons are heated, the ITG mode and TEM coexist, with the ITG mode dominating in the low wavenumber region and the TEM prevailing in the high wavenumber region. The linear growth rate is higher in the low wavenumber region. In this case, compared to when only ions are heated, the inward bulk ion particle flux that is 7.1 times larger and the inward electron particle flux that is 14.3 times larger are generated. Since the bulk ion particle flux is large and $Z\Gamma_z \simeq \Gamma_e - \Gamma_i > 0$, the impurity particle flux is positive and 2.4 times larger than that when only ions are heated. As a result, the density profiles of bulk ions and electrons become significantly peaked, and the impurity density profile is substantially relaxed. It was found from the full-f simulation that these particle fluxes are driven by turbulence, and the neoclassical particle fluxes are an order of magnitude smaller than the turbulent particle fluxes. These results indicate that fuel supply and impurity exhaust can be achieved when the dominant mode is the ITG mode and there is a large electron temperature gradient.

With only a large ion temperature gradient, the dynamics of the densities is roughly determined by the bulk ion and impurity particle fluxes. The presence of a large electron temperature gradient and the resulting significant inward electron particle flux are crucial for achieving both fuel supply and impurity exhaust. To investigate what drives this electron particle flux, we peformed the simulation in the case where ions are strongly heated and electrons are heated. The ITG mode is dominant across the entire spectrum, and the linear growth rate is larger than that when both ions and electrons are heated to the same degree. However, in this case, the turbulent particle fluxes are smaller. The result suggests that the large electron particle flux is not solely driven by the ITG turbulence. We believe that a subdominant TEM

plays a significant role. This is because the turbulent particle fluxes are larger when the contribution rate of the subdominant TEM is large, even when the temperature gradients and linear growth rate are small. It was found that by heating both ions and electrons and maintaining an appropriate ratio of ITG turbulence intensity to TEM turbulence intensity, it is possible to achieve both fuel supply and impurity exhaust.

We plan to perform full-f simulations to investigate whether fuel supply and impurity exhaust can be achieved by gradually increasing the temperature gradients by heating from small temperature gradients. Additionally, it is needed to examine the impurity species dependency in detail. As the charge and mass of impurities increase, instabilities stabilize, implying that high heating power could be required to exhaust of high Z impurities using this method. We plan to investigate the necessary heating power and temperature gradients for their exhaust. In this study, the self-collision operator is employed, so neoclassical transport was not accurately evaluated. There is also a need to implement a multi-species collision operator and precisely evaluate the magnitude of neoclassical transport.

Appendix A

Size probability distribution function analysis

The size probability distribution function (size-PDF) analysis is a method developed to elucidate features of real-space turbulent vortices that cannot be captured by spectral analysis [180]. By using this analysis, the probability distribution function for the size of turbulent eddies and the contribution of each vortex to the heat flux can be obtained. The method initially labels each eddy from the real-space three-dimensional data of the heat flux and electrostatic potential obtained from gyrokinetic simulations, as illustrated in Fig. A.1. Although turbulent eddies inherently possess a three-dimensional structure, in this method, two-dimensional turbulent vortices in a poloidal cross-section are considered independent from those in other poloidal cross-sections. After labeling the turbulence vortices in each poloidal cross-section, these results are aggregated, and statistical outcomes are produced. Therefore, as N_φ increases, the accuracy of the analysis increases. The analysis is conducted using N_φ cores. Each core simultaneously labels the turbulence vortices in a different poloidal cross-section. Therefore, the computational time does not depend on N_φ.

To label the turbulence vortices in real space, the data in two-dimensional polar coordinates $Q(r, \theta)$ is first converted to data in two-dimensional Cartesian coordinates $Q(x, y)$. The conversion formulas are given by $r = x^2 + y^2$ and $\theta = \arctan(y/x)$. The number of meshes in the x direction and y direction is given by $N_I = N_x = N_y = 1500$, which is considerably larger compared to N_r and N_θ. In the Cartesian coordinates, the mesh width is $\Delta x = \Delta y = 2a_0/N_I\rho_i$ and the cell size is $\Delta x \Delta y = (2a_0/N_I)^2\rho_i^2$. Since $Q(x, y)$ is not a value on the nodes in the polar coordinates, it is necessary to evaluate the value through interpolation. In this analysis, the bilinear interpolation, as explained in Fig. A.2, is employed. In Fig. A.2, θ_1, θ_2, r_1, r_2, Q_1, Q_2, Q_3, and Q_4

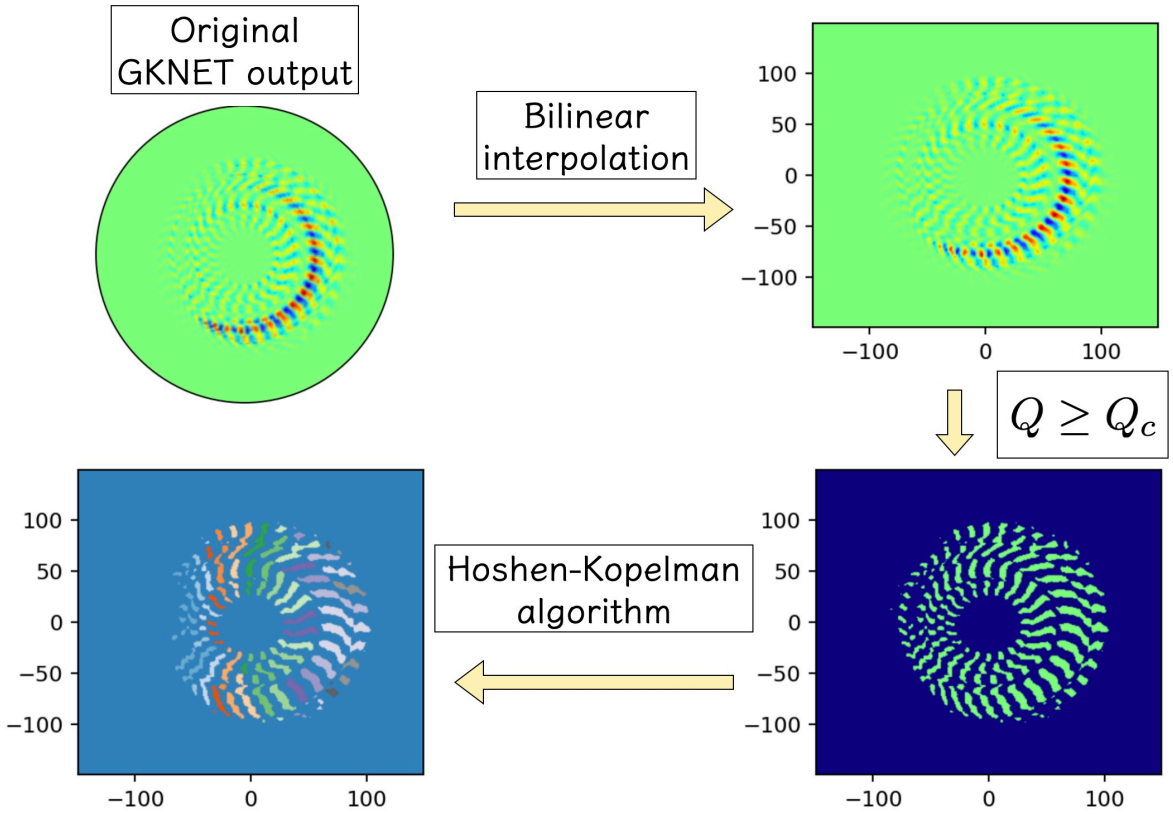

Fig. A.1: Overview of the algorithm for labeling turbulent eddies.

are, respectively, $\theta_1 = \theta - k\Delta\theta$, $\theta_2 = \Delta\theta - \theta_1$, $r_1 = (l-1)\Delta r + \Delta r/2$, $r_2 = l\Delta r + \Delta r/2$, $Q_1 = Q(\Delta r/2 + (l+1)\Delta r, \Delta\theta/2 + (k+1)\Delta\theta)$, $Q_2 = Q(\Delta r/2 + l\Delta r, \Delta\theta/2 + (k+1)\Delta\theta)$, $Q_3 = Q(\Delta r/2 + (l+1)\Delta r, \Delta\theta/2 + k\Delta\theta)$, and $Q_4 = Q(\Delta r/2 + l\Delta r, \Delta\theta/2 + k\Delta\theta)$ where where $k = [\theta/\Delta\theta]$ and $l = [(r - \Delta r/2)/\Delta r] + 1$. The areas colored red, blue, green, and yellow are $w_1 = (r^2 - r_1^2)\theta_1/2$, $w_2 = (r_2^2 - r^2)\theta_1/2$, $w_3 = (r^2 - r_1^2)\theta_2/2$, and $w_4 = (r_2^2 - r^2)\theta_2/2$, respectively. The sum of these areas is

$$w = \sum_{i=1}^{4} w_i = \frac{(r_2^2 - r_1^2)\Delta\theta}{2}. \tag{A.1}$$

Therefore, $Q(x, y)$ is evaluated as

$$Q(x, y) = \frac{1}{w} \sum_{i=1}^{4} w_i Q_i. \tag{A.2}$$

It should be noted that we assume that the values change linearly on the radial and poloidal direction, the interpolation itself is performed in the polar system.

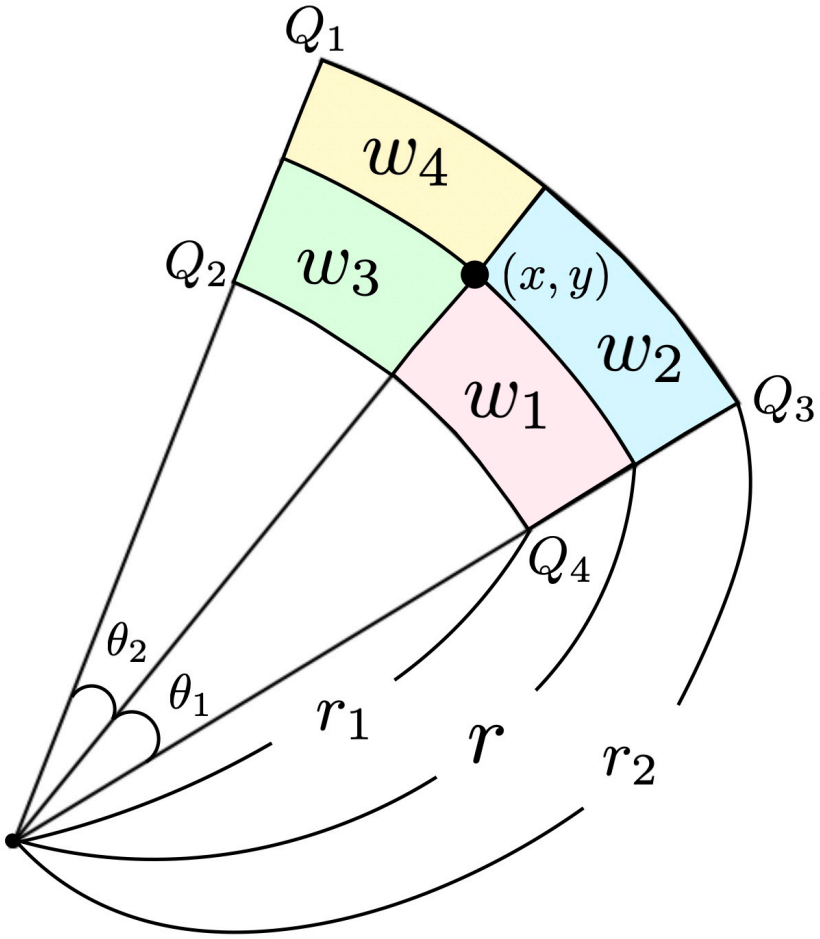

Fig. A.2: Schematic diagram of the bilinear interpolation.

For the case where Q is positive (negative), cells satisfying $Q \geq Q_c$ ($Q \leq -Q_c$) are considered as occupied cells where $Q_c = \beta Q_{\max}$ is a threshold value, and β represents the cutoff ratio to the maximum heat flux $Q_{\max}$. Previous research has shown that $\beta \leq 0.1$ needs to be satisfied [180]. However, in the presence of a magnetic island, the turbulent heat flux cannot be reproduced in Cartesian coordinates unless $\beta \leq 0.01$ as shown in Fig. A.3. Figure A.3 represents the average heat flux at each toroidal angle in both polar and Cartesian coordinates. The red and blue lines respectively represent the positive and negative heat fluxes in Cartesian coordinates, divided by 15. The heat flux corresponds to one at $tv_{Ti}/R_0 = 200$ in the simulation with a magnetic island, as discussed in subsection 5.3.2. (a), (b), and (c) correspond to the cases of $\beta = 0.05$, $\beta = 0.025$, and $\beta = 0.01$, respectively, with the ratio of the net heat flux in Cartesian coordinate to the real net heat flux in polar coordinate being approximately 3%, 56%, and 95%, respectively. In the bottom-right of Fig. A.1, occupied cells are shown in green and unoccupied cells in navy. In order to label clusters composed of occupied cells, the Hoshen-Kopelman algorithm [269], which is based on the union-find algorithm, is employed. Through raster scan, occupied cells are identified and checked

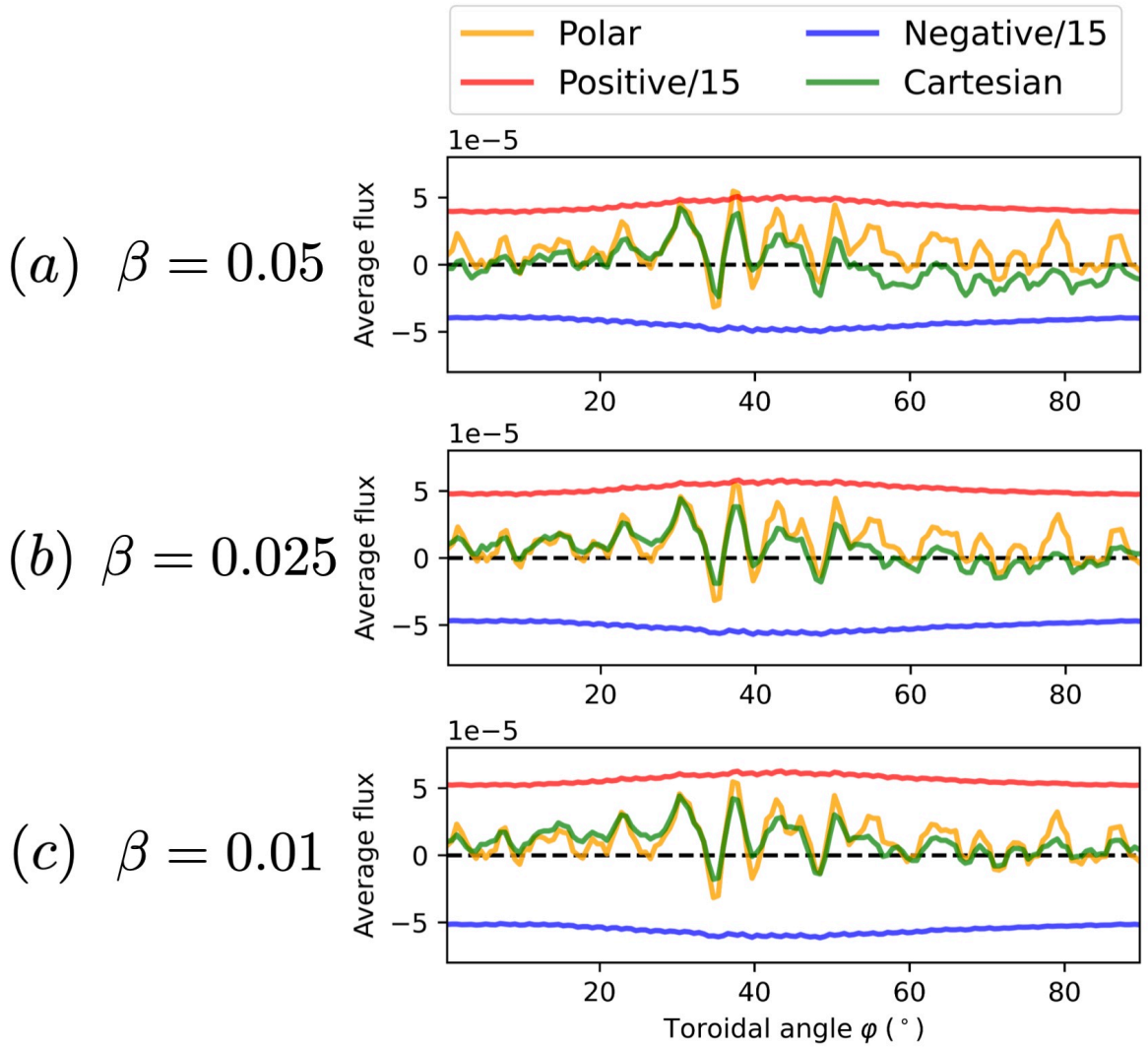

Fig. A.3: Heat flux in each poloidal cross-section in both polar and Cartesian coordinates.

for adjacency with other occupied cells to determine and label clusters. The Hoshen-Kopelman algorithm is described by three functions: `find`, `union`, and `rescan`. They are defined as follows.

function A.1: `find`

```
1 SUBROUTINE find(label_list, k, N, label)
2 IMPLICIT NONE
3 INTEGER k , N , label_list(N) , label
4
5 DO WHILE (label_list(k) .ne. k)
6     k  =  label_list(k)
7 END DO
8     label = label_list(k)
```

```
 9 END SUBROUTINE find
```

function A.2: `union`

```
 1 SUBROUTINE union(left, above, label_list, N)
 2 IMPLICIT NONE
 3 INTEGER left, above, N, label_list(N), x, y
 4
 5 CALL find(label, left, N, x)
 6 CALL find(label, above, N, y)
 7
 8 IF (x .gt. y) THEN
 9     label_list(x) = y
10 ELSE
11     label_list(y) = x
12 END IF
13 END SUBROUTINE union
```

function A.3: `rescan`

```
 1 SUBROUTINE rescan(label, N_I, label_list, N)
 2 IMPLICIT NONE
 3 integer N_I, N, label(N_I, N_I)
 4 integer label_list(N), temp, i, j
 5
 6 DO i = 1 , N_I
 7   DO j = 1 , N_I
 8     IF (label(i, j) .ne. 0) THEN
 9       temp = label(i, j)
10       IF (temp .ne. label_list(temp)) THEN
11         CALL find(label_list, temp, N, label(i, j))
12       END IF
13     END IF
14   END DO
15 END DO
16 END SUBROUTINE rescan
```

`N` is a constant greater than the number of occupied cells and `label_list` records the label for each occupied cell. Initially, each occupied cell is assigned a unique label, therefore, `label_list(k)==k` is satisfied. If `label_list(l)==k` then labels `l` and `k` belong to the same cluster. When there is an occupied cell to the left or above an

occupied cell, `find` is called, and the label of the neighboring occupied cell is assigned to that cell. When there is an occupied cell both to the left and above an occupied cell, `union` is called. In `union`, the labels of the left cell `x` and the upper cell `y` are checked, and the larger label is replaced with the smaller label. After calling `union`, the label of the upper cell is assigned to that cell through `find`. After a raster scan, there still exist the occupied cells that satisfy `label_list(k)`$\neq$`k`. `rescan` aligns all labels of the occupied cells with those provided in `label_list`. Through this algorithm, turbulent vortices are labeled as illustrated in the bottom-left of Fig. A.1. The size of a cluster is determined by the sum of its constituent cells, and the heat flux of the cluster is computed based on the heat flux possessed by its cells. As a result, the relationship between the area and the heat flux of turbulent vortices is obtained.

By labeling the turbulent vortices across all poloidal cross-sections, the number of turbulent vortices generating positive heat flux, N^+, and the number of turbulent vortices producing negative heat flux, N^-, can be determined. To plot the probability distribution function $P^{\pm}(S)$ for the size $S^{\pm}$ of the turbulent vortices on a logarithmic scale, we employ $dS_{\log} = (\log(S_{\max}) - \log(S_{\min}))/N_l$ as the size spacing. N_l represents the number of grid points, $S_{\max}$ and $S_{\min}$ are the maximum and minimum size, respectively, given as $S_{\max} = 5 \times 10^4 \rho_i^2$ and $S_{\min} = \rho_i^2$. The size-PDF $P^{\pm}(S)$ is obtained as

$$P^{\pm}(S) dS_{\text{linear}} = \frac{N_S^{\pm}}{N^{\pm}}, \tag{A.3}$$

where $dS_{\text{linear}} \equiv \exp(\log S + dS_{\log})$ represents the size spacing on a linear scale, and $N_S^{\pm}$ denotes the number of vortices with an area ranging from S to $S + dS_{\text{linear}}$. $P^{\pm}(S)$ satisfies

$$\int_{S_{\min}}^{S_{\max}} P^{\pm}(S) dS_{\text{linear}} = 1. \tag{A.4}$$

It is noted that N_l should be adjusted appropriately, depending on the size and number of turbulent eddies. Figure A.4 shows the size-PDF of the electrostatic potential inside the island. The orange dots display the size-PDF for $N_l = 80$, which is very small compared to analyzing the entire torus, and the blue dots show that for $N_l = 800$. It can be observed that as N_l increases, the size-PDF becomes linear. If the cells are sufficiently small, vortices of exactly the same area do not exist. If the size spacing is exceedingly narrow ($N_l \to \infty$), there exists only one vortex with an area ranging from S to $S + dS_{\text{linear}}$. Hence, the size-PDF becomes a monotonically decreasing straight line.

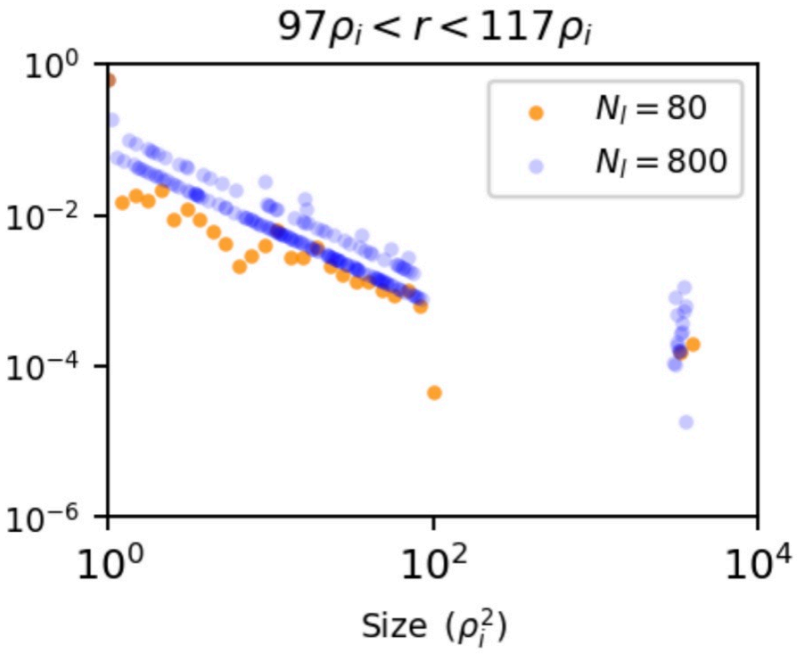

Fig. A.4: Size-PDF of the electrostatic potential inside the island.

Appendix B

Dynamic mode decomposition

A description of the dynamic mode decomposition used to detect the subdominant mode is presented. Dynamic mode decomposition (DMD) is a numerical algorithm that simultaneously extracts the characteristic spatial structures of time series data and its frequencies. This corresponds to finding the eigenfunctions and eigenvalues of the Koopman operator $\mathcal{K}$.

A discrete dynamical system on a state space $\mathcal{S}$ is given by

$$\boldsymbol{x}^{(k+1)} = F\left(\boldsymbol{x}^{(k)}\right), \tag{B.1}$$

using the flow map $F : \mathcal{S} \to \mathcal{S}$ which maps the state $\boldsymbol{x}^{(k)}$ to $\boldsymbol{x}^{(k+1)}$. Defining the Koopman operator $\mathcal{K} : \mathcal{G} \to \mathcal{G}$ as

$$\mathcal{K}g\left(\boldsymbol{x}^{(k)}\right) = g\left(F\left(\boldsymbol{x}^{(k)}\right)\right) = (g \circ F)\left(\boldsymbol{x}^{(k)}\right),$$

which advances observables of the state g linearly on the observable space $\mathcal{G}$, from Eq. (B.1), we obtain

$$g\left(\boldsymbol{x}^{(k+1)}\right) = \mathcal{K}g\left(\boldsymbol{x}^{(k)}\right). \tag{B.2}$$

In DMD, the Koopman operator in Eq. (B.2) is approximated as a matrix $A \in \mathbb{C}^{n\times n}$ that advances the state of a system,

$$\boldsymbol{x}^{(k+1)} \approx A\boldsymbol{x}^{(k)}, \tag{B.3}$$

where n is the dimension of the system state. When m snapshots are collected to make matrices

$$X = \begin{pmatrix} | & | & \dots & | \\ \boldsymbol{x}^{(1)} & \boldsymbol{x}^{(2)} & \dots & \boldsymbol{x}^{(m-1)} \\ | & | & \dots & | \end{pmatrix}, \qquad X' = \begin{pmatrix} | & | & \dots & | \\ \boldsymbol{x}^{(2)} & \boldsymbol{x}^{(3)} & \dots & \boldsymbol{x}^{(m)} \\ | & | & \dots & | \end{pmatrix}, \tag{B.4}$$

Eq. (B.3) becomes

$$X' \approx AX. \tag{B.5}$$

In order to obtain the eigenvalues of A and the corresponding eigenmodes from the time series data, one first finds the matrix A_* that minimizes $J(A) = ||AX - X'||_F^2 \geq 0$, where $||A||_F$ is the Frobenius norm of A. Let a_{ij} be the (i, j) component of A and $A^\dagger$ be the adjoint matrix of A, the Frobenius norm of A is defined as $||A||_F^2 = \mathrm{tr}\left(A^\dagger A\right) = \mathrm{tr}\left(AA^\dagger\right) = \sum_{i,j} a_{ij}^2$. The best fit matrix A_* is given by

$$A_* X X^\dagger = X' X^\dagger. \tag{B.6}$$

When X has r non-zero singular values, the economy singular value decomposition of X is given by

$$X = \hat{U}_r \hat{\Sigma}_r \hat{V}_r^\dagger, \tag{B.7}$$

where $\hat{U}_r$ is an $n \times r$ unitary matrix , $\hat{\Sigma}_r$ is a $r \times r$ diagonal matrix with the ordered singular values along the diagonal and $\hat{V}_r^\dagger$ is the conjugate transpose of a $r \times (m-1)$ unitary matrix $\hat{V}_r$. Substituting Eq. (B.7) into equation Eq. (B.6), A_* is expressed as

$$A_* \hat{U}_r = X' \hat{V}_r \hat{\Sigma}_r^{-1}. \tag{B.8}$$

Since A_* is the large matrix with n rows and n columns, it is unwise to calculate the eigenvalues and eigenvectors of A_*. Using the unitary matrix $\hat{U}_r$ as the change-of-basis matrix, A_* is transformed into a $r \times r$ matrix $\widetilde{A}_*$:

$$\widetilde{A}_* = \hat{U}_r^\dagger A_* \hat{U}_r. \tag{B.9}$$

From Eq. (B.8), $\widetilde{A}_*$ is obtained as

$$\widetilde{A}_* = \hat{U}_r^\dagger X' \hat{V}_r \hat{\Sigma}_r^{-1}. \tag{B.10}$$

$\widetilde{A}_*$ is diagonalized using a invertible matrix W:

$$W^{-1} \widetilde{A}_* W = \Lambda. \tag{B.11}$$

Λ is a $r \times r$ diagonal matrix of eigenvalues of $\widetilde{A}_*$. From Eq. (B.8), (B.9) and (B.11), $A_* \Phi = \Phi \Lambda$ is derived, where Φ is defined as

$$\Phi = X' \hat{V}_r \hat{\Sigma}_r^{-1} W. \tag{B.12}$$

Each column of the $n \times r$ matrix Φ is an eigenfunction representing a characteristic spatial structure. Using the eigenvalues and eigenfunctions, the time evolution from the initial state is described as $\boldsymbol{x}^{(k+1)} = \Phi \Lambda^k \Phi^+ \boldsymbol{x}^{(1)}$, where $+$ denotes the Moore-Penrose pseudoinverse.

The algorithm for DMD is shown below.

1. Create matrices X and X' from time series data. (Eq. (B.4))

2. Approximate X by singular value decomposition as $X = \hat{U}_r \hat{\Sigma}_r \hat{V}_r^\dagger$ (Eq. (B.7))

3. Obtain $\widetilde{A}$ which is a similarity transformation of A as $\widetilde{A} = \hat{U}_r^\dagger X' \hat{V}_r \hat{\Sigma}_r^{-1}$ (Eq. (B.10))

4. Diagonalize $\widetilde{A}$ as $W^{-1}\widetilde{A}W = \Lambda$ (Eq. (B.11))

5. Calculate the eigenmodes of A as $\Phi = X' \hat{V}_r \hat{\Sigma}_r^{-1} W$ (Eq. (B.12))

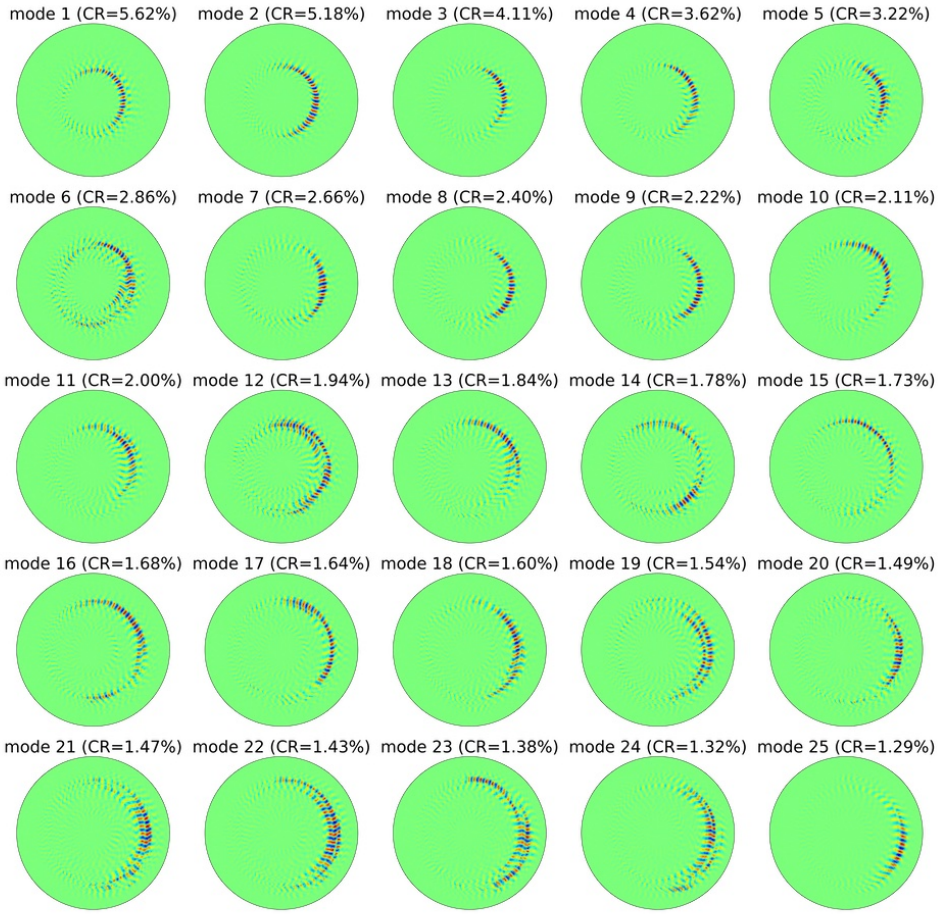

Fig. B.1: Eigenmodes of the $n = 28$ electrostatic potential after nonlinear saturation for Case B in subsection 6.1.4. "CR" is an initialism for contribution rate.

Because it is difficult to apply DMD to the time series data of the turbulent fluctuations after nonlinear saturation, in this study, it is applied to the time series data of

the electrostatic potential in the linear phase to detect subdominant modes. Fig. B.1 shows the eigenmodes of the $n = 28$ electrostatic potential after nonlinear saturation and their contribution rates. It can be seen that there are complex eigenmodes that are a mixture of the IM and ITG mode. It is difficult to separate the eigenmodes into the IM and ITG mode, respectively. The radial electric field changes the phase velocities and ballooning angles, making the problem even more difficult. Figure B.1 also indicates that even with 25 eigenmodes, only 58.1% of the original data can be reproduced. This is because turbulent fluctuations are represented by the superposition of a number of eigenmodes. For the data in the linear phase, the cumulative contribution rate is 93.3% with only three modes, as shown in Fig. 6.14. The difficulty in classifying the many eigenmodes into the IM and ITG mode, respectively, prevents us from determining the relative fluctuation energies of the IM and ITG mode and their contribution to the particle and heat fluxes.

Bibliography

[1] S. Atzeni and J. Meyer-ter-Vehn, *The Physics of Inertial Fusion: BeamPlasma Interaction, Hydrodynamics, Hot Dense Matter*, Oxford University Press (2004)

[2] J. Wesson, *Tokamaks FOURTH EDITION*, Oxford University Press (2011)

[3] S. Li, H. Jiang, Z. Ren, and C. Xu, Abstr. Appl. Anal. **2014**, 940965 (2014).

[4] M. Okamoto, *An Introduction to the Neoclassical Transport Theory (Lecture note)*, RESEARCH REPORT NIFS-PROC Series (1995)

[5] J. Helander and D. J. Sigmar, *Collisional Transport in Magnetized Plasmas*, Oxford University Press (2002)

[6] R. D. Hazeltine and F. L. Waelbroeck, *The Framework of Plasma Physics*, CRC Press (2018)

[7] B. B. Kadomtsev and M. N. Rosenbluth, Sov. Phys. JETP **24**, 1172 (1967).

[8] J. Li and Y. Kishimoto, Plasma Phys. Control. Fusion **44**, A479 (2002).

[9] H. Sugama, J. Plasma Fusion Res. **99**, 346 (2023).

[10] A. Katchalsky and P. F. Curran, *Nonequilibrium Thermodynamics in Biophysics*, Harvard University Press (1981)

[11] H. Sugama and W. Horton, Phys. Plasmas **3**, 304 (1996).

[12] J. Ongena, R. Koch, R. Wolf, and H. Zohm, Nat. Phys. **12**, 398 (2016).

[13] R. G. Littlejohn, J. Math. Phys. **23**, 742 (1982).

[14] J. R. Cary and R. G. Littlejohn, Ann. Phys. **151**, 1 (1983).

[15] R. G. Littlejohn, J. Plasma Physics **29**, 111 (1983).

[16] A. J. Brizard, *Nonlinear gyrokinetic tokamak physics*, Ph. D. dissertation, Princeton University (1990)

[17] H. Sugama, Phys. Plasmas **7**, 466 (2000).

[18] A. J. Brizard and T. S. Hahm, Rev. Mod. Phys. **79**, 421 (2007).

[19] X. Garbet, Y. Idomura, L. Villard, and T. H. Watanabe, Nucl. Fusion **50**, 043002 (2010).

[20] J. A. Krommes, Annu. Rev. Fluid Mech. **44**, 175 (2012).

[21] G. W. Hammett and F. W. Perkins, Phys. Rev. Lett. **64**, 3019 (1990).

[22] G. W. Hammett, W. Dorland, and F. W. Perkins, Phys. Fluids B: Plasma Physics **4**, 2052 (1992).

[23] B. D. Scott, Phys. Plasmas **14**, 102318 (2007).

[24] X. Garbet, L. Garzotti, P. Mantica, H. Nordman, M. Valovic, H. Weisen, and, C. Angioni, Phys. Rev. Lett. **91**, 035001 (2003).

[25] N. Miyato, Y. Kishimoto, and J. Li, Phys. Plasmas **11**, 5557 (2004).

[26] N. Miyato, J. Q. Li, and Y. Kishimoto, Nucl. Fusion **45**, 425 (2005).

[27] H. Sugama, T. H. Watanabe, and W. Horton, Phys. Plasmas **10**, 726 (2003).

[28] W. Horton, Rev. Mod. Phys. **71**, 735 (1999).

[29] H. Sugama, Phys. Plasmas **6**, 3527 (1999).

[30] M. A. Beer, S. C. Cowley, and G. W. Hammett, Phys. Plasmas **2**, 2687 (1995).

[31] O. Kevin, *Study of magnetic shaping effects on plasma flows and micro-instabilities in tokamak plasmas using a full-f gyrokinetic code based on a real space field solver*, Ph. D. dissertation, Kyoto University (2017)

[32] H. Sugama and M. Yagi, J. Plasma Fusion Res. **76**, 1007 (2000).

[33] M. Nunami and M. Nakata, J. Plasma Fusion Res. **99**, 291 (2023).

[34] Z. Zielinski, M. Becoulet, A. I. Smolyakov, X. Garbet, G. T. A. Huijsmans, P. Beyer, and S. Benkadda, Phys. Plasmas **27**, 072507 (2020).

[35] S. I. Braginskii, Rev. Plasma Phys. **1**, 205 (1965).

[36] N. T. Howard, A. E. White, M. L. Reinke, M. Greenwald, C. Holland, J. Candy, and J. R. Walk, Nucl. Fusion **53**, 123011 (2013).

[37] M. Nakata, M. Honda, M. Yoshida, H. Urano, M. Nunami, S. Maeyama, T. H. Watanabe, and H. Sugama, Nucl. Fusion **56**, 2016 (2016).

[38] X. Garbet, P. Mantica, C. Angioni, E. Asp, Y. Baranov, C. Bourdelle, R. Budny, F. Crisanti, G. Cordey, and L. Garzotti *et al.*, Plasma Phys. Control. Fusion **46**, B557 (2004).

[39] W. L. Zhong, K. J. Zhao, X. L. Zou, and J. Q. Dong, Rev. Mod. Plasma Phys. **4**, 11 (2020).

[40] W. L. Zhong, X. L. Zou, C. Bourdelle, S. D. Song, J. F. Artaud, T. Aniel, and X. R. Duan, Phys. Rev. Lett. **111**, 265001 (2013).

[41] T. S. Hahm, Phys. Fluids B: Plasma Physics **3**, 1445 (1991).

[42] D. Grèsillon and M. A. Dubois, *Turbulence and anomalous transport in magnetized plasmas : proceedings of the International Workshop on Small Scale Turbulence and Anomalous Transport in Magnetized Plasmas, held July 6-12th, 1986 at "Institut d'Etude Scientifiques de Cargése", Corse du Sud, France*, Editions de Physique (1987)

[43] N. T. Gladd and Jr., W. Horton, Phys. Fluids **16**, 879 (1973).

[44] S. Hamaguchi and W. Horton, Phys. Fluids B: Plasma Physics **4**, 319 (1992).

[45] Y. Idomura, S. Tokuda, and M. Wakatani, Phys. Plasmas **6**, 4658 (1999).

[46] T. S. Hahm, *Introduction to Tokamak Core Turbulence*, Presented at Kyoto Universiry (2018)

[47] W. Horton, Phys. Rep. **192**, 1 (1990).

[48] A. M. Dimits, G. Bateman, M. A. Beer, B. I. Cohen, W. Dorland, G. W. Hammett, C. Kim, J. E. Kinsey, M. Kotschenreuther, A. H. Kritz *et al.*, Phys. Plasmas **7**, 969 (2000).

[49] W. Horton, Jr., D. I. Choi, and R. D. Estes, Phys. Fluids **22**, 519 (1979).

[50] F. Romanelli and F. Zonca, Phys. Fluids B: Plasma Physics **5**, 4081 (1993).

[51] J. Y. Kim, Y. Kishimoto, M. Wakatani, and T. Tajima, Phys. Plasmas **3**, 3689 (1996).

[52] Y. Kishimoto, J. Y. Kim, W. Horton, T. Tajima, M. J. LeBrun, and H. Shirai, Plasma Phys. Control. Fusion **40**, A663 (1999).

[53] Z. Lin, S. Ethier, T. S. Hahm, and W. M. Tang, Phys. Rev. Lett. **88**, 195004 (2002).

[54] Y. Kishimoto, J. Plasma Fusion Res. **76**, 1280 (2000).

[55] P. Mantica, D. Strintzi, T. Tala, C. Giroud, T. Johnson, H. Leggate, E. Lerche, T. Loarer, A. G. Peeters, A. Salmi *et al.*, Phys. Rev. Lett. **102**, 175002 (2009).

[56] P. Mantica, C. Angioni, C. Challis, G. Colyer, L. Frassinetti, N. Hawkes, T, Johnson, M. Tsalas, P. C. deVries, J. Weiland *et al.*, Phys. Rev. Lett. **107**, 135004 (2011).

[57] R. E. Waltz, G. D. Kerbel, and J. Milovich, Phys. Plasmas **1**, 2229 (1994).

[58] J. E. Kinsey, R. E. Waltz, and J. Candy, Phys. Plasmas **14**, 102306 (2007).

[59] W. Suttrop, M. Kaufmann, H. J. de Black, B. Brüsehaber, K. Lackner, V. Mertens, H. Murmann, J. Neuhauser, F. Ryter, H. Salzmann *et al.*, Plasma Phys. Control. Fusion **39**, 2051 (1997).

[60] J. Citrin, F. Jenko, P. Mantica, D. Told, C. Bourdelle, J. Garcia, J. W. Haverkort, G. M. D. Hogeweij, T. Johnson, and M. J. Pueschel, Phys. Rev. Lett. **111**, 155001 (2013).

[61] M. Barnes, F. I. Parra, E. G. Highcock, A. A. Schekochihin, S. C. Cowley, and C. M. Roach, Phys. Rev. Lett. **106**, 175004 (2011).

[62] P. J. Catto, M. N. Rosenbluth, and C. S. Liu, Phys. Fluids **16**, 1719 (1973).

[63] Y. Kosuga, S. I. Itoh, and K. Itoh, Plasma Fusion Res. **10**, 3401024 (2015).

[64] M. N. Rosenbluth and F. L. Hinton, Phys. Rev. Lett. **80**, 724 (1998).

[65] N. Winsor, J. L. Johnson. J. M. Dawson, Phys. Fluids **11**, 2448 (1968).

[66] K. Itoh, K. Hallatschek, and S. I. Itoh, Plasma Phys. Control. Fusion **47**, 451 (2005).

[67] S. Benkadda, *Turbulent Transport in Fusion Plasmas, First ITER International Summer School*, American Institute of Physics (2008)

[68] H. Sugama and T. H. Watanabe, J. Plasma Physics **72**, 825 (2006).

[69] G. D. Conway, A. I. Smolyakov, and T. Ido, Nucl. Fusion **62**, 013001 (2022).

[70] I. Novikau, *Excitation and damping mechanisms of geodesic acoustic modes in tokamaks*, Ph. D. dissertation, Universität Ulm (2020)

[71] A. Fujisawa, T. Ido, A. Shimizu, S. Okamura, K. Matsuoka, H. Iguchi, Y. Hamada, H. Nakano, S. Ohshima, K. Itoh *et al.*, Nucl. Fusion **47**, S718 (2007).

[72] Y. Asahi, V. Grandgirard, Y. Idomura, X. Garbet, G. Latu, Y. Sarazin, G. Dif-Pradalier, P. Donnel, and C. Ehrlacher, Phys. Plasmas **24**, 102515 (2017).

[73] P. H. Diamond, S. I. Itoh, K. Itoh, and T. S. Hahm, Plasma Phys. Control. Fusion **47**, R35 (2005).

[74] N. Mattor and P. H. Diamond, Phys. Rev. Lett. **72**, 486 (1994).

[75] A. I. Smolyakov, P. H. Diamond, and M. Malkov, Phys. Rev. Lett. **84**, 491 (2000).

[76] R. Balescu, *Aspects of Anomalous Transport in Plasmas*, Institute of Physics Publishing (2005)

[77] P. H. Diamond, and Y. B. Kim, Phys. Fluids B: Plasma Physics **3**, 1626 (1991).

[78] R. F. Abdullatif, *Zonal Flow Generation in Toroidally Confined Plasmas through Modulational Instability of Drift Waves*, Ph. D. dissertation, The Australian National University (2017)

[79] M. Nakata, *Vortices, Zonal Flows, and Transport in Gyrokinetic Plasma Turbulence*, Ph. D. dissertation, The Graduate University for Advanced Studies (2011)

[80] K. Uzawa, Y. Kishimoto, and J. Li, J. Phys. Soc. Japan **77**, 034501 (2008).

[81] Y. Idomura, S. Tokuda, and Y. Kishimoto **45**, 1571 (2005).

[82] J. Li and Y. Kishimoto, Phys. Plasmas **12**, 054505 (2005).

[83] K. Itoh, S. I. Itoh, P. H. Diamond, T. S. Hahm, A. Fujisawa, G. R. Tynan, M. Yagi, and Y. Nagashima, Phys. Plasmas **13**, 055502 (2006).

[84] K. H. Burrell, Phys. Plasmas **4**, 1499 (1997).

[85] Z. Lin, T. S. Hahm, W. W. Lee, W. M. Tang, and R. B. White, Science **281**, 1835 (1998).

[86] N. Miyato, Y. Kishimoto, and J. Li, Phys. Plasmas **11**, 5557 (2004).

[87] N. Miyato, J. Q. Li, and Y. Kishimoto, Nucl. Fusion **45**, 425 (2005).

[88] P. W. Terry, Rev. Mod. Phys. **72**, 109 (2000).

[89] F. L. Hinton and R. D. Hazeltine, Rev. Mod. Phys. **48**, 239 (1976).

[90] Y. B. Kim, P. H. Diamond, and R. J. Groebner, Phys. Fluids B: Plasma Physics **3**, 2050 (1991).

[91] G. Dif-Pradalier, P. H. Diamond, V. Grandgirard, Y. Sarazin, J. Abiteboul, X. Garbet, Ph. Ghendrih, G. Latu, A. Strugarek, S. Ku, and C. S. Cheng, Phys. Plasmas **18**, 062309 (2011).

[92] K. Imadera and Y. Kishimoto, Plasma Phys. Control. Fusion **65**, 024003 (2023).

[93] Y. Camenen, Y. Idomura, S. Jolliet, and A. G. Peeters, Nucl. Fusion **51**, 073039 (2011).

[94] Y. Idomura, M. Ida, T. Kano, N. Aiba, and S. Tokuda, Comput. Phys. Commun. **179**, 391 (2008).

[95] N. Miyato, B. D. Scott, and M. Yagi, Plasma Phys. Control. Fusion **55**, 074011 (2013).

[96] J. R. Cary and R. G. Littlejohn, Ann. Phys. **151**, 1 (1983).

[97] H. Sugama, J. Plasma Fusion Res. **91**, 51 (2015).

[98] M. Nakahara, *GEOMETRY, TOPOLOGY AND PHYSICS SECOND EDITION*, Institute of Physics Publishing (2003)

[99] A. J. Brizard, Phys. Lett. A **291**, 146 (2001).

[100] A. J. Brizard and A. Mishchenko, J. Plasma Physics **75**, 675 (2009).

[101] N. Miyato, B. D. Scott, D. Strintzi, and S. Tokuda, J. Phys. Soc. Jpn. **78**, 104501 (2009).

[102] Y. Idomura, H. Urano, N. Aiba, and S. Tokuda, Nucl. Fusion **49**, 065029 (2009).

[103] Z. Qin, K. Imadera, J. Li, and Y. Kishimoto, Plasma Fusion Res. **13**, 3403083 (2018).

[104] A. Brizard, J. Plasma Physics **41**, 541 (1989).

[105] N. Miyato and B. D. Scott, Plasma Fusion Res. **6**, 1403147 (2011).

[106] K. Obrejan, K. Imadera, J. Q. Li, and Y. Kishimoto, Plasma Fusion Res. **10**, 3403042 (2015).

[107] Y. Idomura, J. Comput. Phys. **313**, 511 (2016).

[108] E. Lanti, B. F. McMillan, S. Brunner, N. Ohana, and L. Villard, J. Phys.: Conf. Ser. **1125**, 012014 (2018).

[109] L. Villard, P. Angelino, A. Bottino, S. J. Allfrey, R. Hatzky, Y. Idomura, O. Sauter, and T. M. Tran, Plasma Phys. Control. Fusion **46**, B51 (2004).

[110] W. W. Lee, J. Comput. Phys. **72**, 243 (1987).

[111] Y. Idomura, J. Plasma Fusion Res. **81**, 581 (2005).

[112] K. Imadera, Y. Kishimoto, K. Obrejan, T. Kobiki, and J. Q. Li, *Proc. 25th Int. Conf. on Fusion Energy*, TH/P5-8, 2014

[113] D. Nakajima, *Study on conservation properties of gyrokinetic equations with multi-species collision operator and magnetic field equilibrium*, master's thesis, Kyoto University (2021)

[114] S. Jolliet, A. Bottino, P. Angelino, R. Hatzky, T. M. Tran, B. F. Mcmillan, O. Sauter, K. Appert, Y. Idomura, and L. Villard, Comput. Phys. Commun. **177**, 409 (2007).

[115] L. Villard, P. Angelino, A. Bottino, S. Brunner, S. Jolliet, B. F. McMillan, T. M. Tran, and T. Vernay, Plasma Phys. Control. Fusion **55**, 074017 (2013).

[116] A. Bottino, B. Scott, S. Brunner, B. F. McMillan, T. M. Tran, T. Vernay, L. Villard, S. Jolliet, R. Hatzky, and A. G. Peeters, IEEE Trans. Plasma Sci. **38**, 2129 (2010).

[117] Y. Idomura, M. Ida, and S. Tokuda, Commun. Nonlinear Sci. Numer. Simul. **13**, 227 (2008).

[118] Y. Idomura, H. Urano, N. Aiba, and S. Tokuda, Nucl. Fusion **49**, 065029 (2009).

[119] Y. Idomura, Phys. Plasmas **21**, 022517 (2014).

[120] V. Grandgirard, M. Brunetti, P. Bertrand, N. Besse, X. Garbet, P. Ghendrih, G. Manfredi, Y. Sarazin, O. Sauter, E. Sonnendrücker *et al.*, J. Comput. Phys. **217**, 395 (2006).

[121] V. Grandgirard, Y. Sarazin, X. Garbet, G. Dif-Pradalier, Ph. Ghendrih, N. Crouseilles, G. Latu, E. Sonnendrücker, N. Besse, P. Bertrand, Commun. Nonlinear Sci. Numer. Simul. **13**, 81 (2008).

[122] G. Dif-Pradalier, P. Ghendrih, Y. Sarazin, E. Caschera, F. Clairet, Y. Camenen, P. Donnel, X. Garbet, V. Grandgirard, Y. Munschy *et al.*, Commun. Phys. **5**, 229 (2022).

[123] Y. Morinishi, T. S. Lund, O. V. Vasilyev, and P. Moin, J. Comput. Phys. **143**, 90 (1998).

[124] Y. Idomura, M. Ida, S. Tokuda, and L. Villard, J. Comput. Phys. **226**, 244 (2007).

[125] A. Arakawa, J. Comput. Phys. **135**, 103 (1997).

[126] A. Kacimi, T. Aliziane, and B. Khouider, Int. J. Numer. Anal. Model. **10**, 571 (2013).

[127] S. Satake, R. Kanno, and H. Sugama, Plasma Fusion Res. **3**, S1062 (2008).

[128] S. Satake, Y. Idomura, H. Sugama, and T. H. Watanabe, Comput. Phys. Commun. **181**, 1069 (2010).

[129] N. Crouseilles, M. Mehrenberger, and H. Sellama, Commun. Comput. Phys. **8**, 484 (2010).

[130] Y. Honda, *Study on gyrokinetic simulations using field solvers in real space*, master's thesis, Kyoto University (2019)

[131] J. Maeda, H. Miki, and S. Tsujimoto, Jpn. J. Ind. Appl. Math. **8**, 23 (2013).

[132] M. Aoki, T. Imamura, M. Yokokawa, and Y. Hirota, Jpn. IPSJ SIG Technical Reports, **2018-HPC-163**, 1 (2018).

[133] D. Pekurovsky, SIAM J. Sci. Comput. **34**, C192, 2012

[134] Ö. D. Gürcan, P. H. Diamond, X. Garbet, V. Berionni, G. Dif-Pradalier, P. Hennequin, P. Morel, Y. Kosuga, and L. Vermare, Phys. Plasmas **20**, 022307 (2013).

[135] Y. Kishimoto, K. Imadera, A. Ishizawa, W. Wang, and J. Q. Li, Philos. Trans. Royal Soc. A **381**, 20210231 (2023).

[136] H. Ozawa, A. Ohmura, R. D. Lorenz, and T. Pujol, Rev. Geophys. **41**, 1018 (2003).

[137] Z. Yoshida and S. M. Mahajan, Phys. Plasmas **15**, 032307 (2008).

[138] G. W. Paltridge, Quart. J. R. Met. Soc. **101**, 475 (1975).

[139] R. D. Lorenz, J. I. Lunine, and P. G. Withers, Geophys. Res. Lett. **28**, 415 (2001).

[140] L. M. Martyushev and S. N. Zubarev, Entropy **2015**, 658 (2015).

[141] J. A. Krommes, Phys. Rep. **360**, 1 (2002).

[142] M. Muto, *Study on entropy dynamics of plasma turbulence in non-equilibrium open system*, master's thesis, Kyoto University (2021)

[143] J. A. Krommes and G. Hu, Phys. Plasmas **1**, 3211 (1994).

[144] T. H. Watanabe and H. Sugama, Phys. Plasmas **9**, 3659 (2002).

[145] N. A. Krall and A. W. Trivelpiece, *Principles of Plasma Physics*, McGraw-Hill (1973)

[146] T. Yabe, R. Tanaka, T. Nakamura, and F. Xiao, Mon. Weather Rev. **129**, 332 (2001).

[147] T. Nakamura, R. Tanaka, T. Yabe, and K. Takizawa, J. Comput. Phys. **174**, 171 (2001).

[148] F. Liese and I. Vajda, IEEE Trans. Inf. Theory **52**, 4394 (2006).

[149] A. Lenard and I. B. Bernstein, Phys. Rev. **112**, 1456 (1958).

[150] T. H. Watanabe and H. Sugama, Phys. Plasmas **11**, 1476 (2004).

[151] J. Candy and R. E. Waltz, Phys. Plasmas **13**, 032310 (2006).

[152] T. H. Watanabe and H. Sugama, Nucl. Fusion **46**, 24 (2006).

[153] S. Jolliet, B. F. McMillan, T. Vernay, L. Villard, A. Bottino, and P. Angelino, Phys. Plasmas **16**, 052307 (2009).

[154] Y. Kosuga, P. H. Diamond, and Ö. D. Gürcan, Phys. Plasmas **17**, 102313 (2010).

[155] M. Nakata, T. H. Watanabe, and H. Sugama, Phys. Plasmas **19**, 022303 (2012).

[156] T. H. Watanabe, H. Sugama, M. Nunami, K. Tanaka, and M. Nakata, Plasma Phys. Control. Fusion **55**, 014017 (2013).

[157] Y. Asahi, A. Ishizawa, T. H. Watanabe, H. Sugama, H. Tsutsuji, and S. Tsuji-Iio, Plasma Fusion Res. **10**, 1403047 (2015).

[158] S. Maeyama, Y. Idomura, T. H. Watanabe, M. Nakata, M. Yagi, N. Miyato, A. Ishizawa, and M. Nunami, Phys. Rev. Lett. **114**, 255002 (2015).

[159] A. A. Schekochihin, S. C. Cowley, W. Dorland, G. W. Hammett, G. G. Howes, G. G. Plunk, E. Quataert, and T. Tatsuno, Plasma Phys. Control. Fusion **50**, 124024 (2008).

[160] T. Tatsuno, W. Dorland, A. A. Schekochihin, G. G. Plunk, M. Barnes, S. C. Cowley, and G. G. Howes, Phys. Rev. Lett. **103**, 015003 (2009).

[161] E. Kawamori, Phys. Rev. Lett. **110**, 095001 (2013).

[162] K. Imadera, Y. Kishimoto, and J. Li, Plasma Fusion Res. **5**, 019 (2010).

[163] G. Dif-Pradalier, P. H. Diamond, V. Grandgirard, Y. Sarazin, J. Abiteboul, X. Garbet, Ph. Ghendrih, A. Strugarek, S. Ku, and C. S. Chang, Phys. Rev. E **82**, 025401(R) (2010).

[164] Y. Kosuga, P. H. Diamond, and Ö. D. Gücan, Phys. Rev. Rett. **110**, 105002 (2013).

[165] H. E. Hurst, Trans. Am. Soc. Civ. Eng. **116**, 770 (1951).

[166] M. Gilmore, C. X. Yu, T. L. Rhodes, and W. A. Peebles, Phys. Plasmas **9**, 1312 (2002).

[167] M. Muto, *Investigation of the temporal characteristics of turbulent transport in fusion plasma with momentum injection*, bachelor's thesis, Nagoya University (2019)

[168] P. H. Diamond and T. S. Hahm, Phys. Plasmas **2**, 3640 (1995).

[169] F. Sattin and M. Baiesi, Phys. Rev. Lett. **96**, 105005 (2006).

[170] R. Sanchez and D. E. Newman, Plasma Phys. Control. Fusion **57**, 123002 (2015).

[171] T. S. Hahm and P. H. Diamond, J. Korean Phys. Soc. **73**, 747 (2018).

[172] P. Bak, C. Tang, and Kurt Wiesenfeld, Phys. Rev. A **38**, 364 (1988).

[173] P. Bak, Physica A **163**, 403 (1990).

[174] T. Hwa and M. Kardar, Phys. Rev. A **45**, 7002 (1992).

[175] R. Sánchez, D. E. Newman, and B. A. Carreras, Nucl. Fusion **41**, 247 (2001).

[176] D. E. Newman, B. A. Carreras, P. H. Diamond, and T. S. Hahm, Phys. Plasmas **3**, 1858 (1996).

[177] X. Garbet and R. E. Waltz, Phys. Plasmas **5**, 2836 (1998).

[178] Y. Sarazin, V. Grandgirard, J. Abiteboul, S. Allfrey, X. Garbet, Ph. Ghendrih, G. Latu, A. Strugarek, and G. Dif-Pradalier, Nucl. Fusion **50**, 054004 (2010).

[179] M. Mavridis, H. Isliker, L. Vlahos, T. Görler, F. Jenko, and D. Told, Phys. Plasmas **21**, 102312 (2014).

[180] W. Wang, Y. Kishimoto, K. Imadera, H. R. Liu, J. Q. Li, M. Yagi, and Z. X. Wang, Nucl. Fusion **60**, 066010 (2020).

[181] B. A. Carreras, B. Ph. van Milligen, M. A. Pedrosa, R. Balbín, C. Hidalgo, D. E. Newman, E. Sánchez, M. Frances, I. García-Cortés, J. Bleuel, and M. Endler *et al.*, Phys. Plasmas **5**, 3632 (1998).

[182] P. A. Politzer, Phys. Rev. Lett. **84**,1192 (2000).

[183] Y. H. Xu, S. Jachmich, R. R. Weynants, A. Huber, B. Unterberg, and U. Samm, Phys. Plasmas **11**, 5413 (2004).

[184] A. Scipioni, P. Rishette, G. Bonhomme, and P. Devynck, Phys. Plasmas **15**, 112303 (2008).

[185] O. Pan, Y. Xu, C. Hidalgo, W. L. Zhong, Z. B. Shi, X. Q. Ji, M. Jiang, B. B. Feng, Y. Zhou, J. Cheng *et. al.*, Nucl. Fusion **55**, 113010 (2015).

[186] M. Kikuchi and M. Azumi, Rev. Mod. Phys. **84**, 1807 (2012).

[187] W. Wang, Y. Kishimoto, K. Imadera, J. Q. Li, and Z. X. Wang, Nucl. Fusion **58**, 056005 (2018).

[188] A. Ishizawa, Y. Kishimoto, and Y. Nakamura, Plasma Phys. Control. Fusion **61**, 054006 (2019).

[189] A. Ishizawa and N. Nakajima, Phys. Plasmas **17**, 072308 (2010).

[190] R. D. Hazeltine and J. D. Meiss, *Plasma Confinement*, Addison-Wesley (1992)

[191] H. P. Furth and J. Killeen, Phys. Fluids **6**, 459 (1963).

[192] P. H. Rutherford, Phys. Fluids **16**, 1903 (1973).

[193] Z. Chang, J. D. Callen, E. D. Fredrickson, R. V. Budny, C. C. Hegna, K. M. McGuire, M. C. Zarnstorff, and TFTR group, Phys. Rev. Lett. **74**, 4663 (1995).

[194] E. Poli, A. G. Peeters, A. Bergmann, S. Günter, S. D. Pinches, Phys. Rev. Lett. **88**, 075001 (2002).

[195] Y. Xu, Matter Radiat. at Extremes **1**, 192 (2016).

[196] K. Ida, N. Ohyabu, T. Morisaki, Y. Nagayama, S. Inagaki, K. Itoh, Y. Liang, K. Narihara, A. Yu. Kostrioukov, B. J. Peterson *et al.*, Phys. Rev. Lett. **88**, 015002 (2002).

[197] M. J. Choi, J. Kim, J. M. Kwon, H. K. Park, Y. In, W. Lee, K. D. Lee, G. S. Yun, J. Lee, M. Kim *et al.*, Nucl. Fusion **57**, 126058 (2017).

[198] K. J. Zhao, Y. J. Shi, S. H. Hahn, P. H. Diamond, Y. Sun, J. Cheng, H. Liu, N. Lie, Z. P. Chen, Y. H. Ding *et al.*, Nucl. Fusion **58**, 026002 (2018).

[199] M. Jiang, W. L. Zhong, Y. Xu, Z. B. Shi, W. Chen, X. Q. Ji, X. T. Ding, Z. C. Yang, P. W. Shi, A. S. Liang *et al.*, Nucl. Fusion **55**, 073022 (2015).

[200] L. Bardóczi, T. L. Rhodes, T. A. Carter, A. Bañón Navarro, W. A. Peeble, F. Jenko, and G. McKee, Phys. Rev. Lett. **116**, 215001 (2016).

[201] K. Ida, K. Kamiya, A. Isayama, Y. Sakamoto, and JT-60 Team, Phys. Rev. Lett. **109**, 065001 (2012).

[202] Y. Koide, M. Kikuchi, M. Mori, S. Tsuji, S. Ishida, N. Asakura, Y. Kamada, T. Nishitani, Y. Kawano, T. Hatae *et al.*, Phys. Rev. Lett. **72**, 3662 (1994).

[203] C. Hidalgo, M. A. Pedrosa, E. Sánchez, R. Balbín, A. López-Fraguas, B. van Milligen, C. Silva, H. Fernandes, C. A. F. Varandas, C. Riccardi *et al.*, Plasma Phys. Control. Fusion **42**, A153 (2000).

[204] J. W. Connor, T. Fukuda, X. Garbet, C. Gormezano, V. Mukhovatov, M. Wakatani, the ITB Database Group, and the ITPA Topical Group on Transport and Internal Barrier Physics, Nucl. Fusion **44**, R1 (2004).

[205] T. Estrada, F. Medina, D. López-Bruna, E. Ascasíbar, R. Balbín, A. Cappa, F. Castejón, S. Eguilior, A. Fernández, J. Guasp *et al.*, Nucl. Fusion **47**, 305 (2007).

[206] K. Ida, S. Inagaki, T. Shimozuma, N. Tamura, H. Funaba, K. Narihara, S. Kubo, S. Murakami, A. Wakasa, M. Yokoyama *et al.*, Phys. Plasmas **11**, 2551 (2004).

[207] N. Kenmochi, T. Minami, T. Mizuuchi, C. Takahashi, G. M. Weir, K. Nishioka, S. Kobayashi, Y. Nakamura, H. Okada, S. Kado *et al.*, Sci. Rep. **10**, 5 (2020).

[208] E. Poli, A. Bottino, and A. G. Peeters, Nucl. Fusion **49**, 075010 (2009).

[209] E. Poli, A. Bottino, W. A. Hornsby, A. G. Peeters, T. Ribeiro, B. D. Scott, and M. Siccinio, Plasma Phys. Control. Fusion **52**, 124021 (2010).

[210] K. S. Fang and Z. Lin, Phys. Plasmas **26**, 052510 (2019).

[211] W. A. Hornsby, A. G. Peeters, E. Poli, M. Siccinio, A. P. Snodin, F. J. Casson, Y. Camenen, and G. Szepesi, EPL **91**, 45001 (2010).

[212] W. A. Hornsby, A. G. Peeters, A. P. Snodin, F. J. Casson, Y. Camenen, G. Szepesi, M. Siccinio, and E. Poli, Phys. Plasmas **17**, 092301 (2010).

[213] W. A. Hornsby, A. G. Peeters, M. Siccinio, and E. Poli, Phys. Plasmas **19**, 032308 (2012).

[214] T. S. Hahm, P. H. Diamond, Z. Lin, K. Itoh, and S. I. Itoh, Plasma Phys. Control. Fusion **46**, A323 (2004).

[215] A. Bañón Navarro, L. Bardóczi, T. A. Carter, F. Jenko, and T. L. Rhodes, Plasma Phys. Control. Fusion **59**, 034004 (2017).

[216] J. M. Kwon, S. Ku, M. J. Choi, C. S. Chang, R. Hager, E. S. Yoon, H. H. Lee, and H. S. Kim, Phys. Plasmas **25**, 052506 (2018).

[217] M. Nunami, R. Kanno, S. Satake, H. Takamaru, and T. Hayashi, Plasma Fusion Res. **1**, 038 (2006).

[218] K. J. Zhao, Y. Nagashima, P. H. Diamond, J. Q. Dong, K. Itoh, S. -I. Itoh, L. W. Yan, J. Cheng, A. Fujisawa, S. Inagaki *et al.*, Phys. Rev. Lett. **117**, 145002 (2016).

[219] O. Sauter, C. Angioni, and Y. R. Lin-Liu, Phys. Plasmas **6**, 2834 (1999).

[220] A. Bergmann, E. Poli, and A. G. Peeters, Phys. Plasmas **16**, 092507 (2009).

[221] D. Zarzoso, W. A. Hornsby, E. Poli, F. J. Casson, A. G. Peeters, and, S. Nasr, Nucl. Fusion **55**, 113018 (2015).

[222] G. Dong and Z. Lin, Nucl. Fusion **57**, 036009 (2017).

[223] Z. X. Wang, J. Q. Li, J. Q. Dong, and Y. Kishimoto, Phys. Rev. Lett. **103**, 015004 (2009).

[224] K. Miyamoto, *Fundamentals of Plasma Physics and Controlled Fusion The Third Edition*, NIFS-PROC-88 (2011)

[225] E. A. Lazarus, J. D. Bell, C. E. Bush, A. Carnevali, J. L. Dunlap, P. H. Edmonds, L. C. Emerson, O. C. Eldridge, W. L. Gardner, H. C. Howe *et al.*, J. Nucl. Mater. **121**, 61 (1984).

[226] E. A. Lazarus, J. D. Bell, C. E. Bush, A. Carnevali, B. A. Carreras, W. J. Casson, J. L. Dunlap, P. H. Edmonds, A. C. England, and W. L Gardner, Nucl. Fusion **25**, 135 (1985).

[227] A. M. Messiaen, J. Ongena, U. Samm, B. Unterberg, G. Van Wassenhove, F. Durodie, R. Jaspers, M. Z. Tokaŕ, P. E. Vandenplas, G. Van Oost *et al.*, Phys. Rev. Lett. **77**, 2487 (1996).

[228] J. A. Boedo, J. Ongena, R. Sydora, D. S. Gray, S. Jachmich, R. W. Conn, A. Messiaen, and TEXTOR Team, Nucl. Fusion **40**, 209 (2000).

[229] Z. W. Wu, J. G. Li, B. N. Wan, H. Y. Guo, X. Gao, L. Q. Hu, G. N. Luo, X. Z. Gong, J. S. Hu, W. Gao *et al.*, J. Nucl. Mater. **438**, S576 (2013).

[230] G. McKee, K. Burrell, R. Fonck, G. Jackson, M. Murakami, G. Staebler, D. Thomas, and P. West, Phys. Rev. Lett. **84**, 1922 (2000).

[231] K. W. Hill, S. D. Scott, M. Bell, R. Budny, C. E. Bush, R. E. H. Clark, B. Denne-Hinnov, D. R. Ernst, G. W. Hammett, D. R. Mikkelsen *et al.*, Phys. Plasmas **6**, 877 (1999).

[232] K. W. Hill, M. G. Bell, R. E. Bell, R. Budny, C. E. Bush, D. R. Ernst, G. W. Hammett, D. R. Mikkelsen, H. K. Park, A. T. Ramsey *et al.*, Nucl. Fusion **39**, 1949 (1999).

[233] H. Takahashi, M. Osakabe, K. Nagaoka, S. Murakami, I. Yamada, Y. Takeiri, M. Yokoyama, H. Lee, K. Ida, and R. Seki, Nucl. Fusion **53**, 073034 (2013).

[234] M. Osakabe, H. Takahashi, K. Nagaoka, S. Murakami, I. Yamada, M. Yoshinuma, K. Ida, M. Yokoyama, R. Seki, H. Lee *et al.*, Plasma Phys. Control. Fusion **56**, 095011 (2014).

[235] F. Nespoli, S. Masuzaki, K. Tanaka, N. Ashikawa, M. Shoji, E. P. Gilson, R. Lunsford, T. Oishi, K. Ida, M. Yoshinuma *et al.*, Nat. Phys. **18**, 350 (2022).

[236] J. Q. Dong, W. Horton, and W. Dorland, Phys. Plasmas **1**, 3635 (1994).

[237] J. Q. Dong and W. Horton, Phys. Plasmas **2**, 3412 (1995).

[238] M. Z. Tokar, J. Ongena, B. Unterberg, and R. R. Weynants, Phys. Rev. Lett. **84**, 895 (2000).

[239] J. Li, Z. X. Wang, J. Q. Dong, Y. Shen, L. F. Wang, M. K. Han, and H. R. Du, Nucl. Fusion **60**, 126038 (2020).

[240] K. Kim, J. M. Kwon, C. S. Chang, J. Seo, S. Ku, and W. Choe, Phys. Plasmas **24**, 062302 (2017).

[241] J. Seo, H. Jhang, and J. M. Kwon, Phys. Plasmas **29**, 052502 (2022).

[242] Y. Shen, B. Lyu, H. Zhang, Y. Li, J. Fu, G. Vogel, X. Wang, H. Xu, D. Wu, Q. Zhang *et al.*, Phys. Plasma **26**, 032507 (2019).

[243] X. Garbet, L. Garzotti, P. Mantica, H. Nordman, M. Valovic, H. Weisen, and C. Angioni, Phys. Rev. Lett. **91**, 035001 (2003).

[244] R. Guirlet, C. Giroud, T. Parisot, M. E. Puiatti, C. Bourdelle, L. Carraro, N. Dubuit, X. Garbet, and P. R. Thomas, Plasma Phys. Control. Fusion **48**, B63 (2006).

[245] S. Futatani, X. Garbet, S. Benkadda, and N. Dubuit, Phys. Rev. Lett. **104**, 015003 (2010).

[246] D. Estéve, Y. Sarazin, X. Garbet, V. Grandgirard, S. Breton, P. Donnel, Y. Asahi, C. Bourdelle, G. Dif-Pradalier, C. Ehrlacher *et al.*, Nucl. Fusion **58**, 036013 (2018).

[247] Y. Idomura, K. Obrejan, Y. Asahi, and M. Honda, Phys. Plasmas **28**, 012501 (2021).

[248] M. R. Wade, W. A. Houlberg, and L. R. Baylor, Phys. Rev. Lett. **84**, 282 (2000).

[249] M. R. Wade, W. A. Houlberg, L. R. Baylor, W. P. West, and D. R. Baler, J. Nucl. Mater. **290**, 773 (2001).

[250] B. Coppi, H. P. Furth, M. N. Rosenbluth, and R. Z. Sagdeev, Phys. Rev. Lett. **17**, 377 (1966).

[251] M. K. Han, W. L. Zhong, J. Q. Dong, Z. X. Wang, X. L. Zou, W. Horton, Y. Shen, A. P. Sun, J. L. Wang, J. M. Gao *et al.*, Nucl. Fusion **61**, 046010 (2021).

[252] J. Hong, S. H. Lee, J. Kim, C. R. Seon, S. G. Lee, G. Y. Park, K. D. Lee, S. S. Henderson, H. Y. Lee, J. S. Park *et al.*, Nucl. Fusion **55**, 063016 (2015).

[253] W. L. Zhong, Y. Shen, X. L. Zou, J. M. Gao, Z. B. Shi, J. Q. Dong, X. R. Duan, M. Xu, Z. Y. Cui, Y. G. Li *et al.*, Phys. Rev. Lett. **117**, 045001 (2016).

[254] K. Ida, M. Yoshinuma, M. Osakabe, K. Nagaoka, M. Yokoyama, H. Funaba, C. Suzuki, T. Ido, A. Shimizu, I. Murakami *et al.*, Phys. Plasmas **16**, 056111 (2009).

[255] A. T. Ramsey, C. E. Bush, H. F. Dylla, D. K. Owens, C. S. Pitcher, and M. A. Ulrickson, Nucl. Fusion **31**, 1811 (1992).

[256] Y. P. Zhang, D. Mazon, X. L. Zou, W. L. Zhong, J. M. Gao, K. Zhang, P. Sun, C. F. Dong, Z. Y. Cui, Y. Liu *et al.*, Nucl. Fusion **58**, 046018 (2018).

[257] K. Mukai, S. Masuzaki, Y. Hayashi, T. Oishi, C. Suzuki, M. Kobayashi, T. Tokuzawa, H. Tanaka, K. Tanaka, T. Kinoshita *et al.*, Nucl. Fusion **61**, 126018 (2021).

[258] J. M. Kwon, L. Qi, S. Yi, and T. S. Hahm, Comput. Phys. Commun. **215**, 81 (2017).

[259] Y. Chen, J. Cheng, and S. E. Parker, Phys. Plasmas **30**, 014502 (2023).

[260] T. Parisot, R. Guirlet, C. Bourdelle, X. Garbet, N. Dubuit, F. Imbeaux, and P. R. Thomas, Comput. Plasma Phys. Control. Fusion **50**, 055010 (2008).

[261] T. Fülöp and H. Nordman, Phys. Plasmas **16**, 032306 (2009).

[262] M. Sakai, Y. Sunada, T. Imamura, and K. Rinoie, Trans. Japan Soc. Aero. Space Sci. **58**, 100 (2015).

[263] E. Kaiser, J. N. Kutz, and S. L. Brunton, Mach. Learn.: Sci. Technol. **27**, 035023 (2021).

[264] S. E. Ahmed, P. H. Dabaghian, O. San, D. A. Bistrian, and lonel M. Navon, Phys. Fluids **34**, 066603 (2022).

[265] T. Romba, F. Reimold, R. J. E. Jaspers, A. J. Edmondson, O. P. Ford, B. Geiger, S. Jabłoński, M. Kubkowska, T. W. C. Neelis, P. Zs. Poloskei *et al.*, Plasma Phys. Control. Fusion **65**, 075011 (2023).

[266] C. Angioni and A. G. Peeters, Phys. Rev. Lett. **96**, 095003 (2006).

[267] C. Angioni, E. Fable, M. Greenwald, M. Maslov, A. G. Peeters, H. Takenaga, and H. Weisen, Plasma Phys. Control. Fusion **51**, 124017 (2009).

[268] C. Bourdelle, Y. Camenen, J. Citrin, M. Marin, F. J. Casson, F. Koechl, M. Maslov, and The JET Contributors, Nucl. Fusion **58**, 076028 (2018).

[269] J. Hoshen and R. Kopelman, Phys. Rev. B **14**, 3438 (1976).

Scientific contributions

Published peer-reviewed papers

- Mikiya Muto and Kenji Imadera, "Global gyrokinetic simulation for toroidal impurity mode turbulence", *Phys. Plasmas* **30**, 072303 (2023).
- Mikiya Muto, Kenji Imadera, and Yasuaki Kishimoto, "Effect of magnetic island on profile formation in flux-driven ITG turbulence", *Phys. Plasmas* **29**, 052503 (2022).
- Mikiya Muto, Kenji Imadera, and Yasuaki Kishimoto, "Gyrokinetic entropy balances and dynamics in toroidal flux-driven ITG turbulence", *Phys. Plasmas* **28**, 082304 (2021).

Presentations at academic conferences

- Mikiya Muto, Kenji Imadera, and Akihiro Ishizawa, "Global gyrokinetic simulation for control of fuel supply and impurity exhaust by selective heating", 28th NEXT Workshop, Kyoto University, August 2nd, 2023. (Poster)
- Mikiya Muto and Kenji Imadera, "Gyrokinetic simulation for impurity mode", 27th NEXT Workshop, Kyoto University, August 8th, 2022. (Poster)
- Mikiya Muto, Kenji Imadera, and Yasuaki Kishimoto, "Full-f gyrokinetic simulation for profile formation inside magnetic island", Confinement and Transport Workshop 2021, National Institute for Fusion Science, December 1st, 2021. (Oral)
- Mikiya Muto, Kenji Imadera, and Yasuaki Kishimoto, "Statistical analysis of magnetic island effects on global turbulent vortex structure", JPS Annual Meeting 2021, Online, September 22th, 2021. (Oral)
- Mikiya Muto, Kenji Imadera, and Yasuaki Kishimoto, "Study of entropy dynamics in open system using full-f gyrokinetic ITG turbulence simulations", 27th NEXT Workshop, Online, March 5th, 2021. (Oral)

- Mikiya Muto, Kenji Imadera, and Yasuaki Kishimoto, "Entropy balances in flux-driven ion temperature gradient mode turbulence", 36th JSPF Annual Meeting, Chubu University, December 1st, 2019. (Oral)

- Mikiya Muto, Kenji Imadera, and Yasuaki Kishimoto, "Entropy dynamics in flux-driven ion temperature gradient mode turbulence", 25th NEXT Workshop, Kyoto University, August 8th, 2019. (Poster)

- Yasuaki Kishimoto, Kenji Imadera, Akihiro Ishizawa, Mikiya Muto, Ryutaro Matsui, Jianfu Liu, Rui Zhao, Wei Wang, and Jiquan Li, "Hierarchical and non-local relaxation dynamics and structure formation in toroidal L-mode plasmas", 39th JSPF Annual Meeting, Toyama International Conference Center, November 23th, 2022. (Oral)

- Kenji Imadera, Yasuaki Kishimoto, Mikiya Muto, Shuhei Okuda, Shuhei Genko, Masatoshi Yagi, Nobuyuki Aiba and Haruki Seto, "Code development and simulation study for particle transport analysis in DEMO reactors", 27th NEXT Workshop, Kyoto University, August 9th, 2022. (Oral)

- Kenji Imadera and Mikiya Muto, "Global gyrokinetic simulation for turbulent particle transport", Plasma Simulator Symposium 2022, Online, September 29th, 2022. (Oral)

- Kenji Imadera, Shuhei Okuda, Shuhei Genko, Mikiya Muto, and Yasuaki Kishimoto, "5D full-f gyrokinetic simulation with HPC infrastructures", 2nd Fusion HPC Workshop, Online, December 2nd, 2021. (Oral)

- Kenji Imadera, Mikiya Muto, Akihiro Ishizawa, and Yasuaki Kishimoto, "Global profile formation and relaxation in flux-driven ITG/TEM turbulence", Max Planck Princeton Center Workshop, Max Planck Institute for Solar System Research, January 22th, 2020. (Oral)

- Kenji Imadera, Akihiro Ishizawa, Daichi Nakajima, Mikiya Muto, Zhihao Qin, Wei Wang, and Yasuaki Kishimoto, "Current status and issues in numerical tokamak research with global gyrokinetic code GKNET", 36th JSPF Annual Meeting, Chubu University, December 1st, 2019. (Oral)

Award

- Kenji Imadera, Yasuaki Kishimoto, Mikiya Muto, Daichi Nakajima, and Hiroaki Ohta, "Gyrokinetic numerical experiment of tokamak with kinetic electron", Award for Excellence in Fusion Large Computer Application Research, 2019.

Outreach activity

- Mikiya Muto, Kyoto University Poster Session 2022, March 18th, 2023. (Judge)
- Mikiya Muto, "Does Artificial Sun Solve Energy Problems?", Hyogo Prefectural Akashi Senior High School, December 8th, 2022. (Lecture)
- Mikiya Muto, "Does Artificial Sun Solve Energy Problems?", Kyoto University Campus Guide (10 Global Leaders High Schools in Osaka Prefecture), November 6th, 2022. (Lecture)
- Mikiya Muto, "Does Artificial Sun Solve Energy Problems?", Hoshino High School, November 1st, 2022. (Lecture)
- Mikiya Muto, "Does Artificial Sun Solve Energy Problems?", Chiben Gakuen Senior High School, October 11th, 2022. (Lecture)
- Mikiya Muto, "Does Artificial Sun Solve Energy Problems?", Osaka Prefectural Tondabayashi High School, December 21th, 2021. (Lecture)
- Mikiya Muto, "Does Artificial Sun Solve Energy Problems?", Hyogo Prefectural Akashi Senior High School, December 9th, 2021. (Lecture)
- Mikiya Muto, "Does Artificial Sun Solve Energy Problems?", Kyoto University Training 2021 (Kyoto Municipal Saikyo Senior High School, Kyoto Municipal Horikawa Senior High School, Kyoto Municipal Murasakino Senior High School), November 13th, 2021. (Lecture)
- Mikiya Muto, "Does Artificial Sun Solve Energy Problems?", Saga Prefectural Saga Nishi High School, October 25th, 2021. (Lecture)